

# **Characterising natural ventilation through open windows in the presence of wind**

A theoretical and experimental investigation into the interaction between window geometry and environmental forces, and its application to envelope flow models of natural ventilation

**Patrick Sharpe, MEng**

Thesis submitted to the University of Nottingham for the degree of Doctor of Philosophy

Department of Engineering

June 2023

# Declaration

Except where stated otherwise, the work presented in this thesis is entirely my own. No part has been submitted for another degree at the University of Nottingham or any other institute of learning.

Patrick Sharpe, June 2023



# Abstract

Natural ventilation systems utilise pressure differentials that arise from wind and buoyancy forces to drive air through buildings. Natural ventilation is typically described using envelope flow models. These are used to size window openings at the design stage, and to predict the annual dynamic thermal performance of buildings. However, envelope flow models rely on highly idealised descriptions of flow through ventilation openings, which do not model realistic window geometries encountered in practice, and assume that ambient air is static. When envelope flow models are applied to building design, inadequate accounting for phenomena relating to wind and opening geometry can lead to under-sized ventilation openings and under-performing buildings.

This thesis develops empirical models that characterise the effect of wind and window geometry on ventilation rates through square orifices and square, hinged openings. To ensure that these models can be applied in the design case to an arbitrary building geometry, these models are characterised using conditions *local* to the opening. Here the effect of wind is accounted for by a simulated cross-flow parallel to the building façade, and dimensional scaling arguments are applied to develop empirical models of wind driven phenomena based on similarity theory. Three experimental conditions are modelled: still-air tests that measure the ventilation capacity of an opening in *idealised* conditions; local pressure tests that measure the wind-induced static pressure differential over an opening when no flow occurs through that opening; and dynamic flow tests that measure the ventilation capacity of an opening between these limits.

To validate the use of these local-scale models in building design, this work is then extended to predict the ventilation in a simple two-zone building. This requires the measurement of the speed and direction of the cross-flow on the building façades, and to that end a novel probe is developed that enables simultaneous measurements of these parameters. Wind-tunnel experiments are then used to measure the ventilation rate achieved in the model building, and the results are compared against the predictions of the local-scale window-characterisation models developed in this thesis. The results show an improvement over current models, which tend to overestimate ventilation rates.

This thesis shows that *free area* models, which are widely used to predict the ventilation capacity of

windows, tend to systematically overestimate ventilation rate through simple hinged openings in still air. The Empirical Effective Area Model described in this thesis can be used to predict *idealised* discharge coefficients with a coefficient of determination of 0.98, compared to 0.57-0.74 for *free area* models.

A wind-driven cross-flow is shown to interact with window geometry to alter the local pressure field over the surface of an opening. This thesis develops experimental techniques to characterise this change in pressure using a *local* pressure coefficient. This is used to specify a *local* dimensionless pressure which is shown to describe the transition between inflow and outflow through an opening. Empirical equations are developed that characterise the *local* pressure coefficient for square hinged windows as a function of flow approach angle and opening angle, with a coefficient of determination of 0.98.

The generation of non-zero *local* pressure coefficients is shown to result in *orifice* discharge coefficients that tend to  $\pm\infty$  as the dimensionless room pressure tends to zero. Dimensional analysis is used to suggest the *total* dimensionless volume flow rate as an alternative metric to characterise the ventilation capacity of an opening. This is shown to tend to the *idealised* discharge coefficient in still-air conditions, and to tend to zero as the *local* dimensionless pressure tends to zero. The *total* dimensionless volume flow rate is shown to be finite across the whole range of potential *local* dimensionless pressure values, and holds positive values for outflow and negative values for inflow. Empirical models are developed to predict the *total* dimensionless volume flow rate through a square orifice and a square, hinged window as a function of *local* dimensionless pressure, flow approach angle and opening angle. Coefficients of determination are between 0.975 and 0.984 for the hinged window and between 0.993 and 0.995 for the square orifice, depending on the opening direction and the direction of flow through the opening.

The speed and direction of the cross-flow on the façade of a model cube in a simulated atmospheric boundary layer were measured using the novel cross-flow probe developed in this thesis. Here, mean cross-flow speeds measured with the novel probe agree well with hot-wire measurements. The cross-flow measurements reveal a tetra-modal distribution in *façade* cross-flow direction, which interacts with a uni-modal variation in cross-flow speed to generate bi-modal distributions in the  $x$  and  $y$  velocity components at all measured wind angles. This data is used to generate profiles of mean cross-flow speed and mean *façade* cross-flow direction with wind angle, which are used as inputs to the empirical equations developed to describe the *total* dimensionless volume flow rate through isolated window openings.

The empirical models used to describe the *total* dimensionless volume flow rate through isolated windows is used to predict measured ventilation rates in a model building with an internal partition, with a coefficient of determination between 0.94 and 0.99, depending on the ventilation configuration. This compares with coefficients of determination between -0.4 and 0.08 found when applying a conventional orifice flow model. Conventional orifice flow models are predicted to provide good estimates of net volume flow rates through

buildings with simple orifice-type openings when the internal resistance is lower than that of either of the external openings. As the internal resistance increases, the orifice flow equation is predicted to increasingly overestimate net volume flow rates.

This work contributes to knowledge by: quantifying the systematic errors arising from the use of *free area* models common to natural ventilation design; developing an empirical model that describes an *idealised* discharge coefficient of a family of hinged openings as a function of geometric parameters; identifying novel dimensionless parameters that characterise the change in static pressure across an opening that results from the interaction between wind and window geometry; developing experimental techniques that provide a simple and unambiguous measurement of the *local* pressure coefficient; experimentally and empirically describing the aerodynamic performance of a simple, square, hinged window in wind-driven conditions; developing a cross-flow probe that can measure the instantaneous speed and direction of wind-driven flow over the surface of a building; quantifying the systematic errors associated with the use of a range of calculation methodologies used to estimate the ventilation rate in a simple model building; and providing practical design guidance to minimise the effect of calculation errors that arise from the use of conventional envelope flow models in wind-driven conditions, when adequate data to describe the phenomena is unavailable.



# Acknowledgements

I would like to thank my supervisors Benjamin Jones and Robin Wilson for their support and enthusiasm throughout. I would also like to thank my wife Hayley Sharpe for her emotional support, and for keeping me motivated when working from home.

I am deeply grateful to the staff of the Centre for 3D Design and the Centre for Mechanical Systems in the Department of Architecture and Built Environment, with special thanks to Malcolm Dugdale, Daniel Cooper and Tony Gospel for their support, input and labour in developing experimental setups and equipment.

I would also like to extend my gratitude to John Owen for the use of the atmospheric boundary layer wind tunnel that has formed the backbone of experimental work undertaken for this thesis. Furthermore, I would like to express my thanks to Tung Nguyen for his support in setting up data measuring equipment and data logging software.

Finally, I am grateful to the EPSRC for providing the funding that made this research possible.





# Publications

- Sharpe, P., Jones, B. Wilson, R. and Iddon, Chris., 2021. What we think we know about the aerodynamic performance of windows. *Energy and Buildings*
- Sharpe, P., Jones, B and Wilson, R. 2021, Modelling methods for predicting the aerodynamic performance of ventilation openings, *CIBSE Technical Symposium*



# Contents

Declaration . . . . .	i
Abstract . . . . .	iii
Acknowledgements . . . . .	vii
Publications . . . . .	ix
Table of contents . . . . .	xviii
List of figures . . . . .	xxiii
List of tables . . . . .	xxvii
Nomenclature . . . . .	xxvii
<b>1 Introduction</b>	<b>1</b>
1.1 Purpose of providing ventilation to buildings . . . . .	1
1.1.1 Indoor air quality . . . . .	1
1.1.2 Thermal comfort . . . . .	2
1.2 Choice of ventilation concept . . . . .	3
1.2.1 Natural ventilation . . . . .	3
1.2.2 Mechanical ventilation . . . . .	4
1.3 The problem with natural ventilation . . . . .	4
1.4 Aims and objectives . . . . .	5
<b>I Natural ventilation context and overview</b>	<b>7</b>
<b>2 Literature Review</b>	<b>9</b>
2.1 Introduction . . . . .	9
2.2 Scope of review . . . . .	10
2.2.1 Type of openings . . . . .	10

2.2.2	Approach to Literature Review . . . . .	11
2.3	Air flow around buildings . . . . .	12
2.3.1	Approaching atmospheric flow . . . . .	13
2.3.2	Upstream impingement . . . . .	15
2.3.3	Flow separation at building edges . . . . .	16
2.3.4	Re-circulation and wake . . . . .	17
2.4	Flow field at a building surface . . . . .	18
2.4.1	Local pressure field . . . . .	18
2.4.2	Local velocity field . . . . .	22
2.5	Air flow through buildings . . . . .	25
2.5.1	Momentum-induced primary air flows . . . . .	26
2.5.2	Buoyancy-induced primary air flows . . . . .	28
2.6	Idealised air flow through openings . . . . .	29
2.6.1	Application to wind-driven ventilation . . . . .	32
2.7	Opening geometry . . . . .	34
2.7.1	Operable windows . . . . .	34
2.7.2	Chimneys, ducted outlets and wind catchers . . . . .	38
2.7.3	Mesh screens . . . . .	39
2.8	Air flow through windows driven by atmospheric wind . . . . .	39
2.8.1	The cross-flow approach to simulating wind-driven flow . . . . .	41
2.8.2	Unidirectional flows through openings in a cross-flow . . . . .	42
2.8.3	Bi-directional flows through openings in a cross-flow . . . . .	46
2.8.4	Impact of wind on the local pressure field . . . . .	49
2.8.5	Unsteady flow phenomena . . . . .	50
2.8.6	Whole-building empirical models . . . . .	51
2.9	Wind-tunnel techniques . . . . .	53
2.9.1	Similarity requirements . . . . .	53
2.9.2	General wind tunnel requirements . . . . .	57
2.9.3	Wind-tunnel techniques at building-scale . . . . .	57
2.9.4	Wind-tunnel techniques at opening-scale . . . . .	59
2.10	Computational Fluid Dynamics techniques . . . . .	60
2.10.1	Turbulence modelling . . . . .	61
2.10.2	CFD for integration with envelope flow models . . . . .	62

2.11	Measurement Techniques . . . . .	62
2.11.1	Measurement of surface pressures . . . . .	62
2.11.2	Measurement of fluid velocity . . . . .	64
2.11.3	Measurement of volume flow rate . . . . .	72
2.11.4	Integration of velocity profile . . . . .	77
2.12	Conclusions . . . . .	77
2.12.1	Flow around buildings . . . . .	78
2.12.2	Airflow through buildings . . . . .	78
2.12.3	Idealised airflow through openings . . . . .	79
2.12.4	Opening geometry . . . . .	79
2.12.5	Air flow through windows driven by atmospheric wind . . . . .	79
2.12.6	Wind tunnel techniques . . . . .	80
2.12.7	Measurement techniques . . . . .	81
2.13	Gaps in the literature addressed by this thesis . . . . .	82
<b>3</b>	<b>Theoretical evaluation of airflow through an opening in a cross-flow</b>	<b>83</b>
3.1	Introduction . . . . .	83
3.2	General empirical models of airflow through openings . . . . .	83
3.3	Bernoulli analysis . . . . .	85
3.4	Behaviour in still-air . . . . .	89
3.5	Local pressure effects . . . . .	89
3.5.1	Pressure generation mechanisms . . . . .	90
3.5.2	<i>Local</i> pressure coefficients . . . . .	90
3.5.3	<i>Local</i> dimensionless pressure . . . . .	90
3.6	Conclusions . . . . .	91
<b>4</b>	<b>Methods</b>	<b>93</b>
4.1	Introduction . . . . .	93
4.2	Flow direction definitions . . . . .	93
4.3	Empirical modelling . . . . .	96
4.3.1	Principles of function selection . . . . .	97
4.3.2	Statistical analysis . . . . .	98
4.4	Cross-flow characterisation experiments . . . . .	99
4.4.1	Wind tunnel setup . . . . .	99

4.4.2	Preconditioning elements . . . . .	99
4.4.3	Plenum design . . . . .	101
4.4.4	Model window . . . . .	102
4.4.5	Orifice flow meter . . . . .	102
4.4.6	Instrumentation . . . . .	105
4.4.7	Experimental protocol . . . . .	106
4.4.8	Calculation of descriptive parameters . . . . .	110
4.4.9	Error analysis . . . . .	112
4.5	Velocity profile measurements . . . . .	114
4.5.1	Experimental setup . . . . .	114
4.5.2	Hot wire anemometer . . . . .	115
4.5.3	Calibration procedure . . . . .	115
4.6	Cross-flow probe . . . . .	116
4.6.1	Operating principle . . . . .	116
4.6.2	Experimental setup . . . . .	118
4.6.3	Calculation of descriptive parameters . . . . .	125
4.6.4	Evaluation of probe outputs . . . . .	127
4.7	Model building experiments - measurement of model inputs . . . . .	129
4.7.1	Experimental setup . . . . .	129
4.7.2	Error analysis . . . . .	130
4.7.3	Surface pressure measurements . . . . .	132
4.7.4	Cross-flow velocity measurements . . . . .	136
4.8	Model building experiments - ventilation rate measurements . . . . .	139
4.8.1	Experimental setup . . . . .	139
4.8.2	Characterising ventilation rate in the building . . . . .	142
4.8.3	Estimating volume flow rate through the model building . . . . .	142
4.8.4	Evaluation of measured results . . . . .	145
4.9	Conclusions . . . . .	146
<b>II</b>	<b>Results</b>	<b>147</b>
<b>5</b>	<b>Characterising airflow through windows in a cross-flow</b>	<b>149</b>
5.1	Introduction . . . . .	149

5.2	Approach flow . . . . .	149
5.2.1	Mean velocity profile . . . . .	150
5.2.2	Turbulence intensity in the approach flow . . . . .	151
5.3	Aerodynamic resistance in still-air . . . . .	152
5.3.1	Empirical Effective Area Model (EEAM) . . . . .	152
5.3.2	Comparison with alternative models . . . . .	154
5.3.3	Measurements of a square window . . . . .	156
5.4	Local pressure phenomena in a cross-flow . . . . .	158
5.4.1	Local pressure coefficients of a square window . . . . .	159
5.4.2	Dependence on Reynolds number . . . . .	160
5.4.3	Effect of boundary layer thickness . . . . .	162
5.4.4	Empirical modelling of local pressure coefficients . . . . .	162
5.5	Aerodynamic resistance in a cross-flow . . . . .	163
5.5.1	Comparison with literature data . . . . .	163
5.5.2	Choice of characteristic parameter . . . . .	166
5.5.3	Aerodynamic resistance of a square hinged opening . . . . .	168
5.5.4	Dependence on Reynolds number . . . . .	169
5.5.5	Effect of boundary layer thickness . . . . .	170
5.5.6	Empirical modelling of <i>total</i> dimensionless volume flow rates . . . . .	171
<b>6</b>	<b>Surface flow field on a model building</b>	<b>175</b>
6.1	Introduction . . . . .	175
6.2	Approach flow . . . . .	175
6.2.1	Mean velocity profile . . . . .	175
6.2.2	Turbulence intensity in the approach flow . . . . .	177
6.3	Surface pressure field . . . . .	178
6.3.1	Surface pressure coefficients . . . . .	178
6.3.2	Window-integrated surface pressures . . . . .	180
6.4	Surface velocity field . . . . .	180
6.4.1	Cross-flow velocity profile . . . . .	182
6.4.2	Cross-flow velocity coefficient . . . . .	184
6.4.3	Component analysis of the cross-flow velocity . . . . .	187
6.4.4	Frequency analysis of the cross-flow velocity coefficient distribution . . . . .	187



6.4.5	Turbulence in the cross-flow . . . . .	190
6.4.6	Mean <i>façade</i> cross-flow direction . . . . .	190
6.4.7	Frequency analysis of the <i>façade</i> cross-flow direction distribution . . . . .	191
6.5	Total pressure loss coefficient . . . . .	193
6.5.1	<i>Local</i> pressure coefficients . . . . .	194
<b>7</b>	<b>Ventilation rate in a model building</b>	<b>199</b>
7.1	Introduction . . . . .	199
7.2	Ventilation rate predictions . . . . .	199
7.2.1	Predictions for a single-zone building . . . . .	199
7.2.2	Impact of an internal resistance . . . . .	201
7.2.3	Predictions for a two-zone building . . . . .	202
7.3	Ventilation rate measurements . . . . .	204
7.3.1	Dimensionless <i>building</i> flow rate . . . . .	204
7.3.2	Absolute ventilation rates . . . . .	207
<b>III</b>	<b>Discussion and conclusions</b>	<b>211</b>
<b>8</b>	<b>Discussion</b>	<b>213</b>
8.1	Introduction . . . . .	213
8.2	Characterising airflow through windows in a cross-flow . . . . .	213
8.2.1	Approach flow characteristics in the simulated cross-flow . . . . .	214
8.2.2	<i>Idealised</i> discharge coefficient of hinged windows . . . . .	216
8.2.3	<i>Local</i> pressure coefficients of hinged windows . . . . .	218
8.2.4	Aerodynamic resistance in a cross-flow . . . . .	220
8.3	Surface flow field on a model building . . . . .	224
8.3.1	Cross-flow probe . . . . .	224
8.3.2	Surface pressure field . . . . .	226
8.3.3	Window-integrated surface pressures . . . . .	227
8.3.4	Cross-flow velocity profile . . . . .	228
8.3.5	Cross-flow velocity coefficient . . . . .	229
8.3.6	Mean <i>façade</i> cross-flow direction . . . . .	230
8.3.7	Temporal variation in the cross-flow . . . . .	231

8.3.8	Total pressure loss in the cross-flow . . . . .	231
8.4	Ventilation rates in a model building . . . . .	232
8.5	Limitations of this thesis . . . . .	235
8.6	Alternative applications . . . . .	236
8.7	Suggestions for future work . . . . .	236
8.8	Advice for practitioners . . . . .	238
<b>9</b>	<b>Conclusions</b>	<b>239</b>
	<b>Bibliography</b>	<b>241</b>
	<b>Appendices</b>	<b>261</b>
<b>A</b>	<b>Derivations of the orifice equation</b>	<b>263</b>
A.1	Standard derivation . . . . .	263
A.2	Non-uniform streamline height . . . . .	264
A.2.1	Flow from a reservoir of non-uniform density . . . . .	265
A.2.2	Flow between zones of different density . . . . .	267
A.3	Non-uniform pressure profile . . . . .	269
<b>B</b>	<b>Modelling the impact of flow connection on driving pressures and ventilation efficiency</b>	<b>273</b>
B.1	Introduction . . . . .	273
B.2	Analytical model . . . . .	273
B.3	Comparison with literature data . . . . .	275
B.4	Implications for design . . . . .	277
<b>C</b>	<b>Evaluation of <i>Free area</i> models</b>	<b>279</b>
C.1	Introduction . . . . .	279
C.2	Common method of evaluating different techniques . . . . .	279
C.3	<i>Free area</i> models . . . . .	279
C.4	BB101 model . . . . .	281
<b>D</b>	<b>Interpretation of literature data</b>	<b>283</b>
D.1	Introduction . . . . .	283
D.2	Surface pressure coefficients . . . . .	283
D.3	Cross-flow velocity coefficient data . . . . .	284

D.4	<i>Idealised</i> discharge coefficient data . . . . .	286
<b>E</b>	<b>Matlab code for the cross-flow probe</b>	<b>287</b>
E.1	Introduction . . . . .	287
E.2	Master Routine . . . . .	287
E.3	Subroutine Data collate . . . . .	288
E.4	Subroutine Data format . . . . .	290
E.5	Subroutine Calculate surface flow . . . . .	292
E.6	Calibration curve fit . . . . .	295
<b>F</b>	<b>Cross-flow characterisation curves of simple window geometries</b>	<b>299</b>
F.1	Introduction . . . . .	299
F.2	Square orifice . . . . .	300
F.3	Square, outward opening, hinged window . . . . .	301
F.4	Square, inward opening, hinged window . . . . .	306
<b>G</b>	<b>Distributions of the cross-flow velocity coefficient and the direction of the cross-flow on a model building</b>	<b>311</b>
G.1	Introduction . . . . .	311
G.2	Cross-flow velocity coefficient distributions . . . . .	312
G.3	Cross-flow direction . . . . .	319

# List of Figures

2.1	Breakdown of key properties that affect how airflow through window openings can be modelled.	11
2.2	Diagram depicting flow round a notional block building.	13
2.3	Surface-averaged and local surface pressure coefficient correlations for the centre-point of a cube building.	22
2.4	Pattern of streamlines around a simple, isolated building in plan and section, and velocity vectors.	22
2.5	Cross-flow velocity coefficient as a function of wind angle	24
2.6	Comparison between the model of flow through a constriction, and its application to flow through a sharp-edged opening.	30
2.7	Common types of operable window	35
2.8	Diagram depicting a range of different methods of modelling <i>free</i> area identified in the literature.	36
2.9	Definition of simplified dimensional parameters used to describe a notional hinged opening.	37
2.10	Diagram depicting the effect projecting opening geometry can have on flow patterns and local pressure fields.	40
3.1	Pattern of streamlines near an isolated opening for inflow and outflow.	86
4.1	Flow diagram illustrating the experimental procedures performed in this thesis	94
4.2	Diagram of airflow patterns around a notional building, and its interaction with windows mounted on the façade.	95
4.3	Wind tunnel setup for the window characterisation experiments.	100
4.4	Alternative preconditioning elements used in the window characterisation experiments.	101
4.5	Key dimensions of preconditioning elements.	102
4.6	Details of the plenum chamber used in the characterisation experiments	103
4.7	Plenum chamber and details of the diffuser array.	104

4.8	Window opening modelled in the characterisation experiments, and its dimensions. . . . .	104
4.9	Air-flow over window elements during characterisation experiments. . . . .	105
4.10	Diagram of the experimental setup, with the arrow denoting the direction of the airflow. . . .	106
4.11	Flow chart describing the experimental protocol used for the window characterisation experiments. . . . .	107
4.12	Flow chart describing the experimental protocol used for the zero readings, still-air tests, dynamic flow tests, and local pressure tests. . . . .	108
4.13	Difference in mean calibration voltage measured before and after each run of window characterisation experiments. . . . .	113
4.14	Hot wire anemometer used to measure the velocity profile in the wind tunnel. . . . .	115
4.15	Calibration curve for the hot wire anemometer used in the wind tunnel. . . . .	116
4.16	Photographs and isometric drawings of the cross-flow probe . . . . .	117
4.17	Diagram of the experimental setup used to calibrate and test the cross-flow probe. . . . .	118
4.18	Cross-flow probe and the mounting frame used for calibration. . . . .	119
4.19	Plot of the surface pressure coefficients for the cross-flow probe as a function of <i>façade</i> cross-flow direction. . . . .	120
4.20	Probability density function of the pressure coefficient on the surface of the cross-flow probe. . . . .	121
4.21	Frequency decompositions of the cross-flow probe surface pressure coefficients. . . . .	122
4.22	Cross-flow probe and the static pressure splitter boxes. . . . .	123
4.23	Range of dynamic pressures evaluated by the cross-flow probe compared against the range of dynamic pressures measured in the jet. . . . .	124
4.24	Range of <i>façade</i> cross-flow directions evaluated by the cross-flow probe plotted against the mean measured dynamic pressure in the jet. . . . .	125
4.25	Frequency decomposition of dynamic pressure and <i>façade</i> cross-flow direction evaluated by the cross-flow probe. . . . .	126
4.26	Spire used for velocity and turbulence profile preconditioning in the model building experiments. . . . .	130
4.27	Isometric drawing of the model building with exchangeable opening plates. . . . .	131
4.28	Diagram of instrumentation used to measure surface pressure coefficients on a model building. . . . .	133
4.29	Relationship between the surface pressure coefficient on a model building with a surface pressure tapping or a square opening and Reynolds number. . . . .	135
4.30	Relationship between the surface pressure coefficient on a model building with a hinged opening and Reynolds number. . . . .	135
4.31	Image of the three techniques used to measure the speed and direction of the cross-flow . . . .	136

4.32	Diagram of the experimental setup used to measure volume flow rate through a model building.	139
4.33	Diagram of the different ventilation configurations modelled, and how the wind angle is defined for each configuration. . . . .	141
5.1	Plot of the surface boundary layer in the wind tunnel with height. . . . .	150
5.2	Plot of the turbulence intensity in the surface boundary layer with height. . . . .	151
5.3	<i>Idealised</i> discharge coefficient of a square, butt hinged opening plotted against opening angle.	157
5.4	<i>Idealised</i> discharge coefficient plotted against opening Reynolds number. . . . .	157
5.5	<i>Local</i> pressure coefficient plotted against the flow approach angle. . . . .	159
5.6	<i>Local</i> pressure coefficient plotted against opening angle. . . . .	160
5.7	<i>Local</i> pressure coefficient plotted against cross-flow Reynolds number. . . . .	161
5.8	Comparison between the <i>local</i> pressure coefficients evaluated with the <i>thick</i> and <i>thin</i> boundary layers. . . . .	161
5.9	Comparison between measured values of the <i>local</i> pressure coefficient and those predicted using Equation 5.5. . . . .	164
5.10	Plot of <i>local</i> pressure coefficient of hinged, outward-opening windows as a function of opening angle and flow approach angle. . . . .	164
5.11	<i>Orifice</i> discharge coefficient of a square orifice plotted against dimensionless room pressure. . . . .	165
5.12	Alternative characteristic parameters for describing volume flow rate through openings, plotted against dimensionless room pressure. . . . .	167
5.13	Plot of the <i>total</i> dimensionless volume flow rate against <i>local</i> dimensionless pressure. . . . .	168
5.14	Reynolds number achieved during dynamic tests against <i>local</i> dimensionless pressure. . . . .	169
5.15	Plot of the inverse <i>total</i> dimensionless volume flow rate against the inverse <i>local</i> dimensionless pressure for a range of opening geometries exposed to a cross-flow with either a <i>thick</i> or <i>thin</i> boundary layer. . . . .	170
5.16	Plot of the relationship between measured values of the normalised <i>total</i> dimensionless volume flow rate against those predicted using the empirical equations derived in this chapter. . . . .	173
6.1	Plot of the velocity profile in the wind tunnel with height. . . . .	176
6.2	Plot of the turbulence intensity in the wind tunnel with height. . . . .	177
6.3	Comparison between measured surface pressure coefficients on the model building and surface pressure coefficients given in the literature. . . . .	178
6.4	Plot of the measured surface pressure coefficients on the model building against wind angle with a surface pressure tapping or a square opening. . . . .	179

6.5	Plot of the standard deviation in measured surface pressure coefficients against wind angle with a square opening or a surface pressure tapping. . . . .	180
6.6	Plot of the measured opening pressure coefficients against wind angle for a building with left and right mounted windows. . . . .	181
6.7	Plot of the standard deviation in measured opening pressure coefficients against wind angle for different opening types. . . . .	181
6.8	Plot of the cross-flow velocity coefficient as a function of wind angle at a range of distances from the building façade. . . . .	182
6.9	Diagrams of the three different types of velocity profile observed, and plots of the measured data for different wind angles. . . . .	183
6.10	Comparison between the measured cross-flow velocity coefficient and those measured in the literature. . . . .	185
6.11	Plot of the cross-flow velocity coefficient measured using the hot-wire anemometer and the cross-flow probe as a function of wind angle. . . . .	186
6.12	Component analysis of the cross-flow velocity coefficient measured using the cross-flow probe as a function of wind angle. . . . .	188
6.13	Plot of distribution of the cross-flow velocity coefficient at a range of wind angles. . . . .	189
6.14	Plot of the turbulence intensity in the cross-flow as a function of wind angle. . . . .	190
6.15	Plot of the mean <i>façade</i> cross-flow direction against wind angle. . . . .	191
6.16	Plot of distribution of <i>façade</i> cross-flow direction at a range of wind angles. . . . .	192
6.17	Plot of the mean total pressure loss coefficient against wind angle. . . . .	193
6.18	Plot of the <i>local</i> pressure coefficient of the square opening against wind angle. . . . .	194
6.19	Plot of the <i>local</i> pressure coefficient of the hinged opening against the flow approach angle. . . . .	195
6.20	Plot of predicted and measured <i>local</i> pressure coefficients occurring at a left mounted window opening against wind angle. . . . .	196
6.21	Plot of the opening pressure coefficients predicted using the characterisation data for a left-mounted window against wind direction alongside measured data for left-mounted and square openings. . . . .	196
7.1	Plot of the predicted dimensionless <i>building</i> flow rate against wind angle for a range of ventilation configurations in a single-zone building. . . . .	200
7.2	Plot of the predicted wind-angle-averaged dimensionless <i>building</i> flow rate against the area ratio of the internal resistance. . . . .	201

7.3	Ratio of the wind-angle-averaged dimensionless <i>building</i> flow rate predicted using the cross-flow characterisation model to that predicted by the orifice flow model, plotted against the area ratio of the internal resistance. . . . .	202
7.4	Plot of the predicted dimensionless <i>building</i> flow rate for a range of ventilation configurations against wind angle, with an internal resistance created by a partition. . . . .	203
7.5	Plot of the measured dimensionless <i>building</i> flow rate against wind angle for a range of different ventilation configurations. . . . .	205
7.6	Plot of predicted and measured values of the dimensionless <i>building</i> flow rate against wind angle for a range of different ventilation configurations. . . . .	206
7.7	Plot of relationship between predicted and measured values of the dimensionless <i>building</i> flow rate for a range of different models. . . . .	207
7.8	Plot of the measured absolute dimensionless <i>building</i> flow rate against wind angle for a range of different ventilation configurations. . . . .	209
8.1	Diagram of inflow through inward and outward opening windows at wind directions of 0 and 180 degrees. . . . .	222
8.2	Diagram of the mechanism by which interaction between hinged openings and the cross-flow can reinforce or inhibit surface pressure variations generated by an oscillating wind direction. . . . .	228
B.1	An illustration of the difference between an expanding jet from a small or a large opening . . . . .	274
B.2	Comparison between CFD data presented by Seifert <i>et al.</i> [1] and the predictions of Equations B.1 and B.2. . . . .	276
F.1	Cross-flow characterisation curve for a square orifice . . . . .	300





# List of Tables

5.1	Fitted coefficients for the Empirical Effective Area Model . . . . .	153
5.2	Deviation between predicted and measured <i>idealised</i> discharge coefficients for different modelling techniques as a function of opening angle. . . . .	155
5.3	Models of <i>idealised</i> discharge coefficients in the form of Equation 5.1, their coefficients and the reduced chi squared value ( $\chi_v^2$ ) and coefficient of determination ( $R^2$ ) of their fit. . . . .	158
5.4	Fitted coefficients of Equations 5.5-5.8 and the resultant regression statistics. . . . .	163
5.5	Fitted coefficients of Equations 5.9-5.16 for inflow and outflow through inward and outward opening hinged windows, and the resultant regression statistics. . . . .	172
5.6	Fitted coefficients of Equation 5.9 for inflow and outflow through a simple square orifice, and the resultant regression statistics. . . . .	172
7.1	Regression statistics for the ventilation rates in a model building predicted by the orifice equation, the corrected orifice equation, and the cross-flow characterisation models. . . . .	208
C.1	Coefficients of Equation C.30 presented in the BB101 discharge coefficient calculator [2]. . . . .	282
F.1	Cross-flow characterisation curves for a square, outward opening, hinged window at an opening angle of 90 degrees, for flow approach angles between 0 and 180 degrees. . . . .	301
F.2	Cross-flow characterisation curves for a square, outward opening, hinged window at an opening angle of 60 degrees, for flow approach angles between 0 and 180 degrees. . . . .	302
F.3	Cross-flow characterisation curves for a square, outward opening, hinged window at an opening angle of 30 degrees, for flow approach angles between 0 and 180 degrees. . . . .	303
F.4	Cross-flow characterisation curves for a square, outward opening, hinged window at an opening angle of 15 degrees, for flow approach angles between 0 and 180 degrees. . . . .	304
F.5	Cross-flow characterisation curves for a square, outward opening, hinged window at an opening angle of 5 degrees, for flow approach angles between 0 and 180 degrees. . . . .	305

F.6	Cross-flow characterisation curves for a square, inward opening, hinged window at an opening angle of 90 degrees, for flow approach angles between 0 and 180 degrees. . . . .	306
F.7	Cross-flow characterisation curves for a square, inward opening, hinged window at an opening angle of 60 degrees, for flow approach angles between 0 and 180 degrees. . . . .	307
F.8	Cross-flow characterisation curves for a square, inward opening, hinged window at an opening angle of 30 degrees, for flow approach angles between 0 and 180 degrees. . . . .	308
F.9	Cross-flow characterisation curves for a square, inward opening, hinged window at an opening angle of 15 degrees, for flow approach angles between 0 and 180 degrees. . . . .	309
F.10	Cross-flow characterisation curves for a square, inward opening, hinged window at an opening angle of 5 degrees, for flow approach angles between 0 and 180 degrees. . . . .	310
G.1	Cross-flow velocity coefficient distributions on the surface of a model cube at wind angles of 0 and 15 degrees. . . . .	312
G.2	Cross-flow velocity coefficient distributions on the surface of a model cube at wind angles of 30 and 45 degrees. . . . .	313
G.3	Cross-flow velocity coefficient distributions on the surface of a model cube at wind angles of 60 and 75 degrees. . . . .	314
G.4	Cross-flow velocity coefficient distributions on the surface of a model cube at wind angles of 90 and 105 degrees. . . . .	315
G.5	Cross-flow velocity coefficient distributions on the surface of a model cube at wind angles of 120 and 135 degrees. . . . .	316
G.6	Cross-flow velocity coefficient distributions on the surface of a model cube at wind angles of 150 and 165 degrees. . . . .	317
G.7	Cross-flow velocity coefficient distributions on the surface of a model cube at wind angles of 180	318
G.8	Normalised frequency distributions of <i>façade</i> cross-flow direction on the surface of a model cube at wind angles of 0 degrees (top), 15 degrees (middle), and 30 degrees (bottom). . . . .	319
G.9	Normalised frequency distributions of <i>façade</i> cross-flow direction on the surface of a model cube at wind angles of 45 degrees (top), 60 degrees (middle), and 75 degrees (bottom). . . . .	320
G.10	Normalised frequency distributions of <i>façade</i> cross-flow direction on the surface of a model cube at wind angles of 90 degrees (top), 105 degrees (middle), and 120 degrees (bottom). . . . .	321
G.11	Normalised frequency distributions of <i>façade</i> cross-flow direction on the surface of a model cube at wind angles of 135 degrees (top), 150 degrees (middle), and 165 degrees (bottom). . . . .	322

G.12 Normalised frequency distributions of *façade* cross-flow direction on the surface of a model  
cube at wind angles of 180 degrees. . . . . 323



# Nomenclature

$X$	Arbitrary measured parameter
$X_i$	Parameter measured at location $i$
$X_z$	Parameter measured at height $z$
$X_R$	Reference value of a measured parameter
$X_E$	Parameter measured in the <i>external</i> environment
$X_I$	Parameter measured in the <i>internal</i> environment
$X_c$	Parameter measured in the cross-flow
$X_{vc}$	Parameter measured in the <i>vena contracta</i>
$X_{fs}$	Parameter measured in the <i>free stream</i>
$X_H$	Parameter measured in air that has relatively high density
$X_L$	Parameter measured in air that has relatively low density
$X_{out}$	Parameter measured in the air that is leaving a space through an opening
$X_{in}$	Parameter measured in the air that is entering a space through an opening
$X_{net}$	Parameter relating to the <i>net</i> flow of air through an opening
$X_x$	Component of Parameter in the $x$ direction
$X_y$	Component of Parameter in the $y$ direction
$X_L$	Parameter measured <i>local</i> to a window opening
$\Delta X$	Difference in parameter X

$X^*$	Dimensionless parameter
$g$	Acceleration due to gravity
$z$	Distance in the opposing direction to gravity
$z_n$	Height of the neutral pressure level
$h$	Height of an opening
$w$	Width of an opening
$L_c$	Characteristic length
$\phi$	Opening angle of a window
$\alpha$	Flow approach angle between opening geometry and a cross-flow
$\beta$	<i>Façade</i> cross-flow direction
$\kappa$	Von Karman constant
$\sigma$	Aspect ratio of an opening
$A$	Measurement of area
$A_{min}$	Minimum area through which a fluid passes
$A_f$	<i>Free</i> area of an opening
$A_{eff}$	<i>Effective</i> area of an opening
$P$	Static pressure
$P_d$	Dynamic pressure
$P_T$	Total pressure
$P_L$	Average static pressure acting on the external surface of an opening
$\rho$	Density of a fluid
$T$	Temperature of a fluid
$\nu$	Kinematic viscosity of a fluid
$U$	Speed of the flow

$u^*$	friction velocity
$Q$	Volume flow rate
$c$	Concentration of tracer
$S$	Rate of emission of tracer gas
$f$	frequency
$C$	Arbitrary coefficient
$C_P$	Pressure coefficient
$C_{P(O)}$	Surface pressure coefficient measured in with opening geometry present
$C_{P_L}$	<i>Local</i> pressure coefficient
$C_{P_{dc}}$	<i>Cross-flow</i> dynamic pressure coefficient
$C_{P_T}$	Total pressure coefficient
$C_{\Delta P_T}$	Total pressure loss coefficient
$P_R^*$	Dimensionless room pressure
$P_L^*$	<i>Local</i> dimensionless pressure
$P_{z_n}^*$	Dimensionless neutral pressure
$z_n^*$	Dimensionless neutral height
$P_P^*$	Dimensionless plume pressure
$P_B^*$	Dimensionless local buoyancy pressure
$C_c$	Contraction coefficient
$C_f$	Friction loss coefficient
$C_d$	Discharge coefficient
$C_{d_o}$	<i>Orifice</i> discharge coefficient
$C_{d_I}$	<i>Idealised</i> discharge coefficient
$C_{d_B}$	<i>Bernoulli</i> discharge coefficient



$Q_{\Delta P}^*$	Dimensionless volume flow rate due to a pressure differential
$Q_B^*$	Dimensionless volume flow rate due to local buoyancy
$Q_{U_L}^*$	Dimensionless volume flow rate due to a cross-flow
$Q_T^*$	<i>Total</i> dimensionless volume flow rate
$Q_B^*$	Dimensionless <i>building</i> flow rate
$F_L$	Dimensionless flow number
$F_R$	Froude number
$S_i$	Directional indicator
$Re$	Reynolds number
$Re_i$	Reynolds number through the opening
$Re_L$	Reynolds number in the cross-flow
$St$	Strouhal frequency
$\chi_v^2$	Reduced chi squared statistic that describes fit quality
$I$	Turbulence intensity

# Chapter 1

## Introduction

### 1.1 Purpose of providing ventilation to buildings

Ventilation is defined as the process by which outdoor air is provided to building occupants [3]. The supply of outdoor air affects both the health and comfort of building occupants [4]. Ventilation systems can be designed to manage two key aspects of environmental performance: indoor air quality, and thermal comfort [5, 6].

#### 1.1.1 Indoor air quality

The principal role of ventilation is to provide an acceptable level of indoor air quality by removing and diluting airborne contaminants [5]. Where these contaminants may cause harm to occupants, they are referred to as pollutants, and ventilation is provided to reduce the risk to occupants to acceptable levels. Minimum ventilation rates to ensure acceptable indoor air quality are typically set by national standards; in the UK, these can be found in Approved Document F [7].

The type and quality of ventilation provided to a building has the potential to impact on health and well-being issues ranging from acute medical concerns, to comfort and cognitive performance, to joy and happiness [8]. The medical impacts of ventilation are primarily associated with indoor air quality. Pollutants can arise from either indoor or outdoor sources, and can lead to both acute and chronic health impacts. Many pollutants, such as carbon monoxide, are not perceived at all or only at levels that are already harmful. Occupant perceptions are therefore important in terms of user satisfaction, but are not a reliable indicator of air quality and health risk [8].

Inadequate supply of ventilation for indoor air quality can have serious consequences. Poorly ventilated

buildings are associated with higher incidence of sick building syndrome and building related illness [9, 10]. Inadequate ventilation can increase the risk of mould growth, and increase the risk of transmission of airborne diseases [11]. Ensuring minimum ventilation rates are met is important in maintaining the health, comfort and productivity of building occupants [4].

The *perception* of air quality is a psychological phenomena. Beyond objective measures of indoor air quality, the *perception* of air freshness can be related to temperature, humidity, air velocity, and the smell of the air in the environment [12]. Furthermore, indoor air quality, occupant satisfaction and productivity are closely linked, with ventilation being one of the most important factors affecting task performance [8, 13].

The Covid-19 pandemic has highlighted the importance of good ventilation in buildings: in addition to the other health and well-being impacts of outdoor air [8, 14], it is seen as a crucial part of a mitigation strategy for illnesses transmitted by airborne aerosols [15].

### 1.1.2 Thermal comfort

Thermal comfort is defined as "*that condition of mind that expresses satisfaction with the thermal environment*" [16]. The environmental conditions that create a condition of thermal comfort are subjective, and depend on individual perception [17]. However, it can be qualitatively stated that thermal discomfort occurs when the environment becomes either too cold or too hot.

Ventilation can interact with thermal comfort in a number of ways. When the outdoor air is cold, direct contact between occupants and ventilation supply air can lead to discomfort [3]. This can be resolved by preheating the supply air, or by ensuring the supply air mixes with the room air before it reaches the occupants [5]. In addition to this, removal of room air results in a loss of thermal energy from the space. Here, the rate of loss of thermal energy through ventilation is proportional to the ventilation rate and the temperature difference between the internal and external environment. To maintain comfort conditions, thermal energy needs to be supplied to the space to replace that which is lost.

Discomfort can also arise due to overheating [5]. This is most common in the summer months. Heat gains from the sun, building occupants and other internal energy sources cause the internal temperature to rise above the external temperature. If this temperature rise is too great, this can lead to discomfort. One method of removing this heat is through ventilative cooling. Here, hot internal air is removed from the space and replaced with relatively cool outdoor air. The rate of loss of thermal energy through ventilation is proportional to the ventilation rate and the temperature difference between the internal and external environment. This form of cooling is only possible where the external air does not exceed the comfort temperature. Volume flow rates required for ventilative cooling are typically an order of magnitude greater

than those required for indoor air quality. Another method by which ventilation can impact overheating discomfort is through its motion. High indoor air velocities increase the rate of convective heat loss from the skin of occupants and latent heat loss from the evaporation of sweat, which increases the perception of cooling [3, 16, 18].

## 1.2 Choice of ventilation concept

When designing a ventilation system for a building, there is a choice of two fundamental concepts: natural ventilation, and mechanical ventilation.

### 1.2.1 Natural ventilation

Natural ventilation systems utilise naturally occurring pressure differentials arising from wind and buoyancy forces to drive air through buildings. These pressures are typically small compared to those produced by mechanical ventilation systems. As such, natural ventilation systems are characterised by large openings, low velocities and low resistance components. Typically, the occupied spaces themselves comprise the ductwork by which outdoor air moves around the building. The pressure differentials that drive natural ventilation are weather dependent, and are therefore not consistent year round. This provides challenges to design and control, and leads to the perception that natural ventilation is unreliable.

The principal advantages of natural ventilation systems are their low energy consumption, and potential to induce large volume flow rates through spaces. Where people have control over their thermal comfort via the opening of windows, they have a sense of agency over their environment that results in greater tolerance for temperature extremes [19, 17]. Consequently, occupants can be more comfortable in naturally ventilated buildings than mechanically-ventilated buildings, and an adaptive thermal comfort model can be used to assess thermal comfort [19, 20, 2]. As such, adequately designed natural ventilation can reduce or eliminate the need for mechanical cooling in buildings [21]. Natural ventilation for the mitigation of summer overheating is seen as a key low-energy technology, the use of which is increasingly required by local and national planning guidance [22, 23]. In the context of a warming climate and increasingly adiabatic thermal constructions, accurate design of natural ventilation systems is increasingly important in ensuring that buildings do not overheat during the summer months. However, as the low pressures associated with natural ventilation preclude the use of heat energy recovery devices such as heat exchangers, the use of natural ventilation for the provision of fresh air during the winter months is becoming increasingly infeasible in new buildings [24].

Natural ventilation systems designed for comfort cooling are often capable of providing significantly

greater ventilation rates than mechanical ventilation systems designed for mechanical cooling [25]. For this reason, natural ventilation can be more resilient to unexpected ventilation demands, such as those adopted in response to the Covid-19 pandemic. Indeed, for much of the year achievable ventilation rates in naturally ventilated buildings are limited by the capacity of the heating system, and not the ventilation system.

### 1.2.2 Mechanical ventilation

Mechanical ventilation systems utilise mechanical fans to provide the pressure differential to drive ventilation through buildings. The pressure differentials that can be achieved are considerably greater than those available for natural ventilation, enabling more complex systems of high resistance components to be used to supply ventilation air [26]. Supply air is typically distributed around the building in ducts, allowing deeper spaces to be supplied with outdoor air. The high flow velocities achievable with mechanical ventilation enables easy integration into *targeted* ventilation systems such as cooker extract hoods. The high pressure differentials involved also enable the integration of energy saving technology such as heat exchangers [27], and air cleaning technology such as particulate filters [28, 29].

The principal advantage of mechanical systems is their reliability and ease of automated control. However, mechanically ventilated buildings may be less resilient in the event of mechanical failure than naturally ventilated buildings.

In contrast with natural ventilation, mechanical systems require the consumption of power to move ventilation air. This power consumption increases with both volume flow rate, and the flow resistance of the ventilation network [16]. Furthermore, the lack of direct occupant control means that occupants are less tolerant of temperature extremes in mechanically ventilated buildings than naturally ventilated buildings [19, 17, 30, 31]. This means more rigorous overheating criteria needs to be applied, which may necessitate the use of mechanical cooling [19, 20, 2]. As the climate warms and insulation standards improve, the proportion of energy consumption attributable to mechanical cooling and fans is expected to increase [32]. In some climates, the energy consumed by ventilation fans is already the single greatest contributor to the energy consumption of the heating, ventilation and air conditioning (HVAC) systems [33].

## 1.3 The problem with natural ventilation

For the reasons described in Section 1.2, natural ventilation provides a wide range of benefits that justify its importance as a key design technique for the future of building design. However, natural ventilation is often perceived by designers and clients to be unreliable. Natural ventilation is dependent on weather conditions, and as a result it is hard for designers to guarantee ventilation rates that can be achieved year-round. In

addition to this, field measurements of indoor air quality suggest that naturally ventilated buildings tend to be under-ventilated in practice, and to a greater degree than mechanically ventilated buildings [34, 35]. To encourage the widespread use of natural ventilation, reliability issues need to be addressed.

A primary task when designing a natural ventilation strategy is the sizing of ventilation openings [25]. The achieved ventilation rate is proportional to the size of the opening; if the openings are too small, inadequate ventilation would be provided. This could lead to unacceptable indoor air quality or overheating in the building. Current practice applies a highly simplified method to characterise wind-driven ventilation rates based on the outdoor wind speed, and the size and orientation of a window within a façade. This method is applied over a year of hourly weather data to estimate indoor air quality and overheating risk during building operation. Although the large volume of data necessitates the use of a computationally simple flow model, these models take no account of the complexities of window geometry or the flow along a building façade. This is thought to be a major source of prediction error in the design of naturally ventilated buildings [36, 37, 5, 38].

## 1.4 Aims and objectives

The aim of this thesis is to develop techniques to *characterise* the influence of window geometry and the flow along a building façade on the ventilation rate through typical window openings. Theoretical and experimental analysis needs to be at the scale of an individual window as opposed to building scale, so that the outputs can be applied in the design case to buildings with varied geometry. Furthermore, the characterisations developed in this thesis need to evaluate computationally simple relationships to enable integration into airflow network models that can be applied in design over a full year of weather data. The use of the characterisations developed in this thesis is intended to reduce systematic errors that lead to the under-sizing of window openings, and consequently to under-performing buildings. To achieve this aim, the following objectives have been identified:

- Apply dimensional scaling arguments to identify key similarity parameters that describe the influence of wind-driven flows, static pressure differentials, and opening geometry on volume flow rates through window openings.
- Develop techniques for characterising the aerodynamic performance of notional window openings in wind-driven flows, independently of the building in which they are located.
- Measure the ventilation characteristics for a simple hinged window at a range of hinged angles and flow speeds and directions, as an example of a typical window geometry.

- Develop empirical models to describe the dependence of ventilation parameters determined by dimensional scaling arguments on the similarity parameters used to describe window geometry and local environmental conditions.
- Develop a low-cost probe to measure the speed and direction of the surface flow on the façade of a model building.
- Measure the surface pressure and velocity distributions on a model cube building as a function of wind angle.
- Use the measured surface pressure and velocity distributions to predict ventilation rate through the model building using the empirical characterisation models developed in this thesis and conventional envelope flow models. Two ventilation will be considered: where two windows are located in opposite façades, known as *cross ventilation*, or in adjacent façades, known as *corner ventilation*. Differences in prediction between the two models will be compared.
- Experimentally measure the ventilation rate in the model building. This will be used to validate the characterisation model developed in this thesis, and identify any improvement over current methods.

## Part I

# Natural ventilation context and overview





# Chapter 2

## Literature Review

### 2.1 Introduction

Natural ventilation in buildings is complex problem in fluid mechanics. Airflow in buildings is governed by the interaction between wind and buoyancy forces with physical geometry.

In theory, the flow field in and around a building for a given set of environmental conditions can be evaluated by solving the Navier-Stokes equations, providing that molecular diffusion and heat transfer are satisfactorily modelled. However, direct solution of the Navier-Stokes equations is computationally intensive, and is dependent on a wide range of assumptions made in the modelling process. Moreover, solutions found are valid only for the specific geometry and environmental conditions modelled. Natural ventilation design in practice typically requires simulation over large time periods, in the order of a year, which would be impractical to evaluate using complex computational methods. It is therefore of practical use to develop simple analytical and empirical models to describe ventilation flow rates that are more general.

When designing a natural ventilation strategy for a building there are two key stages [39]. The first is to define the desired pattern of air flow within the building, which often varies seasonally to best satisfy occupant comfort. The second task is to design the envelope. This involves positioning and sizing openings so that the required airflow pattern and volume flow rates are achieved under the design conditions [25]. In practice, this is typically achieved using envelope flow models. The main attraction of these models is their simplicity: in many cases basic hand calculations suffice [5, 3, 25].

Envelope flow models are widely used in practice to design and specify natural ventilation systems for buildings. Therefore, the accuracy of these models is essential in ensuring that naturally ventilated buildings are adequately ventilated. This review investigates the approaches used to estimate ventilation in envelope

flow models, identifies areas where inadequate modelling can lead to significant errors in ventilation rate predictions, and analyses the degree to which existing research addresses these errors.

## 2.2 Scope of review

The task of characterising natural ventilation of buildings can be broken down into three separable, but interconnected problems [6]:

- Evaluation of pressure and velocity fields in the flow around the outside of buildings
- Calculation of gas exchange rates through openings
- Evaluation of pressure and velocity fields inside occupied spaces

The fundamental principle behind envelope flow models is that the conditions within a space or zone are governed by exchanges at its boundaries [25, 6]. For this reason, this thesis primarily focuses on the calculation of gas exchange rates through openings in the building envelope. However, as flow through an opening is dependant on the nature of the flow at both its internal and external surfaces, it is necessary to have an appreciation of the mechanisms that drive flow behaviour in and around buildings, and the typical flow patterns that can be expected. An introduction to these phenomena is given in Sections 2.3 and 2.5.

Study of the broader flow field around the outside of buildings are of interest to pedestrian comfort [40, 41] and outdoor pollutant transport [42, 43, 44, 45]. Similarly, the study of the flow field inside spaces is important for understanding thermal comfort of occupants [46, 47] and indoor pollutant transport [48, 49, 50]. These topics are covered extensively elsewhere, and are included in this review only where relevant to their effect on gas exchange rates through building openings.

### 2.2.1 Type of openings

Openings in a building envelope can be divided into two types: adventitious openings and purpose provided openings (PPOs) [37]. Adventitious openings are unintentional, and comprise cracks and gaps in the building envelope. PPOs are created intentionally as part of the ventilation scheme, and often take the form of operable windows or vents. Airflow through adventitious openings is known as infiltration. A large body of research exists into infiltration [51]. However, as new buildings are built with progressively more airtight envelopes, infiltration plays a smaller role in ventilation of buildings [39]. All the theory described henceforth concerns PPOs, and assumes that adventitious openings account for a negligible fraction of overall ventilation rates.

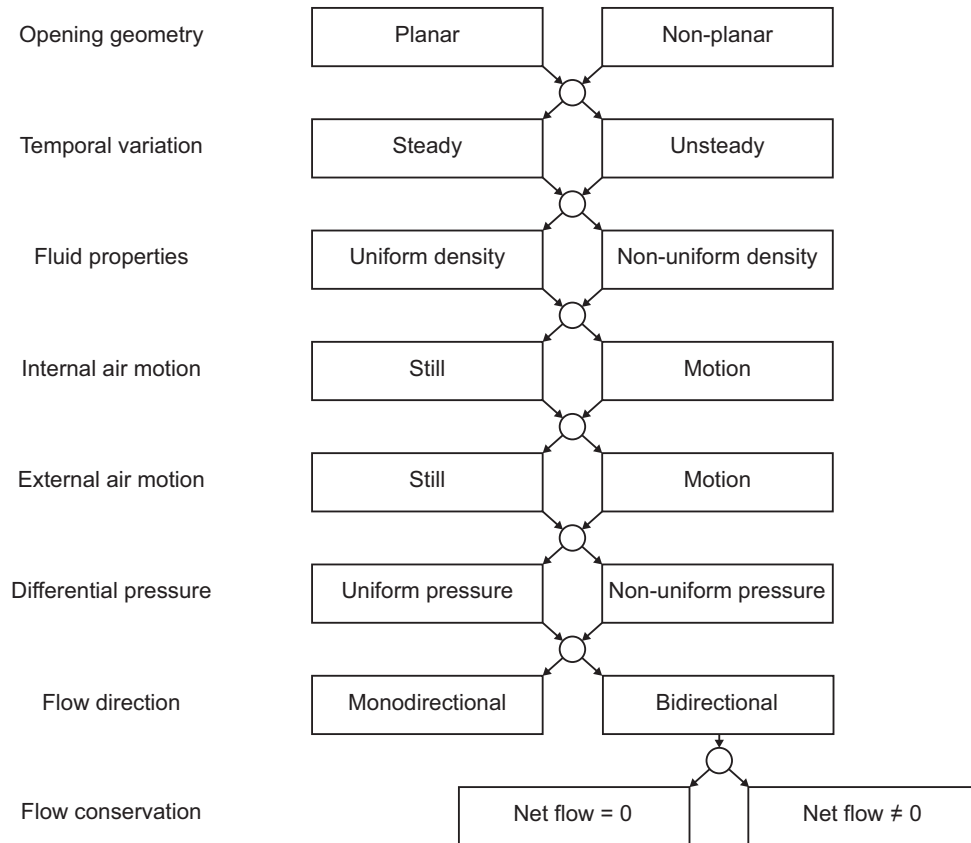


**Figure 2.1:** Breakdown of key properties that affect how airflow through window openings can be modelled.

### 2.2.2 Approach to Literature Review

In practice, envelope flow models are used to predict ventilation rate in buildings during the design stage, with a wide range of building geometry. This review takes the approach that flow through an opening can be described independently of building geometry based on the environmental conditions at its internal and external surfaces. The desire to find solutions to this problem forms the focus of this review. The conditions at the external surface are determined as a function of building and environmental geometry and weather conditions, and are specific to a given building design. The conditions at the internal surface are determined as a function of room layout, flow through openings at the room boundary, heat exchanges through the building fabric, and internal activity. Both problems are complex design tasks, and are not considered in detail here.

To structure this review and subsequent analysis, the problem of estimating flow through window openings is broken down into assumptions affecting the mechanisms that drive flow through them, and organised into a decision tree; see Figure 2.1. Each path taken through this structure represents a unique set of physical

conditions that might be expected to be described by a different descriptive equation. The decision tree has been arranged such that the left branch of each choice represents the simplest set of assumptions for analytical modelling. The use of this framework allows scenarios to be identified where key modelling assumptions are broken, and enables the impacts when each of these assumptions are invalid to be systematically investigated. In addition to system properties described in Figure 2.1, some common assumptions about the properties of the working fluid (incompressible, inviscid gas) are also made.

It is useful to identify here how the physical driving forces behind ventilation are likely to affect the assumptions detailed in the decision tree. Mechanically induced ventilation is likely to be the simplest: where fans induce a steady, relatively large and uniform pressure drop across small openings, and good mixing is often achieved by design. The presence of wind violates the still-air assumption, and introduces unsteady behaviour to the flow. Buoyancy forces result in a non-uniform pressure profile across the opening, and may induce internal density profiles that are non-uniform. The final two categories - flow direction and flow conservation - are primarily influenced by the layout of the ventilation network. A room with a single opening, for example, requires that air flows both into and out of the same opening, and that these flows satisfy conservation of mass.

This review investigates the influence of window geometry on ventilation performance, and focuses exclusively on ventilation driven by wind alone. As the simplest scenario for wind-driven ventilation occurs when the external air is still close to the opening - such as in a stagnation zone - purely mechanically driven gas exchange through windows by supply or extract only systems are also covered in this analysis.

## 2.3 Air flow around buildings

The interaction of wind with building geometry is complex. Even moderately complex building shapes, such as 'L' or 'U' shaped structures, can generate flow patterns too complex to generalise for design [16]. This is further complicated with the introduction of nearby buildings, which generates sufficiently complex flow patterns to preclude the use of simple rules of thumb [52]. For most practical applications, physical or computational modelling are required to determine the pattern of flow around a building and its environment [16].

Flow around buildings is often simplified by considering flow around isolated, rectangular block obstructions. Becker *et al.* break down the flow around a notional isolated building into five zones [53]; see Figure 2.2.

1. Approaching atmospheric flow

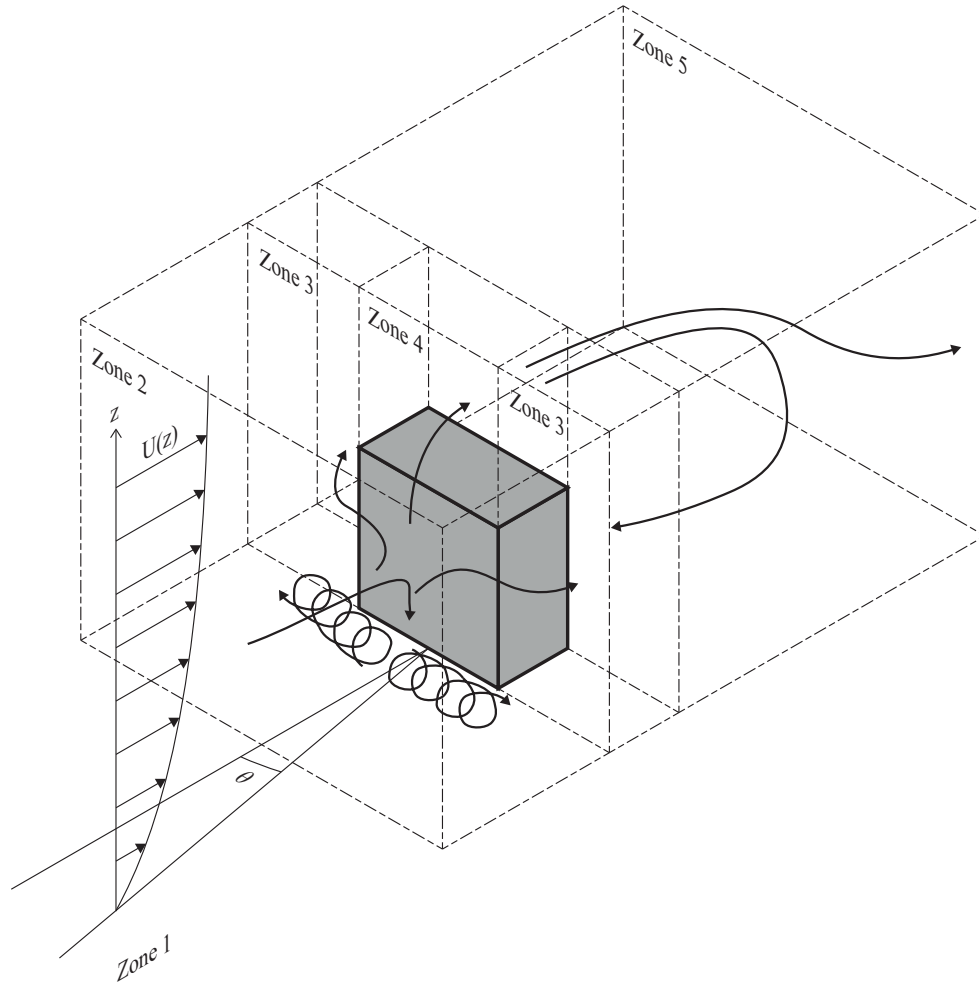


**Figure 2.2:** Diagram depicting flow round a notional block building and the five key zones in the flow field, after Becker *et al.* [53].

2. Upstream impingement
3. Flow separation around the sides of the building
4. Flow separation over the top of the building
5. Recirculation and wake

### 2.3.1 Approaching atmospheric flow

The Atmospheric Boundary Layer (ABL) can be identified as the layer of air directly above the earth's surface in which the effects of skin friction play a direct role in flow dynamics [54]. In terms of flow around buildings, this is defined in a region sufficiently far upwind of the building that the building has no influence

on the flow pattern. A distinct gap has been observed in the power spectrum of wind with a time period of 1 hour [55]. This divides atmospheric motions into two categories: micro-meteorological variations due to turbulence and local terrain features with a time period of less than one hour, and a quasi-steady mean flow that varies diurnally and seasonally, with time period greater than one hour [55, 25]. To facilitate easy analysis, Reynolds decomposition is typically applied to divide the flow velocity into mean and fluctuating components [54]. This analysis is usually applied to the high frequency component of wind speed variations using hourly weather data [55].

The approach flow in the atmospheric boundary layer is typically characterised using three parameters: the velocity profile in the vertical plane, the turbulence intensity profile with height, and the Reynolds number of the flow [54, 56]. The velocity profile in the horizontal plane is usually required to be uniform.

The shape and turbulence characteristics of the ABL are determined by the roughness of the terrain. Roughness categories are typically described qualitatively in international standards, ranging from relatively smooth surfaces such as open sea to relatively rough, urban conditions [3, 55, 54, 56]. Recommended values for the velocity profiles and turbulence characteristics have been observed to vary considerably in international codes and standards [57]. This reflects the variability in the approach flow that occurs in the natural environment. When using wind-tunnels for design purposes, the generation of a suitable boundary layer profile is critical in ensuring applicability of results.

The shape of the velocity profile is typically described using either a power law or a log law model [58, 59]. The power law model describes the vertical variation in mean atmospheric flow speed normalised by measurements at a reference height, and is characterised by an exponent that is a function of terrain roughness; see Equation 2.1. While not analytically correct for the bottom ten meters of the atmospheric boundary layer, the power law model remains widely used due to its simplicity [54, 60, 61].

$$\frac{U(z)}{U_R} = \left( \frac{z}{z_R} \right)^\alpha \quad (2.1)$$

where  $U(z)$  is the average wind speed ( $m/s$ ) at a height  $z$  ( $m$ ) above ground level,  $U_R$  is a reference velocity ( $m/s$ ) measured at a reference height  $z_R$  ( $m$ ), and  $\alpha$  is an empirically derived constant that is related to the roughness of the terrain.

Sutton developed a logarithmic model of the atmospheric boundary layer that provides a better description of low-level wind speeds [59]. This is given by

$$\frac{U(z)}{u^*} = \frac{1}{\kappa} \ln \frac{z - z_d}{z_0} \quad (2.2)$$

where  $u^*$  is the friction velocity ( $m/s$ ),  $\kappa$  is the experimentally-derived Von Karman constant,  $z_d$  is a displacement height that accounts for the presence of large roughness elements  $m$ , and  $z_o$  is the aerodynamic roughness of the terrain  $m$ . The coefficients of this equation are notoriously difficult to fit experimentally, and as such many technical standards adopt a simplified log-law model normalised by flow velocity at a reference height [3, 62]. However, Eurocode EN 1991-1-4:2005 identifies considerable uncertainty at low level due to the influence of neighbouring structures [62]. Consequently, a constant wind speed is assumed below a critical height for the purposes of wind loading calculations.

Turbulence in the approach flow depends on the roughness of the terrain, and the size and spacing of upstream elements [63]. Following Holmes, Eurocode EN 1991-1-4:2005 defines a logarithmic law for estimating the longitudinal turbulence intensity in an atmospheric boundary layer [64, 62]. Here,

$$I_u(z) = \frac{1}{\ln \frac{z}{z_o}} \quad (2.3)$$

where  $I_u$  is the longitudinal turbulence intensity. Below a minimum height, EN 1991-1-4:2005 takes the longitudinal turbulence intensity to be a constant value. Turbulence intensity typically varies depending on the axis of measurement. Counihan gives a ratio between the longitudinal, lateral, and vertical turbulence intensities of 1:0.75:0.5 [65]. Holmes provides a similar ratio of 1:0.88:0.55 [64]. However, substantial variation in this ratio may be expected to occur in different natural boundary layer flows [57]. Many natural ventilation studies do not report the turbulence intensity in the approach flow, do not specify the direction in which the turbulence intensity is measured, or provide only a single turbulence measurement at a specific or unspecified height [61, 66, 67].

Adequate simulation of turbulence is generally considered to be more essential than simulation of the mean velocity profile [68, 69, 57]. However, Hearst *et al.* find that the flow structure in the immediate proximity of a cube is not strongly dependent on the turbulence in the incoming flow [70]. This is fortuitous for ventilation studies, which are primarily concerned with conditions close to the building surface.

While the shape and turbulence in the atmospheric boundary layer does not fundamentally change the structure of the flow around the building, it has been shown to alter the dimensions and locations of characteristic vortex structures in the wake [53, 70]. This occurs due to changes in turbulent momentum exchange between the wake and the outer flow.

### 2.3.2 Upstream impingement

The second zone comprises the flow immediately upstream of a building. Here the flow is slowed by the presence of the obstruction, and forced to flow around it. For wind angles normal to the façade, a number of



key flow features are observed. Where flow hits the building, it slows down. This results in a high pressure stagnation zone part-way up the façade [16]. Atmospheric flow is directed away from the stagnation zone towards the top, bottom and sides of the building. As the downward flow hits the floor, it is redirected to form a characteristic horseshoe vortex system in front of the obstacle that spirals outwards to leave via the lateral sides of the building [71]. As the wind angle deviates from the normal, the stagnation one disappears and the surface flow is redirected to follow the façade downstream.

The horseshoe vortex at the base of the building is associated with a region of high turbulent kinetic energy [72]. Yakhot *et al.* utilise computational fluid dynamics with direct numerical simulation to investigate the velocity distributions in this flow [73]. When the wind is normal to the façade, they identify a clear bimodal distribution in the vertical component of the velocity in the vortex. Here the flow flips between two states - a dominant state where the flow is moving down, and a secondary state where the the flow is moving upwards. The frequency of these oscillations can be described by a dimensionless Strouhal number, which is given by

$$St = \frac{fL_c}{U} \quad (2.4)$$

where  $f$  is the frequency of oscillation ( $Hz$ ),  $L_c$  is a characteristic length ( $m$ ), taken to be equal to the building height, and  $U$  is the flow velocity ( $m/s$ ). Here, a dominant Strouhal number of 0.08 is observed in the vertical component of the velocity in the horseshoe vortex [73]. This is thought to arise from two overlapping distributions resulting from invicid-viscous interactions between the horseshoe vortex and a narrow band of positive vorticity attached to the floor in front of the cube [73, 74]. Similar results are observed experimentally by Depardon *et al.* [75]. This highlights the dynamic character of flow in this region that is not visible in traces of mean flow direction or steady CFD simulations.

### 2.3.3 Flow separation at building edges

The third and fourth zones describe flow separation at sharp edges of the sides and top of the building respectively. At sharp edges, fluid flow cannot follow the path of the object surface. As a result, the flow separates from the object. This separation point is fixed in space, which results in flow patterns that are relatively independent of Reynolds number. This is not the case for smooth, curved surfaces. When the wind is normal to the building façade and the building is sufficiently long, the separated flow can re-attach to the wall or roof further downstream. The area enclosed by this zone is termed the recirculation cavity, which contains a highly turbulent vortex of recirculating flow [52]. Here, the main effect of turbulence in the upstream flow is to promote reattachment to the roof and sides of the body [71, 70]. Flow reattachment

is inherently unstable, and as a result substantial temporal variation in the location of flow reattachment occurs [52]. Intermittency of reattachment has been found to reduce as turbulence in the flow increases, which correlates to a reduction in wake length [70]. As the wind angle deviates from the normal, the leeward side zone merges with the wake, and the upwind side zone merges with the upstream impingement zone.

At a wind angle of 45 degrees, strong corner vortices are created over the building roof [52, 71]. These vortices are highly turbulent, and associated with low pressure regions on the roof [71]. No flow attachment is observed to occur at this wind angle, either to the roof or the downstream walls [71].

### 2.3.4 Re-circulation and wake

The fifth zone comprises the recirculation and wake region downstream of the building. This region is large and unsteady, and is associated with typical quasi-periodic bluff-body wake dynamics [72]. For a normal angle of incidence, the wake behind a building contains a characteristic portal vortex caused by the shear from flow separation at the building's top and sides [53, 76, 77]. As the wind angle deviates from the normal, the footprint of the portal at the downstream edge of the building becomes smaller and tighter, and shifts towards the building. Becker *et al.* find that, for a building with an aspect ratio (W:H:L) of 1:2:2.9, the footprint of the downstream portal transitions to the side of the obstacle at a 45 degree wind angle, and transitions to the top of the obstacle at a wind angle of 60 degrees [53]. Different results might be expected for a cube building, which would be symmetrical at a wind angle of 45 degrees. Becker *et al.* find that the wake decays to a free stagnation zone at the edge of the recirculation region [53]. Beyond this, the atmospheric flow re-attaches to the tunnel floor downstream of the building [16, 70]. Hearst *et al.* find that the reattachment length in the wake of a cube building is relatively independent of turbulence in the approach flow [70]. However, the length of the wake is shown to monotonically decrease with increasing turbulence intensity, as a result of heightened turbulence levels promoting wake recovery [70]. Flow in the wake is chaotic. Two proximate points close to the top of a building have been shown to follow very different paths through the turbulent wake vortices [53]. This adds complexity to pollutant transport models in this region. Although flow in the wake has a high level of local turbulence, Castro and Robins find that the turbulent kinetic energy in this region is lower than that in the approach flow [71]. This arises due to the low mean local velocities measured in the wake. Despite significant differences in the nature of the flow near the cube, the flow in the far wake at a distance of six building heights from the model centre has been found to be relatively independent of model orientation [71].

When air flows around a bluff body, periodic Strouhal vortex shedding has been observed [53, 78, 79, 72]. These vortices are shed alternately by each edge of the building, resulting in quasi-periodic vortex patterns

that progress through the downstream wake. Frequency analysis has revealed that dominant frequency in area above the building is twice that which occurs in the areas to either side [53]. Together with visual experiments, this suggests that for each alternating vortex shed by the side of the obstacle a corresponding vortex is shed by the top [53]. However, Hurst *et al.* demonstrate that turbulence in the atmospheric boundary layer flow leads to a reduction in strength of a dominant shedding frequency [70]. In some cases, this can result in the wake being treated as non-periodic when a simulated atmospheric boundary layer is used in the approach flow [53, 71]. Schröder *et al.* identify that Strouhal frequencies in the wake are strong for laminar flow, peaking at around  $St = 0.1$  consistent with literature results [80, 74, 72]. However, for turbulent flow more consistent with atmospheric wind, vortex shedding is much less pronounced and shifted towards higher frequencies. The power spectral density is reduced by a factor of two, and is much broader spectrum than observed for laminar flow. The studies of Schröder *et al.* are achieved at relatively low Reynolds numbers of around 8000 [72]. At higher Reynolds numbers typical in atmospheric flow, it is likely that the the periodic shedding behaviour will be further eroded by turbulence in the atmospheric flow [53].

Hearst *et al.* present results for the pre-multiplied frequency spectra in the approach flow and wake of cubic buildings. The pre-multiplied spectrum identifies the frequencies that carry the most energy in the flow. Here, a clear frequency peak around  $St = 10^{-2}$  is identified in the approach flow. In the wake however, this peak is eliminated, and the energy redistributed to frequencies near  $St = 0.13$ . This is in the range typically observed for turbulent vortex shedding in the wake of a cube elsewhere in the literature [71], and suggests that shedding frequencies in the wake may be masked by free stream turbulence rather than eliminated [70].

## 2.4 Flow field at a building surface

While the study of air flow around buildings is important for models of pollutant dispersal and pedestrian comfort, the broader flow field around a building is of secondary importance for envelope flow models. As ventilation in a space is governed by gas exchanges at its boundaries, the conditions close to the surface of a façade on a building are of primary interest. This is characterised by the surface pressure and velocity field - its speed, direction, turbulence characteristics, and their distribution. Here, the broader flow field represents the boundary conditions that determine the character of the local flow field.

### 2.4.1 Local pressure field

The pressure field at a building surface is typically described using surface pressure coefficients, where the static pressure increment relative to that in the approach flow is normalised against the dynamic pressure in

the approach flow [3, 5, 25]. Surface pressure coefficients on simple rectangular buildings vary considerably with wind approach angle, and to a lesser extent with building geometry [81]. Surface pressures also vary spatially with position on a building surface, particularly close to the edges [81, 71], and exhibit substantial temporal variation [78, 6]. For buildings with sharp edges, surface pressure coefficients are typically assumed to be a constant, and independent of Reynolds number [82]. This occurs because the sharp building edges fix the location of the separation point in space, and is supported by high Reynolds numbers in the atmospheric flow. However, at low wind speeds, the pattern of atmospheric wind can be influenced by airflow patterns driven by thermal convection around buildings arising from incident solar radiation [82]. Full-scale measurements have identified considerable scatter in surface pressure coefficients at low wind speeds [83]. However, it is not clear whether this scatter arises from interaction between wind-driven and buoyancy-driven flow structures, or whether it arises due to increased measurement error at low pressure differentials.

The reference dynamic pressure used to normalise the surface pressures is usually taken at the height of the building [25, 84], although conventions taken at window height [85] or 10m reference height [61] are sometimes used. The main advantage of choosing a fixed height for measurement of the reference dynamic pressure is experimental simplicity. It is consistent with the bulk of measurements in the literature and in technical guidance [3, 5, 84]. It also increases the ease of integration into envelope flow models, as it removes the need to calculate wind speed at the height of each opening. However, when measuring with a fixed reference height, surface pressure coefficients are dependent on terrain factors that change the shape of the upstream velocity profile. Atkins and Cermak find that dependence on terrain and building height is insignificant when the dynamic pressure at window height is used to normalise the surface pressures as opposed to measurements at a fixed height [86, 84]. However, this can cause problems when evaluating pressure coefficients at low level, which can tend to infinity as the reference velocity tends to zero [86].

It is common in natural ventilation design to apply façade-averaged and time-averaged surface pressure coefficients to predict ventilation rates [5, 25, 84]. Here, it is assumed that surface pressure fluctuations have an insignificant effect on mean ventilation rates, and that the variation in surface pressure between windows mounted on different façades is large compared to the variation in surface pressure on a given façade. This significantly reduces the volume of data that needs to be parsed in natural ventilation design.

Although surface-averaged pressure coefficients are widely used in practice to predict ventilation rates, the use of local pressure coefficients is much more common in the academic literature [87, 1, 88]. A CFD study of cross ventilation by Shirzadi *et al.* find that prediction errors in the use of envelope flow models reduce substantially when local pressure coefficients are used in place of surface-averaged pressure coefficients across a wide range of flow configurations [87]. However, a comparison between early stage-modelling and ventilation measurements in a full-scale building by Belleri *et al.* finds that, although the use of local

pressure coefficients improves the accuracy of ventilation rate predictions, the effect size is smaller than that of occupant window-opening behaviour and wind-speed profile [89].

Castro and Robins show that the pressure distribution on the façade of a cube is fairly uniform in the wake region, where flow-reattachment has not occurred [71]. However, upstream where flow is attached to the surface, significant spatial variation in pressure is found to occur as the surface flow accelerates round the building. This spatial variation is most pronounced on the lateral faces when the wind is normal to the cube. These faces are parallel to the cube, and in turbulent flow contain both a recirculating cavity and a fluctuating flow reattachment point [71]. This leads to substantial spatial variation in pressure that makes façade-averaged pressure coefficients unsuitable. Spatial variation in surface pressure is of particular importance when multiple openings are located on the same façade [78]. Daish *et al.* find that, where two openings are located on the same façade, spatial and temporal variations in surface pressure can be the dominant driver of gas exchange [78]. Here, spatial and temporal variations in surface pressure increase as the separation between the openings increases relative to the length of the façade, which results in increased ventilation rates.

Full-scale measurements of the surface pressure field on a cube exposed to atmospheric wind show reasonable agreement with those measured in wind tunnel studies [90]. Richards *et al.* find that the agreement is strongest for upstream faces and for non-normal wind angles [90]. For normal wind angles, pressure coefficients on the side and leeward walls are typically higher in magnitude at full scale than at model scale, corresponding to an increased suction effect. This could arise from differences in free stream turbulence between the full-scale and wind tunnel scenarios, or from Reynolds number effects [70]. This is consistent with changes in reattachment frequency and wake length reported in wind-tunnel studies [70, 71, 72].

### Sources of surface pressure coefficients

Airflow network models and building energy models typically apply wind-pressure coefficients derived from literature data-sets in a simplified way [82]. Simulation software require the interpretation of literature data-sets to avoid the need for costly wind-tunnel or numerical simulation to determine surface pressure coefficients for a specific building geometry. However, as even relatively simple variations on a rectangular floor plan such as L-shaped buildings generate complex flow patterns that are difficult to generalise [16], analytical models to predict pressure coefficients for the arbitrary design case have not to date been capable of generating reliable and effective results [91, 92, 93]. A review of wind-pressure coefficient data widely used in airflow network models and building energy models finds values that are quite different depending on the source adopted [82]. These differences are particularly prominent for sheltered buildings, where different sources even present different trends [82]. Accurate predictions of surface pressure coefficients and consequently ventilation rates

are still dependent on wind-tunnel or numerical modelling of a building and its environment. Consequently, reliance on extrapolated literature data sets for the prediction of surface pressure coefficients is likely to be a greater source of error in airflow network models than the use of surface-averaged pressure coefficients.

The Air Infiltration and Ventilation Centre is an international reference that is widely used by simulation software as a source of surface wind pressure coefficients [82]. This comprises tabulated surface-averaged wind pressure data compiled by Orme and Liddament for a range of sources [94, 95]. Data is provided at wind angle increments of 45 degrees, and while this data is heavily caveated, it has been widely used and reproduced due to its conciseness and simplicity [82, 95]. The tabulated data presented by Orme and Liddament are reproduced in industry technical guidance for ease of use of designers, such as in CIBSE Guide A, but without reproduction of the caveats printed in the original document [96, 3].

Swami and Chandra present correlations for predicting the surface pressure coefficients on building surfaces based on a review of literature data [84, 97]. They find that surface-averaged pressure coefficients are adequate for the purpose of ventilation prediction in low-rise buildings, with correlations presented as a function of wind-direction and aspect ratio. Here, errors arising from the use of surface-averaged pressure coefficients as opposed to local pressure coefficients are typically around 5% [97]. However, for high-rise buildings where the height is greater than or equal to the minimum building length, surface-averaged pressure coefficients are found to be not sufficient [84]. Here, correlations are presented as a function of wind-angle, aspect ratio, and the location co-ordinates. However, this correlation is based on the results of a single study [86], and therefore lacks the broader support that the correlations evaluated for the low-rise buildings can draw upon [84]. Similar empirical models have since been developed to extend surface pressure coefficient predictions to sheltered buildings. These include the CpCalc+ tool developed by Grosso for COMIS [91, 98], and the Cp generator developed by Knoll *et al.* for the Dutch TNO that accounts for obstruction from a nearby block building [92].

Figure 2.3 presents the surface-averaged and local surface pressure coefficient correlations for the centre-point of a cube building presented by Swami and Chandra [84], Grosso [91], and Knoll *et al.* [92]. Figure 2.3 shows strong similarities between the presented surface pressure coefficient correlations and tabulated data commonly used in simulation software [84, 91, 92, 96]. However, substantial diversity has been found between the results of different experimental practitioners. For the surface-averaged pressure coefficient correlation given by Swami and Chandra, where the greatest range of data are used to fit the model, the coefficient of determination is as low as 0.8 [84]. This increases to 0.89 for the local pressure coefficient correlation, which is fit to data from a single study [86]. This is a significant jump in agreement given the increase in complexity of predicting local surface pressure variation, and reflects the diversity of surface pressure coefficient results that can be found between different authors [84].

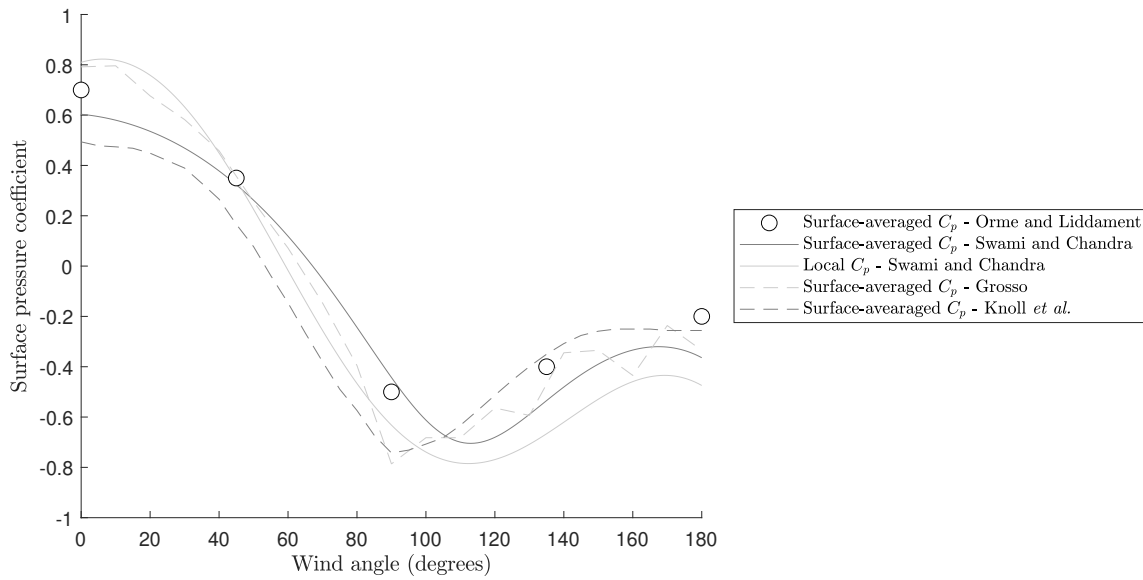


**Figure 2.3:** Surface-averaged and local surface pressure coefficient correlations for the centre-point of a cube building presented by Swami and Chandra [84], Grosso [91], and Knoll *et al.* [92]. Tabulated data collated by Orme and Liddament are shown by circular markers [94, 3].

#### 2.4.2 Local velocity field

When wind impinges on a façade, the surface redirects the flow so that it runs parallel to it [81, 61, 99, 100]. This applies whether the impinging flow comes directly from the atmospheric wind or from recirculation currents generated in the turbulent wake [52]; see Figure 2.4. The thickness of this quasi-parallel flow layer increases with distance from the point where the flow impinges on the surface [66]. Closer to the surface of the façade, skin friction causes a surface boundary layer to develop within the parallel flow layer [81]. The thickness of this boundary layer can be expected to depend on the surface roughness, the distance from

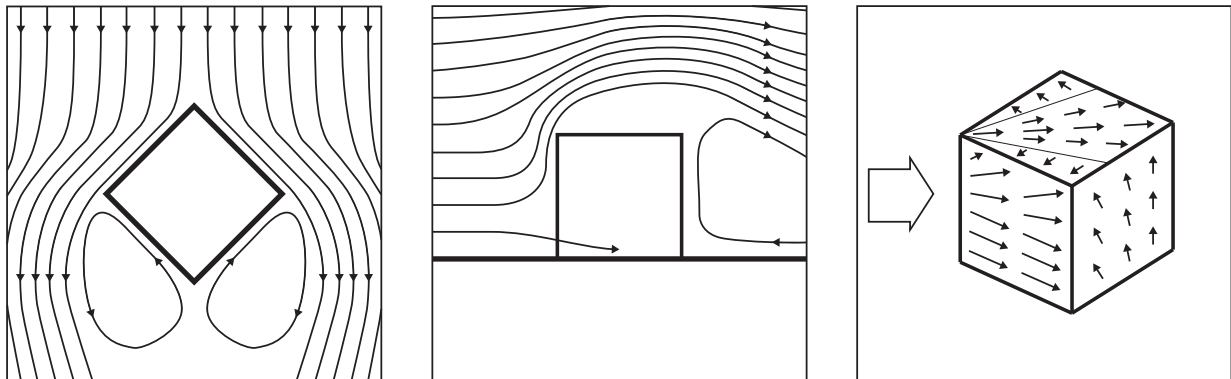


**Figure 2.4:** Pattern of streamlines around a simple, isolated building in plan (left), and section (centre), and the pattern of surface velocity vectors (right), after ASHRAE [16] and Wilson [52]

the point where the flow impinges on the surface, and the turbulence characteristics of the impinging flow. Instantaneous Particle Image Velocimetry (PIV) experiments on the roof of a cube building show that the wall-normal velocity is close to zero within a distance of 0.05 building heights from the façade [72]. This suggests that flow is reliably parallel in this region, even without time averaging.

Air flow close to the surface of a building can therefore be thought of as a pattern of parallel flow on each of the façades. This structure of air flow parallel to the façade is known as a *cross-flow* [100, 66], where external air currents run *across* the plane of the window openings. This is to be distinguished from *cross ventilation*, where ventilation air flows *across* the occupied space. While the flow field around bluff bodies has been extensively studied, systematic studies of the flow field close to a building surface are considerably more scarce. This is largely attributed to the difficulty in applying conventional oil-film visualisation techniques to vertical surfaces [101], which are commonly used to visualise shear stress and consequently mean surface velocity vectors. Wilson uses dye injection to visualise the direction of airflow over the surfaces of a cube in a water channel, with mean flow directions evaluated by visual analysis [52]; see Figure 2.4. Depardon *et al.* use near-wall PIV measurements to quantify the mean and instantaneous flow velocities on the surfaces of a cube [101, 75]. These visualisations reveal swirl patterns on the lateral faces of the cube where a vortex attaches to the surface. This suggests that, for some wind angles, façade-averaged flow directions are unlikely to be sufficient to predict flow behaviour [101, 75]. Near-wall PIV techniques have been recently applied in combination with computational methods to investigate the mean surface flow field on square cylinders [102, 103]. In all cases, visualisations are limited to a small number of wind angles. For application to ventilation design, measurements for a more complete range of wind angles would be required.

Numerous studies have investigated the relationship between the mean speed of the cross-flow on a building surface and the wind angle [85, 99, 61, 67]; see Figure 2.5. Although there is considerable spread in the results, the general pattern of flow behaviour is the same. A significant cross-flow velocity occurs at a wind angle of 0 degrees - despite notionally being a stagnation zone. The cross-flow velocity increases as the wind angle deviates from the normal, reaching a peak at a wind angle of around 60 degrees. The cross-flow velocity rapidly decreases as the wind angle moves towards 180 degrees, reaching a minimum at 180 degrees when the opening is in the lee of the building.

Variation between different sources can largely be attributed to experimental differences between studies. All studies shown in Figure 2.5 use buildings of different aspect ratios. Cross-flow velocity coefficients have been shown to vary across a façade [85, 104]. Furthermore, different studies utilise different measuring techniques to measure the cross-flow velocity. These techniques can affect the measurement output; see Section 2.11.2.

Kurabuchi *et al.* identify that the cross-flow velocity varies with distance from the façade; taking the



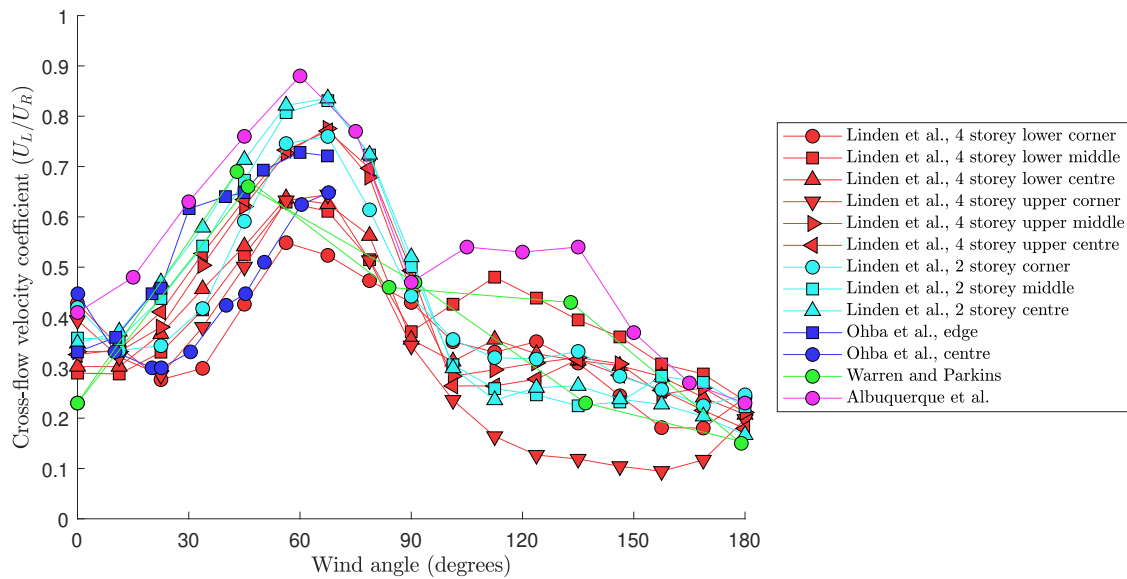


**Figure 2.5:** Cross-flow velocity coefficient as a function of wind angle, where the reference velocity is taken at building height. Data from Linden *et al.* for a four storey building with an aspect ratio (W:H:L) of 2.6:1:1 are denoted by red markers [85]. Data from Linden *et al.* for a two storey building with an aspect ratio of 4.8:1:1.9 are denoted by cyan markers [85]. Data from Ohba *et al.* for a building with a 2:1:2 aspect ratio are denoted by blue markers [99]. Data from Warren and Parkins for a building with a 4.5:1:2 aspect ratio are denoted by green markers [61]. Finally, data from Albuquerque *et al.* for a building with an aspect ratio of 1.7:1:1.3 are denoted by magenta markers [67]. Here, the building width is defined as the width of the façade on which the test window is mounted.

form of a wall jet or boundary layer flow [66]. Therefore, the magnitude of the cross-flow velocity coefficient is dependent on the distance from the façade at which the cross-flow velocity is measured. However, most studies do not record the distance from the façade that cross-flow velocity measurements are taken [85, 61, 67]. Furthermore, Kurabuchi *et al.* identify that the distance from the façade at which the total pressure measured in the cross-flow corresponds to that measured in the inflow jet varies depending on wind angle [104], and that the determination of a suitable location to measure the cross-flow velocity is non-trivial.

Linden *et al.* present an equation relating the speed of the cross-flow normalised by the wind speed at opening height to the wind angle [85]; see Equation 2.5. This equation applies in the wind angle range  $0 \leq \theta \leq 180$ , and is empirically derived from experimental studies of 2 and 4 storey buildings [85].

$$\frac{U_L}{U_{Z_w}} = 0.527e^{-0.000638(\theta-62)^2} + 0.25 - 0.00028\theta \quad (2.5)$$

Although several ventilation studies have measured the cross-flow speed, few studies also measure the direction of the cross-flow. Those that do typically measure flow direction for the purpose of orienting measuring probes, and do not report the results. Warren and Parkins use a wool tuft to measure the flow direction, which they use to orient their hot-wire anemometer [61]; Kurabuchi *et al.* measure the flow direction using a split-film anemometer, which is used to orient the pitot-tube used to measure total pressure; and Chiu and Etheridge rotate their hot-wire anemometer within the cross-flow until a maximum reading is recorded. Kurabuchi *et al.* identify that, for a simple rectangular orifice, the discharge coefficient of an opening is relatively independent of the direction of the cross-flow [66]. As a result, many subsequent studies do not attempt to measure the cross-flow direction [99, 105]. This is particularly problematic when characterising three dimensional opening geometry, where the flow direction might be expected to have a significant impact on opening performance. In a study of a range of window geometries by Ohba *et al.*, the direction of the simulated cross-flow is neither considered nor reported, making the results difficult to apply for comparative purposes [105].

## 2.5 Air flow through buildings

Air flow within spaces is traditionally treated as a separate problem to evaluating flow through openings [39], and are of primary concern to models of pollutant transport and thermal comfort [106, 48, 49, 2]. Here, envelope flow models are used to provide the air flow rate through openings, which form the momentum and mass flow inputs to indoor airflow models [6, 39]. In this conception, prediction of the pattern of air flow within buildings is a secondary problem in envelope flow models, relevant here only to the extent that the

indoor air flow structures can affect flow through openings.

Envelope flow models commonly assume that the internal air is static [38, 25]; see Section 2.6. This assumption not only implies that the resistance to airflow caused by the internal space can be neglected, but that patterns of internal air movement cannot interfere with the dynamics of flow through PPOs. In reality, internal air movement can come from a number of sources [107]. Thermal plumes rising from occupants and machinery, gusting from mixing fans and turbulence from movements within the space can all play a role. These factors are complex to predict, and even when they are known it would be difficult to design an experimental procedure to account for the range of possibilities. Furthermore, the internal configuration of a space, including the location and shape of furniture can all interact with and alter the pattern of internal airflow. Therefore, it is difficult to derive general results concerning air flow patterns in indoor spaces. However, an understanding of the key airflow structures likely to be present in a space is helpful in ascertaining their potential impact on envelope flows.

Air motion within a room can generally be divided into two categories: primary and secondary flows. Primary flows such as jets and plumes have a coherent structure and point of origin. Secondary flows, by contrast, do not generally have a coherent structure or point of origin, and extend over most of the volume of the space [6].

One way of classifying primary air flows is to consider the type of mechanism of flow generation. Here momentum-induced primary flow structures such as jets, and buoyancy-induced primary flow structures such as plumes are considered. In reality, many flow structures such as those that occur through window openings in the building envelope exhibit both buoyancy and momentum-induced behaviour.

### 2.5.1 Momentum-induced primary air flows

The main type of momentum-induced flow structure is the jet [16, 6]. A jet is defined as a stream of fluid issuing into a reservoir of fluid with lower momentum, and is a well understood engineering phenomenon [6]. Perfect jets are characterised by a constant momentum flux, but the volume flow rate of the jet increases with distance from the source. This is caused by entrainment of air from the surrounding medium into the jet. This mechanism causes the jet to mix with the room air, and so they are widely used in mechanical ventilation to distribute fresh air throughout a room volume [26, 16, 108, 6].

Where there is no temperature difference between indoor and outdoor spaces, natural ventilation through open windows can be treated as a low velocity jet entering the space [6]. In mechanical ventilation, the main use of jets is to ensure mixing of the supply air with the room air [26, 6]. This can be for thermal comfort reasons - to reduce the velocity and increase the temperature of the supply air - or to ensure even mixing

of pollutants within the space and to transport pollutants to the extract [6, 108]. Similarly, envelope flow models of natural ventilation typically assume that the momentum in the inflow jet fully dissipates within the space, resulting a well-mixed internal environment with no transport of momentum between the inlet and the outlet [38, 1, 109]. However, wind tunnel and CFD studies by Endo *et al.* have identified that conserved momentum from the jet of air entering a space through an inflow opening can increase the static pressure at the outflow opening available to drive ventilation [105]. This is supported by the CFD studies of Seifert *et al.*, which identify the formation of a stream-tube between inflow and outflow openings where kinetic energy is conserved, resulting in volume flow rates that exceed the predictions of envelope flow models [1]. Here, the formation of this stream-tube is primarily linked to the alignment of the inflow and outflow openings with the dominant wind direction. This is consistent with the propagation of a jet between the inlet and outlet openings. Kinetic energy dissipation is also found to be dependent on opening size, where kinetic energy in the inflow jet is increasingly conserved as the opening size increases [1, 38, 109].

Consequently, the conventional orifice flow equation tends to underestimate volume flow rates through the openings [1, 38, 109]. This implies that ventilation systems over-perform the predictions of the orifice flow model when openings are closely aligned, and consequently that the effect can be ignored for the purposes of natural ventilation design [25, 39]. Nonetheless, an appreciation of the phenomena involved is necessary to enable experimental design that either eliminates or measures the effect of flow connection ventilation phenomena. Furthermore, airflow within a stream tube may bypass the occupied portion of a room and could be less effective at removing contaminants from there [16]. This is consistent with established guidance for mechanical ventilation, whereby supply and extract terminals need to be separated [26]. An analytical approach to modelling flow under these conditions is developed in Appendix B, which describes novel predictive models for both volume flow rates and pollutant removal rates and identifies characteristic parameters.

In operation, outdoor air tends to have a different temperature to the indoor air. Buoyancy forces cause the flow to deflect as it is accelerated due to gravity [16], and so flow through openings may require treatment as a buoyant jet [6]. Where the temperature difference is large, the initial momentum of the jet may often be neglected [6]. In this case, the inflow air can be treated as a plume; see Section 2.5.2.

### **Coherent momentum-induced secondary structures**

Jets within an enclosed space behave differently to those in an unbounded environment [6]. A coherent set of secondary structures are formed known as recirculation currents [108, 110]. These currents transport pollutants emitted within a space, where they can be entrained into primary flows and ultimately extracted. The formation of these flows are highly complex. Computational predictions show flow patterns are highly

dependent on internal geometry as well as the direction and intensity of flow through inlet openings [110]. This is supported by visualisations from flume experiments, which reveal considerable variation in internal flow pattern arising from relatively small changes in opening layout [108].

Recirculation currents formed within a space will induce a cross-flow close to the inside face of openings mounted in the wall, similar to the cross-flow caused by wind on the exterior faces of a building [110]. These currents have been hypothesised to influence flow through window openings in the same manner as wind-driven cross-flow [25, 100]. However, secondary flow structures are likely to have significantly lower velocities than external wind driven flows, and therefore a comparatively small impact on airflow through window openings. In CFD simulations, Shetabivash [110] identifies that the velocity profile of an opening is insignificantly altered by its location, despite substantial variation in the pattern of recirculation currents occurring in the internal spaces. This suggests that a study of internal air movement may be unimportant for predicting volume flow rates through ventilation openings.

### 2.5.2 Buoyancy-induced primary air flows

The main type of buoyancy-induced flow structure is the plume. Plumes differ from jets in that they do not have a constant momentum flux - the buoyancy force leads to an increase in momentum over the height of the plume [6, 111]. Plumes have a higher entrainment rate than jets, which is likely related to the influence of buoyancy on the turbulence at their edges [6, 111].

The main significance of plumes in ventilation is their ability to transport heat around the space, and to capture pollutants emitted by heat sources. In the context of envelope flow models, this is significant in its effect on the internal pressure field and the consequent static pressure differentials available to drive air through openings [25, 111, 106]. In still air, plumes rise from heat sources and collect near the ceiling [6, 111]. This forms a stratified, well mixed layer of hot air - a phenomena that forms the basis of displacement ventilation strategies [106, 25].

One potential impact of buoyancy sources on flow through openings is the introduction of a vertical velocity field into the internal space. This could be of particular importance when the source of buoyancy is located close to the inlet or outlet of ventilation openings, such as radiators placed underneath windows. Radiators or perimeter heaters are commonly placed directly beneath ventilation openings such as windows to minimise the risk of cold draughts within a space [26]. Here, the heat source is located with the express intent of interfering with the incoming airflow by mixing and entraining the supply jet and preventing it from dropping straight to the floor [112, 113]. Hall finds that the presence of an internal heater located below a bottom hung, inward opening window can reduce buoyancy driven single sided ventilation rates by up to

20% [112]. A thorough review of the literature has not identified any studies on the effect of a heat emitter on wind-driven cross ventilation. This is unlikely to be a significant issue for summertime overheating, where central heating systems are likely to be switched off. However, given that it is common to locate emitters beneath windows to prevent cold downdraughts, further research into this phenomena is warranted.

## 2.6 Idealised air flow through openings

In a conventional envelope flow model, airflow through PPOs is described by the orifice flow equation; see Equation 2.13 [5, 3, 25]. This represents an idealised model of flow through planar, sharp-edged openings, and assumes steady, unidirectional flow between reservoirs of still air of uniform pressure and density. Flow is treated as incompressible and irrotational. This corresponds to conditions within the framework illustrated in Figure 2.1 where the left decision is taken at every juncture.

The names and definitions of the terms used in this equation vary between sources, particularly those describing measurements of area. Therefore, this chapter follows the convention of Jones *et al.* [37] to avoid ambiguity.

The orifice flow equation can be derived trivially by application of the Bernoulli equation to a streamline passing through a constriction [25, 16, 5]; see Figure 2.6. First, an expression for the flow velocity at a point in the constriction is evaluated by comparing the total pressure at a point upstream of the opening with the total pressure at a point in the constriction:

$$P_{T(1)} = P_1 + \rho_1 g z_1 + \frac{1}{2} \rho U_1^2 \quad (2.6)$$

$$P_{T(2)} = P_2 + \rho_2 g z_2 + \frac{1}{2} \rho U_2^2 \quad (2.7)$$

$$P_{T(1)} - P_{T(2)} = P_1 - P_2 + \rho_1 g z_1 - \rho_2 g z_2 + \frac{1}{2} \rho_1 U_1^2 - \rho_2 U_2^2 \quad (2.8)$$

$$U_2 = \sqrt{\frac{2}{\rho_2} \left( P_1 - P_2 + \rho_1 g z_1 - \rho_2 g z_2 + \frac{1}{2} \rho_1 U_1^2 - \Delta P_T \right)} \quad (2.9)$$

where the subscripts 1 and 2 correspond to locations in in the upstream flow and the constricted flow respectively, as depicted in Figure 2.6,  $P_T$  and  $P$  denote the total pressure and static pressure respectively,  $\rho$  denotes the density of the fluid,  $g$  denotes the acceleration due to gravity,  $z$  denotes the height above a reference plane, and  $U$  denotes the fluid velocity. When the variation in height and fluid density along the streamline can be neglected, this reduces to:

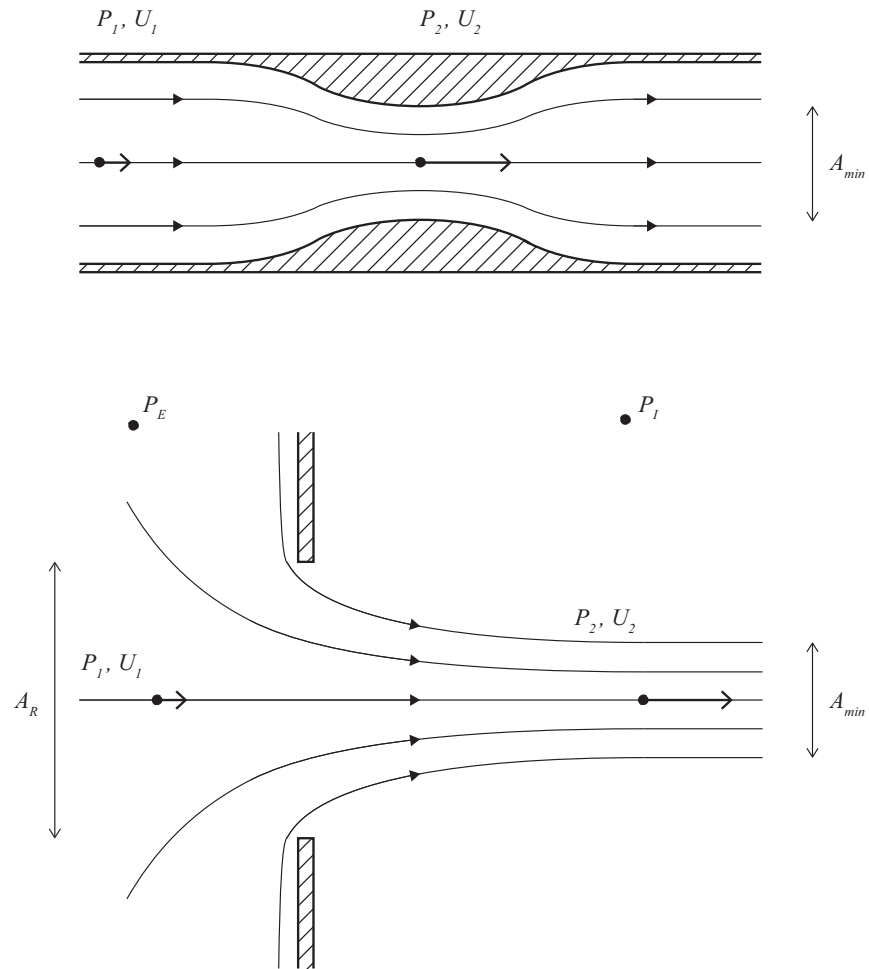


**Figure 2.6:** Comparison between the model of flow through a constriction (top), and its application to flow through a sharp-edged opening between an external and internal space (bottom). Static pressures and flow speeds are denoted by  $P$  and  $U$  respectively, with subscripts  $E$  and  $I$  referring to external and internal spaces respectively, and subscripts 1 and 2 corresponding to points in the flow. The *reference* area and the *minimum* area through which the fluid passes are denoted by  $A_R$  and  $A_{min}$  respectively.

$$U_2 = \sqrt{\frac{2}{\rho} \left( P_1 - P_2 + \frac{1}{2} \rho U_1^2 - \Delta P_T \right)} \quad (2.10)$$

This corresponds to the conditions of an isothermal, incompressible flow. The volume flow rate through the constriction can then be found by integrating the flow velocity over the area of the constriction. Where a uniform flow velocity is assumed, this yields:

$$Q = A_2 \sqrt{\frac{2}{\rho} \left( P_1 - P_2 + \frac{1}{2} \rho U_1^2 - \Delta P_T \right)} \quad (2.11)$$

Where the flow occurs between two reservoirs of still air, the upstream location in the streamline used in this analysis can be chosen at a location where the flow velocity  $U_1$  can be neglected. When no loss in total pressure occurs along the streamline, this represents flow under *idealised* conditions, and results in the equation:

$$Q = A_2 \sqrt{\frac{2}{\rho} (P_1 - P_2)} \quad (2.12)$$

It is common in envelope flow models to treat PPOs as sharp-edged orifices [25, 38]. When fluid flows through a sharp-edged opening, flow separation occurs at the edges. This results in a characteristic flow pattern where the fluid passes through a contracted area smaller than the opening, known as the *vena contracta* [38, 114]; see Figure 2.6. This corresponds to the minimum area  $A_2$  specified in Equation 2.12. At the *vena contracta*, streamlines are parallel, and the pressure in the flow tube attains the pressure in the receiving basin [109]. Therefore, the pressure  $P_1$  in Equation 2.12 corresponds to the static pressure upstream reservoir, and the static pressure in the *vena contracta*  $P_2$  corresponds to the static pressure in the downstream reservoir.

The ratio of the area of the *vena contracta*,  $A_{min}$ , to a *reference* area for the opening,  $A_R$ , is the contraction coefficient  $C_c$  [38]. A *free* area  $A_f$  is typically specified as the *reference* area for the opening, which is commonly defined as the minimum unobstructed area perpendicular to the flow, although this varies between sources [37, 115, 116]. The flow separation caused by the sharp edges means that the value of the contraction coefficient does not vary significantly with Reynolds number [25]. An additional factor,  $C_f$ , is included to account for frictional resistance [38]. The product of these is termed the discharge coefficient,  $C_d$ , and results in the orifice equation in its traditional form:

$$Q = C_d A_R \sqrt{\frac{2}{\rho} (P_1 - P_2)} \quad (2.13)$$



The contraction coefficient of a two dimensional slit can be derived theoretically, and evaluates to approximately 0.611 [6]. This is very close to experimentally derived values of the discharge coefficient for a sharp edged circular orifice, which typically lie between 0.6 and 0.65 [5, 16]. While the discharge coefficient would be expected to be different for different opening geometries, a discharge coefficient of *circa* 0.61[3] or 0.65 [16] is commonly used to model any arbitrary PPO. Although the measurement of *free* area is trivial for a circular hole, it becomes much more complex and ambiguous for real PPO geometries; see Section 2.7.1.

The product of the discharge coefficient and the *reference* area is known as the *effective* area,  $A_{eff}$ , which represents the aerodynamic properties of the opening in still air. Equation 2.13 can be used to directly calculate the volume flow rate through an opening with a known *effective* area, or rearranged to find the *effective* area of openings required to provide a given flow rate under a design pressure difference. Similarly, Equation 2.13 can be rearranged to calculate a measured discharge coefficient from experimental data. The discharge coefficient defined using Equation 2.13 is henceforth referred to as the *orifice* discharge coefficient, and denoted  $C_{d_o}$ . Where the *orifice* discharge coefficient is measured under idealised conditions - that is, steady, unidirectional flow between reservoirs of still air of uniform pressure and equal density - it is henceforth referred to as the *idealised* discharge coefficient, and is denoted by  $C_{d_I}$ .

Appendix A summarises a range of Bernoulli derivations for flow through openings under non-standard conditions.

### 2.6.1 Application to wind-driven ventilation

The traditional approach to deriving the orifice equation assumes that the air both upstream and downstream of the opening is still. This is evidently not true for wind-driven ventilation. For outflow, these conditions may be well approximated: here the upstream zone is the interior room of a building, which may be considered a relatively static reservoir of air. The static pressure in the *vena contracta* is then equated with the static pressure at the building surface where the opening is located. A justification for modelling wind driven ventilation at inflow openings using the orifice equation can be arrived at by considering total pressure in a streamline between a point in the upstream flow and a point on the façade where the opening is located, when no opening is present. This represents conditions at the surface of a sealed-body wind tunnel model used for wind pressure coefficient tests.

$$P_{T(1)} = P_1 + \rho g z_1 + \frac{1}{2} \rho U_1^2 \quad (2.14)$$

$$P_{T(O)} = P_O + \rho g z_O + \frac{1}{2} \rho U_O^2 \quad (2.15)$$

$$P_{T(1)} - P_{T(O)} = P_1 - P_O + \rho g (z_1 - z_O) + \frac{1}{2} \rho (U_1^2 - U_O^2) \quad (2.16)$$

$$P_1 + \frac{1}{2} \rho U_1^2 = P_O + \rho g (z_1 - z_O) + \frac{1}{2} \rho U_O^2 + \Delta P_{T(1 \rightarrow O)} \quad (2.17)$$

where the subscript O denotes conditions at a point in the streamline at the location of the opening, when no opening in the façade is present. When the variation in height along the streamline can be neglected, this can be substituted into Equation 2.11, assuming total pressure loss along the streamline cannot be neglected:

$$Q = A_2 \sqrt{\frac{2}{\rho} \left( P_O - P_2 + \frac{1}{2} \rho U_O^2 - \Delta P_{T(1 \rightarrow 2)} + \Delta P_{T(1 \rightarrow O)} \right)} \quad (2.18)$$

If it is assumed that all the total pressure loss along the streamline between locations 1 and 2 occurs due to flow around the building, no total pressure loss occurs due to flow through the opening, and that the opening is sufficiently small that its influence on airflow around the building can be neglected,  $\Delta P_{T(1 \rightarrow 2)}$  can be equated with  $\Delta P_{T(1 \rightarrow O)}$ . This generates an expression in terms of the static and dynamic pressures at the location of the opening, as opposed to in the free stream, which is given by:

$$Q = A_2 \sqrt{\frac{2}{\rho} \left( P_O - P_2 + \frac{1}{2} \rho U_O^2 \right)} \quad (2.19)$$

To reduce this to the orifice equation, it must be assumed that the flow velocity at the location of the opening is equal to zero. This might be approximately true in the stagnation zone that forms at the front of a building, or in the low velocity wake of the building, but is unlikely to be generally true. Nevertheless, this assumption is universally applied in envelope flow models of natural ventilation. Due to the no-slip principle, airflow is stationary at the surface of a building. When the window opening is extremely small, a justification for neglecting the fluid velocity can be made by assuming that airflow through the opening will originate from within the surface boundary layer of the wall. However, for flow through windows mounted on an up-wind façade, computational analysis by Kurabuchi *et al.* reveals that total pressure in the stream-tube that passes through an opening is largely conserved between its origin in the atmospheric boundary layer, impingement on the façade, and transport to the opening [66]. This refutes the assumption implicit in the

conventional application of the orifice flow equation that flow through openings draws from a static surface boundary layer in which all the dynamic pressure in the flow around the building is consumed.

## 2.7 Opening geometry

One of the most common simplifications of model geometry assumes that any PPO can be modelled as planar, where all elements that form the boundaries of the opening exist within the same plane. This implies the existence of sharp edges that reduce dependence on Reynolds number, and also that it does not interact with or obstruct components of the the flow that act parallel to the plane of the opening. It also implies an unambiguously calculable *free* area defined by the unobstructed area within the opening plane; see Section 2.6.

Much of the literature uses the planar opening assumption explicitly, both in simplified physical models [117, 118, 106, 100] and CFD analysis [119, 110, 120, 87]. Many other sources study flow behaviour using three-dimensional window geometries [121, 122, 123], but assume that they can be represented as planar openings using unvalidated area conversions; see Section 2.7.1. This makes it especially difficult to compare results between sources.

While the planar opening condition is well approximated for openings where all components share a common plane with the structural opening (such as sliding windows; see Figure 2.7), it cannot be said to be valid for opening geometries that contain elements that project from the plane of the structural opening. The projecting elements associated with three dimensional openings can act to restrict flow, alter the shape and direction of the streamlines passing through them, and change the way openings interact with external flow. A few studies directly examine the impact of non-planar opening geometry for cross ventilation [124, 125, 108], single sided ventilation [126, 61, 67], and for specialised airflow units [127, 128], but this approach is not widespread.

### 2.7.1 Operable windows

One of the most common types of PPOs are operable windows. This thesis follows the conventions given in CIBSE Guide B2 [26] for the naming of common window geometries shown in Figure 2.7. For the purposes of evaluating *effective* area, opening types (i-ii), and types (iii-v), can be considered identical, and are subsequently referred to as pivot and hinged openings, respectively. Most operable windows are non-planar, and therefore might be expected to interact with the components of atmospheric flow generated by wind and internal flow patterns that occur parallel to the surface in which the window is mounted. However, most window openings fulfill the requirements of being sharp-edged, and therefore the airflow characteristics are

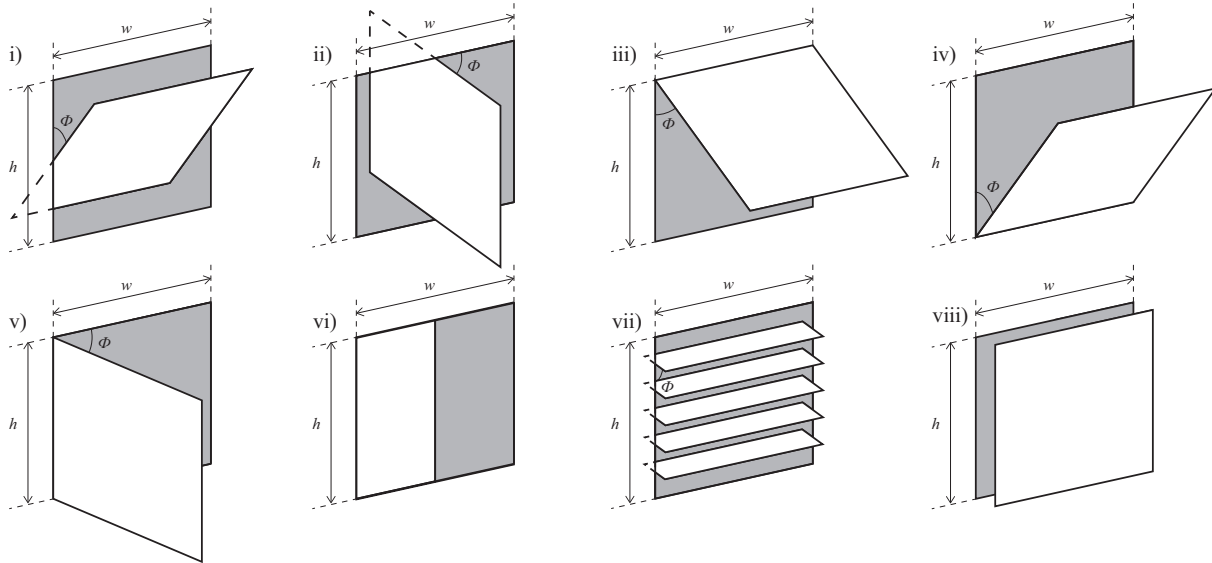


**Figure 2.7:** Common types of operable window: (i) horizontal pivot; (ii) vertical pivot; (iii) top hung; (iv) bottom hung; (v) side hung; (vi) sliding; (vii) louvre; (viii) parallel plate [26]

only weakly dependent on Reynolds number.

### Abstraction to planar geometries - *free-area* models

When estimating airflow through an opening, it is necessary to characterise its resistance to airflow. For design purposes, the most important determinant of resistance is the *effective* area of the opening [5, 37]. While it is conventionally assumed that the flow capacity of an operable window is dependent only on the total area [113], knowledge of the resistance distribution, and hence the area distribution, is required when the pressure across the opening is non-uniform.

In practice, it is common to calculate the *effective* area of an operable window by assuming a constant *orifice* discharge coefficient, and evaluating the *free* area based on inspection of the window geometry, given by

$$A_{eff} = C_{d_o} A_f(\phi, h, w) \quad (2.20)$$

where  $\phi$  is the opening angle,  $h$  is the height of the opening,  $w$  is the width of the opening, and  $A_f \leq hw$ . Estimating the *free* area of a window is often assumed to be a trivial problem. Consequently, there has not been a systematic study of how this is done, or of the impacts of any errors associated with its estimation on predictions of window performance. However, it is clear from the literature that the definition of *free* area is ambiguous, and that different practitioners approach it in different ways [37, 121, 123, 126, 129, 124, 125, 116].

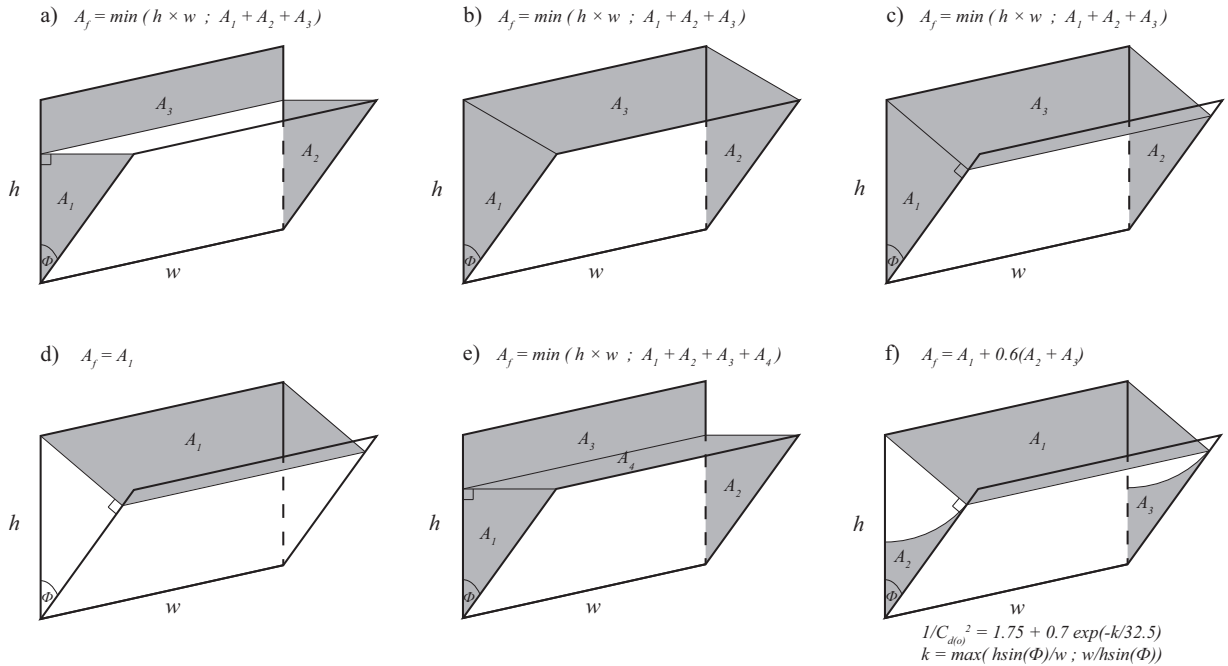


**Figure 2.8:** A range of different methods of modelling *free* area [121, 123, 126, 129, 124, 125, 116]. Model *f* is semi-empirical, and includes a coefficient allowing for reduced efficiency of the side areas that is adjusted to fit experimental data.

Figure 2.8 illustrates a range of approaches to calculating the *free* area of hinged openings, all of which are based on the sum of different measured areas. Little theoretical justification is given for each area model, and comparison with empirical data is very rare. This ambiguity is a major source of error both in practice and in academia [37].

Jong and Bot [124, 125] produce empirical data based on still-air pressurisation tests for simple hinged openings, which they use to fit coefficients to analytical *free* area model 'f' shown in Figure 2.8. This model however is unnecessarily complicated by a number of analytical factors that could be readily combined, and predicts air flow rates that tend to infinity as the height to width ratio tends to infinity.

An alternative approach is to define a fixed, easily measurable area for an opening and to evaluate the *orifice* discharge coefficient experimentally as a function of opening angle. This defines the *effective* area and the *orifice* discharge coefficient as

$$A_{eff} = C_{d_o}(\phi, \sigma) h w \quad (2.21)$$

$$C_{d_o}(\phi, \sigma) = \frac{Q}{h w} \sqrt{\frac{\rho}{2 \Delta P}} \quad (2.22)$$

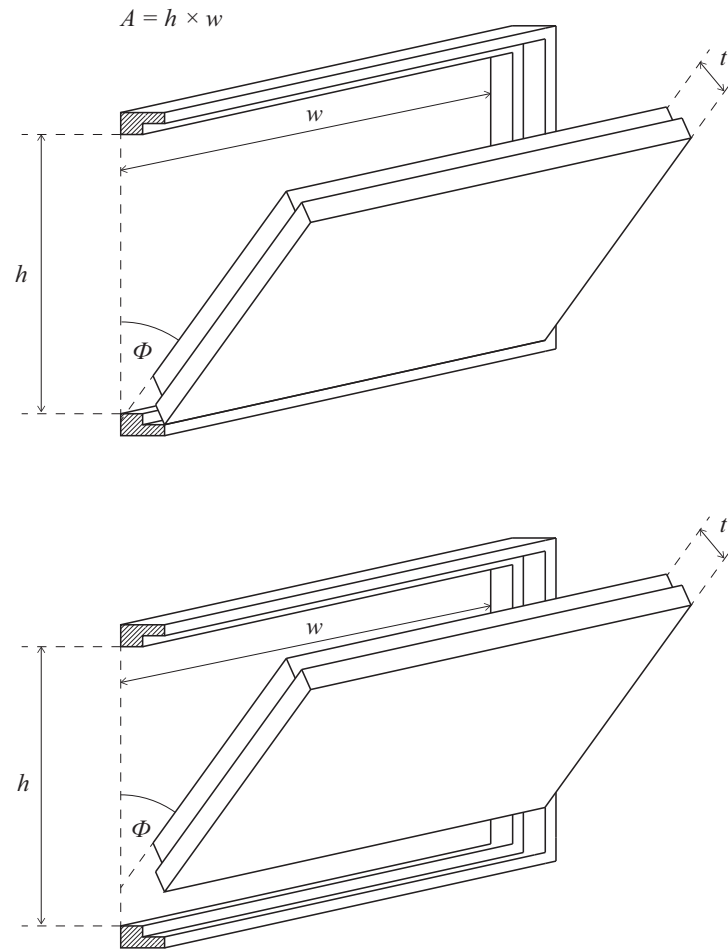


**Figure 2.9:** Simplified measurement method to define the dimensions of an opening, where  $A$  is the reference area of the opening,  $h$  is the internal height of the fixed frame,  $w$  is the internal width of the fixed frame,  $t$  is the thickness of the opening sash, and  $\phi$  is the angle between the planes of the fixed frame and opening sash known as the opening angle. A summary of its application to different opening geometries is given in Figure 2.7.

where  $\sigma$  is the aspect ratio,  $h:w$ . Figure 2.9 describes how the characteristic dimensions of a nominal window opening – its height, width, area, opening angle, and thickness – can be measured. Note that these definitions are applicable to all opening types given in Figure 2.7, as well as to windows that use sliding hinges where the pivot point moves in the vertical plane as  $\phi$  varies.

The UK design guidance for the ventilation of school buildings, Building Bulletin 101 [2] (BB101), presents a simple statistical model of the variation in the *idealised* discharge coefficient with opening angle based on this approach, fitted to proprietary data<sup>1</sup>. A new empirical model that uses academic data is developed in Section 5.3.1 for use in design, and benchmarked against existing models in Section 5.3.2.

<sup>1</sup>All versions available from DOI: 10.13140/RG.2.2.10748.08323

### **Influence of obstructions on airflow characteristics**

To allow the properties of an opening to be determined separately from the room in which it is installed, it is often assumed that airflow rates are unaffected by local obstructions, such as sills and reveals. However, sills and reveals can restrict the area available for air to pass through, as well as affect how the window geometry interacts with external airflow.

In academia and in practice it is common for these local obstructions to be accounted for as a reduction in *free* area [113, 116]. While the technique makes analytical sense, it is subject to the same ambiguities and errors associated with the geometric models discussed in Section 2.7.1.

The analytical technique developed by Hall [112] to improve the prediction of single sided ventilation rates was found to reduce errors in predicted performance at very small opening angles. However, the technique requires empirical data to calibrate it and no justification is given for extrapolating the results to higher opening angles or to cross ventilation configurations. In the absence of experimental data, the resultant errors cannot be quantified.

In addition to the physical obstructions that occur due to the installation position of a PPO within a building's fabric, it is possible that external obstacles - such as trees or louvres - or internal obstacles - such as people, blinds, furniture, and partitions - could interact with the structure of airflow through the openings. A through review of the literature did not identify any existing research that quantifies the effect of these obstacles on the performance of any PPO.

### **2.7.2 Chimneys, ducted outlets and wind catchers**

A range of ventilation technologies use long ducts to transport air around a building, either to access deeper spaces or provide access to favourable pressure conditions [100, 25]. These opening types typically cannot be modelled as sharp-edged; their *idealised* discharge coefficient needs to be given as a function of Reynolds number [25]. The use of *idealised* discharge coefficients that are dependent on Reynolds number allows these types of opening to be integrated into conventional envelope flow models.

In addition to their effect on the *idealised* discharge coefficient, these technologies affect the driving forces available for natural ventilation. Chimneys increase the stack height available for buoyancy-driven ventilation [25, 3, 5]; solar chimneys increase the air temperature within the stack, raising buoyancy pressure; and wind catchers, chimney tops and roof cowls alter the wind pressure coefficients at either the inlet or the outlet to enhance flow [130, 131, 5, 25]. While in many cases these pressures can be evaluated independently of flow rates through the ducts [127, 25, 100], this is not universally true. As a result, purely empirical models are sometimes used to quantify the airflow performance of these components under a range of conditions [132].

### 2.7.3 Mesh screens

To improve security and reduce the risk of ingress of bugs and animals, mesh screens are often installed in ventilation openings. Flow through these screens has been the subject of considerable study, and a summary of experimental data and modelling methods is given by Bailey *et al.* [133]. The *idealised* discharge coefficients of screens are highly dependent on Reynolds number [25, 133], and this relationship can be expressed as a function of the porosity of the screen and the thickness of the wires [133, 134]. Alternatively, flow rates can be characterised by a power law [135] or quadratic relationship [25] instead of the conventional orifice flow equation.

Mesh screens are typically installed within other opening types, with which they could interact aerodynamically. Bailey *et al.* suggest calculating the combined resistance to airflow caused by a mesh screen set within a window frame by summing the resistance factors ( $F = 1/C_d^2$ ) determined for the two components in isolation, but provide no experimental data to support this. A similar approach is taken by Syrios and Hunt to predict ventilation rate through roof mounted ventilation towers where components are connected in series, although again the predictions are not compared against measured data [134]. Tabulated design equations for the integration of mesh screens with louvres are given by Holzer and Psomas [131]. It is not clear how these screens would interact with other opening geometries.

## 2.8 Air flow through windows driven by atmospheric wind

When the wind drives flow, the air proximate to the external surface of an opening can be expected to be in motion for the majority of cases. However, most envelope flow models implicitly assume that the external air is static; see Section 2.6.

In many cases the aerodynamic properties measured in the presence of wind may be similar to those measured in still-air, but significant differences are also possible. The presence of external air movement can alter the shape and directions of streamlines passing through an opening, and projecting opening geometries can interact with external flows to alter the pressure field near the surface of an opening; see Figure 2.10. Venturi ventilators can be used to ensure suction pressures over outlets, which can achieve pressure coefficients as low as -1 [130, 131]. Here, pressure coefficients derived from bluff bodies are not suitable for use with real window geometries. This interaction also affects the surface pressures for some distance around the opening, introducing additional uncertainties if other openings are present [136]. Furthermore, wind-induced pressure fields on buildings and near openings can be spatially varied, introducing more complex flow patterns than might be expected with a uniform pressure field.



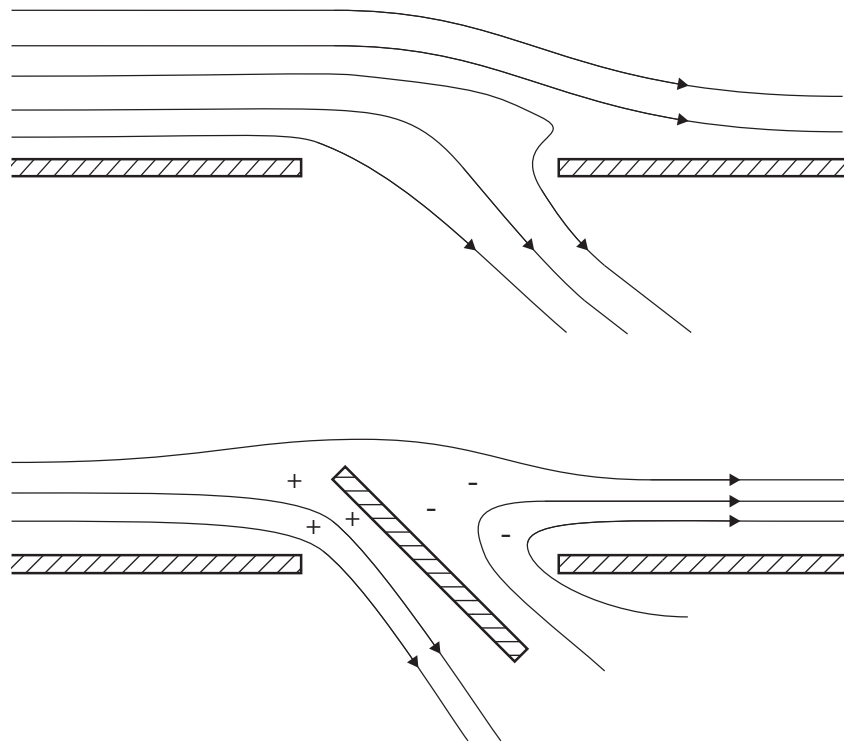


**Figure 2.10:** Diagram depicting the effect of a cross-flow on the anticipated shape of streamlines passing through a planar opening (Top, after Vickery and Karakatsanis [81]), and the effect projecting opening geometry can have on flow patterns and local pressure fields (Bottom); see Section 2.8.4 and Iqbal *et al.* [136].

In addition to this, the turbulent flow structures and other unsteady behaviour associated with atmospheric wind have been proposed as another mechanism for driving ventilation [61, 25, 78], with the potential to drive bidirectional flows through openings.

### 2.8.1 The cross-flow approach to simulating wind-driven flow

One approach to evaluating the impact of wind is to consider the performance of openings when exposed to a cross-flow; see Section 2.4.2. This aims to describe the airflow through a window opening in terms of the properties of the flow local to that opening: typically the internal and external static pressures, and the velocity of the cross-flow that occurs parallel to the façade at the location of the opening. This separates the phenomena of flow through openings from the specifics of building geometry, which allows the results to be generalised for use in envelope flow models.

Two approaches to evaluating the impact of a cross-flow on ventilation rates can be distinguished:

1. Whole-building models
2. Local-flow models

#### Whole-building models

In *whole-building* models, flow through a whole building is simulated. Here, the speed of the cross-flow and the internal and external pressures are evaluated by sampling the flow in and around a model building, and measurements of ventilation rate are made [100, 66]. Modelling the entire building ensures that the flow structure of the cross-flow is realistic, with a velocity distribution and turbulence intensity appropriate to the simulated building type and approach flow. However, modelling the whole building requires that the window openings are comparatively small [100, 38]. This introduces challenges in modelling the window geometry in sufficient detail, and in the spatial resolution of velocimetry measurements. The smaller opening sizes also present more potential Reynolds number scaling issues - although this effect may be less important for most PPOs due to the presence of sharp edges [25, 88]. Furthermore, modelling whole buildings introduces additional variables that need to be controlled, such as building geometry, local terrain, and the location, size, and distribution of window openings [66]. Finally, when modelling whole buildings, it is difficult to decouple flow through openings from the internal flow patterns [105, 1]; see Section 2.3. These issues make the identification of the mechanisms responsible for measured flow phenomena a challenging task.

### Local-flow models

In *local-flow* models, flow through windows is simulated independently of the building in which it may be installed, with the aim of experimentally replicating the *local* flow field on either side of the opening [66, 105, 61, 67]. In contrast with *whole-building* models, *local-flow* models offer considerably more control over the structure of the flow, and the local environmental conditions. The increase in scale permits more spatially resolved measurements of flow around the openings, and more detailed modelling of representative window geometry [99, 67]. However, the *local-flow* approach faces a challenge of ensuring that the simulated local phenomena are representative of those that occur on real buildings. This is compounded by a dearth of available data on the structure and properties of cross-flows observed on typical building geometries; see Sections 2.3 and 2.4. Furthermore, it is unlikely that appropriately scaled space-volumes can be simulated due to space constraints [66]. This affects the *indoor* velocity distribution, and constrains the development of inflow jets from window openings. It also reduces the compressibility of the indoor air. Due to the large internal volumes of buildings, this can be an important feature of unsteady flow behaviour, particularly in the modelling of single-opening ventilation [137, 138]. Therefore, studies should ideally compare measurements at both *building* and *local* flow scales [66, 67].

### 2.8.2 Unidirectional flows through openings in a cross-flow

Vickery and Karakatsianis were the first to hypothesise that the presence of a cross-flow could reduce the unidirectional flow rate through openings in wind-driven cross ventilation [81]. Vickery and Karakatsianis take the *whole-building* approach to investigating wind-driven cross ventilation, and find that the orifice flow equation systematically overestimates flow rates in the presence of wind. While they do not measure the velocity of the cross-flow at the building surface, they hypothesise that the reduction in *orifice* discharge coefficient of the openings arises from the distortion in streamline shape that can be expected to occur due to momentum in the exterior flow; see Figure 2.10 [81]. Vickery and Karakatsianis find that the over-prediction of volume flow rates by the orifice flow equation increase as the wind angle deviates from the normal [81]. This correlates with an increase in cross-flow velocity, but also with an reduction in uniformity of the surface pressure distribution on the building's façade; see Sections 2.4.1 and 2.4.2. As such, the mechanism responsible for the measured reduction in volume flow rate cannot be determined from this study.

### Similarity models of ventilation in a cross-flow

Several authors have applied dimensional analysis to the problem of ventilation in a cross-flow in order to identify similarity parameters that can be used to characterise ventilation performance [66, 99, 100, 25].

Kurabuchi *et al.* apply dimensional arguments to describe a dimensionless room pressure, which is defined as the ratio of the static pressure drop across an opening to the dynamic pressure in the cross-flow [66]. This model aims to ensure dynamic similarity based on local flow conditions, and is therefore given the moniker of the *Local Dynamic Similarity Model* (LDSM) [66, 104, 99, 105]. Chiu and Etheridge describe a dimensionless cross-flow velocity as an alternative parameter used to characterise the relative strength of a cross-flow [100]. This is defined as the ratio of the velocity of the cross-flow to the mean speed of flow through the opening, which in turn is described by the ratio of the volume flow rate through the opening to a reference opening area [100, 25]. This parameter is also derived from dimensionless similarity arguments, and describes the same phenomena as the dimensionless room pressure developed by Kurabuchi *et al.* [25, 66]. Here, the dimensionless cross-flow velocity described by Chiu and Etheridge is equal to zero under *still-air* conditions [100, 25]. Etheridge describes this as a key advantage over the use of the dimensionless room pressure, which tends to infinity for still-air conditions [39]. However, this can be resolved by taking the inverse of the dimensionless room pressure, which would allow the *idealised* discharge coefficient to be presented graphically.

### Inflow through simple orifices

Kurabuchi *et al.* and Ohba *et al.* have produced a series of CFD and wind tunnel investigations into the influence of a cross-flow on inflow rates through ventilation openings at both building-scale and local-scale [66, 104, 99]. Here, a clear relationship between the *orifice* discharge coefficient and the dimensionless room pressure is established, whereby the *orifice* discharge coefficient tends to *still-air* values as the dimensionless room pressure tends to infinity, and reduces to a minimum value as the dimensionless room pressure tends to zero. A similar relationship is identified by Chiu and Etheridge, who present a small CFD study that applies a local-scale approach to predict inflow through a sharp-edged orifice in a cross-flow [100]. This study investigates the influence of Reynolds number, unsteady driving pressures, and the dimensionless cross-flow velocity on flow through an opening, and finds that the dimensionless cross-flow velocity is the dominant source of variation in the *orifice* discharge coefficient. Here, the value of the *orifice* discharge coefficient is predicted to slightly increase at very small values of the dimensionless cross-flow velocity, and then decrease as the dimensionless cross-flow velocity becomes larger. This agrees with early technical data from Idelchik concerning flow in merging pipes [139].

The use of CFD studies permits a detailed analysis of a stream-tube that passes through an opening [66]. Kurabuchi *et al.* identify a reduction in total pressure arising from the generation of turbulent kinetic energy as the stream-tube is deflected to pass through an opening by a static pressure differential across the facade [66]. This is hypothesized to be the cause of the observed reduction in the measured *orifice* discharge

coefficient [66, 104]. However, as the approach flow and the shape of the streamlines is significantly altered by the momentum of the cross-flow, there is no reason to expect that the *orifice* discharge coefficient would be the same as that observed under *idealised* conditions [81, 25, 38].

While the building-scale experiments presented by Kurabuchi *et al.* identify the presence of a surface-boundary layer that can affect cross-flow measurements, most local-scale experiments are designed to ensure a uniform velocity field in the cross-flow [66, 104, 99, 105]. This reduces the degree to which these local-scale experiments are representative of building flows, but corresponds to a worst-case scenario where the window experiences its maximum deviation from *still-air* performance. It also simplifies the choice of location at which to measure the speed of the cross-flow.

Kurabuchi *et al.* investigate the direction of the inflow jet entering from a window opening in a cross-flow [66]. Similarly, this can be characterised using the dimensionless room pressure. Here, the angle of inflow jet tends to the normal as the dimensionless room pressure tends to infinity, and becomes parallel to the opening when the dimensionless room pressure tends to zero. These limits correspond to *still-air* conditions and single-opening conditions, where there is no static pressure drop across the opening, respectively. The relationship presented by Kurabuchi *et al.* assumes a thin opening that does not significantly interact with the horizontal component of the momentum in the cross-flow. Where the opening depth is not insignificant compared to the size of the opening, this is unlikely to be true: wind tunnel studies by Heiselberg *et al.* find that, as the opening size in a façade decreases, the inflow jet becomes increasingly normal to the façade, resembling static-pressure driven flow [38]. This phenomena could be more important in real buildings, where windows are set within walls of significant thickness.

### Outflow through simple orifices

Etheridge predicts that the rate of outflow through ventilation openings would be relatively independent of cross-flow velocity [25]. Here, the outlet flow condition fixes the static pressure in the *vena contracta* to that of the ambient fluid, and flow upstream is drawn from the comparatively static indoor air [109, 25]. However, Endo *et al.* identify a similar relationship between the measured *orifice* discharge coefficient and the dimensionless room pressure for outflow through a rectangular orifice to that observed by Kurabuchi *et al.* for inflow openings [105, 66]. Here, parallel wind-tunnel and CFD experiments are used to investigate the structure of flow through an outflow opening in a cross-flow based on the *local-flow* approach. Endo *et al.* identify that a cross-flow can interact with the outflow jet from an opening, causing it to deflect in the direction of the cross-flow. This deflection can be strong enough to cause the outflow jet to attach to the external wall, and restricts the area of the *vena contracta* through which fluid can flow [105]. This is hypothesised to be the mechanism responsible for the measured reduction in *orifice* discharge coefficient [105].

A peak in the measured *orifice* discharge coefficient is observed at values of the dimensionless room pressure close to one, which exceeds the *idealised* discharge coefficient measured in still-air. This is hypothesised to occur as a result of local pressure changes caused by interaction between the cross-flow and the outgoing flow stream, which enhances the pressure differential available to drive flow [105]. Endo *et al.* illustrate that this peak disappears when these local pressure changes are appropriately accounted for [105]. However, the method used to account for local pressure changes is not reported.

### **Influence of window geometry on ventilation in a cross-flow**

For a simple, rectangular orifice, Kurabuchi *et al.* find that the relationship between *orifice* discharge coefficient and dimensionless room pressure is independent of the direction of the cross-flow [66]. However, a thin, planar opening such as a rectangular orifice presents a similar section to the cross-flow regardless of the approach direction. This is not generally true for other window geometries such as hinged or pivoted openings, which might be expected to interact differently depending on the direction of a cross-flow; see Section 2.7.1 and Figure 2.10. Therefore, the independence from cross-flow direction observed by Kurabuchi *et al.* is likely to be specific to symmetrical opening geometries [66]. Ohba *et al.* apply the local-scale approach presented by Kurabuchi *et al.* to characterise the *orifice* discharge coefficient of a range of other window geometries as a function of the dimensionless room pressure [66, 99]. However, as they have assumed independence of cross-flow direction following Kurabuchi *et al.*, the influence of cross-flow direction on aerodynamic performance is not investigated, and the cross-flow direction and opening orientation used in the experiment are not reported in the study [99].

Chiu and Etheridge utilise the whole-building approach to investigate the performance of different kinds of opening in a cross-flow [100]. Here, two kinds of opening are distinguished: long openings such as chimneys, and short openings, such as windows. For a simple orifice mounted in the wall of a building, a clear relationship between *orifice* discharge coefficient and the dimensionless cross-flow velocity is observed. Here, a dimensionless cross-flow velocity of zero corresponds to still-air conditions, with substantial reductions in *orifice* discharge coefficient of 50% or more observed as the dimensionless cross-flow velocity increases [100]. This depends primarily on the magnitude of the dimensionless cross-flow velocity and is relatively independent of local turbulence; a finding supported by wind-tunnel experiments by Chu *et al.* [140]. For long openings such as chimneys, significant dependence on Reynolds number is observed [100, 25, 141]. Where the outlet lies within the external flow, the impact of a cross-flow on *orifice* discharge coefficient is found to be negligible [100]. However, a significant impact is observed when the inlet is located in the external flow. Here, dependence on Reynolds number is weaker in the presence of a cross-flow, which leads to significantly increased values of the *orifice* discharge coefficient at low Reynolds numbers compared to those

measured under still-air conditions. This effect is important, as it increases the likelihood of flow-reversal occurring in chimneys [141, 100]. However, Chiu and Etheridge find that the inclusion of a cover over the top of the chimney eliminates the effect of a cross-flow on the *orifice* discharge coefficient [100]. In general, Chiu and Etheridge show that long openings experience significantly less dependence on the dimensionless cross-flow velocity than sharp-edged openings such as windows [100]. This could have important implications on buildings where windows are located within deep wall reveals, which could invalidate the sharp-edged assumption common in analytical and experimental approaches to evaluating flow through window openings.

Wind is expected to have an even greater effect on ventilation rates where the opening projects into the external flow. This may commonly occur for outward opening and pivoted window types [136], as well as for ducted opening types such as wind cowls [25]. Kurabuchi *et al.* identify some cases where the *orifice* discharge coefficient rises sharply as the dimensionless room pressure approaches zero [66]. For inflow through a roof-mounted centre-pivot window, Iqbal *et al.* identify discharge coefficients that tend to infinity as the reference wind speed becomes large compared to the average flow speed through the opening [88]. Etheridge [25] also identifies *orifice* discharge coefficients for inflow through a wind cowl rising towards infinity as the dimensionless cross-flow velocity increases. This may be caused by the opening interacting with external wind flows to evolve static pressure at the opening surface that is not accounted for in the definition of the orifice equation [136, 131]. This would cause a non-zero volume flow rate to occur through the opening when the measured pressure differential between the indoor and outdoor air approaches zero, resulting in infinite values of the evaluated *orifice* discharge coefficient. Under inflow conditions, Etheridge demonstrates that values of the discharge coefficient can be kept finite by including the cross-flow dynamic pressure term in the orifice equation; see Equation 2.19. This can be derived from Bernoulli analysis of airflow through an opening in a cross-flow; see Section 2.6.1 and Chapter 3.

### 2.8.3 Bi-directional flows through openings in a cross-flow

The orifice equation commonly used in envelope flow models predicts unidirectional flow rates through openings [6, 5]. However, gas exchange through ventilation openings can occur in both directions. Bidirectional flows are important in single-opening ventilation, where ventilation in a space occurs through one window only [61, 142, 117, 3]. In this case, conservation of mass requires that the flows into and out of an opening are balanced, such that the temporally averaged net flow through the opening is zero. A thorough review of the literature did not identify any research studying unbalanced bidirectional flows in the presence of wind. This can introduce difficulties for airflow network models, which have to interpolate between solutions for single opening ventilation and envelope flows without the benefit of supporting data [143, 144]. Therefore,

the subsequent discussion concerns balanced flows only.

### Pressure-driven flows

Envelope flow models assume that the wind pressure acting on a ventilation opening is the same as the wind pressure acting on the façade of the building in which the window is located, at the location of the window opening. This surface pressure is typically measured without openings present [96, 94, 5, 38]. Most envelope flow models assume that wind pressures acting on an opening are uniform across its surface. However, Daish *et al.* find that the pressure differential between two points on a façade increases with the square-root of the separation scaled by the building width [78]. Therefore, the validity of this assumption is likely to break down when the openings are not small compared to the size of the façade [38, 25, 117]. While non-uniformity in the surface pressure field has the potential to affect unidirectional volume flow rates through ventilation openings, a thorough review of the literature did not identify any research into this phenomena.

Where the differential pressure changes in sign across the area of an opening, bidirectional flow is driven through it. This introduces an additional flow path that is not accounted for by conventional envelope flow models. A thorough review of the literature suggests that integration of the non-uniform wind profiles induced by wind into envelope flow models has to-date relied purely on empirical correlations [117]. Larsen and Heiselberg include the maximum deviation in surface pressure coefficient over the area of an opening as a statistical coefficient in their correlation for single opening ventilation driven by wind and buoyancy [117]. Here, a *whole building* approach is taken to the investigation, where multiple parameters are varied simultaneously and fit to a statistical model. This means that a systematic investigation into the effect of the spatial variation in static pressure of ventilation performance could not be undertaken. Warren and Parkins and Albuquerque *et al.* apply a *local-flow* approach to characterise wind-driven single-opening ventilation in a cross-flow [61, 67]. Here, the local pressure variations are not directly measured, but the combined effect of both pressure and shear-driven ventilation rates is characterised by a flow number that can be evaluated by experiment. Again, the static pressure differential across the area of the opening could not be systematically varied. Therefore, the impacts of spatial variation in surface pressure on ventilation rates are difficult to quantify based on the available literature data.

Non-uniform pressure profiles can also occur due to the interaction between a cross-flow and window geometry. Iqbal *et al.* apply a *whole-building* approach to investigate the effect of a roof-mounted centre-pivot window on the local pressure field [136]. Here, they find that airflow passing over a centre pivot window can generate variations in static pressure across its surface that are sufficient to drive steady-state bidirectional flow; see Figure 2.10. Air enters at the windward side of the opening, and leaves via the leeward side. This phenomena is visualised using smoke, but the impact on bidirectional flow rates is not quantified.



### Turbulent shear

In addition to local pressure variations, a key driver of single opening ventilation is turbulent shear. When a layer of fast moving fluid passes over a layer of stationary fluid, shear forces cause a transfer of momentum from the fast moving to the stationary fluid layers. This occurs when a cross-flow over the surface of a building interacts with stationary indoor air across an opening in the façade. This transfer of momentum generates a turbulent mixing layer, where fluid is exchanged between the internal air and the cross-flow [61, 145]. This phenomena was first described by Warren and Parkins as a mechanism for driving single-opening ventilation, where no pressure variation occurs over the surface of the opening [61]. The theoretical analysis assumes a symmetrical mixing layer where the rate of entrainment is equal on the internal and external faces of the opening [61]. However, several experimental studies have shown that entrainment is higher on the internal face of the opening, leading to an asymmetric mixing layer [146, 147, 145]. Regardless of the mechanism, the ventilation rate can be characterised empirically using a dimensionless flow number [145, 67, 61], where

$$F_L = \frac{Q}{A_R U_L} \quad (2.23)$$

Analytical values of the flow number for a planar orifice range from 0.013 [61] to 0.051 [145], which compares to an experimentally derived range of 0.025-0.06 [148, 149, 150, 61]. Experimental measurements have shown that the flow number is increased by local turbulence [61, 149], which would be expected to increase the rate of mixing between the indoor and outdoor air. Increased turbulence may also drive ventilation by pulsation mechanisms; see Section 2.8.5.

The impact of simple hinged opening geometries on shear driven ventilation rate has been investigated experimentally [67, 61]. Here, measured values of the flow number describe the combined effect of both turbulent mixing mechanisms and differential pressure mechanisms. Contrary to the models that are applied in industry [5, 3, 16, 151], ventilation rates are found to be dependent on the direction as well as the speed of the cross-flow [67, 61]. Interestingly, this is true even for inward opening windows, where the opening vane can act either to direct entrained air into the room or to redirect it out [67]. The opening vanes of common window geometries can therefore act either to inhibit or enhance flow depending on the configuration and local conditions [67]. Here the flow number is not a constant, but described as a function of the opening angle of the window, and the direction of the cross-flow [67, 61]. As no analytical model exists to describe this phenomenon, experimental characterisation is required to account for the impact of real opening geometries. To date, experimental data is confined to simple, hinged openings at 90 degree increments in cross-flow direction [67, 61].

### 2.8.4 Impact of wind on the local pressure field

Wind pressure coefficients applied in envelope flow models typically measure the static pressure at the surface of a building façade in the absence of window geometry [95, 96, 5]. However, wind has the potential to interact with window geometry to alter the local pressure coefficient near an opening. Much of the information in the literature that describes this phenomena is anecdotal. Holzer and Theofanis discuss Venturi ventilators that can be used to achieve pressure coefficients as low as -1 over ventilation outlets, although no data or methodology are provided [131]. Etheridge discusses the effect of ducted openings such as wind cowls and of small local obstructions such as rainwater down-pipes on the local pressure field, but provides no details of supporting measurements [25].

Some of the most detailed measurements investigating the impact of window geometry on the local pressure field are provided by Iqbal *et al.* [136]. Iqbal *et al.* apply a *whole-building* approach to investigate the effect of a roof-mounted centre-pivot window on the local pressure field [136]. Here, pressure taps are mounted around the perimeter of the window frame and on the roof surface around the window. This illustrates the difficulty in measuring local pressure changes over the plane of the opening, as the opening itself restricts the locations for pressure taps. Iqbal *et al.* identify that the presence of a centre-pivot window can significantly alter the local pressure field. This effect is strongest close to the window, and for wind angles normal to the axis of the pivot. Here, local pressure coefficients can be altered by up to a factor of eight depending on the opening angle, and in some cases are changed in sign compared to measurements without the window present. If this change in local pressure is not adequately accounted for, then this phenomenon could be responsible for the infinite values of the *orifice* discharge coefficient evaluated by numerous authors at high wind speeds [25, 66, 88]; see Section 2.8.2. Both the magnitude of the effect and the trends are observed to vary with wind angle, and are absent when the wind angle is parallel with the axis of opening. Small-opening angles were found to significantly alter the local pressure distribution over an area around the window up to 1.5 times the area of the opening. Large opening angles were found to significantly alter the local pressure distribution over an area around the window up to 4 times the opening area [136]. This suggests that the interaction between different openings can be important when they are located close together, which introduces errors compared to results measured for a single opening in isolation [136]. Unfortunately, it is not uncommon in natural ventilation design to have many openings in close proximity to one another [5, 130, 131]. This could be a source of error that is difficult to account for in a general way for ventilation design purposes.

In addition to interaction with fixed window geometry, a wind-generated cross-flow has been shown to interact with the flow structures generated by flow through an opening [105]. Endo *et al.* apply a *local flow*

approach to systematically investigate the impact of a cross-flow on the outflow jet that emerges from a ventilation opening into the external air [105]. In still-air, the jet emerges perpendicular to the opening in the façade, and continues straight until the jet decays via entrainment of the surrounding fluid [6, 108]. In a wind-driven cross-flow the fluid in this jet intercepts the cross-flow, resulting in deflection of the outflow jet. The cross-flow slows and increases in pressure at its leading edge, accelerates as it deflects over the bending jet, and forms a low pressure wake in its lee [152]. This results in a spatially varied pressure field in the vicinity of the opening, which is capable of altering flow through it [105]. This phenomenon is thought to be responsible for the enhanced *orifice* discharge coefficients measured when the dimensionless room pressure is close to unity [105, 139], and could result in some local bidirectional gas exchange through the opening at low values of the dimensionless room pressure. A jet in a cross-flow is a well described phenomena in fluid mechanics, and behaves differently from the free jet typically assumed in the derivation of the orifice equation [153, 154]. However, most of the literature focuses on the topology of the jet as opposed to its effect on volume flow rate through, or pressure drop across, an orifice [155, 156]. The influence of the cross-flow generates considerable vorticity within and around the jet [156]. The turbulent vortices in the cross-flow cause the outer layer of fluid in the jet to erode and be carried downstream as the jet is distorted by the pressure from the cross-flow [152]. This illustrates flow behaviour that is significantly different to the idealised jet treated with a Bernoulli approach. The impact of this behaviour on ventilation flow phenomena is unclear, and requires more extensive research.

### 2.8.5 Unsteady flow phenomena

Atmospheric wind is by nature unsteady, and results in a fluctuating pressure and velocity field near the openings in a building envelope [25, 16]. Turbulent eddies can pass through openings in a building envelope and penetrate into spaces, even where driving pressures are not available [137, 6]. This interaction is complex and difficult to model for integration into envelope flow models, and depends on the size, strength, and distribution of turbulent eddies in the external flow as well as the size and shape of the opening.

Most models of unsteady ventilation apply a quasi-steady assumption [25]. Here, the volume flow rate through ventilation openings is assumed to be described by the steady flow equations, with the problem reduced to describing the pressure fluctuations as a function of time. This requires a constant streamline pattern to be assumed, and the inertia of the fluid to be neglected [25]. Daish *et al.* identify periodic variations in driving pressure arising from vortex shedding in the wake of a building [78]. In some ventilation configurations, this has been shown to generate pumping flow, where air periodically switches between flowing in through one opening and out of the other. While this results in ventilation rates that are poorly described

by steady-state models, there is no suggestion that this flow cannot be described with steady-state discharge coefficients, and fluctuating instantaneous driving pressures [78].

In large spaces, the compressibility of the indoor air becomes important [25, 138, 157]. Here, the internal pressure varies isentropically as mass flows into it, in accordance with ideal gas laws. This provides a mechanism for pressure-driven gas exchange even where the time-averaged pressure difference across an opening is zero [25, 138, 157]. This mechanism is described in the literature as pulsation theory, and was first proposed by Cockroft and Robinson [138]. The theory assumes that all air entering or leaving the building mixes perfectly and instantaneously with the indoor or outdoor air respectively [138, 25]. The mean ventilation rate, therefore, can be given as half the sum of the magnitudes of the instantaneous flow rates through all openings [25]. However, where fluctuations in volume flow rate are sufficiently rapid, pollutants present in the air leaving the space may re-enter before it has time to disperse into the outdoor environment. This results in real gas exchange rates that are lower than those predicted by unsteady ventilation models [158].

A CFD and experimental study by Yamanaka *et al.* shows that pulsation theory is not adequate to describe wind-driven single-opening ventilation rates [150]. Pulsation theory predicts a maximum gas exchange rate at a wind angle of zero degrees, defined normal to the façade [138, 150]. However, measured ventilation rates are found to peak at a wind angle between 30 and 75 degrees [150]. Local-scale CFD confirms the presence of the mixing layer predicted by Warren and Parkins [150, 61]. However, the dependence of ventilation rate on turbulence identifies the importance of fluctuating wind pressures on driving single opening ventilation. Model-building experiments present a challenge in adequate scaling of the building volume to account for compressibility effects [159, 25]. Therefore, it is likely that compressive pulsation phenomena will be more important in full-scale buildings than at experimental scale.

Temporal effects can also have an impact on ventilation driving pressures. For example, flow reversal in a chimney reduces the driving pressure due to buoyancy, and therefore reduces the potential for the intended ventilation pattern to recover [141, 25].

### 2.8.6 Whole-building empirical models

Envelope flow models of natural ventilation typically treat the flow around buildings, the flow through window openings, and the flow through buildings independently. An alternative approach is to model the entire building, including its internal and external surroundings, and develop an empirical description of the measured ventilation rate through the building based on measured or simulated weather conditions [39]. A whole building approach allows the external and internal flow phenomena to be directly coupled, without the

need to understand or explicitly model their behaviour [160]. This approach offers potentially high accuracy for a specific building, but lacks generality.

Everette applies a full-scale approach to studying the thermal performance of real buildings [161]. This approach develops empirical models that allow building performance to be calibrated. However, the calibration of these models requires extensive and expensive field work, and is not suitable for design-stage modelling [39]. For this reason, scale modelling approaches are more common.

Carey and Etheridge apply direct wind-tunnel modelling to investigate ventilation rates in a model building [159]. The principal advantage of direct modelling is the implicit inclusion of temporal and turbulent effects, which steady-state envelope flow models are not able to evaluate [159, 25, 38]. It enables the generation of empirical ventilation models that are calibrated to a specific building, and eliminates the requirement for separate measurements of surface pressure distributions. However, wind tunnel measurements of ventilation rate in and around buildings present significant scaling difficulties. The requirement to model a sufficiently large area around a building including adjacent buildings necessitates that the model building be relatively small. However, the requirement to model the internal layout in sufficient detail and Reynolds number scaling requirements for modelling the window openings require the model building to be relatively large. It is also difficult to appropriately scale the building's internal volume to account for compressibility effects. For these reasons, direct wind-tunnel modeling for empirical calibration of wind-driven ventilation rates is uncommon [159].

Computational Fluid Dynamics offers a potential solution to this problem, as the computational domain can simulate flows at full-scale Reynolds numbers [40]. However, direct simulation of both the internal and external environments presents significant computational overheads [160, 162, 163]. This limitation, while not to be underestimated, can be expected to decrease as computational power increases. Due to the low cost of natural ventilation and the financial importance of maintaining a suitable indoor climate, the use of CFD modelling to analyse flow through buildings is well developed in the agricultural industry [160]. Norton *et al.* provide a thorough review of the state of the art in this context, which highlights the need for experimental validation, and for CFD studies that focus on generative design data as opposed to phenomena observation [160].

Shirzadi *et al.* use Computational Fluid Dynamics simulations to evaluate airflow through a notional building [87]. Here, the impact of indoor and outdoor flow phenomena on airflow through openings are modelled simultaneously. The results are used to evaluate an adaptive discharge coefficient which is a function of wind angle, opening location, and building geometry. This adaptive discharge coefficient represents the correction factor that would be required for the predictions of a simple envelope flow model to match the airflow predictions of the CFD. In essence, this technique results in the creation of an empirical dimensionless

model for the prediction of ventilation rates for a specific building, fitted to CFD data. This is potentially a powerful tool to tailor airflow network models to specific building geometries, particularly where building geometry or the local environment is complex.

## 2.9 Wind-tunnel techniques

Etheridge divides scale-modelling experiments into two categories: the design application, and the validation application [39].

In the design application, full-scale pressure and velocity values are calculated from measurements at model scale using similarity arguments [39, 25, 159]. Here the similarity requirements are most demanding, requiring accurate simulation of the atmospheric boundary layer in addition to satisfying dynamic similarity with the relevant dimensionless scaling parameters. Fully satisfying the similarity requirements at model scale is generally impossible, particularly when heat transfer is involved [39].

By contrast, the validation application is much less demanding, as similarity requirements do not have to be met [39, 100]. Here, mathematical models are validated by comparing calculated values with those measured at the model scale. Accurate simulation of the atmospheric boundary layer is not required: the simulated conditions merely have to be *representative* of the types of flows that occur in natural conditions [100, 159]. This approach is much more common in academic literature involved in the development of general mathematical models for application in design [100, 61, 67].

### 2.9.1 Similarity requirements

A key task when performing wind-tunnel scale models is ensuring that the simulated flow field achieves similarity with those anticipated at full-scale. This typically involves the selection of dimensionless similarity parameters that describe the flow, and generating conditions at model scale that match the values of these similarity parameters at full-scale.

Cermak identifies general similarity requirements for wind-engineering problems [164]. Here, general similarity of two flow systems is taken to require geometric similarity, dynamic similarity, thermal similarity, and similarity of boundary conditions.

Geometric similarity is preserved when a common length scale is applied for all dimensions. Kinematic similarity requires that the velocity at all points in a flow are proportional by the same scale to all geometrically similar points in another flow. Kinematic similarity is implied when all other similarity requirements are met [164, 6].

Cermak identifies three dimensionless dynamic similarity parameters and two thermal similarity requirements important to the modelling of atmospheric flows [164]. The dynamic requirements comprise the Reynolds number, which is a measure of the ratio of momentum to viscous forces, the bulk Richardson number, which describes the relationship between vertical temperature and velocity distributions, and the Rossby number, which describes the influence of the Coriolis force arising from the earth's rotation on geostrophic flows [164]. For atmospheric flows at a scale relevant to ventilation of buildings, vertical temperature variation and the effect of the earth's rotation can typically be neglected [25]. Thus, the Reynolds number is the most important dynamic similarity requirement. However, where sharp edges fix the location of flow separation, the requirement for Reynolds number conservation can typically be relaxed [164, 6, 53].

The thermal similarity requirements comprise the Prandtl number, which describes the ratio of the momentum diffusivity to the thermal diffusivity, and the Eckert number, which characterises heat transfer dissipation. Where the working fluid is air, Prandtl similarity is automatically conserved. Furthermore, flow similarity does not depend strongly on the Eckert number until the flow approaches the speed of sound. Consequently, the thermal similarity requirements applicable to wind tunnel simulations of atmospheric flows can usually be neglected [164].

Finally, flow similarity requires similarity of boundary conditions. Similarity of boundary conditions is a poorly defined category of similarity criteria, and requires some degree of insight into a flow problem to identify the relevant parameters. In atmospheric flows, these boundary conditions typically include the temperature and roughness distribution over the area of interest, the longitudinal pressure variation, and the distribution of temperature and velocity in the incoming flow [164]. Where these boundary conditions are considered part of the problem space, an additional challenge is introduced in determining dimensionless parameters that describe these boundary conditions. This can also be a problem when investigating small-scale phenomena such as flow through window openings, where the local flow structures relevant to the problem are less well defined than in the broader atmospheric flow.

One approach to selecting the dimensionless parameters required to describe a given flow phenomenon is through the application of Buckingham Pi Theorem [165, 166]. This states that if a dependent variable is completely described by a set of  $n$  independent variables, of which  $k$  are dimensionally independent, then a suitable dimensionless dependent variable would be completely determined by  $n - k$  dimensionless similarity parameters. Where some of these variables are constant for all cases of interest, the number of dimensionless similarity parameters can sometimes be reduced through the application of a generalized Buckingham Pi Theorem [167]. Here, if there are  $n_f$  independent variables held constant, of which  $k_f$  are dimensionally independent, then the number of dimensionless similarity parameters required to describe the problem are reduced by  $n_f - k_f$ .

A decisive step in the application of the Buckingham Pi Theorem to dimensional analysis is the determination of the set of independent variables used to describe a given flow phenomena, which is described here as the *system*. These variables are determined by inspection of the system, which relies on human intuition or experimental experience. As such, application of Buckingham Pi theorem does not preclude dependence on variables that have not been considered.

For complex geometry, geometrical similarity and consequently dynamic similarity could depend on any number of independent variables used to describe the geometry of a system, which would consequently be described by any number of dimensionless similarity parameters. Here, reduction requires identification of which geometrical parameters are important, and which can be ignored. For instance, while the width to height ratio of windows are often reported in the literature, the window depth is seldom mentioned [108, 66, 67, 125]. Here it is commonly assumed that windows are sufficiently thin that the influence of window depth can be neglected. However, Chiu and Etheridge note that, as flow phenomena are highly dependent on the geometry close to the flow separation point, discharge coefficients might be expected to be sensitive to this parameter [100].

Moreover, uncontrolled or uninvestigated variables might lead to incorrect dimensionless parameters used to describe phenomena. For example, a range of flow phenomena in buildings are commonly described using an opening porosity, which is defined as the ratio of the area of an opening to the area of a façade [81, 109, 38]. While ubiquitous in the literature, the opening porosity does not have a physical meaning in terms of flow phenomena. For flow connection, jet entrainment theory would indicate similarity parameters based on opening area and distance between openings, as opposed to opening area and facade area [1]. With regards to determining the shape of an inflow jet, the opening depth could play an important role in redirecting the cross-flow into the space [38]. These factors are seldom controlled for, and often vary concurrently with opening porosity in experimental and CFD studies [38, 1]. Similarly, a range of similarity parameters concerning temporal and spatial phenomena in the approach flow, such as turbulence and dimensionless velocity profile, are seldom considered in dimensional analysis or controlled for experimentally, despite playing an important role in mixing phenomena [100, 66, 61, 67, 140]. Even where turbulence intensity is considered, its full complexity is seldom investigated. Here, the turbulent length scale, eddy distribution, and the directional components of turbulence intensity might all be expected to play a role in ventilation phenomena.

In many cases multiple different formulations of similarity parameters are possible. For wind-driven, isothermal flow, the most commonly cited similarity parameter is the Reynolds number. The Reynolds number is a dimensionless ratio that represents the ratio of inertial to viscous forces within a flow. The value of the Reynolds number in a given system depends on how the velocity and length scales are defined, which are typically chosen by inspection of the flow problem being investigated. For example, for flow around



buildings, a the length scale and velocity are commonly, but not exclusively defined as the height of the building, and the speed of the atmospheric flow at building height respectively [100, 25, 53]. By contrast, flow through an opening is usually characterised using either the area or length of the opening as a length scale, and the average velocity through the opening as a velocity scale, defined in terms of volume flow rate [100, 25]. Where both buildings and openings are present in the same model, the preservation of both Reynolds numbers becomes important [100, 66, 159].

When modelling flow around buildings, the large scaling factors involved mean that achieving full-scale Reynolds numbers is usually impractical. However, the sharp-edges of common building geometries fix the location of flow separation in space, which results in a degree of independence from Reynolds number [164, 25]. Experimental studies have observed that dependence on Reynolds number decreases as Reynolds number increases [25, 53]. As Reynolds numbers in the atmospheric flow around a full-scale building are expected to be significantly higher than those that can be achieved at laboratory scale, it can be assumed that flow around buildings is generally independent of Reynolds number. As such, an important element of experimental studies is to show that Reynolds numbers are sufficiently high that dependence on Reynolds number can be neglected, and that dynamic similarity is preserved. Although experimental results typically support a gradual reduction in dependence on Reynolds number as Reynolds number increases, studies typically define a *critical* Reynolds number, above which the effects of Reynolds number can be ignored. Flow distortion effects and the consequent impact on pressure distributions are generally considered negligible for Reynolds numbers in excess of  $10^4$  [55]. Nevertheless, the frequency spectra of turbulence is known to be dependent on Reynolds number, so care is needed when extrapolating measured transient phenomena to full scale [55]. A similar independence of Reynolds number arising from flow separation is observed for flow through sharp-edged orifices such as windows [100, 25, 36]. However, when windows are tested in isolation from window geometry, scaling factors are typically less extreme, which allows full-scale Reynolds numbers to be achieved [115].

Dimensional analysis requires the application of intuition to determine the independent variables that describe a flow phenomena. In some cases, this can lead to the formulation of different, but equally valid dimensionless parameters. When analysing flow through an opening in a cross-flow, Chiu and Etheridge define a dimensionless cross-flow velocity that describes dynamically similar flow scenarios, and Kurabuchi *et al.* define a dimensionless room pressure that describes the same phenomena [100, 66]. While composed of different independent variables, they describe the same phenomena and are both derived from the same dimensional analysis, and can therefore to some extent be considered equivalent.

Dimensional analysis is a powerful tool to investigate fluid phenomena. It enables scale-modelling by describing conditions for dynamic similarity, and the extrapolation of measured data to a wide range of flow

scenarios. However, the arguments presented above illustrate the limitations to its application, and the care required to interpret results arising from this approach.

### 2.9.2 General wind tunnel requirements

Wind tunnel studies attempt to replicate unconstrained outdoor atmospheric flows within an enclosed space. The size of this enclosed space limits the boundary layer depth that can be modelled, and the size of turbulent eddies that can form. Furthermore, models can cause a blockage in the wind tunnel which can speed up and distort the flow over and around the model. Therefore, it is important to select a model scale where the influence of tunnel walls and blockage can be minimised.

Distortion effects from tunnel blockage can be safely neglected when the blockage ratio is less than 5% [55]. For blockage ratios between 5% and 10%, distortion effects become significant and need to be considered. For blockage ratios greater than 10% the validity of data needs to be assessed using tests at a smaller scale [55].

Another typical requirement of wind-tunnels is that the longitudinal pressure gradient arising from frictional resistance from the tunnel walls can be neglected [164, 55]. Many atmospheric tunnels incorporate a sloped roof. Here, the expansion in cross sectional area is calibrated to compensate for frictional losses, and results in a negligible longitudinal pressure gradient in the working section of the wind tunnel [164, 54, 57, 168].

### 2.9.3 Wind-tunnel techniques at building-scale

The observed gap in the power spectrum of wind at time periods of around one hour greatly simplifies the simulation of atmospheric wind. Here, wind during a particular hour of weather data is typically approximated using locally steady mean wind speed and turbulent properties, with the main focus of the wind tunnel design being to suitably model the mean and fluctuating flows at the micro-meteorological scale [55]. Variation in wind speed and direction of time periods greater than an hour are typically simulated by adjusting the wind tunnel flow speed and by rotating a building on a turntable [55].

Many authors stress the importance of a suitable upstream velocity profile on the validity of results from wind-tunnel testing. The most representative atmospheric boundary layers are achieved by letting the boundary layer develop naturally over a long roughness fetch, typically in the range of 20 – 30m [60, 56]. However, many wind tunnels do not have sufficient length to achieve this, which necessitates the use of artificial thickening devices such as barriers or mixing devices [60, 57, 55]. Furthermore, simulation of the full atmospheric boundary layer implies a scale factor that is only suitable for the study of high-rise buildings. Measurements of low-rise buildings common in natural ventilation studies inevitably require part-

height simulations of the atmospheric boundary layer [55]. Here, simulated atmospheric boundary layers are inevitably less representative than those achieved in full-height simulations [60, 55]. However, for the validation application of wind tunnel modelling, this limitation is less significant [39, 100].

Where the wind-tunnel is too short to naturally develop a surface boundary layer of sufficient thickness, or where part-depth simulations of the atmospheric boundary layer are required to investigate smaller scale factors, thickening devices such as barriers and mixing devices are used [60, 168]. The purpose of thickening devices is to artificially increase the thickness of the surface boundary layer in a short wind tunnel, with the aim of simulating the flow that would occur over a longer fetch [60, 55]. However, a wide variety of simulation hardware are presented in the literature, with no clear consensus on which is best [54, 60, 169, 170, 171, 172, 173, 174, 175]. Nevertheless, while the physical geometry varies considerably between designs, the components of thickening devices detailed in the literature play broadly similar roles [60]. Cook breaks down the key components of artificial boundary layer thickening devices into three elements: the roughness fetch, barriers, and mixing devices [60].

The role of the surface roughness in artificially thickened ABL simulations is essentially the same as that where the boundary layer is grown naturally over a long fetch [60]. The surface roughness represents the roughness of the full-scale ground surface. It acts as a momentum sink, reducing the velocity of the flow close to ground level. This establishes a profile of Reynolds stress through the approach flow, which in turn determines the velocity profile and turbulence characteristics [60]. Surface roughness elements almost exclusively take the form of a staggered array of rectangular prisms along the floor of the tunnel, spanning the whole length from the model to the start of the upstream fetch [172, 173, 174]. The size and spacing of these prisms varies depending on the simulated terrain, with the aim of reproducing the correctly scaled drag and roughness lengths of the local environment [176].

The barrier and mixing devices are used to provide an artificially thick boundary layer at the start of the roughness simulation, simulating the effect of a larger upstream fetch. Here, the role of the barrier device is to provide an initial momentum deficit at the bottom of the boundary layer. The mixing devices then generate turbulence, which mixes the momentum deficit provided by the barrier into the developing flow [60]. The experimental setup developed by Counihan consists a set of elliptic wedge vorticity generators, with an upstream castellated barrier wall [172, 65]. Here, the castellations add an increased momentum deficit behind the mixing devices, to compensate for the locally increased momentum arising from the mixing process. In the setup developed by Cook, a grid-based mixing device is located upstream of the barrier element, in which perforations near the top were added to assist in mixing [174]. An alternative approach was developed by Standen, whereby the barrier and mixing devices are combined into a single component: a row of tapering spires [173]. Here, the drag generated by the spires introduces the desired velocity profile,

and vortex shedding at its sharp edges mixes this momentum deficit into the approach flow [173].

The design of barrier and mixing elements has typically been performed on a trial and error basis, and consequently designs presented in the literature are typically specific to a given terrain and scale [172, 174]. However, the flat-plate spires first presented by Standen are given as a family of devices suitable for simulating a range of terrain types [173]. Design formulae for the use of flat plate spires of this type were later developed by Irwin [175, 177]. This substantially increases the flexibility of this technique for use in different design scenarios.

De Bortoli *et al.* investigated the use of different roughness, barrier, and mixing techniques for part-depth ABL simulations [168]. Here, Counihan and Standen type setups are compared against atmospheric data for a sub-urban ABL. Good agreement was found for both mean and fluctuating components of the velocity profile. Both techniques present a similar quality of fit to the atmospheric data [168]. Literature data concerning simulation of urban ABLs are compared by Farell and Iyengar [178]. Here, substantial variation between the results of different practitioners is highlighted.

The barrier and mixing techniques described above represent passive techniques for preconditioning the approach flow. However, the degree of turbulence that can be achieved with passive devices is limited, and minimal control is offered over turbulence intensity and frequency [179]. Active devices such as active grids or jets present a greater opportunity to tailor turbulence levels and momentum deficit independently of wind speed, and systematically investigate the impact on measured phenomena [179, 70, 180, 60]. However, sensitivity to initial conditions can mean that active devices yield less repeatable results [181]. Furthermore, the use of active devices to control turbulence characteristics implies that turbulence characteristics are not determined by surface roughness. Consequently, simulations with active boundary layer control inevitably introduce artificiality into the simulated flow [60].

#### 2.9.4 Wind-tunnel techniques at opening-scale

In contrast to measurements of the upstream velocity profile at the building scale, very little guidance is available for simulating the velocity profile at the scale of an opening. One reason for this is a lack of detailed velocimetry available in the literature concerning the boundary layer flow that occurs over building surfaces, either at full-scale or at model scale.

Limited investigations into the boundary layer on the surface of a model building were made by Kurabuchi *et al.* [66]. Here, a hot-wire anemometer was used to investigate the mean velocity of the cross-flow with height over a surface. The measured distribution of flow velocities is consistent with a classical surface boundary layer or wall-jet, with the mean cross-flow speed tending to zero at the surface and increasing to a steady

*free-stream* value with distance from the wall [66]. This is consistent with the analytical model of a cross-flow described in Section 2.4.2. However, the wind angles at which these measurements were made have not been recorded. Furthermore, no indication of the turbulence characteristics in the cross-flow is provided.

Warren and Parkins investigated the impact of free stream turbulence on wind-driven ventilation in rooms with a single opening in a cross-flow [61]. Here a local-approach is taken whereby a wind-tunnel is used to generate a cross-flow across the surface of an opening. Two conditions are studied: a low turbulence case with no upstream flow conditioning elements, and a high-turbulence case where turbulence is induced using a grid in the upstream flow. Longitudinal turbulence was measured as 9.0% with grid-induced turbulence, compared to 0.8% in the unmodified flow. Increased turbulence is found to increase the ventilation rate by 60% for slot openings, and 40% for square openings. This demonstrates that the transient features of a cross-flow can have a significant impact on flow through openings. However, while it is noted that the simulated turbulence will not be sufficient to fully-represent full-scale flows, no attempt was made to measure turbulence in the cross-flow either at model scale or at building scale. Furthermore, no attempt was made to measure the mean velocity profile in the surface boundary layer.

Similar experiments are presented by Albuquerque *et al.* [67]. Here a near-uniform velocity profile in the simulated cross-flow is achieved through the use of a honeycomb lattice. Turbulence intensities in the simulated cross-flow are recorded in the range of 13% – 16%. This is consistent with the turbulence intensity in the ABL used for whole-building wind tunnel experiments. However, no measurements are presented that suggest that this is representative of the cross-flow on the building surface.

Ohba *et al.* and Endo *et al.* present local-scale experiments to investigate the impact of a cross-flow on unidirectional flow rates through openings [99, 105]. Here, a test chamber is built flush with a short, thin plate raised above the surface of a wind tunnel floor. This aims to achieve a near uniform velocity profile in the cross-flow over an opening by creating a minimal region of fetch. This velocity profile may represent a worst-case scenario, where the cross-flow has the greatest potential impact on flow through the window. However, the use of a uniform velocity profile is not supported by cross-flow measurements at building scale. This setup precludes the development of fully developed boundary layer flow, raising the possibility that results are affected by flow separation at the leading edge of the artificial floor. Furthermore, no measurements of the turbulence intensity in the simulated cross-flow are reported.

## 2.10 Computational Fluid Dynamics techniques

Computational Fluid Dynamics (CFD) refers to the use of numerical analysis to provide quantitative predictions of fluid flow phenomena through the solution of the Navier-Stokes Equations. Computational solutions

must satisfy the three laws of conservation: conservation of mass, conservation of momentum, and conservation of energy. The Navier-Stokes equations are a set of partial differential equations that describe the motion of a fluid. As these cannot be explicitly solved, numerical analysis is required to find a convergent solution. Many CFD approaches convert these partial differential equations into a system of algebraic equations that is more amenable to computational analysis.

Although not strictly a measurement technique, CFD is widely used in place of physical experiments to investigate the flow field in and around buildings. The widespread use of CFD in contemporary research can be to some extent attributed to its low cost and accessibility: no experimental equipment is required except for validation purposes. It also enables modelling of flow scenarios at *full-scale*, which removes the need for dimensional scaling arguments to achieve similarity. This could be seen to be a powerful advantage over wind-tunnel modelling, where full-scale Reynolds numbers can seldom be achieved. CFD also increases the ease with which parametric studies can be performed to investigate a range of alternative design configurations. However, CFD simulations represent analytical predictions, and are not yet sophisticated enough to be a substitute for physical experiments. Limitations on the accuracy of CFD simulations are widely reported, with results highly dependent on the experience and competence of practitioners and not merely the use of verified code [182]. As a result, the use of CFD in academic studies requires experimental validation and extensive sensitivity analyses as essential components of quality assurance [40].

CFD can be considered to be a non-intrusive area technique. The fluid properties can be evaluated at any location within the flow field without the introduction of measuring apparatus that interfere with flow patterns. The spatial resolution of the output is limited only by the spatial resolution of the grid. This allows fluid pressure, velocity, and volume flow rate to be calculated without the need for separate measurement techniques. However, the high level of detail produced by CFD simulations can lead to perceived confidence in the results that may not be consistent with the uncertainty in the model.

### 2.10.1 Turbulence modelling

As direct solutions to the Navier-Stokes equations are computationally expensive, approximate forms of these equations are often used. This usually relies on the use of alternative models to describe the effect of turbulence. These can be grouped into two categories: steady models that use temporally averaged quantities such as Reynolds-Averaged Navier Stokes Models (RANS), and unsteady models such as Large Eddy Simulation (LES) [40]. The suitability of different turbulence models for different applications is the subject of considerable debate. However, Ferziger and Peric note that, in most workshops held on the evaluation of different turbulence models, the difference between solutions produced by different authors

using notionally the same model are equal to if not greater than the differences between the results of the same author using different models [183]. The uncertainties arising from turbulence modelling can be avoided through direct solution of the Navier-Stokes equations, but due to high computational overheads this has typically only been achieved for relatively low-Reynolds number flows [73].

### 2.10.2 CFD for integration with envelope flow models

CFD produces results that are specific to a given building configuration, for a given set of environmental conditions. However, similarly to wind tunnel studies, the results of CFD can be non-dimensionalised to extend their application to other environmental conditions [66, 105]. In this way, CFD simulations can be used as quasi-empirical techniques to optimise the performance of conventional envelope flow models [87].

## 2.11 Measurement Techniques

The experiments described in this thesis require the measurement of fluid pressure, fluid velocity, and volume flow rate. This section presents a range of measurement techniques present in the literature, and summarises the advantages and disadvantages of each technique. This enables suitable techniques to be developed for experimental design: see Chapter 4.

### 2.11.1 Measurement of surface pressures

Many of the experiments described in this thesis require the measurement of differential pressures. This is important when measuring the surface pressures on a building facade, the pressure drop across an opening, or the dynamic pressure in the atmospheric flow.

#### Optical manometers

Optical manometers have traditionally been widely used to measure differential pressures in fluid systems. The most familiar optical manometer is likely to be the U-tube manometer. This consists of a U-shaped tube where the bend is filled with a fluid that is immiscible with the fluid in which the pressure is measured - in wind tunnel studies air. A static pressure difference between the two tubes results in a difference in height of the manometric fluid on each side of the U-bend, from which the differential pressure can be determined through the application of hydrostatic theory. The main advantage of this technique is its simplicity and low cost. However, the results can only be interpreted visually, and are not suitable for digital data collection. Furthermore, optical devices cannot measure transient pressure fluctuations due to high hydraulic resistance

of the device, which lends them to the study of mean flow behaviour only. Optical manometers also have a relatively low precision, which presents difficulties when measuring low pressure differentials commonly encountered in natural ventilation. To some extent, precision can be improved by using a manometric fluid of a density similar to that of the fluid in which the pressure is measured, measuring the fluid displacement in an inclined plane, or through the use of optical magnification [184, 108].

### **Electrical pressure transducers**

Electrical pressure transducers are ubiquitously used in wind-tunnel experiments to measure differential pressures [66, 81, 100, 140]. These transducers typically consist of two chambers separated by a diaphragm, to which the static-pressure in the sampled fluid is transmitted through manometric tubes [185, 186, 187]. A pressure differential across the diaphragm causes it to deflect, which alters its electrical properties. The displacement of the diaphragms is typically measured by strain gauges, or with inductance or capacitance transducers, but other designs have been used [188, 189, 190, 191]. The main advantages of electrical pressure transducers are the support for digital data collection, high precision, and high frequency response. This permits the measurement of transient pressure phenomena in naturally ventilated systems, and the collection and interpretation of large quantities of data. However, pressure transducers require prior calibration to determine the zero-pressure response [192]. The output from pressure transducers are also dependent on temperature, which may require temperature compensation to ensure accurate interpretation of results [192, 191].

### **Pressure Sensitive Paint**

An alternative technique for measuring surface pressure distributions is through the use of pressure-sensitive paint. Here, a form of paint that has photo-luminescent properties is applied to a three dimensional body [193]. Photo-luminescent paint has a luminescence that is proportional to the partial pressure of oxygen in the air, in accordance with the Stern-Volmer relation. Measuring the instantaneous luminescence of the paint therefore enables the pressure across the surface to be measured [194, 195, 190].

Pressure-sensitive paint is an area technique, which allows the surface pressure field over a wide area to be visualised and quantified. The technique has a high spatial resolution, and techniques have been developed that enable a high-frequency response for the investigation of transient flows [196]. However, this technique is typically applied at high flow velocities, with greater errors occurring in subsonic flows [193]. While some work has been done to extend the application to lower pressure and velocity ranges, there remains a barrier to measuring the small pressure differentials common to natural ventilation problems [197, 198]. Furthermore, the luminescent response is temperature sensitive, and requires extensive calibration [193]. The



application and measurement of pressure sensitive paint is currently a complex, high-cost technique, which requires access to specialist equipment. As a result, its application in building design is likely to be limited.

### Combined velocimetry

Techniques have been presented for estimating the pressure field on and around a building using the velocity field. Here, velocimetry data measured using Particle Image Velocimetry (PIV) is used to specify the boundary conditions for a Computational Fluid Dynamics (CFD) model, which is used to estimate the pressure field that is required to generate a given velocity field [199]. The benefit of these techniques is that they can evaluate a spatially resolved pressure field to a high level of detail. This avoids a common difficulty in pressure measurement, where only point values can be acquired. Furthermore, this technique is non-intrusive, and allows pressure to be evaluated at points in the flow field far from the building surface that are difficult to measure experimentally. However, PIV-supported CFD is best described as semi-empirical. The accuracy of the pressure measurements is determined by the validity of the CFD model used to describe it, and are therefore comprise a prediction of the pressure field as opposed to a measurement. Furthermore, the error in CFD predictions has been shown to be greatest close to the boundary of the building [199]. Unfortunately, this is the region of primary interest when evaluating pressure coefficients for use in envelope flow models.

### 2.11.2 Measurement of fluid velocity

Many of the experiments described in this thesis require the measurement of fluid velocity. This is important when measuring the speed of the flow in the atmospheric boundary layer generated by the wind tunnel, and also in measuring the speed and direction of the cross-flow on a building surface.

Measurement of fluid velocity can be broadly divided into two components - measurement of flow speed, and measurement of flow direction. For some purposes, only knowledge of the former is required. This is generally simpler, and requires less complicated equipment - particularly when the direction of the flow is known *a priori*.

Measurement techniques can be broadly broken down into two types: those that measure fluid velocity at a point, and those that measure flow velocity over a wide area [40]. The latter techniques are potentially more powerful, but typically require more expensive equipment and more extensive and time consuming data processing. Envelope flow models typically require the measurement of flow conditions at a point - at a reference location in the atmospheric flow and at each opening in the building façade [5]. This permits the use of simpler point measurement techniques when generating design data.

### Pitot-static tubes

Pitot-static tubes are widely used in fluid mechanics to measure the dynamic pressure in a fluid flow [200]. A pitot-static tube comprises two concentric tubes. The central tube is open at its end, and faces into the flow. At this opening the airflow stagnates, meaning that it samples the sum of the static and dynamic pressures in the flow. The outer tube is sealed at the end, with small holes around its perimeter at right angles to the flow. This samples the static pressure in the flow. Therefore, the pressure differential between the pitot tube and the static tube corresponds to the dynamic pressure in the flow. A correction factor can be applied to this relationship to account for non-stagnant flow at the entrance to the pitot tube and slowed flow near the static pressure tapings, but ISO 3699:2020 identifies that this value is practically equal to unity for Pitot-tubes described by the document, and can be neglected [201].

The accuracy of pitot-static tubes is dependent on its alignment with the flow [202]. As such, it is typically used in areas where the flow direction is known a-priori, such as when measuring atmospheric flow in wind-tunnels [203, 204, 52, 168], flow in ducts [201, 205], or the relative speed of fluid flow past moving ships or aircraft [206, 207]. ISO 3966:2020 identifies that error in reported dynamic pressures can be neglected when the flow direction deviates by less than 3 degrees [201]. However, Legg notes that the error arising from misalignment is small, amounting to errors of less than 1% in recorded dynamic pressure for up to 10 degrees yaw and pitch [205]. In spite of dependence on flow alignment, it is widely recognised that pitot-static tubes can be used for both turbulent and non-turbulent flow [206]. Pitot-static tubes are an intrusive technique, in that the presence of the probe interferes with the atmospheric flow. This has the potential to be particularly problematic, as the sensors typically need to be placed upstream of the model under study to prevent interference from the model on measurements of wind speed. As a result, placement of the pitot-static tube is crucial to ensure that it is simultaneously far enough from the model that its influence on the flow can be neglected, and that it measures the atmospheric flow speed at a location that is representative of the atmospheric flow incident on the model.

Pitot-static tubes have also been used to measure flow around buildings. Kurabuchi *et al.* use a pitot-tube to measure the total pressure in the cross-flow that occurs close to a building surface, and to measure the total pressure in an inflow jet that occurs when air enters a building through a window [66]. This requires the use of a split-film anemometer to first evaluate the direction of the flow, which allows the pitot-tube to be oriented in the mean flow direction. As a pitot-tube needs to be oriented carefully towards steady wind flow, this technique will be insensitive to turbulent fluctuations in cross-flow direction. Furthermore, Kurabuchi *et al.* identify that this process is labour-intensive, and not suitable for determining opening position in the design stage [104].

The use of pitot-static tubes in measurements of surface pressure coefficients offers a number of advantages. Firstly, the static pressure tapping on the pitot-static tube can be used for the reference static pressure against which the façade surface pressure is measured. This minimises duplication of equipment, and ensures consistency in the measurement of reference pressure. Secondly, pitot-static tubes provide a direct measure of the dynamic pressure in the flow, which is used to normalise the surface pressure in the generation of surface pressure coefficients. Therefore, when using a pitot-static tube to directly measure dynamic pressure, the surface pressure coefficients can be evaluated as the ratio of two directly-measured differential pressures. This minimises the error propagation issues associated with measurement of flow speed, and avoids the need to estimate the density of the working fluid.

### Hot-wire and hot-film anemometry

Hot-wire anemometers consist of a fine wire, typically  $1 - 20\mu\text{m}$  in diameter with a length of  $0.5 - 3\text{mm}$ , through which a current is passed. This current causes the wire to heat up to significantly above the ambient temperature, typically with a  $180 - 200\text{K}$  temperature difference [40]. When air passes over the wire, it causes it to cool by forced convection. This change in temperature alters the electrical resistance of the wire, which can be related to flow speed by prior calibration.

Due to the low thermal mass of the wires, hot-wire anemometers typically have a high frequency response, and a high spatial resolution due to their small size [208]. However, a single-wire anemometer can only measure the component of the wind velocity acting in the plane perpendicular to the wire [209]. Furthermore, the wire is insensitive to flow direction within this plane, and therefore cannot identify flow reversal. This is to some extent resolved by using an array of perpendicularly mounted wires. Cross-wire anemometers measure the flow speed in two perpendicular planes [210]. Three-wire anemometers comprise three perpendicularly mounted wires, which allows the flow speed in three perpendicular planes to be evaluated.

The outputs from a three-wire anemometer can be used to evaluate the magnitude of the velocity component in the axis of each wire. This allows the mean flow speed to be evaluated irrespective of the flow direction. To some extent, they can also be used to evaluate the direction of the flow. However due to its insensitivity to flow reversal, any combination of velocity components output by the probe could correspond to eight potential flow directions [211]. Therefore, these devices can be used to measure perturbations in flow direction when the octant within which the flow occurs is known, but not in the general case where flow could occur from any direction.

Hot-wire anemometry is an intrusive measurement technique, which requires the probe and probe supports to be mounted within the flow that is being measured [40]. This interaction might be expected to alter the dynamics of the flow, particularly when the frame mounting is upstream of the measurement location.

For this reason, careful experimental design is important in order to reduce errors. Even when measuring flow speeds across a large flow field, sensing using hot wire anemometers is typically performed with a single sensor [104]. This reduces the impact of flow obstruction on results, but precludes the possibility of simultaneous velocity measurements across multiple locations in the flow field. Flow velocity measurements across a large flow field are also labour intensive, reducing the number of measurement locations, wind directions, or flow configurations that can be achieved within a limited experimental time.

Albuquerque *et al.* use two perpendicularly-mounted single wire probes to measure the horizontal and vertical components of cross-flow near an opening [67]. This relies on the assumption that flow occurs exclusively in the plane parallel to the façade, whereby the horizontally mounted wire measures the vertical component of the flow velocity, and the vertically mounted wire measures the horizontal component. Here the flow speed parallel to the facade is found by pythagorean addition of these two components. In this configuration, any turbulent vortices in the direction perpendicular to the façade would be expected to result in an overestimation of flow velocity parallel to the façade. However, due to the insensitivity to flow reversal, this device was not used to measure the direction of the cross-flow. Kurabuchi *et al.* measure the cross-flow velocity using a single wire probe mounted perpendicular to the façade [66]. This allows the speed of the cross-flow to be determined irrespective of flow direction, providing the cross-flow velocity vector lies within a plane parallel to the façade. This set-up is insensitive to any component of the cross-flow velocity that occurs perpendicular to the façade.

Hot film anemometers operate on a similar principle to hot-wire anemometers. However, here the conducting material is spread over a two dimensional surface instead of a one dimensional wire. These anemometers typically have shorter sensing lengths and are more robust than hot-wire anemometers [40]. One form of hot-film anemometer is the hot-sphere anemometer. Due to its symmetry, the hot-sphere anemometer can be used to measure the wind speed independently of its direction in three dimensions [212]. However, it does not provide any method of measuring flow direction. For these reasons, hot sphere anemometers are commonly used in indoor air studies to evaluate air speed for thermal comfort, where the direction of airflow is unknown and not important.

Linden *et al.* use a hot film anemometer to evaluate the speed of the cross-flow on the façade of two and four storey buildings [85]. Here the hot film is mounted on a circular disk, so that it is sensitive to the component of air velocity in the plane of the disk, and relatively insensitive to the component of air velocity in the axis perpendicular to the disk. Here, this is mounted such that the plane of the disk is perpendicular to the façade and parallel to the ground. Therefore, the sensor will be insensitive to the vertical component of the cross-flow, and will consequently underestimate the speed of the cross-flow.

Split-film anemometers are able to determine directly determine the three-dimensional velocity vector

by measuring the flow speed in three planes, and identifying the octant within which the flow occurs [213]. This overcomes the primary issue with hot-wire sensors, and enables detailed measurements of turbulent flow characteristics at a point [214]. Split-film probes have been used effectively by Kurabuchi *et al.* to measure the velocity vectors in the flow around buildings [66]. This enables the flow field to be investigated in detail, and would also be suitable for measuring cross-flow velocity vectors.

### Irwin Probes

Irwin developed an omnidirectional velocity sensor for use in wind-tunnel studies of pedestrian-level wind speed [215]. This sensor is conceived to measure the speed of flow parallel to the floor plane, in the region where the airflow is restricted to a plane parallel to the surface. The probe consists of a hole in the model surface, through which protrudes a small tube that extends perpendicular to the plane to a given height above the surface. As wind flows over the probe, a pressure differential is created between the base of the probe and the top of the sensor tube. This pressure differential can be correlated with the speed of the flow using a calibration formula, which assumes that the top of the probe is within the log-law dominated part of the surface boundary layer [40]. This may not be true for all locations in the flow. Furthermore, it is important to set the height of the sensor at the desired measurement height above the surface of the plane, to avoid errors caused by extrapolation of the boundary layer profile [216].

The principal advantage of the Irwin probe is the potential to rapidly measure the speed of flow across a surface at multiple locations. Furthermore, the axisymmetry of the design prevents the need to realign the sensor at different wind angles. The Irwin probe is capable of measuring the speed of a cross-flow, but provides no information on the flow direction [215, 216, 40]. Therefore, alternative measurement techniques are required where flow direction is important. This may preclude simultaneous measurement of the speed and direction of airflow at a point.

Irwin probes have been widely used to measure pedestrian level wind speeds [40], and have also been used to measure velocity coefficients on building roofs [217]. Irwin's surface wind sensor has been used by Kurabuchi *et al.* to measure the cross-flow speed on the building façade [104]. While this is an intrusive technique, Irwin probes are small, and interact minimally with the cross-flow compared with the probe mountings of the hot wire anemometer. However, in the experiments of Kurabuchi *et al.* a hot-wire anemometer was used to calibrate and determine the regression coefficients for the Irwin probe [104]. Therefore, any interaction between the hot wire probe mounting and the surface flow will be incorporated into the calibration of the Irwin probe, and all subsequent measurements. Due to their small size, an array of sensors can be mounted on a façade without significantly altering the dynamics of the cross-flow over its surface [215]. Kurabuchi *et al.* identify that the flow speed measured by an array of sensors is not significantly different to

measurements of flow speed at a single point, greatly reducing the time taken to collect measurements and enabling simultaneous measurement of flow speed [104]. Kurabuchi *et al.* use this sensor array to generate contour maps of dynamic pressure distribution across a façade that can be applied in ventilation design to help determine the optimum location of window openings [104].

### Laser-Doppler Anemometry (LDA)

Laser Doppler Anemometry uses the doppler shift in a laser beam to measure the flow velocity at a point [218]. First the flow is seeded with small particles that are suspended in the flow. If these particles are small and of a similar density to the working fluid, they will track the flow as it moves around a building. The measuring location is formed by two beams of collimated, monochromatic and coherent laser light that crosses at a point to create a set of straight fringes [40]. As the particles in the flow pass through the fringes they scatter the light. The frequency of this scattering can be related to the velocity of the particles. If the particles are assumed to track the flow of the fluid, the flow velocity can be evaluated [219].

While Pitot-static tubes, mechanical anemometers, hot-wire anemometers, and Irwin probes are all intrusive techniques, Laser Doppler Anemometry (LDA) is generally considered to be non-intrusive [40]. This is only true when the apparatus for seeding the flow is not considered a flow intrusion, that the seeding particles are sufficiently small that their momentum can be neglected, and that the seeding particles are sufficiently similar in density to the working fluid that buoyancy can be neglected. As the seeding apparatus is by necessity upstream of the building model, this could have a significant impact on the flow field. Therefore, seeding should ideally occur prior to preconditioning of the approach flow.

The main advantages of LDA are its high spatial resolution and directional sensitivity, which enables it to provide detailed velocimetry on flows with a high turbulence intensity [40]. However, LDA is a high-cost technique, which requires significant resources and expertise to apply. Algieri *et al.* note that the accuracy of LDA is strongly dependent on the quality of the seeding [220]. Here, particles of diameters in the order of  $\sim 1\mu m$  are found to track the fluid velocity well, whereas the use of large particles that are often used in LDA experiments due to their lower cost and cleanliness can introduce non-negligible errors, which are reported in the 13% – 16% range [220]. Frequency resolution is also limited by the quality of the seeding, as the momentum of the suspended particles limits the extent to which they can track the fluid flow [40].

Laser Doppler Anemometry has been used extensively to measure flow around bluff bodies such as buildings [221, 222, 80, 53]. This data has been used to validate CFD models used to evaluate urban pollution dispersion [45], which requires modelling of the broader flow field for particle tracking. LDA has also been used in studies of pedestrian level wind speed, [223, 40], where flow speed measurement close to the ground plane is required. This has similarities to the requirements for measuring cross-flow velocity on

the plane of a building's façade.

### **Particle Image Velocimetry (PIV)**

Particle Image Velocimetry (PIV) uses rapid photographs to track the flow of seeding particles around buildings. Here, tracer particles are illuminated by pulses of light from a laser sheet, and the particle velocity evaluated by the change in position of the particle between frames. PIV enables simultaneous measurement of flow velocity over a wide area. It is generally considered a non-intrusive technique, providing that the seeding of the flow is not considered to be a flow intrusion [40].

PIV shares a lot of the limitations of Laser-Doppler Anemometry, in that flow measurement is dependent on the quality of the seeding; see Section 2.11.2. In addition to this, frequency measurement is limited by the speed at which the flow can be photographed, and evaluation of the results can be computationally intensive [224]. The requirement for laser light shielding can also make implementation of the technique difficult. Many PIV experiments measure the flow velocity in two dimensions only [67], although techniques do exist for evaluating particle velocity in three dimensional flows [225]. The use of PIV in wind tunnel studies is limited as a result of its high cost, and the level of resources and expertise required to apply the technique.

Several studies have identified that laser reflections from transparent walls can affect measurements close to the surface of model buildings [67, 226, 227]. This poses a particular problem when using PIV to measure cross-flow velocity, where the dynamics of the flow close to the building surface is the object of measurement [67].

PIV has been widely used to investigate the broader flow field around buildings [228, 229, 230, 70]. The technique has been used to generate datasets for the validation of CFD models, which are then used as a less time and resource-intensive technique to investigate flow phenomena [231, 232]. PIV is often used for the purposes of flow visualisation across the broader flow field, which assists researchers in the interpretation of quantitative data [233, 67].

### **Flow visualisation**

Numerous studies utilise non-quantitative or semi-quantitative visualisation techniques to gain an understanding of the flow field around buildings. Humans are naturally adept at interpreting visual data, and as a result these techniques can be powerful for communicating the results of aerodynamics research to non-technical audiences [108, 40]. These techniques can also improve the understanding of the researcher performing their experiments, enabling them to adapt and finesse their experimental design as well as assisting in the interpretation of gathered numerical data [234, 235].

Water channel models often permit easier visualisation than wind tunnel models. Wilson uses dye injection to investigate the direction of fluid flow around a range of simple building structures [52]. Here, a thin stream of dye is injected into the flow, and the mean flow direction determined by its subsequent motion through the fluid. While a relatively simple technique, interpretation can be difficult. Wilson notes that turbulent instability in the flow causes the location of streamlines to fluctuate. As a result, observation periods in the order of  $\sim 10s$  are required in order to determine a mean flow direction [52]. In the zone of fluctuating flow reattachment on building faces that are parallel to the atmospheric flow, no mean flow direction could be observed. Furthermore, high turbulence generated in the shear layers at the edge of the recirculation cavity causes rapid diffusion of dye injected into this zone [52]. This illustrates some of the limitations of tracer-visualisation techniques in highly turbulent flows.

Sand erosion is widely used in studies of pedestrian-level wind speed to visualise the velocity field over a wide area [40, 236, 237, 234]. Here, a thin layer of sand or similar powder is deposited on the floor of an empty wind tunnel. The wind tunnel speed is then gradually increased until the sand blows away. This sets a threshold wind speed that is sufficient to displace the sand. This is then repeated with the model building in the tunnel. Wind speed is increased in stages, and the sand allowed to erode at each step. At each stage, the sand that has eroded is recorded using photography. This enables the production of flow velocity contours across the ground plane. This technique is best described as a semi-quantitative technique, that provides continuous information about the velocity field over a wide area [40]. The primary advantages of this technique are its simplicity, low cost, and ability to provide clear visual information over a wide flow field. This can be used as a preliminary study over a wide area, which allows more quantitative techniques to be focused over an area of interest [234]. However, there are several disadvantages to the use of the sand erosion technique. It can only be used on horizontal surfaces, precluding its possibility for investigating cross-flow velocity on building façades. Furthermore, the relationship between the sand erosion patterns and flow velocity is not completely understood [40]. It is strongly affected by turbulence, so sand erosion typically indicates peak gust strength as opposed to mean wind speeds, and downstream-erosion from displaced up-wind sand can interfere with results. Finally, there are practical limitations to the application of this technique in open-loop wind tunnels of the form present in the University of Nottingham - namely the transport and deposition of airborne sand to connecting spaces.

The oil-film method is widely used to visualise time-averaged wall shear on model surfaces [53, 71, 238]. Here, a thin layer of oil is spread on a surface, in which a fine powder is suspended. As air flows over the surface, it moves the suspended particles into a consistent pattern. If the oil film is thin enough not to be affected by pressure gradients, then the mean displacement of these particles in the suspension is locally parallel to the mean velocity vector of the air just above the surface [238]. This technique is used to visualise



surface flows, which is used to infer the flow patterns in the broader flow field [71, 53] and to identify key locations such as nodes and saddles in the flow [238, 77]. While comparatively simple to apply, the technique can only provide information on the direction of the mean surface flow field on horizontally-mounted surfaces. It cannot be applied on vertical surfaces, or to measure instantaneous flow behaviour.

Smoke injection is a widely used technique to visualise air flow around bluff bodies [238, 108]. Here, smoke is released from a thin tube, and the direction of travel of the injected smoke observed. Paraffin oil is traditionally used for this purpose [238], although other techniques have been used [108].

Filament tracers are commonly used in wind tunnel studies to determine local flow direction. This technique involves fixing light threads within the flow field. As the air passes over the thread, viscous drag on the thread causes it to point in the direction of the flow. Here, the force exerted on the thread due to viscous drag must be large compared to the force acting on the thread due to gravity, and also compared to the forces arising from resistance to bending within the thread. As a result of these requirements, filament tracers typically employ threads that are as thin as possible, and work best where the speed of the flow is large. Mass and internal resistance add inertia to the thread, which mean that it will not precisely follow the instantaneous flow. Filament tracers work best when the turbulence in the flow is small, due to the requirement to interpret the mean flow direction through visual analysis of the thread position. This technique is non-quantitative, and provides information on the flow field at a point as opposed to a large area. Warren and Parkins use a wool tuft to determine the direction of cross-flow on a building façade, and enable the anemometer to be positioned at the optimum angle to measure local flow speed [61]. Teppner *et al.* use thread probes to determine the direction of airflow through window openings in a wind tunnel model of a naturally ventilated building [235]. Here, the thread probes are used to help interpret the quantitative wind speed data output by velocity transducers, which are insensitive to flow direction.

### 2.11.3 Measurement of volume flow rate

Many of the experiments described in this thesis require the measurement of volume flow rate. This is important in measuring the ventilation rate through model buildings, and for measuring the ventilation rate through single openings in *local-scale* experiments.

Two categories of technique can be discerned here: those that measure unidirectional volume flow rates, and those that measure bidirectional gas exchange rates.

Techniques for measuring uni-directional volume flow rates include positive displacement gas meters and pressure differential devices. The main advantages of these techniques are their high potential precision, and compatibility with conventional airflow-network models that assume unidirectional flow through each

opening. This is important when considering multi-zonal models, as the unidirectional component of flow through an opening influences the volume flow rate of air into neighbouring spaces. However, measurement of the unidirectional component of volume flow rates does not capture the effect of bidirectional mechanisms on gas exchange. This means that an incomplete picture of ventilation rates is provided for the measured zone. Furthermore, most unidirectional flow devices are intrusive, requiring airflow to be passed through regulated measuring apparatus. This introduces complications when trying to measure wind-driven ventilation rate through a model building, for example.

Tracer gas measurements are the dominant technique for measuring bidirectional gas exchange rate. The principal advantage of these is that they provide a direct measure of the ventilation rate in a zone, which encompasses both uni-directional and bidirectional mechanisms. These techniques are also non-intrusive, enabling measurements to be made in spaces without significantly altering the flow behaviour within them. However, these measuring techniques typically have comparatively low precision, and cannot distinguish between the unidirectional and bidirectional components of ventilation rate. This makes them less suitable for validation of unidirectional envelope flow models.

### **Positive-displacement gas meters**

Positive displacement gas meters are an accurate method of measuring the volumetric quantity of gas passing through pressurised systems [239]. They are widely used by energy companies to meter the use of natural gas, and have been applied by Chiu and Etheridge to measure the volume flow rate extracted or supplied to a model building [100]. Here, a physical mechanism separates finite quantities of fluid that are transmitted mechanically from one side of the meter to the other [240]. The total volume that flows through the meter over a fixed period of time can therefore be evaluated by counting the number of cycles. This can be used to evaluate an average volume flow rate over the measurement period. The widespread use of positive displacement meters in the gas industry means that instruments are typically well calibrated and traceable. However, positive displacement meters can be expensive tools.

Because positive displacement flow meters deliver packets of gas with a fixed quantity, this introduces a pulsation into the supply or extract flow stream [241]. This introduces temporal behaviour where the frequency scales with the volume flow rate, which may interfere with experiments where a steady flow rate is intended [100]. The characteristics of the pulsation phenomena are directly related to the design of the flow meter, and cannot be easily adjusted to investigate the impact on ventilation phenomena [241]. Volume flow rates through positive displacement meters are also limited by the size of the meter and the rate at which the mechanical elements can be moved. This poses significant limitations in ventilation experiments where large volume flow rates of air are required.

### Pressure differential devices

Pressure differential devices refer to a family of techniques that measure the flow rate of fluid passing through a pipe by means of a pressure differential caused by an obstruction or constriction in the flow. When connected in series to a system with a single opening, the mass flow rate in the pipe can be equated to the unidirectional component of mass flow through the opening.

Pressure differential devices are well regulated by technical standards, with the general principles and requirements described in BS EN ISO 5167-1:2003 [242]. These pressure differential techniques require steady, well-developed flow in the pipe. Two straight lengths of cylindrical pipe are required to precondition the flow and ensure it complies with the standards. This can introduce significant spatial limitations to using the measuring technique.

Four types of primary flow device are described by the BS EN ISO 5167-1:2003: orifice plates, nozzles, Venturi tubes, and cone meters [243, 244, 245, 246]. Orifice plates are the easiest solution to manufacture, and consist of a circular hole in a flat plate mounted within the pipe flow. Here, as the fluid in the pipe is constricted to pass through the smaller orifice aperture, a static pressure differential occurs between the upstream and downstream zones that can be correlated with mass flow rate. BS EN ISO 5167-2 describes symmetrical and asymmetrical configurations of the orifice plate and pressure tapings, depending on whether flow measurement is required to be reversible [243]. Nozzles and Venturi tubes have more complex geometry, requiring a carefully designed inlet and outlet profile. The principal advantages of these techniques are reduced total pressure losses across the component, which reduces the restriction on achievable volume flow rates, and increased static pressure differentials, which reduces the influence of measurement error on volume flow rates. Here, pressure tapings sample the static pressure at the point of maximum constriction and at a location upstream of the constriction. BS EN ISO 5167-3/4 do not describe symmetrical configurations of jets and nozzles, and so they are not suitable for reversible flow [244, 245]. Cone meters measure the pressure differential between the upstream flow and the surface pressure in the lee of a cone mounted in the centre of a pipe. Some advantages of a cone meter are reduced total pressure losses compared to an orifice meter, and reduced length compared to a Venturi tube. However, the uncertainty of an uncalibrated cone meter is relatively high compared to other ISO 5167 measuring devices, and the meter is not suitable for measuring reversible flow [246].

One disadvantage of the pressure differential devices described by ISO 5167 is their high spatial requirements, and the need to be separated from the model building. Vickery and Karakatsanis describe the use of a small pressure differential device that connects to a model building and fits in the space beneath the wind-tunnel turntable [81]. However, the use of this device or similar devices requires prior calibration with

a standardised measuring technique [81, 242]. Space is typically less restricted when measurements focus on individual openings as opposed to flow through buildings. Endo *et al.* use an orifice meter in the form described by BS EN ISO 5167-2 to measure the volume flow rate induced through outflow openings [105, 243]. Many reported studies do not describe the techniques used to evaluate volume flow rate [66, 104, 99].

### Tracer gas techniques

Bidirectional flow rates in a space are commonly measured using a tracer gas technique. Here, a tracer gas is emitted into a space, and the ventilation rate is inferred from measurements of the concentration of this tracer. Three techniques are commonly used: tracer decay, constant emission, and constant concentration [247].

These measurement techniques are based on a mass-balance model, which assumes instantaneous, uniform mixing of gas within an air volume that is equal to the internal volume of the space, and that the only method of tracer removal is through ventilation [5, 25]. This model results in the concentration equation, which is given by

$$c(t) = c_E + \frac{S}{Q} - \left( c_E + \frac{S}{Q} - c(0) \right) e^{-\frac{Q}{V}t} \quad (2.24)$$

where  $c(t)$  is the concentration of the tracer gas at time  $t$ ,  $c_E$  is the external concentration of the tracer gas,  $c(0)$  is the concentration of the tracer gas at time  $t = 0$ ,  $S$  is the tracer generation rate,  $Q$  is the volume flow rate,  $V$  is the mixing volume, and  $t$  is time. The ratio of the volume flow rate to the mixing volume is known as the air change rate, given by

$$\phi = \frac{Q}{V} \quad (2.25)$$

All techniques described here for measuring volume flow rate using the tracer gas technique are dependent on the concentration equation for analysis. Consequently, the assumptions required for the derivation of the concentration equation are sources for potential error in tracer gas measurement techniques. One of the most important assumptions here is the uniform and instantaneous mixing of gas. This assumption implies independence from measuring location, and that all outgoing air has the same tracer gas concentration as that in the indoor space. Buggenhout *et al.* investigate the impact of measuring location on tracer gas measurement in a small chamber with a known inflow and outflow rate [248]. Here they identify significant spatial variation in tracer concentrations arising from imperfect mixing, resulting in errors in predicted ventilation rate of up to 86%. The optimal location to measure the tracer concentration is identified as being in the outlet. However, in naturally ventilated buildings the location of the outflow is not always known or

constant. This is a particular problem for single-opening ventilation, and represents a source of considerable uncertainty. To combat this, a number of authors use mixing fans to try to ensure a uniform concentration of pollutants in the space [61, 117]. However, this introduces a source of turbulence that could drive gas exchange, leading to further uncertainty in the results.

Furthermore, the use tracer gas techniques introduces further complications in multi-zonal buildings, where ventilation air can enter from other spaces that contain the injected tracer. Here, the conventional concentration equation cannot be readily applied, as inter-zonal and extra-zonal interactions cannot be distinguished. This limitation has been overcome with some success through the use of different tracer gases in each zone, such that the source and destination of the tracer can be easily identified [25, 249, 250, 251]. However, the experimental complexity increases with the number of zones, and the requirement to find tracers and measuring devices that are sufficiently inexpensive and do not interact with each other can become prohibitive. Consequently, the majority of tracer-gas measurements found in natural ventilation literature concern single-zone models [247].

**Tracer decay** The decay method is by far the most common tracer gas technique used in ventilation research [117, 118, 252, 67]. Here, a tracer is emitted into a space until the concentration is high and uniformly distributed. When the tracer emission is shut off, fresh-air supplied to the space causes dilution of the tracer, resulting in a characteristic decay curve. During pollutant decay, the generation rate  $S$  can be set to zero, which yields

$$c(t) = c_E - (c_E - c(0)) e^{-\phi t} \quad (2.26)$$

Typically, this equation is rearranged into a linear form, allowing the air change rate to be evaluated as the gradient of a linear fit:

$$\ln(c(t) - c_E) = -\phi t + \ln(c(0) - c_E) \quad (2.27)$$

The principal advantage of the decay method is its experimental simplicity, requiring only the measurement of tracer concentration and time [247]. The low equipment costs likely contribute to the ubiquity of the decay technique in the literature. However, the potential for error using the decay technique is large. Recording periods can be short, requiring many repeats to sufficiently reduce the random error [253]. In addition to this, evaluating the volume flow rate requires the use of a mixing volume. The selection of an appropriate mixing volume has been identified as a significant source of systematic error, particularly in full-scale buildings, where the volume of people and furniture need to be subtracted from the space volume

[253, 34].

**Constant emission and constant concentration techniques** In contrast to the decay method, both constant emission and constant concentration require a steady state to be achieved. After a long period of time, the time dependent portion of the concentration equation tends to zero, yielding

$$c(t) = c_{ss} = c_E + \frac{S}{Q} \quad (2.28)$$

This can be solved for volume flow rate, where

$$Q = \frac{S}{c_{ss} - c_E} \quad (2.29)$$

The constant emission and constant concentration methods differ only in which parameter,  $S$  or  $c_{ss}$ , is controlled, and which is measured. The constant emission and constant concentration methods permit long measurements of the steady-state concentration that enable the error to be reduced [253]. Consequently, these methods have a greater potential precision than the decay technique. However, the experimental equipment required can be expensive: the constant emission method requires a precise way of measuring the mass flow rate of gas, which needs to be kept constant, and the constant concentration method requires both measurement of the gas' mass flow rate, and a feedback mechanism to regulate the rate of gas supply.

#### 2.11.4 Integration of velocity profile

An alternative technique for measuring the volume flow rate through an opening is to measure the velocity profile across its area, and integrate over the area of the opening. This approach is commonly used in CFD simulations to evaluate flow through openings [1, 87, 123, 254]. Although some studies apply anemometry within the plane of an opening, its use to experimentally evaluate volume flow rates through openings is rare [255, 235]. Detailed measurements are required to achieve an adequate spatial resolution, with many studies relying on jet contraction assumptions to compensate for a lack of detailed data [235]. Nevertheless, opening-plane anemometry techniques provide significant potential to improve understanding of the dynamics of gas exchange at an opening, particularly when applied to large-scale models [255, 67, 121].

## 2.12 Conclusions

The literature review presented in this chapter allows the following conclusions to be drawn, broken down by section.

### 2.12.1 Flow around buildings

Mean surface pressure distributions around simple, isolated buildings are well described in the literature. However, considerable variation is evident between different practitioners, arising from differences in upstream velocity profile, choice of reference velocity and pressure, and measurement techniques [84, 82]. Furthermore, limited information is available describing the unsteady component of surface pressures, with transient modelling typically focused on the broader velocity field [40, 74].

In general, time-averaged streamline patterns are well described for flow around cubes. However, data describing temporal variation in flow direction is more scarce, and is limited to specific locations in the upstream horseshoe vortex and the downstream wake [73, 70]. Detailed studies of flow around cubes are typically limited to a few key wind directions - commonly 0 and 45 degrees, and focus on the broader flow patterns around the cube as opposed to the near-façade flow patterns important for ventilation [71, 73, 70, 72, 57]. Furthermore, visualisations of flow on façade surfaces are rare due to the influence of gravity inhibiting the use of the oil-film technique [75].

Limited information is available in the literature concerning cross-flow velocity distributions. Available data is limited to describing the relationship between mean cross-flow speed and wind direction [66, 67, 61, 99, 85]. However, measurements of the unsteady component of cross-flow speeds, or any quantitative measure of cross-flow direction, are generally absent from the literature. More detailed measurements of these phenomena are required for opening-scale experiments to be conducted that simulate representative local flow conditions.

### 2.12.2 Airflow through buildings

Air motion inside bounded spaces such as the internal rooms of buildings is a complex phenomena to predict. While patterns of airflow within spaces play an important role in pollutant transport and buoyancy-driven ventilation, many internal flow structures can be ignored when investigating envelope flow models of isothermal, wind driven ventilation.

The most significant internal flow phenomena affecting envelope flow models of wind-driven ventilation is likely to be flow-connection. This occurs where the inflow jet from the upwind opening aligns with the downstream opening, and results in the conservation of momentum between the two [1, 105, 38]. Understanding this phenomena is important in the design of suitable experiments that either measure or eliminate the effect.

### 2.12.3 Idealised airflow through openings

The conventional orifice flow equation applied in models of natural ventilation requires a number of simplifying assumptions in its derivation. One of the most significant of these is that the regions both upstream and downstream of the opening can be represented by reservoirs of still air [38, 25]. Consequently, the conventional orifice flow equation used to describe flow through openings has been shown to have no analytical basis to describe wind-driven ventilation, where the air upstream of the flow through the opening is non-stationary.

### 2.12.4 Opening geometry

The influence of opening geometry on the aerodynamic performance of PPOs is poorly described in the literature. It is commonly assumed that three-dimensional opening geometries can be represented by a planar orifice through the use of *free area* models. However, the application of *free area* models is ambiguous. Sources from both industry and academia routinely apply different methods of estimating the *free area*, leading to a wide range of aerodynamic performance predictions for the same window geometry [121, 123, 126, 129, 124, 125, 116]. These models are typically applied uncritically, with false assumption that they are accurate and intuitive. Despite the availability of standardised techniques, experimental measurement of the aerodynamic performance of PPOs for is rare even under *idealised* conditions [115]. This makes the suitability of different analytical models difficult to assess.

### 2.12.5 Air flow through windows driven by atmospheric wind

While most airflow network models commonly used in industry for simulation of natural ventilation assume *orifice* discharge coefficients equal to those occurring in still-air, a substantial body of literature identifies that this is not the case [81, 66, 104, 99, 105, 100]. Wind tunnel and CFD simulations at both building-scale and opening-scale have identified that a wind-driven cross-flow can significantly reduce the measured *orifice* discharge coefficient of simple, sharp-edged orifices [66, 100]. This phenomenon has been identified for both inflow and outflow conditions, and can be characterised using either a dimensionless room pressure or a dimensionless cross-flow velocity [66, 105, 100]. While both have been shown to be suitable similarity parameters to describe ventilation rate in a cross-flow, the use of the dimensionless room pressure is more widespread in the literature [104, 105, 100].

While building-scale investigations have identified a surface boundary layer in the cross-flow, most local-scale experiments have been designed to simulate a uniform velocity profile [66, 99, 105, 100]. This is intended to represent a *worst-case* scenario where wind has the greatest influence on ventilation performance, and



also to simplify the choice of a reference location for measuring the dynamic pressure in the cross-flow. However, the lack of a suitable surface boundary layer inevitably makes the results less representative of those occurring on a real building. Furthermore, while limited measurements have been made of the mean surface velocity profile of a notional building at a specific wind angle, no systematic study has been made into the unsteady behaviour, or the influence of wind angle or building geometry on the velocity distribution in the cross-flow [104].

Studies of ventilation through more realistic opening geometries in a wind-driven cross-flow are much more limited. While some limited measurements have been made for specific opening geometries, incorrect assumptions about independence from wind direction were made [99]. Consequently, the influence of wind direction and opening orientation on aerodynamic performance has not been adequately investigated, and the existing data is insufficient to support integration into airflow network models. Furthermore, while it is recognised in the literature that projecting opening geometry can alter the local pressure field, much of the available information is anecdotal [131, 25]. Where variations in pressure are explicitly described, they focus on the region surrounding the opening as opposed to within the opening plane itself [136]. This reflects experimental difficulties of pressure measurement within window openings, but limits its applicability to modelling ventilation phenomena. Descriptions of the impact of pressure interactions on ventilation rates are not present in the literature.

### 2.12.6 Wind tunnel techniques

Experiments using wind tunnel simulation require the use of scale models. Modelling full-scale environmental flows at a scale suitable for wind-tunnel modelling requires the application of dimensional analysis to determine conditions for dynamic similarity [165, 55]. Here, care must be taken to ensure that all the relevant variables are characterised, and have some physical meaning with respect to the flow problem under study. While the Reynolds number is one of the most important similarity parameters that needs to be conserved between similar flows, this requirement can typically be relaxed where flow separation from sharp-edges is a significant feature of the flow field [55, 25].

In addition to conservation of dimensionless similarity parameters, the boundary conditions to the full-scale and model-scale flows need to be similar [164, 55]. One of the most important boundary conditions in environmental flows is the velocity distribution in the approach flow.

The approach flow requirements for wind-tunnel measurements of flow around buildings are well documented in the literature [55, 174, 60]. However, wind tunnel measurements at the scale of typical naturally ventilated buildings require the use of barrier and mixing devices to provide a part-depth simulation of

the atmospheric boundary layer [60]. This inevitably results in a comparatively poor-quality simulation of atmospheric boundary layer flows [60, 54]. Fortunately, the validation application of wind tunnel modelling has far less strenuous similarity requirements than the design application [100]. Here, it is only necessary to simulate conditions that are representative of the types of flow experienced in nature. Numerous experimental methodologies have been developed for the purpose of generating representative part-depth atmospheric boundary layers.

By contrast, the approach flow requirements for local-scale modelling of the cross-flow on a building façade is poorly defined in the literature. This can largely be attributed to a lack of measurement of the velocity distribution in typical cross-flows either at full-scale or at model-scale. Consequently, the design of an appropriate approach flow for local-scale experiments remains largely determined by the intuition of the experimental designer. Much of the existing literature applies a uniform velocity profile, which is inconsistent with the limited available data on boundary layer flows near building surfaces [66, 99, 105, 100, 67].

### 2.12.7 Measurement techniques

Differential pressure transducers are the most widely used technique for measuring differential pressure, due to their low cost and potential for digital data collection. A key limitation is that they only permit point pressure measurement, and cannot measure the pressure field over a wide area. However, this is not a significant problem for natural ventilation studies, where surface pressure coefficients applied in envelope flow models typically refer to point pressures at the location of the window opening.

A wide-range of techniques exist for measuring the flow velocity either at a point or over a wide area. However, the techniques that yield the most detailed data can be prohibitively expensive. While hot-wire anemometers and Irwin probes provide low cost methods of measuring flow speed in a plane, no low-cost methods have been identified for measuring the instantaneous flow direction. This could be important in understanding how the cross-flow on a building façade interacts with opening geometry to drive ventilation. Therefore, this thesis identifies the need for a low-cost method of measuring the instantaneous speed and direction of flow on a façade simultaneously.

Differential pressure flow meters represent a comparatively cheap method of measuring large volume flow rates. They also have the benefit of being well regulated by technical standards, which eliminates the requirement for calibration of experimental apparatus. However, these techniques have significant spatial constraints, which limits their potential applications when measuring flow through buildings. Where space constraints are significant, unregulated pressure differential devices can be used to measure flow rates. These devices typically require prior calibration, and may be expected to offer a lower accuracy than regu-

lated devices. Pressure differential devices are only capable of measuring unidirectional flow rates. Where bidirectional gas exchange is important, tracer gas measurement of ventilation rate is required. While constant emission techniques offer objectively higher precision than decay techniques, choice of experimental method is likely to be constrained by access to equipment. Furthermore, the results of tracer gas measurements have been shown to be highly dependent on internal flow dynamics. Tracer gas techniques become complex when studying multi-zone buildings, which limits the practical application of the technique.

## 2.13 Gaps in the literature addressed by this thesis

This thesis addresses the following gaps in the literature:

1. No quantification of the errors associated with the application *free area models* - addressed in Chapter 5 where the *idealised* discharge coefficient predicted using *free area* models is compared against literature data [108, 124, 125].
2. No empirical models for the *idealised* discharge coefficient of hinged openings based on peer-reviewed literature data - addressed in Chapter 5 through the creation of an Empirical Effective Area Model (EEAM).
3. No experimental methods described that quantify the change in local pressure that arises due to the interaction between window geometry and a cross-flow - addressed in Chapter 5 through the measurement of *local* pressure coefficients for square, hinged openings.
4. Lack of experimental data or empirical models describing the volume flow rate through hinged openings in a cross-flow with flow approach angle and opening angle - addressed in Chapter 5 through wind tunnel and empirical modelling of ventilation through a square, hinged opening in a cross-flow. Chapter 7 then goes on to validate these local-scale experiments with model-scale ventilation studies.
5. No low-cost methods have been identified for simultaneously measuring the instantaneous flow speed and direction in a cross-flow - addressed in Chapter 6 through the development of a cross-flow probe.
6. Lack of measurements concerning the fluctuating components of the surface pressure coefficients on a cube - addressed in Chapter 6 where frequency distributions of surface pressure coefficients are evaluated for 15 degree increments in wind angle.
7. Lack of measurements of the mean and fluctuating components of the speed and direction of the cross-flow on the surface of a cube - addressed in Chapter 6 for wind angles in 15 degree increments.

## Chapter 3

# Theoretical evaluation of airflow through an opening in a cross-flow

### 3.1 Introduction

Chapter 2 identified that the interaction of wind with building geometry results in a cross-flow across its surface that can significantly alter the behaviour of flow through window openings. This cross-flow violates the still-air assumption that is essential to the derivation of the orifice equation. Therefore, an alternative description of airflow through openings in a cross-flow is required.

### 3.2 General empirical models of airflow through openings

Natural ventilation can be driven by a wide range of mechanisms that can be difficult or even impossible to describe analytically. This results in a wide range of design equations that apply only to specific configurations of openings under specific environmental conditions [3, 5, 25, 131]. For modelling purposes, it would be useful to have a general description of flow behaviour that can be applied over a wide range of conditions. One way of achieving this is to construct empirical models based on dimensionless parameters. All that follows assumes uniform density profiles in both internal and external reservoirs, and still indoor air.

This analysis begins with a discussion of different dimensionless ventilation rates that can be constructed based on different driving mechanisms. Dimensionless flow rates caused by pressure driven flow are denoted by  $Q_{\Delta P}^*$ , those due to local buoyancy are denoted  $Q_B^*$ , and those driven by a cross-flow are denoted by  $Q_{U_L}^*$ . Here

$$Q_{\Delta P}^* = \frac{Q}{L_c^2 \sqrt{\frac{2}{\rho} \Delta P}} \quad (3.1)$$

$$Q_B^* = \frac{Q}{L_c^2 \sqrt{g \frac{\Delta \rho}{\rho} L_c}} \quad (3.2)$$

$$Q_{U_L}^* = \frac{Q}{L_c^2 U_L} \quad (3.3)$$

Where the characteristic length  $L_c$  is taken to be the square root of the window area. Note that  $Q_{\Delta P}^*$  has the same definition as the *orifice* discharge coefficient;  $Q_B^*$  is a measurement of the Froude number; and  $Q_{U_L}^*$  is the local flow number; see Section 2.6 and 2.8.3.

These metrics are particularly useful when considering the impact of different mechanisms on flow rates - for instance, identifying whether wind increases or reduces buoyancy driven flows. They are graphically intuitive, where a higher dimensionless volume flow rate universally corresponds to increased ventilation rates [141].

One issue with these characterisations is that they tend to infinity when other mechanisms dominate flow. For an arbitrary combination of driving forces, a *total* dimensionless volume flow rate can therefore be constructed by combining the characteristic pressures associated with each potential driving force, where

$$Q_T^* = \frac{Q}{L_c^2 \sqrt{\frac{2}{\rho} (|\Delta P| + |\frac{1}{2} \Delta \rho g L_c| + |\frac{1}{2} \rho U_L^2|)}} \quad (3.4)$$

This parameter is much more useful in providing general characterisation for ventilation phenomena under a range of conditions, but is less intuitive for comparative purposes: a higher *total* dimensionless volume flow rate under different conditions does not necessarily correspond to a higher volume flow rate.

The *total* dimensionless volume flow rate can be described as a function of dimensionless parameters that describe the environmental conditions. The relevant dimensionless parameters are broken down into four categories: those that characterise driving forces; those that describe characteristics of the flow; those that characterise direction; and those that describe geometric parameters.

The first set of dimensionless parameters describe the ratio of the driving forces, and comprise: the ratio of the static pressure differential across an opening to local buoyancy forces  $P_P^*$ ; the ratio of the static pressure differential across an opening to the dynamic pressure in the cross-flow  $P_R^*$ , and the ratio of the local buoyancy forces to the dynamic pressure in the cross-flow  $P_B^*$ .

$$P_P^* = \frac{\Delta P}{\frac{1}{2}\Delta\rho g L_c} \quad (3.5)$$

$$P_R^* = \frac{\Delta P}{\frac{1}{2}\rho U_L^2} \quad (3.6)$$

$$P_B^* = \frac{\Delta\rho g L_c}{\rho U_L^2} \quad (3.7)$$

The second set of dimensionless parameters relate to characteristics of the flow such as Reynolds number. Where turbulence is important, turbulence intensity parameters need to be derived. Relevant turbulence parameters may be related to pressure, velocity or direction. It is possible that non-uniformity in velocity profiles, wind pressure profiles, and density gradients may also be characterised, but not in a way that is completely general.

The third set of dimensionless parameters relate to direction. These include the direction of a cross-flow, and the direction of a density gradient. Characterising a fractional density difference  $\rho^* = \Delta\rho/\rho$  also integrates information about the validity of the Boussinesq approximation.

Finally, for families of openings with a common phenotype, geometric parameters such as height to width ratio and opening angle may also require characterisation.

### 3.3 Bernoulli analysis

To analytically model airflow through windows in wind-driven conditions, a simplified set of conditions can be described based on analysis of the pressure and velocity fields close to ventilation openings described in Section 2.4. Figure 3.1 depicts the pattern of airflow through a simple window opening in a cross-flow of uniform velocity for inflow and outflow conditions.

Inflow through the opening can be evaluated by applying Bernoulli analysis between a point in the cross-flow sufficiently far from the opening that the pressure and velocity is unaffected by flow through the opening, known as the *free stream*, and the point of maximum flow velocity in the *vena contracta*; see Figure 2.4. Comparing total pressures along the streamline yields an expression for the fluid velocity in the *vena contracta*, which can then be integrated over the area of the stream tube in this location to evaluate the volume flow rate, assuming a uniform velocity distribution in both the cross-flow and the *vena contracta*. Here, the static pressure and velocity in the *free stream* are equivalent to the external surface pressure  $P_E$  and the cross-flow velocity  $U_L$  measured on a building with no openings present. The static pressure in the *vena contracta* is set by the static pressure of the fluid into which it discharges, and is therefore equivalent to

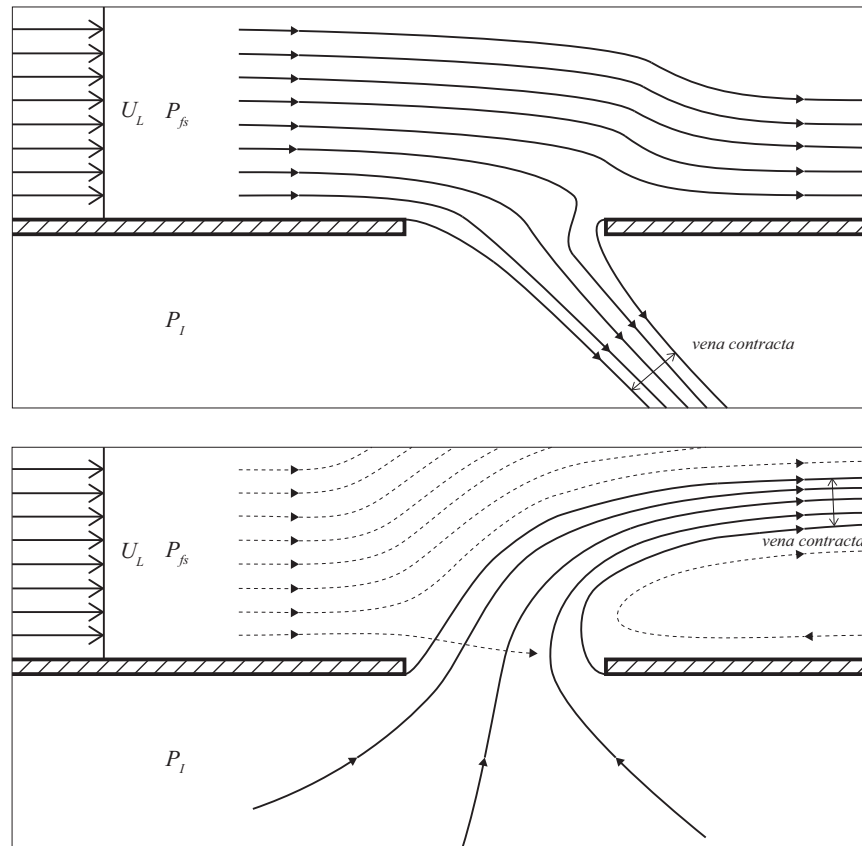


**Figure 3.1:** Pattern of streamlines near an isolated opening for inflow (top, after Vickery and Karakatsanis [81] ) and outflow (bottom, after Endo *et al.* [105]). The cross-flow velocity ( $U_L$ ), free stream pressure ( $P_{fs}$ ), internal pressure ( $P_I$ ), and *vena contracta* are labelled.

the indoor air pressure  $P_I$  for inflow. Variation in height and fluid density along the streamline is neglected. This yields

$$P_{T(fs)} = P_{fs} + \rho g z + \frac{1}{2} \rho U_{fs}^2 \quad (3.8)$$

$$P_{T(vc)} = P_{vc} + \rho g z + \frac{1}{2} \rho U_{vc}^2 \quad (3.9)$$

$$U_{fs} \equiv U_L \quad (3.10)$$

$$P_{fs} \equiv P_E \quad (3.11)$$

$$P_{vc} \equiv P_I \quad (3.12)$$

$$P_{T(fs)} - P_{T(vc)} = P_E - P_I + \frac{1}{2} \rho U_L^2 - \frac{1}{2} \rho U_{vc}^2 \quad (3.13)$$

$$U_{vc} = \sqrt{\frac{\rho}{2} \left( P_E - P_I + \frac{1}{2} \rho U_L^2 - (P_{T(fs)} - P_{T(vc)}) \right)} \quad (3.14)$$

$$Q_{in} = \int^{A_{vc}} U_{vc} = A_{vc} \sqrt{\frac{\rho}{2} \left( P_E - P_I + \frac{1}{2} \rho U_L^2 - (P_{T(fs)} - P_{T(vc)}) \right)} \quad (3.15)$$

$$C_d = \frac{A_{vc}}{A_R} \sqrt{1 - \frac{P_{T(fs)} - P_{T(vc)}}{P_E - P_I + \frac{1}{2} \rho U_L^2}} \quad (3.16)$$

$$Q_{in} = C_d A_R \sqrt{\frac{\rho}{2} \left( P_E - P_I + \frac{1}{2} \rho U_L^2 \right)} \quad (3.17)$$

where  $P_{fs}$  denotes the static pressure in the free stream of the cross-flow,  $P_{vc}$  denotes the static pressure in the *vena contracta*; and  $U_L$  denotes the speed of the cross-flow; see Figure 3.1. The subscript *in* denotes inflow through the opening. Here the discharge coefficient can be seen to be a product of a contraction coefficient that describes the ratio of the area of the *vena contracta* to a reference area for the opening, and a friction coefficient that describes the loss in total pressure along the streamline.

A similar analysis can be applied to outflow through window openings. Here, air is drawn from the internal air, and emitted into the external cross-flow. Where the cross sectional area of the indoor space is large compared to the area of the window, the velocity in the *free stream* upstream of the opening can be neglected, and the static pressure equated with the indoor air. This yields



$$P_{T(fs)} = P_{fs} + \rho gz + \frac{1}{2}\rho U_{fs}^2 \quad (3.18)$$

$$P_{T(vc)} = P_{vc} + \rho gz + \frac{1}{2}\rho U_{vc}^2 \quad (3.19)$$

$$U_{fs} \equiv U_I \approx 0 \quad (3.20)$$

$$P_{fs} \equiv P_I \quad (3.21)$$

$$P_{T(fs)} - P_{T(vc)} = P_I - P_{vc} - \frac{1}{2}\rho U_{vc}^2 \quad (3.22)$$

$$U_{vc} = \sqrt{\frac{\rho}{2} (P_I - P_{vc} - (P_{T(fs)} - P_{T(vc)}))} \quad (3.23)$$

$$Q_{in} = \int^{A_{vc}} U_{vc} = A_{vc} \sqrt{\frac{\rho}{2} (P_I - P_{vc} - (P_{T(fs)} - P_{T(vc)}))} \quad (3.24)$$

$$C_d = \frac{A_{vc}}{A_R} \sqrt{1 - \frac{P_{T(fs)} - P_{T(vc)}}{P_I - P_{vc}}} \quad (3.25)$$

$$Q_{out} = C_d A_R \sqrt{\frac{\rho}{2} (P_I - P_{vc})} \quad (3.26)$$

where the subscript *out* denotes outflow through the opening.

The static pressure in the *vena contracta* is set by the static pressure of the reservoir into which the ventilation jet discharges. For inflow, this is equivalent to the internal pressure of the space,  $P_I$ . For outflow, its value is less easily evaluated. Projecting window geometry or the outflow jet itself can interact with the cross-flow to generate a spatially varying pressure field [136, 105]. The pressure in the *vena contracta* is set by its location within this pressure field, and may not be simply equivalent to the free stream pressure in the cross-flow. The static pressure in the cross-flow field at the location of the *vena contracta* can be expressed as a pressure coefficient, which yields

$$C_{P(vc)out} = \frac{P_{vc(out)} - P_E}{\frac{1}{2}\rho U_L^2} \quad (3.27)$$

$$Q_{out} = C_d A_R \sqrt{\frac{\rho}{2} \left( P_I - P_E - C_{P(vc)out} \frac{1}{2}\rho U_L^2 \right)} \quad (3.28)$$

where  $C_{P(vc)out}$  denotes the pressure coefficient at the *vena contracta* of the outflow jet, which is described relative to the reference static and dynamic pressures in the cross-flow. In the absence of explicit knowledge of this value, a discharge coefficient that retains exclusively finite values can be ensured by setting a theoretical minimum bound that maximises the ventilation driving pressure. This is achieved here by assuming a minimum pressure coefficient at the *vena contracta* of -1. This simplification allows a single expression to

be used for both inflow and outflow, given by

$$Q = S_i C_{d_B} A_R \sqrt{\frac{2}{\rho} \left( S_i (P_I - P_{fs}) + \frac{1}{2} \rho U_L^2 \right)} \quad (3.29)$$

where  $S_i$  is a directional indicator, and is equal to -1 for inflow, and 1 for outflow. Here, the discharge coefficient  $C_{d_B}$  can be shown to be a generalised form of the *Bernoulli* discharge coefficient defined by Equation 2.19, that is applicable for both inflow and outflow. Equation 3.29 reduces to the orifice equation in the absence of a cross-flow, so the *orifice* discharge coefficient and *Bernoulli* discharge coefficients are equivalent in still-air conditions.

When the density difference between zones is neglected, the definition of the *Bernoulli* discharge coefficient arrived at analytically is very similar to that of the *total* dimensionless volume flow rate, defined by Equation 3.4. This form enables more convenient integration into the general empirical models of airflow characteristics described in Section 3.2.

### 3.4 Behaviour in still-air

Still-air conditions occur as the dimensionless room pressure tends to  $\pm\infty$ ; see Section 2.8.2. Therefore, the ventilation capacity of an opening in still-air can be seen to be a special case of ventilation in a cross-flow, and defines an important limit to this relationship.

When the density difference between zones can be neglected, the definitions of the *orifice* discharge coefficient, the *Bernoulli* discharge coefficient and the magnitude of the *total* dimensionless volume flow rate become equivalent in still-air. The value of this parameter is equivalent to the *idealised* discharge coefficient, which can be measured by pressurisation experiments and is considered to be a fundamental property of an opening.

### 3.5 Local pressure effects

A cross-flow can interact with projecting window geometry to generate a spatially varied pressure field close to an opening [136]. This can alter the dynamics of flow through an opening relative to that anticipated from the free stream pressure, with the potential to drive steady-state bidirectional flows [88].

### 3.5.1 Pressure generation mechanisms

Changes in static pressure close to a ventilation opening arise from two key mechanisms: change in flow velocity along streamlines, and wake turbulence.

Projecting elements of an opening can obstruct and slow the cross-flow. Here, the dynamic pressure in the cross-flow is converted into static pressure. Similarly, air moving across surfaces can accelerate, resulting in the conversion of static pressure into dynamic pressure. Flow separation results in a turbulent wake that forms behind obstructions, characterised by low pressures and low flow velocities.

### 3.5.2 Local pressure coefficients

The static pressure at a point in the flow relative to that in the free stream can be characterised by pressure coefficients, given by

$$C_p = \frac{P_i - P_{fs}}{P_{d(fs)}} \quad (3.30)$$

where  $P_i$  is the static pressure at a point in the flow,  $P_{fs}$  is a reference static pressure in the free stream, and  $P_{d(fs)}$  is a reference dynamic pressure in the free stream. If the reference pressures are located on the same streamline as the pressure measurement of interest, the pressure coefficient has a maximum value of 1, and is unlikely to drop below -1.

Here it is hypothesised that the spatially varied pressure field near a ventilation opening can be averaged to derive a *mean* pressure that describes the influence of the pressure field on *mean* flow rates. This *mean* pressure is henceforth referred to as the *local pressure*  $P_L$ , and allows a *local* pressure coefficient to be defined, where

$$C_{P_L} = \frac{P_L - P_{fs}}{P_{d(fs)}} \quad (3.31)$$

### 3.5.3 Local dimensionless pressure

A key boundary condition that defines the *local* pressure is that when the *local* pressure acting on the external surface of the opening is equal to the *internal* pressure, no net flow occurs through the opening. This allows a *local* dimensionless pressure to be defined, where

$$P_L^* = \frac{P_I - P_L}{P_{d(fs)}} = P_R^* - C_{P_L} \quad (3.32)$$

This is proposed as a better descriptive parameter with which to describe the dependence of volume flow

rate on a cross-flow. Here, a change in sign of the *local* dimensionless pressure corresponds to a change in direction of net flow rate through the opening.

## 3.6 Conclusions

A Bernoulli analysis of airflow through open windows in a cross-flow yields a descriptive equation that is different to the orifice equation. This description includes a dynamic pressure term that enables the influence of a cross-flow on ventilation driving pressures to be accounted for. This can be shown to be well described by the *total* dimensionless volume flow rate defined by Equation 3.4.

This analysis identifies three key properties that are useful to describe the ventilation capacity of an opening in a cross-flow: the *total* dimensionless volume flow rate, the *idealised* discharge coefficient and the *local* pressure coefficient. The *total* dimensionless volume flow rate describes the volume flow rate through an opening, and can be described as a function of dimensionless room pressure. The *idealised* discharge coefficient and the *local* pressure coefficient describe key limits to this relationship. The *idealised* discharge coefficient evaluates the magnitude of the *total* dimensionless volume flow rate in still-air, and represents the limit as the dimensionless room pressure tends to  $\pm\infty$ . The *local* pressure coefficient describes the pressure increment over the opening that arises due to interaction between the window and the cross-flow, and corresponds to the value of the dimensionless room pressure where the net flow transitions between inflow and outflow. Independent methods for measuring these three properties are described in Section 4.4.



# Chapter 4

## Methods

### 4.1 Introduction

This chapter describes experimental and analytical techniques to characterise the aerodynamic performance of window openings, measure the pressure and velocity in the surface flow field on the façade of a model building, predict ventilation rates in a notional building, and validate these predictions using measured volume flow rates.

The experiments carried out in this thesis, their intended outputs, and the connections between them are summarised in Figure 4.1. Here, cross-flow characterisation experiments are performed as described in Section 4.4. These procedures evaluate models of the aerodynamic performance of window openings in a cross-flow that are intended to be integrated into envelope flow models of natural ventilation.

To validate these cross-flow characterisation models, predictions need to be made that can be verified by experiment. Here, these models are used to predict ventilation rate in a notional building; see Section 4.8.3. To achieve this, the cross-flow characterisation models require measurements of the surface pressures and the cross-flow velocity at the location of all openings in the building envelope; see Section 4.7. This in turn necessitates the development of a cross-flow probe to measure the speed and direction of the cross-flow; see Section 4.6. Finally, these predictions can be compared against measured ventilation rates in the building according to the experiments described in Section 4.8.

### 4.2 Flow direction definitions

Figure 4.2 illustrates the definition of a range of angles relating to the flow of air around buildings. The wind angle  $\theta$  is defined as the angle between the atmospheric wind and the façade. The *façade* cross-flow direction

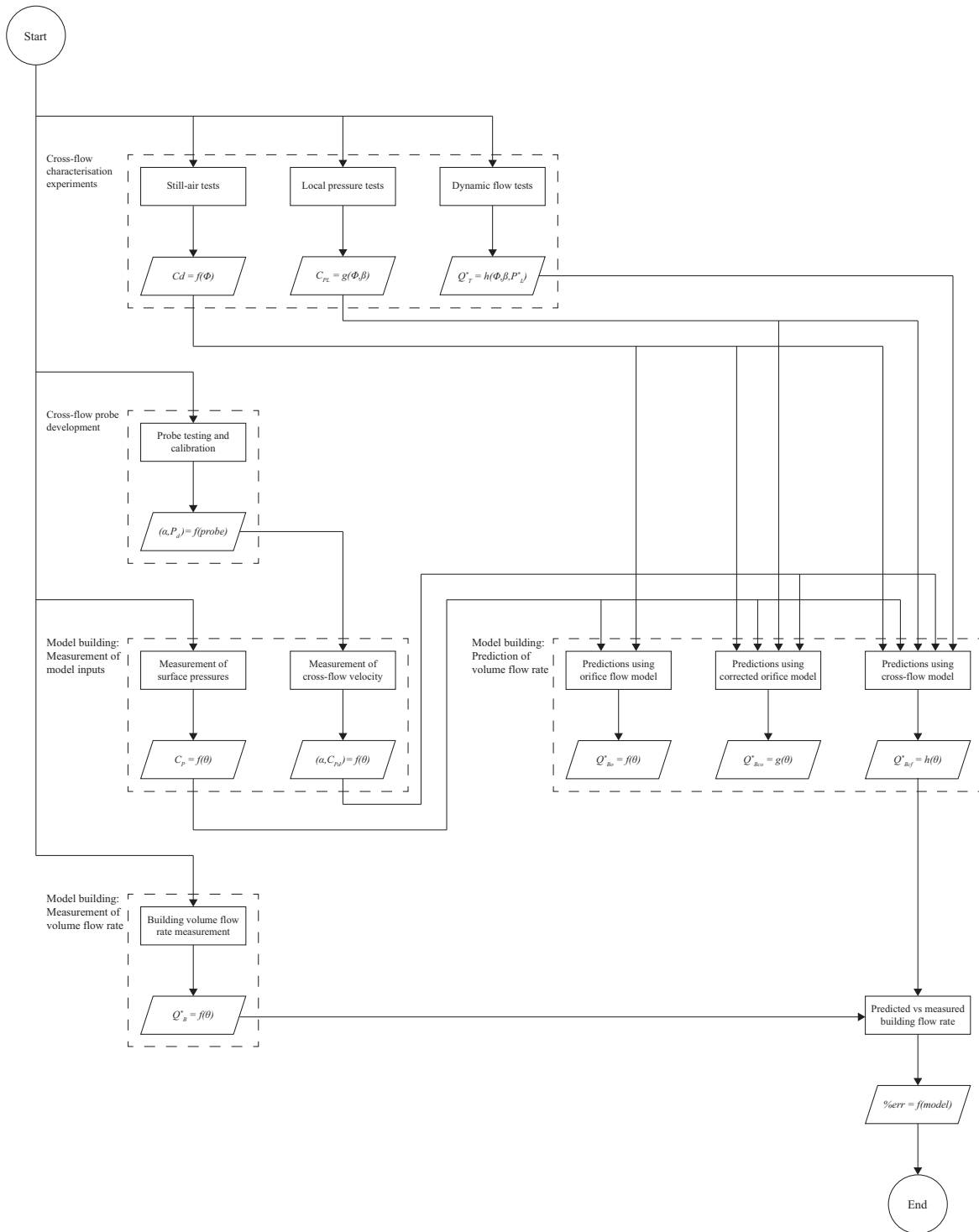


**Figure 4.1:** Flow diagram illustrating the relationship between the experimental procedures performed in this thesis and their intended outputs

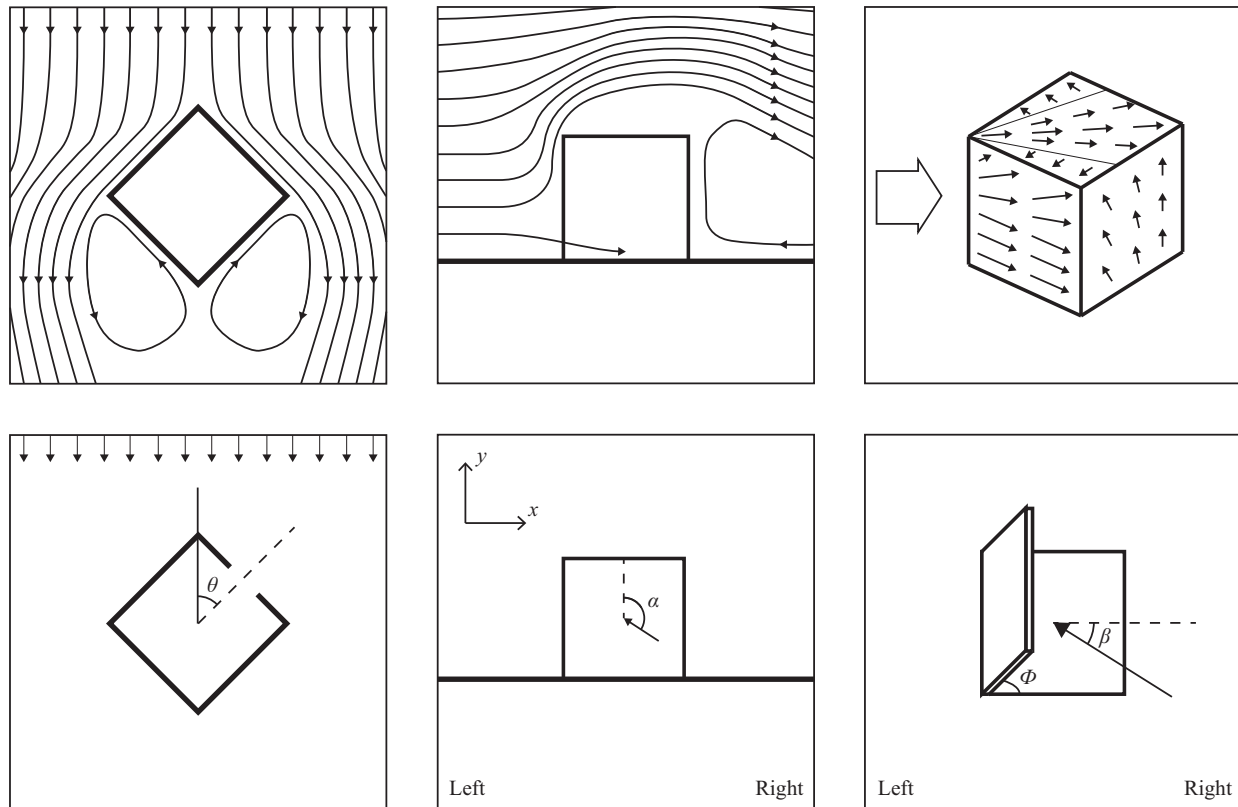


**Figure 4.2:** Diagram of airflow patterns around a notional building, and its interaction with windows mounted on the façade. The top row illustrates mean streamline patterns, after ASHRAE [16] and Wilson [52]. The bottom row defines a range of different angle measurements used in this thesis. Here, the wind angle is represented by  $\theta$ , the *façade* cross-flow direction by  $\alpha$ , the flow approach angle by  $\beta$ , and the opening angle by  $\phi$ .



$\alpha$  is defined as the angle between the cross-flow velocity vector parallel to the façade and the vertical. The flow approach angle  $\beta$  defines the direction of the cross-flow velocity vector relative to the principal axis of a given window geometry; see Figure 4.8. The definition of left and right, and the  $x$  and  $y$  directions are defined based on a view of the façade in elevation, and of any windows within that façade; see Figure 4.2.

This flow approach angle can be transformed from the *façade* cross-flow direction. For left-mounted openings,  $\beta = \alpha - 90$ ; for right-mounted openings,  $\beta = \alpha + 90$ ; for bottom hung windows,  $\beta = \alpha$ ; and for top hung windows,  $\beta = \alpha + 180$ . The opening angle of the window is denoted by  $\phi$ , and is defined as the angle between the plane of the opening vane and the plane of the opening.

### 4.3 Empirical modelling

The analytical and experimental work presented in this thesis aims to express airflow through windows in terms of dimensionless parameters. Here, dimensional analysis is used to identify dimensionless aerodynamic properties that can be expressed as a function of dimensionless geometric and environmental parameters.

A number of empirical models are created that fit statistical curves to measured data. This is required to reduce large sets of empirical data to simple design equations. When the dimensionless aerodynamic property of interest is a function of multiple dimensionless parameters, design equations are fit sequentially by treating the data as a family of curves [256]. This approach adopts the following process:

1. The dimensionless aerodynamic property of interest is identified as the dependent variable.
2. Dimensionless similarity parameters are identified as independent variables that could influence the value of the dependent variable.
3. One of these dimensionless similarity parameters is chosen to be the primary independent variable.
4. The dependent variable is plotted against the primary independent variable, while all remaining independent variables are held constant.
5. A suitable equation is chosen to describe this relationship based on analytical solutions and visual observation of the shape of the plot; see Section 4.3.1.
6. A family of coefficients are fitted to the data for all possible combinations of the remaining independent variables.
7. Steps 3–6 are repeated for the fitted family of coefficients. Here, each coefficient is treated as the dependent variable, which is expressed as a function of all remaining independent variables.

8. This process is repeated until a single expression is derived comprised of nested single-variable functions.
9. The coefficients of this expression are re-fit to minimise the difference between predicted and measured data across the whole data-set.

Coefficients are fit using the MATLAB fit function [257], which outputs best-fit coefficient values and their confidence intervals using a weighted least squares minimisation. Where uncertainty in the data is known, weights are specified as the inverse square of the standard error.

### 4.3.1 Principles of function selection

A key requirement of the technique for fitting a family of curves is that secondary variables must be kept constant during data collection. Therefore, any variable that cannot be kept constant during data collection must be specified as the primary variable.

When selecting a suitable functional relationship to fit the data, consideration is given to the theoretical properties of the modelled performance curve.

Curves that model the relationship between the *idealised* discharge coefficient and opening angle must pass through the origin; a fully closed window has no admittance to flow. Similarly, the *local* pressure coefficient can be assumed to be equal to that of the square orifice when the opening angle is equal to zero, or the flow approach angle is equal to 90 degrees. Here, the window geometry interacts minimally with the cross-flow.

Curves that model the *total* dimensionless volume flow rate as a function of *local* dimensionless pressure must also have specific features. Curves must pass through the origin, and approach an asymptote as the *local* dimensionless pressure tends to  $\pm\infty$ . As this represents still-air conditions, the curve should be asymptotic to the *total* dimensionless volume flow rate in still air, with a magnitude equal to the *idealised* discharge coefficient.

The hinged openings characterised in Chapter 5 are symmetric about their principal axis; see Figure 4.8. Therefore, when modelling the relationship between any measured parameter that describes these openings and flow approach angle, a form of equation that is periodic in 360 degrees, and symmetric about zero and 180 degrees is required. Here, a Fourier series is adapted to construct an equation in this form. The final expression has the required properties only if all its terms also have these properties. Therefore, the adapted Fourier series comprise only cosine functions. A modelled parameter that is periodic in 360 degrees and symmetric about zero and 180 degrees can be expressed in the form:

$$f(\beta) = \sum_{n=0}^{n=i} a_n \cos(n\beta) \quad (4.1)$$

Once key theoretical properties are accounted for, the selection of suitable shape functions is derived based on visual analysis of the measured data. Several potential functions are selected in each case, and subjected to iterative testing to identify equations that provide the closest fit to the measured data with the minimum number of empirical coefficients.

### 4.3.2 Statistical analysis

Two techniques are used to evaluate the quality of a model fit. The first is the coefficient of determination,  $R^2$ . The coefficient of determination describes the proportion of the variation in the data that is explained by the model, and is given by

$$R^2 = 1 - \frac{\sum (X - X_p)^2}{\sum (X - \bar{X})^2} \quad (4.2)$$

where  $X$  is a measured parameter,  $X_p$  is the value of that parameter predicted by the model, and  $\bar{X}$  is the mean value of the measured parameter over the whole data set. Where a model perfectly matches observed values, the coefficient of determination is equal to one. Where a model would be equally well described by a constant, the coefficient of determination is equal to zero. A negative value of the coefficient of determination implies that the model is a poorer fit to the data than a simple mean. The coefficient of determination is useful because it describes the ability for an equation to model measured variation. This is an essential property in an empirical model that is used for design purposes. However, the coefficient of determination does not account for uncertainty in the data. This can be useful when producing empirical models from literature data, where uncertainty is often difficult to evaluate.

Where uncertainty in the data is known, a reduced chi squared statistic ( $\chi_v^2$ ) is evaluated to describe the quality of the model fit [258], given by

$$\chi_v^2 = \frac{1}{N_v} \sum \left( \frac{X - X_p}{\sigma_M} \right)^2 \quad (4.3)$$

where  $N_v$  is the number of degrees of freedom, and  $\sigma_M$  is the standard error in the mean. The reduced chi squared statistic describes the degree to which deviation between predicted and measured values are explained by the uncertainty in the data. For a good fit,  $\chi_v^2$  should be close to one, with higher  $\chi_v^2$  values corresponding to a poorer fit to the data. A  $\chi_v^2$  value of less than one implies that the fit is better than can be explained by the uncertainty. This suggests that over-fitting may have occurred, or that the error in the

data may have been overestimated.

## 4.4 Cross-flow characterisation experiments

The cross-flow characterisation experiments aim to characterise the aerodynamic performance of window openings in wind-driven flow, independently of the building in which they are installed. The resulting performance data are characteristic to a given window geometry, and are used to develop empirical models that can be integrated into envelope flow models to predict airflow through a notional building.

The experimental methodology is based on the premise that wind induces a cross-flow that occurs parallel to the building surface; see Section 2.4.2. While this is valid for openings in the middle of a wall, this premise is likely to break down close to building corners. Here a wind tunnel is used to simulate the conditions on a small part of the surface of a large building, where the opening is small compared to the size of the facade; see Figure 4.3.

### 4.4.1 Wind tunnel setup

The experimental setup consists of an open loop wind tunnel with a plenum chamber mounted in the floor; see Figure 4.3. A model window opening can be mounted in the top face of the plenum chamber, which corresponds to a maximum blockage ratio of 0.9%, and provides an air transfer route between the tunnel and the chamber. The plenum chamber represents the building interior, and is mounted such that the window opening is flush with the tunnel surface. The wind tunnel induces a flow across the surface of the opening, simulating the cross-flow that occurs on building façades.

A pipe issues from the chamber through which air can be supplied or extracted. This induces air flow through the opening, which simulates the behaviour under cross ventilation. The mass flow rate in the pipe is measured using an orifice flow meter, and is equivalent to the net mass flow rate occurring through the window. Air is supplied to or extracted from the chamber using a variable speed centrifugal fan, which can be reconfigured to operate in either supply or extract mode. Finally, a flow control valve enables the plenum to be sealed, so that the window represents the only flow path whereby air can enter or leave the plenum.

### 4.4.2 Preconditioning elements

Two alternative sets of preconditioning elements are used to create the surface boundary layer in the wind tunnel; see Figure 4.4. These preconditioning elements are labelled 1 in Figure 4.3. The first creates a notionally *thin* surface boundary layer, with a boundary layer thickness of approximately 350mm, and a

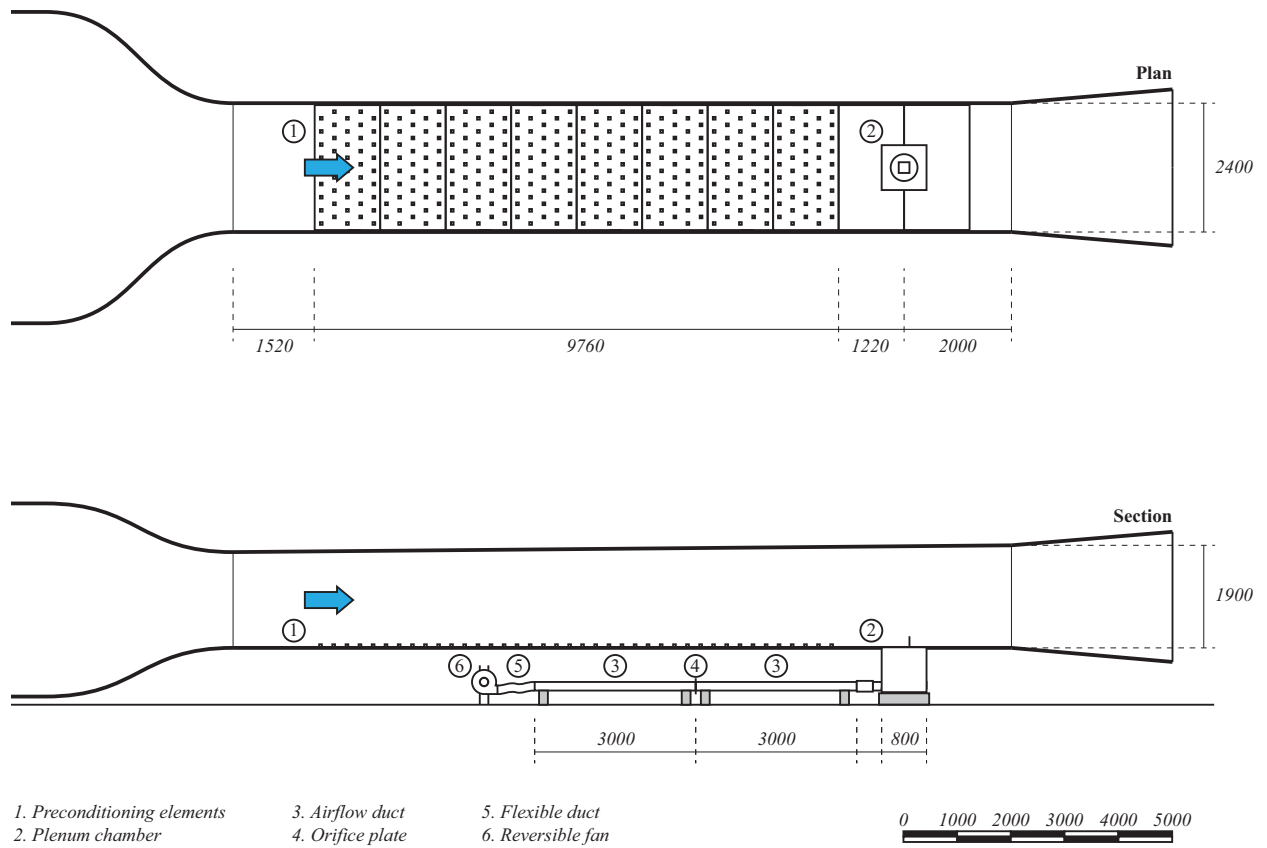


**Figure 4.3:** Wind tunnel setup for the window characterisation experiments, with dimensions given in millimeters. The direction of flow is denoted by the blue arrow.



**Figure 4.4:** Alternative preconditioning elements used in the window characterisation experiments. The MDF sheets intended to create a *thin* boundary layer are shown on the left, and the roughness elements intended to create a *thick* boundary layer are shown on the right.

roughness scale similar to that anticipated from common construction materials. Here, a series of MDF sheets are mounted on the surface of the tunnel, flush with the surface of the window opening. The second set of preconditioning elements creates a notionally *thick* surface boundary layer, with a boundary layer thickness of approximately 500mm. Here, the MDF sheets are replaced with a roughness layer consisting of staggered 50mm cubes; see Figure 4.5. The preconditioning elements begin 1220mm upstream from the centre of the window opening, and continue to 10980mm upstream; see Figure 4.3.

#### 4.4.3 Plenum design

The plenum chamber is labelled 2 in Figure 4.3, and comprises an 836mm MDF cube, with an interior dimension of 800mm; see Figures 4.6 and 4.7. A model window is fixed to a mounting plate, which sits in a recessed circle in the top face of the chamber, such that its upper surface is flush with the surface of the plenum. To prevent jetting in outflow mode, a diffuser system is installed in the base of the plenum; see Figure 4.7. Here, the supply duct distributes air along the base of the plenum to encourage mixing, and reduce the dynamic pressure in the supply jet. Supply air then passes through a mesh filter, which is intended to increase the uniformity of the pressure and velocity distribution in the supply air; see Figure 4.6. Aluminium tape is used to seal the plenum, and ensure that it is air-tight.

The design of the plenum chamber is consistent with the requirements EN 13141-1 for the performance testing of ventilation components [115], and the interior dimensions exceed the limits identified by Ohba *et al.* that are required to ensure independence of ventilation performance in a cross-flow from chamber dimensions [99].

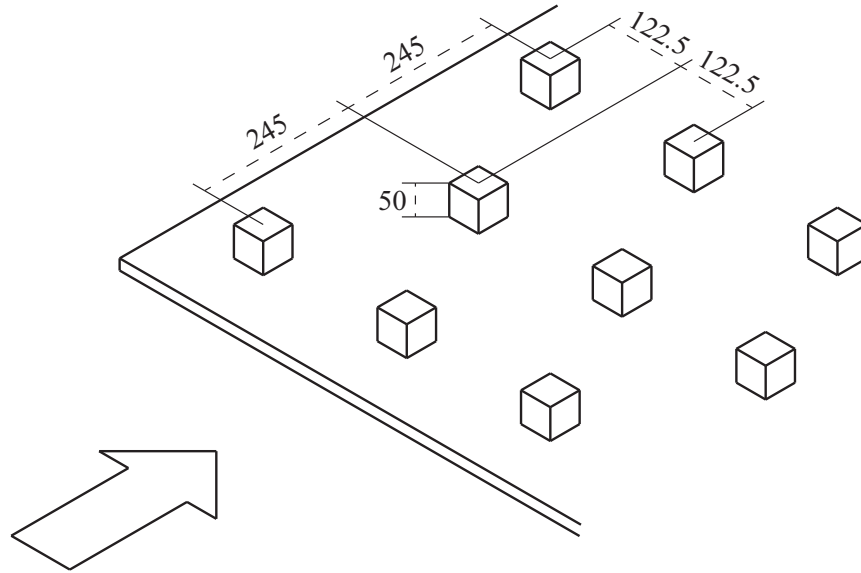


**Figure 4.5:** Key dimensions of preconditioning elements. The direction of the wind tunnel flow is denoted by an arrow

#### 4.4.4 Model window

The modelled windows are mounted on a 500mm diameter circular mounting plate comprised of 3mm thick steel; see Figure 4.8. A 200mm square hole cut in the centre simulates a square orifice. A range of 3mm steel vanes can then be bolted to the mounting plate, which simulate a hinged window at opening angles of 5, 15, 30, 60, and 90 degrees respectively. Bolt holes in the perimeter of the mounting plate allow the opening to be rotated in 22.5 degree increments relative to the direction of the wind tunnel flow, which enables the simulation of a range of flow approach angles; see Figure 4.9. Finally, the mounting plate can be inverted to simulate windows that open *outwards* (i.e. out from the plenum, and into the simulated cross-flow) or *inwards* (i.e. into the plenum).

#### 4.4.5 Orifice flow meter

The mean mass flow rate through the window opening is equivalent to the mass flow rate into or out of the plenum chamber. This is measured using a bidirectional orifice flow meter mounted in the supply and extract duct, which is labelled 4 in Figure 4.3. The design of the orifice flow meter is consistent with the requirements of BS EN ISO 5167-1 [242] and BS EN ISO 5167-2 [243], and consists of a 3mm thick steel plate with a 114mm diameter circular orifice, mounted within a 150.2mm diameter pipe. The supply and extract pipe extends for 3000mm up and downstream of the orifice to ensure adequately preconditioned flow [242]. Flange type pressure tapings are used to measure the pressure drop across the orifice, which are

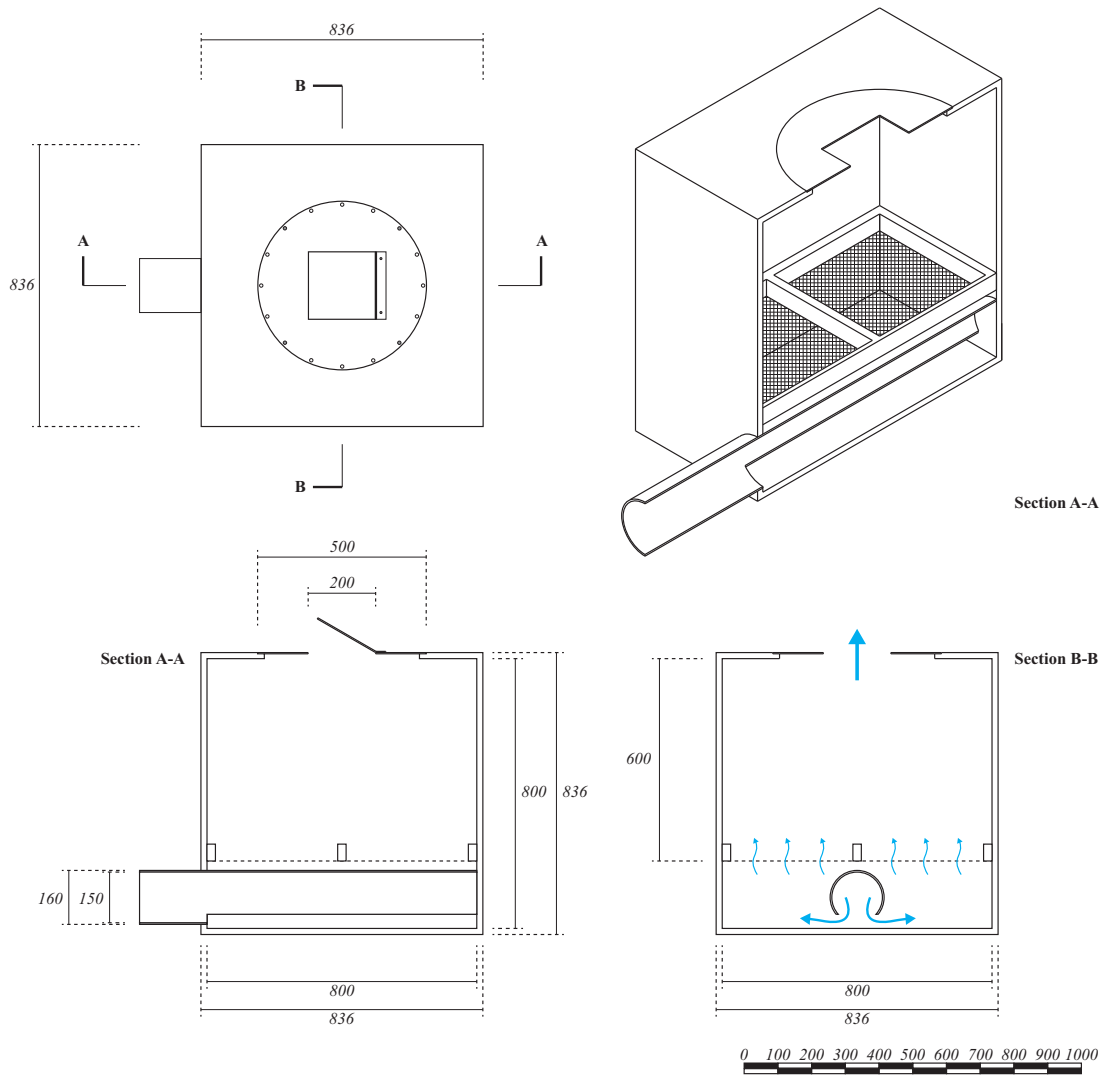


**Figure 4.6:** Details of the plenum chamber used in the window characterisation experiments, in plan view (top left), orthographic section (bottom left and right), and isometric section (top right). Dimensions are given in millimeters. The intended flow path when the fan is in supply mode is denoted with blue arrows.





**Figure 4.7:** Plenum chamber (left) and details of the diffuser array (middle and right). The middle image depicts a partially constructed plenum, with the mesh filter visible. The right image depicts the interior of the supply duct, and the slits that distribute air into the plenum.

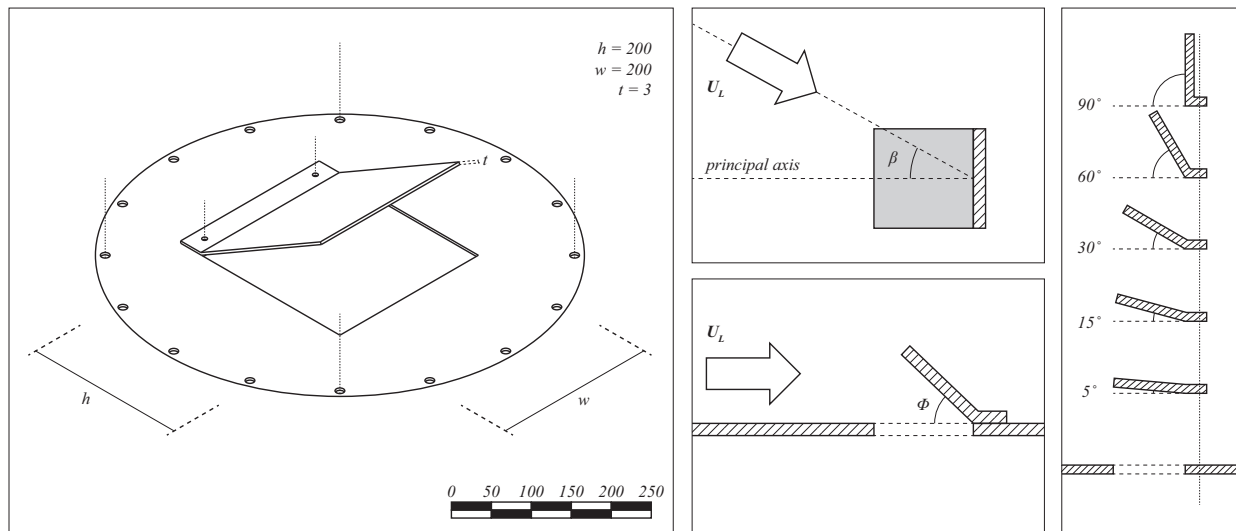


**Figure 4.8:** Isometric drawing depicting the opening modelled for experiment (left), where the opening height, width and thickness are denoted by  $h$ ,  $w$  and  $t$  respectively, with distances given in millimeters. Plan (middle top) and section (middle bottom) diagrams illustrate the definitions of the flow approach angle and the opening angle, denoted by  $\beta$  and  $\phi$  respectively. The cross-flow velocity vector by is denoted by  $U_L$ . A range of window vanes open to fixed angles can be mounted on the opening plate (right).

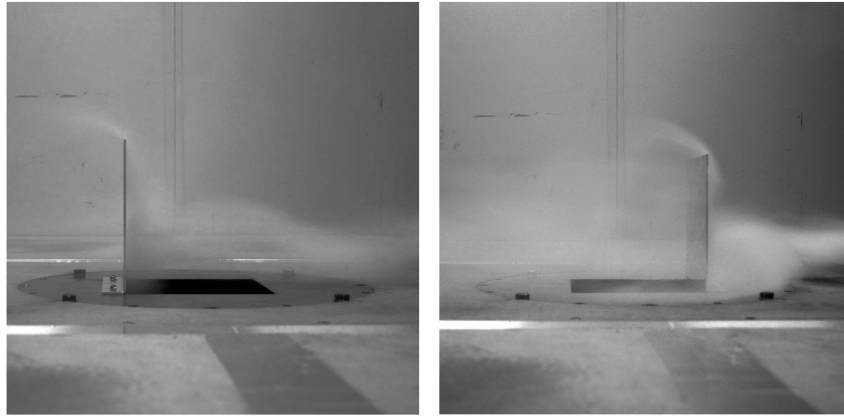


**Figure 4.9:** Air-flow over window elements during characterisation experiments. Both images represent conditions where no net flow occurs through the opening. The left image corresponds to a flow approach angle of zero degrees, and the right image corresponds to a flow approach angle of 180 degrees.

located 25.4mm upstream and downstream of the orifice plate respectively [243].

#### 4.4.6 Instrumentation

Characterisation of airflow performance in this setup requires the use of three differential pressure measurements. Each of these are measured using a SensorTechnics HCLA 02X5-B differential micromanometer.

A pitot-static tube located in the free stream is used to sample the dynamic pressure in the cross-flow. The dynamic pressure is directly measured by connecting the total pressure tapping and the static pressure tapping on the pitot-static tube to the positive and negative port of the differential micromanometer respectively; see item *10a*) in Figure 4.10. The pitot-static tube is mounted 500mm above the tunnel surface, 450mm from the tunnel wall and 1000mm upstream of the window centre.

A second differential micromanometer measures the pressure difference between a pressure tapping in the plenum chamber and the static pressure tapping on the pitot-static tube, which are connected to the positive and negative ports of the differential manometer respectively; see item *10b*) in Figure 4.10. This measures the static pressure difference between the plenum and the free stream, which is equivalent to the difference between the internal pressure in a space, and the external pressure as measured on the surface of a sealed body wind tunnel model, in the absence of window geometry. This avoids the difficulty of directly measuring pressure changes close to the opening caused by the interaction between the cross-flow and window geometry, and ensures the results can be applied in the design case by aligning measurement techniques with design methodologies. The pressure tapping on the inside of the plenum is located on the upstream face of the chamber, to minimise the potential for interaction with the inflow jet.

Finally, the third micromanometer measures the pressure drop across the orifice plate mounted in the

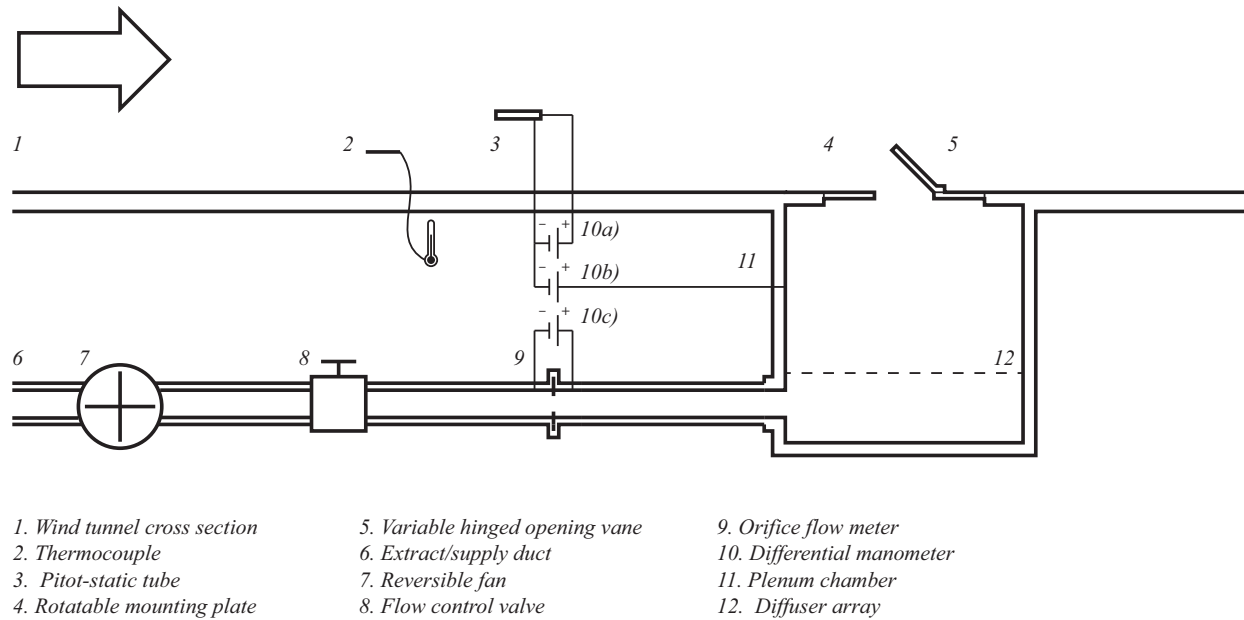


**Figure 4.10:** Diagram of the experimental setup, with the arrow denoting the direction of the airflow.

supply and extract duct; see item 10c) in Figure 4.10. The pressure drop across the orifice is used to evaluate the mass flow rate of air through the duct in accordance with BS EN ISO 5167-2 [243]. Airflow extracted from the chamber is denoted by a negative mass flow rate, and airflow supplied to the chamber is denoted by a positive mass flow rate.

#### 4.4.7 Experimental protocol

The apparatus described in Section 4.4.1 is used to perform three key experiments: still-air pressurisation tests, dynamic flow tests, and local pressure measurements. These experiments are performed sequentially for a fixed opening angle, flow approach angle and orientation of the supply and extract fan, and then repeated for different combinations of these parameters. Zero measurements used to calibrate the differential micromanometers are taken before and after each experiment. A summary of the experimental protocol is given in Figures 4.11 and 4.12.

##### Still-air pressurisation tests

Still-air pressurisation tests measure the *idealised* discharge coefficient of an opening, which is considered to be a fundamental property of that opening [25]. These represent conditions where  $P_R^* \rightarrow -\infty$  for inflow and  $P_R^* \rightarrow +\infty$  for outflow.

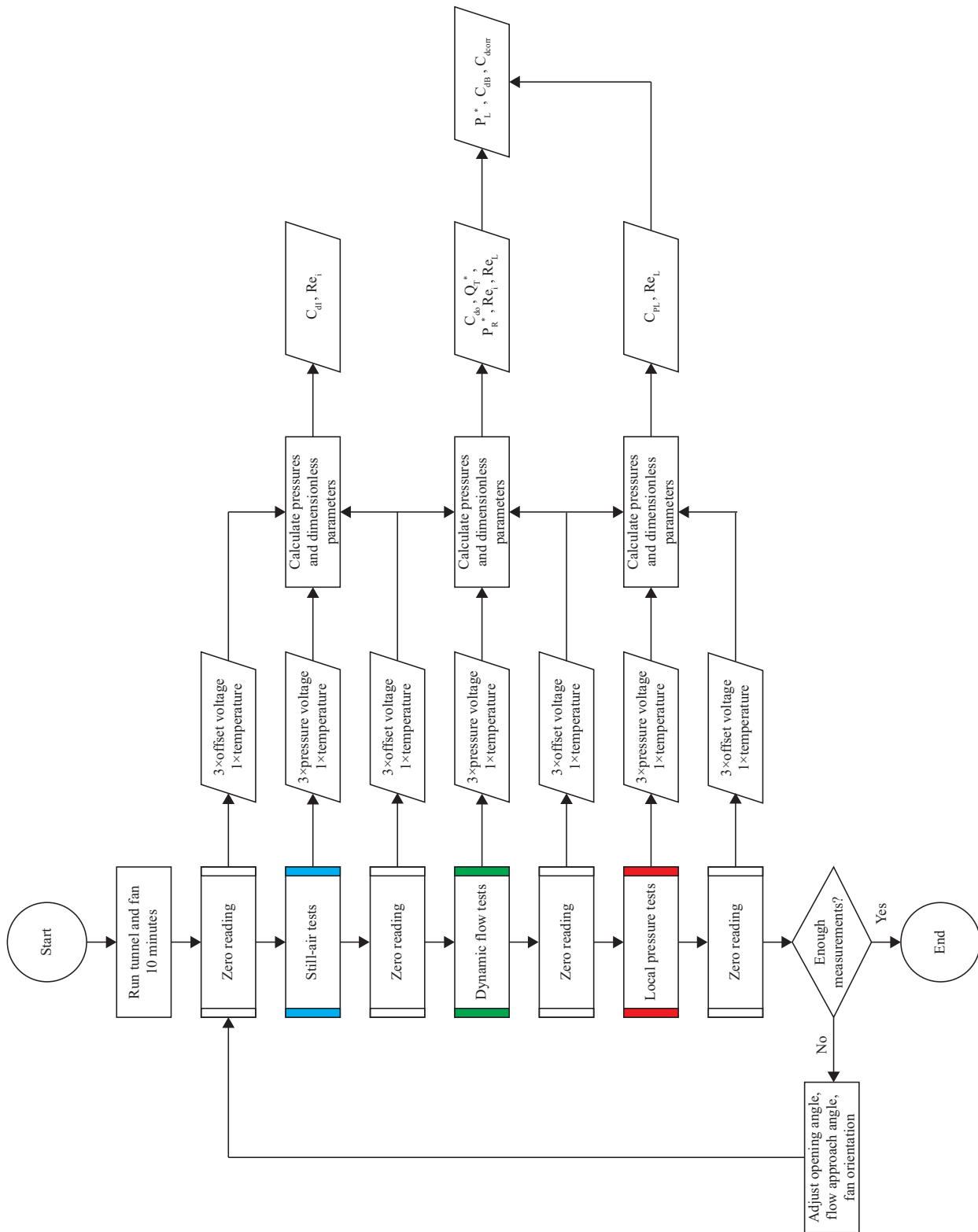


**Figure 4.11:** Flow chart describing the experimental protocol used for the window characterisation experiments. The subroutines *Zero reading*, *Still-air tests*, *Dynamic flow tests*, and *Local pressure tests* are described in Figure 4.12.

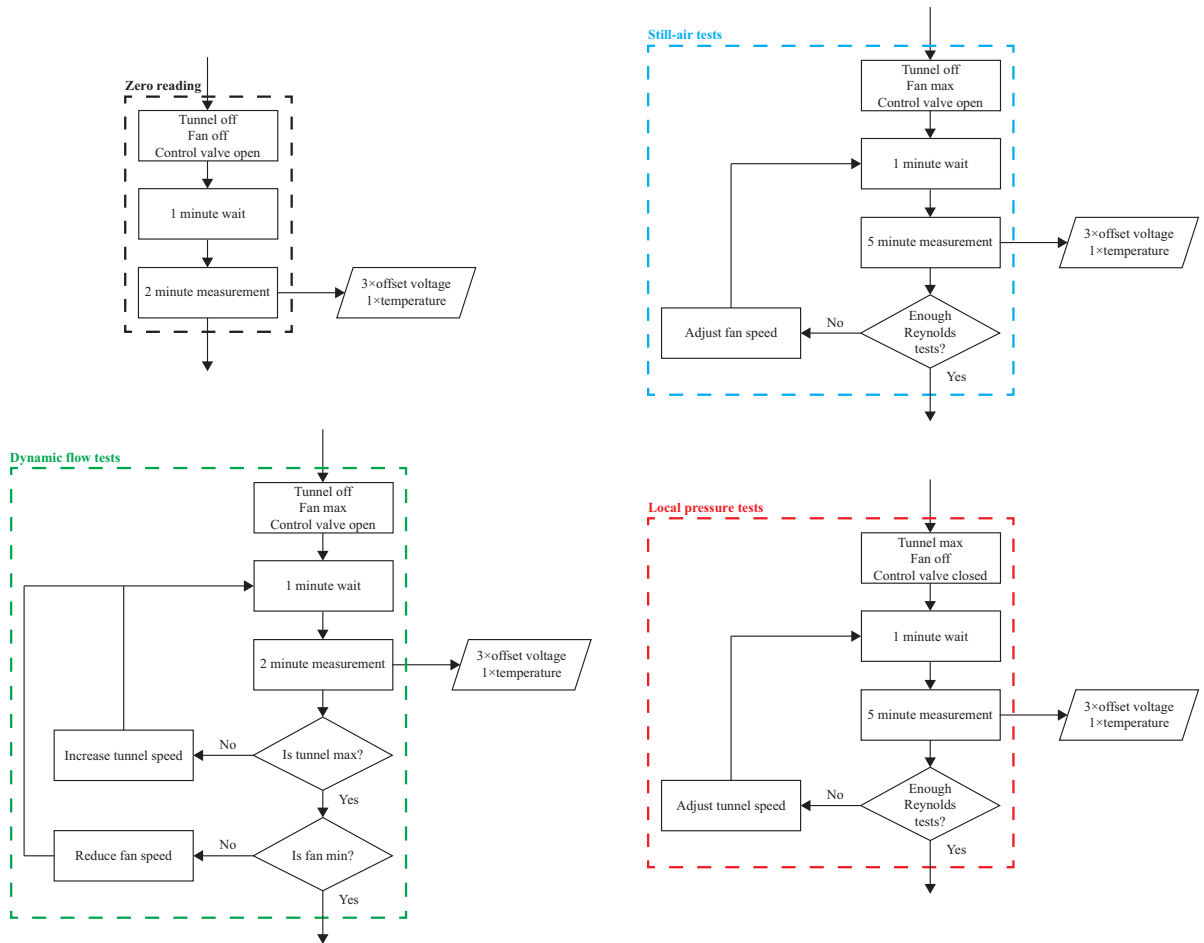


**Figure 4.12:** Flow chart describing the experimental protocol used for the window characterisation experiments.

In these tests the wind tunnel is turned off, and the extract/supply fan is used to induce a pressure difference across the opening. The speed of the fan can be varied to simulate different opening Reynolds numbers, where the opening Reynolds number is defined using a reference area and the mean flow velocity in the opening, and is given by

$$Re_i = \frac{Q}{v\sqrt{A_R}} \quad (4.4)$$

Here, the opening Reynolds number is permitted to take negative values, which allows inflow and outflow conditions to be distinguished.

### Local pressure tests

A key boundary condition that defines the local pressure is that when the local pressure acting on the external surface of an opening is equal to the internal pressure, no net flow occurs through that opening. This allows an experiment to be designed that directly measures the local pressure at the boundary condition, making no assumptions about the pressure distribution or any analytical averaging process. This is used to calculate a *local* pressure coefficient, which is taken to be a constant independent of net flow rate through the opening. Although it is likely that flow through an opening affects the local pressure field [105], a constant *local* pressure coefficient preserves the fundamental property of determining the flow direction, and provides an unambiguous and quantitative measure of the degree to which the interaction between a window and a cross-flow can enhance or inhibit ventilation driving pressures.

In these tests, the outlets to the plenum chamber are closed, and the wind tunnel is run. Sealing the chamber ensures that there is no net flow through the opening. This in turn implies that the *mean* pressure acting across the opening is zero. Equating the local pressure with the internal pressure reveals that, under sealed conditions, the difference in static pressure between the local pressure and the external flow can be directly measured, and is equivalent to the measured pressure difference between the internal and external pressures. The speed of the wind tunnel can be varied to determine the influence of the cross-flow Reynolds number on *local* pressure coefficients. The cross-flow Reynolds number is defined in terms of the free stream velocity in the wind tunnel outside the surface boundary layer, and is given by

$$Re_L = \frac{U_L\sqrt{A_R}}{v} \quad (4.5)$$

The advantage of this method of measuring the interaction between the window and the cross-flow is that the measurement process is unambiguous, and easy to apply for characterisation by window manufacturers. The experimental setup also ensures that the mean pressure that is measured is equivalent to the mean

pressure that drives net flow under a fixed set of conditions. However, this technique is unable to measure the local pressure that occurs when air is flowing through the opening. This is important for understanding the fundamental physical mechanisms behind flow behaviour, but may not be necessary for characterisation purposes.

### Dynamic flow tests

Dynamic flow tests are designed to understand how the ventilation capacity of a window opening varies in the presence of wind. Here, the wind tunnel and extract fan are run simultaneously. Varying the relative speeds of the two fans allows different dimensionless room pressures to be simulated.

Measurements focus on high-Reynolds number scenarios. Here, aerodynamic properties are expected to become constant, and it is assumed that higher Reynolds numbers are achieved on full-scale buildings than can be achieved in the wind tunnel. High-Reynolds number tests also maximise the pressure differences measured by the differential manometers, and therefore reduce the percentage errors associated with their measurement.

The experimental procedure involves running the extract/supply fan at its maximum speed, and gradually increasing the speed of wind tunnel until it reaches its maximum. Then, the speed of the extract fan is gradually reduced until it is turned off. The valve on the extract/supply duct is then gradually closed, allowing lower pressures across the opening to be investigated.

### 4.4.8 Calculation of descriptive parameters

The differential manometers described in section 4.4.6 output a voltage that is linearly related to the pressure drop across its terminals. The measured voltage across the terminals is converted into a pressure differential using the following equations:

$$\Delta P = 125 \times (V - \bar{V}_0) \quad (4.6)$$

$$\bar{V}_0 = \frac{\bar{V}_1 + \bar{V}_2}{2} \quad (4.7)$$

where  $\Delta P$  denotes the pressure differential measured by the manometer,  $V$  denotes the measured voltage across the manometer,  $\bar{V}_0$  denotes the mean voltage across the manometer measured when the pressure drop across the manometer is equal to zero, and  $\bar{V}_1$  and  $\bar{V}_2$  denote the mean zero voltages measured before and after each set of experiments.

The mass flow rate  $\dot{m}$  is a function of the pressure drop measured by the micromanometer 10c) in Figure 4.4.6, and is evaluated as described in BS EN ISO 5167-2 [243].

Arithmetic means of all input parameters are employed prior to the evaluation of the following equations:

$$P_R^* = \frac{\Delta P_b}{\Delta P_a} \quad (4.8)$$

$$C_{P_L} = \frac{\Delta P_b}{\Delta P_a} (\dot{m} = 0) \quad (4.9)$$

$$P_L^* = P_R^* - C_{P_L} \quad (4.10)$$

$$\rho = 1.225 \frac{288.15}{T} \quad (4.11)$$

$$Q = \frac{\dot{m}}{\rho} \quad (4.12)$$

$$C_{d_o} = \frac{Q}{A_R \sqrt{\frac{2}{\rho} |\Delta P_b|}} \left( \frac{\Delta P_b}{|\Delta P_b|} \right) \quad (4.13)$$

$$C_{d_o,corr} = \frac{Q}{A_R \sqrt{\frac{2}{\rho} |\Delta P_b - C_{P_L} \Delta P_a|}} \left( \frac{P_L^*}{|P_L^*|} \right) \quad (4.14)$$

$$C_{d_B} = \frac{Q}{A_R \sqrt{\frac{2}{\rho} \left( \frac{P_L^*}{|P_L^*|} \Delta P_b + \Delta P_a \right)}} \left( \frac{P_L^*}{|P_L^*|} \right) \quad (4.15)$$

$$Q_T^* = \frac{Q}{A_R \sqrt{\frac{2}{\rho} (|\Delta P_a| + |\Delta P_b|)}} \quad (4.16)$$

$$Re_i = \frac{Q}{v \sqrt{A_R}} \quad (4.17)$$

$$Re_L = \frac{\sqrt{A_R \frac{2}{\rho} \Delta P_a}}{v} \quad (4.18)$$

Where  $\Delta P_a$  and  $\Delta P_b$  denote the pressure differences measured by manometers 10a) and 10b) on Figure 4.10 respectively;  $T$  is the temperature in Kelvin measured by thermocouple 2 in Figure 4.10;  $A_R$  is a reference area for the opening, here equal to  $0.04m^2$ ; and  $v$  is the kinematic viscosity of air, here taken to be equal to  $1.47 \times 10^{-5}m^2s^{-1}$ . The expression for density assumes that the dominant source of density variation in the air is temperature, and does not account for variation in atmospheric pressure or moisture content. Similarly, the kinematic viscosity of air is assumed to be a constant independent of temperature variation and moisture content.



### 4.4.9 Error analysis

For the purposes of this analysis, the statistical parameter of greatest concern is the uncertainty in the mean. This is evaluated using the standard error in the mean, which applies the central limit theorem to express the confidence in mean values using a normal distribution [258].

The error in the mean values of the voltage and temperature measurements output by the micromanometers and thermocouple respectively are evaluated by analysis of the distribution of measured data, where

$$\sigma_M = \sqrt{\frac{\sum (X - \bar{X})^2}{N^2 - N}} \quad (4.19)$$

where  $\sigma_M$  is the standard error in the mean,  $X$  and  $\bar{X}$  are instantaneous and mean values of a parameter respectively, and  $N$  is the total number of measurements.

The kinematic viscosity of air and the atmospheric pressure are not measured in the experiment. Where they appear in calculations, values of  $1.47 \times 10^{-5} \text{ m}^2\text{s}^{-1}$  and  $101325 \text{ Pa}$  are used respectively. Standard errors equal to  $0.05 \times 10^{-5} \text{ m}^2\text{s}^{-1}$  and  $500 \text{ Pa}$  are assumed to account for variations that may reasonably be expected over the course of experimental measurements.

Uncertainty in the measured variables are propagated through Equations 4.7–4.18 using the calculus approximation to determine the uncertainty in any calculated parameters [258]. This assumes that the uncertainty in measured data is small compared to the magnitude of the mean. Uncertainty in mass flow rate also comes from the use of the orifice flow meter. In this case, uncertainty is calculated according BS EN ISO 5167-2 [243]. and added arithmetically to the uncertainty calculated by error propagation of measured parameters.

An important component of the error in evaluated pressure measurements is the error in the zero measurements used to calibrate the micromanometers. The zero measurements cannot be collected simultaneously with pressure data. Therefore, zero drift coupled with the temporal lag between calibration and measurement may cause systematic errors in reported differential pressures.

Figure 4.13 plots the difference in zero measurements taken before and after each round of experiments. This is used as a proxy for the variation in the zero offset that might be expected to occur during measurement. A portion of this error is associated with the temperature drift that occurs over the course of the experiments. This is particularly true for sensor 10b) in Figure 4.10, which shows a strong correlation between temperature drift and zero drift; see Figure 4.13. However, this correlation between temperature drift and zero drift is weak when the temperature increases over the measurement period. Due to the experimental protocol of increasing the tunnel speed over the course of dynamic flow tests, the majority of data points are collected in the range where temperature correlation is weak. Furthermore, the relationship between zero

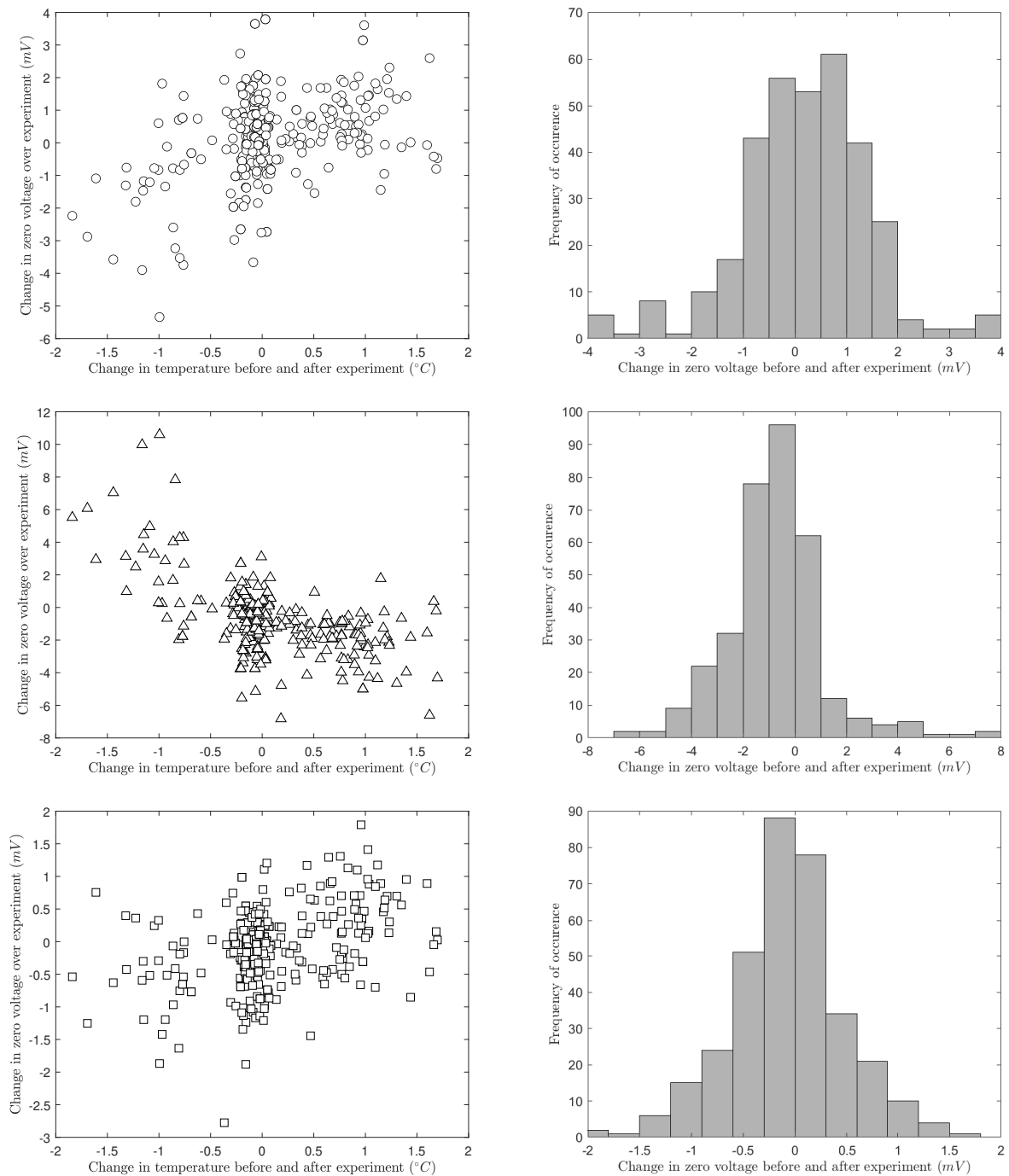


**Figure 4.13:** Difference in mean calibration voltage measured before and after each run of experiments, plotted against the difference in mean tunnel temperature measured before and after each run of experiments (left), and their frequency distribution (right). Mean voltage measurements from Manometer 10a), 10b), and 10c) in Figure 4.10 are shown top, middle, and bottom respectively.

drift and temperature drift is weak for both of the other sensors. Therefore, the zero drift is treated as a random variable. The standard deviation of the drift in zero voltage over each round of experiments is used to specify the standard error in the zero voltage used to evaluate the pressure measured by the transducers. The standard error in the zero voltage is evaluated as  $1.3\text{ mV}$ ,  $2.1\text{ mV}$  and  $0.57\text{ mV}$  for micromanometers 10a), 10b), and 10c) in Figure 4.10 respectively.

### Repeat measurements

Flow configurations that are symmetrically equivalent are aggregated as repeat measurements. Here the aerodynamic properties of a hinged opening measured in a cross-flow are symmetrical about a flow approach angle 0 degrees. The equivalence relation can be given

$$X(\beta) \equiv X(-\beta) \quad (4.20)$$

where  $X$  denotes a measured aerodynamic property, and  $\beta$  denotes the flow approach angle relative to the principal axis; see Figure 4.8. For still-air tests, there is no simulated cross-flow and consequently no flow approach angle. Therefore, all orientations of the window in still-air tests are aggregated as repeat measurements.

## 4.5 Velocity profile measurements

Many of the experiments presented in this thesis require the velocity profile in the wind tunnel to be measured. This is required to understand the importance of velocity variation with height and width on measured phenomena, and to ensure that other researchers can repeat experimental measurements.

### 4.5.1 Experimental setup

A hot wire anemometer is mounted on a traverse within the wind tunnel; see Figure 4.14. This enables the velocity in the wind tunnel to be measured at a range of points in a plane perpendicular to the wind flow, at the same distance upstream from the experimental model as the pitot-static tube. Velocity profile measurements in the vertical plane are measured in the horizontal centre of the wind tunnel, and velocity profile measurements in the horizontal plane are measured at the height of the pitot-static tube. These tests are repeated at the centre of the model with the model removed from the tunnel, to ensure that the measured flow velocity at the location of the pitot-static tube are representative of those at the location of the model.

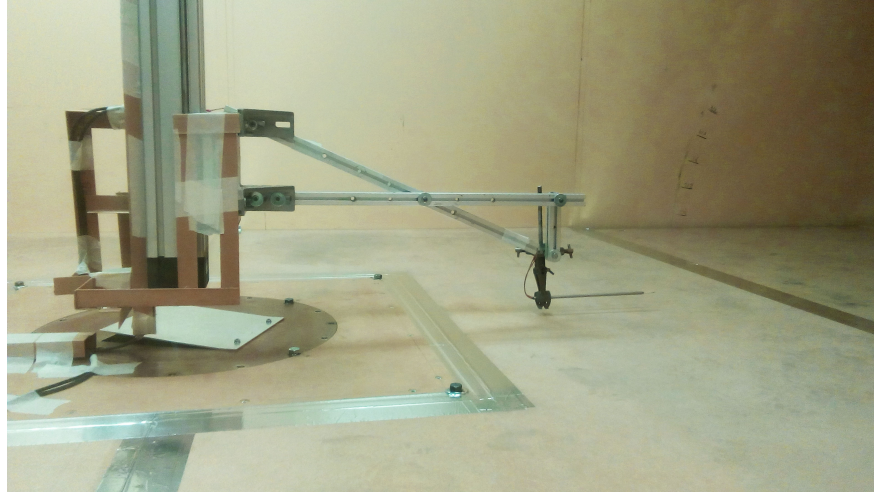


**Figure 4.14:** Hot wire anemometer used to measure the velocity profile in the wind tunnel.

### 4.5.2 Hot wire anemometer

The hot wire anemometer works by passing a voltage through a thin wire, which causes it to heat up. When air flows over the wire, it causes it to cool down, which changes its electrical resistance. The voltage drop across the wire can therefore be correlated to the velocity of the flow across it. In accordance with the operating manual, a corrected voltage is used to account for the effect of air temperature on the voltage measurements, given by

$$V_c = V \sqrt{\frac{T_w - T_c}{T_w - T}} \quad (4.21)$$

where  $V_c$  and  $V$  are the corrected and measured voltage drop across the hot wire respectively;  $T_w$  is the wire temperature, taken to be  $250^\circ\text{C}$ ;  $T_c$  is a calibration temperature, taken to be  $20^\circ\text{C}$ ; and  $T$  is the air temperature.

### 4.5.3 Calibration procedure

The hot-wire used in the tunnel is calibrated using a TSI calibrator prior to measurement. Here, pressurised air is supplied to a chamber with a calibration nozzle, which creates a jet of air that passes over the hot wire. A range of flow velocities are simulated by adjusting valves in the pressurised air supply line, which alters the pressure drop across the calibration nozzle. A Furness FC510 micromanometer is used to measure the static pressure difference between the calibration chamber and atmospheric pressure, which is equivalent to the dynamic pressure in the jet. A thermocouple is used to measure the air temperature inside the calibration chamber. The calibrated flow velocity is then plotted against the corrected voltage measured by the hot wire

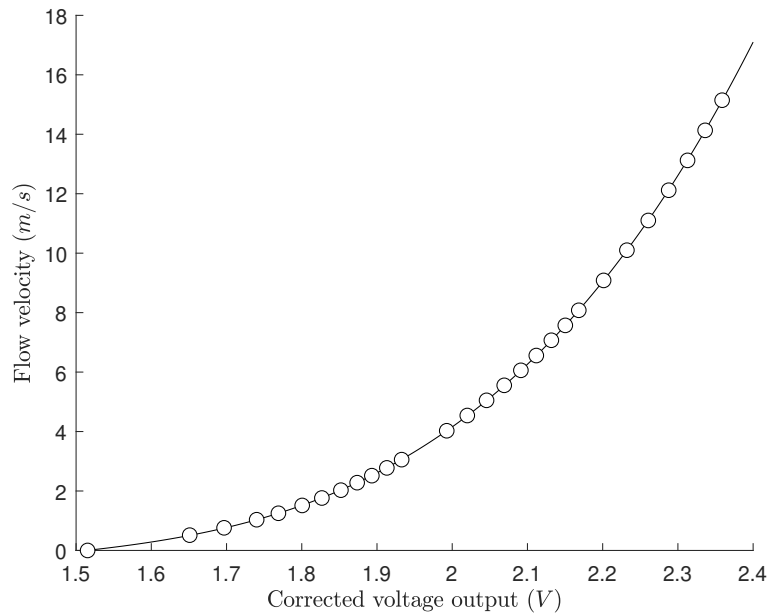


**Figure 4.15:** Calibration curve for the hot wire anemometer used in the wind tunnel, with a fourth order polynomial fit.

anemometer, and a fourth order polynomial is fit to the data; see Figure 4.15.

## 4.6 Cross-flow probe

Chapter 5 develops empirical models to predict airflow through windows according to the methods described in Sections 4.3 and 4.4. These empirical models require both the speed and direction of the cross-flow as key inputs, in addition to the surface pressure coefficients that are required for conventional envelope flow models. To this end, this thesis develops cross-flow probe that can simultaneously measure the speed and direction of the cross-flow on the façade of a model building.

### 4.6.1 Operating principle

The probe is conceived as a sharp-edged rectangular obstruction projecting into the cross-flow. The principle behind this probe is to describe the surface pressure coefficients of the probe as a unique function of *façade* cross-flow direction. This function can be solved for the *façade* cross-flow direction when the surface pressures of the probe are known.

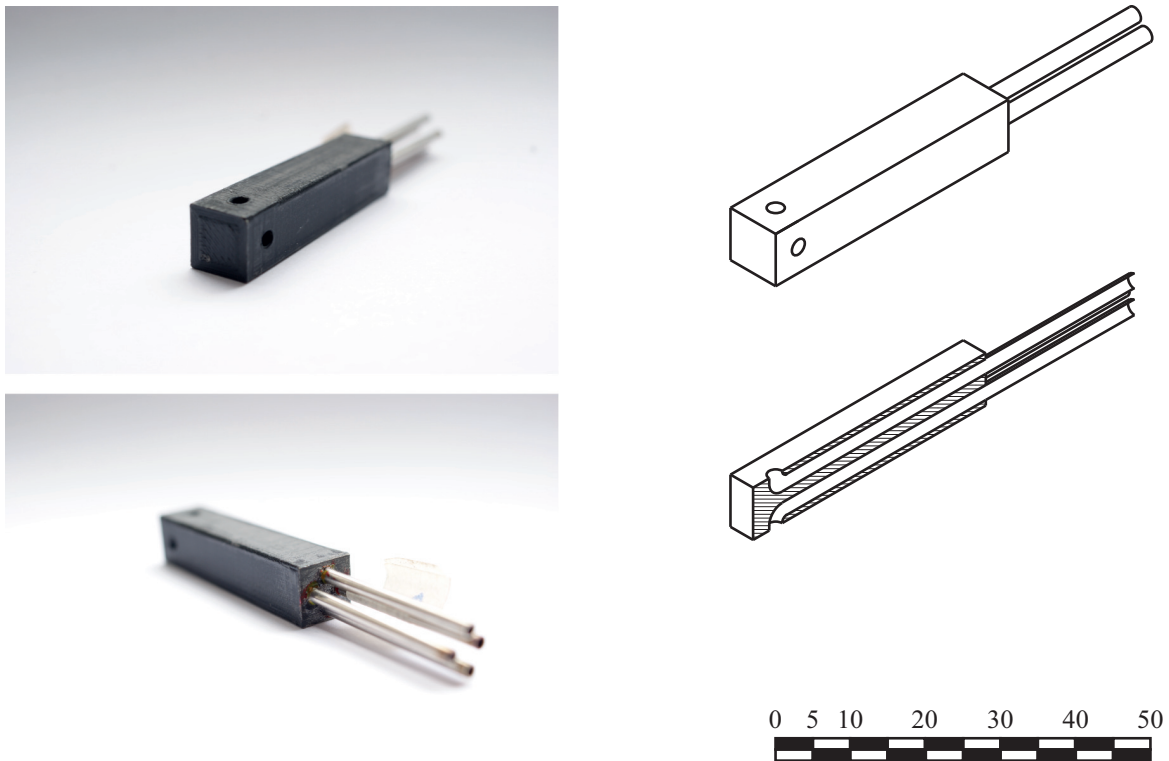


**Figure 4.16:** Photographs (left), isometric drawing (top right), and isometric section (bottom right) of the cross-flow probe. Dimensions on the isometric scale are given in millimeters.

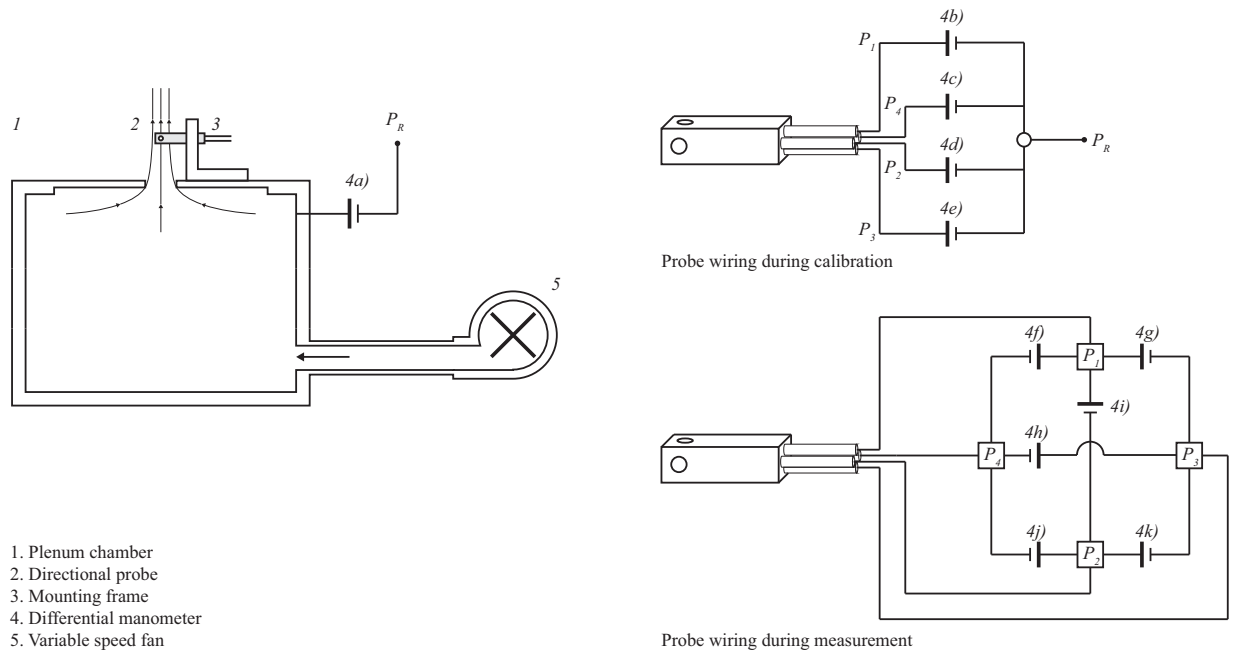


**Figure 4.17:** Diagram of the experimental setup used to calibrate and test the cross-flow probe. A diagram illustrating the apparatus used to create the calibration jet is shown on the left. The wiring of the probe used during calibration is depicted on the top right, and the wiring of the probe used during measurement is depicted on the bottom right.

## 4.6.2 Experimental setup

The cross-flow probe comprises a 36mm long 3D-printed plastic prism with a 7mm square cross section; see Figure 4.16. 2mm diameter holes in each of the four faces form pressure tappings in the surface. These pressure tappings are located 3.5mm from the top and 3.5 mm from either edge of the probe. The four tapping holes are each connected to a shaft running the length of the probe. 2mm diameter steel tubes are mounted in each shaft, to which manometric tubing can be connected.

To calibrate the probe, it must be mounted within an air jet of known speed and direction. The jet is created using a circular orifice mounted on the surface of a plenum chamber, to which air is supplied with a variable speed fan; see figure 4.17. The plenum chamber and fan are identical to that described in Section 4.4.3. The orifice is comprised of a 2mm thick perspex sheet with a 30mm diameter circular hole cut in the centre.

When air is supplied to the chamber, the internal volume of the plenum is pressurised. This pressure differential induces airflow through the orifice, resulting in the formation of a jet perpendicular to the plane of the orifice. Assuming that air velocity in the plenum chamber and loss in total pressure in the formation of the jet can both be neglected, the dynamic pressure of the jet in the *vena contracta* should be equivalent to

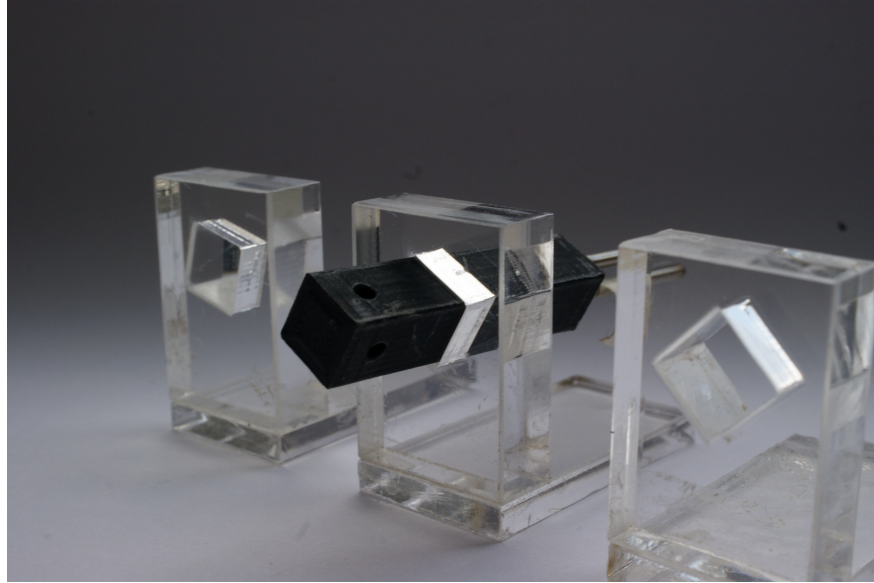


**Figure 4.18:** Image of the cross-flow probe and the mounting frame used to investigate different flow approach angles.

the static pressure differential between the plenum interior and the plenum exterior. This pressure differential is measured using a SensorTechnics HCLA 02X5-B differential micromanometer, labelled  $4_a$ ) in Figure 4.17.

The probe is mounted in the calibration jet using a mounting frame. The mounting frame consists of a perspex bracket that can be mounted on the surface of the orifice plate, with a square hole cut into the vertical component of the bracket within which the probe can be mounted; see Figure 4.18. This mounting frame ensures that the probe is located at a consistent height within the jet, and that the probe sits perpendicular to the jet. The probe is mounted at a height of 22mm above the surface of the orifice plate, which is far enough from the orifice to be beyond the *vena contracta*, but not too far that the total pressure in the jet would appreciably decay.

To simulate different *façade* cross-flow directions, the probe is rotated within the jet. This is achieved through the use of a range of mounting frames, where the square hole within which the probe is mounted is rotated in 15 degree increments. This ensures that the angle between the probe and the jet can be precisely and consistently varied through 360 degrees.

#### **Characterisation of the surface pressure coefficients of the probe**

To calibrate the cross-flow probe, it is necessary to characterise the surface pressure coefficients on each of the four faces of the probe that are perpendicular to the plane of the cross-flow as a function of the *façade* cross-flow direction. Here the pressure difference between the surface pressure tapping on the probe and a reference pressure outside the plenum chamber is measured using a SensorTechnics HCLA 02X5-B



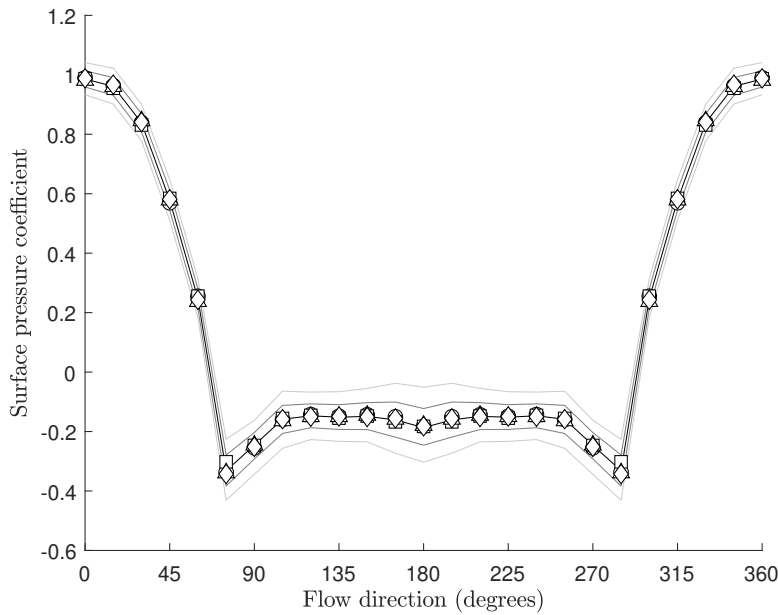


**Figure 4.19:** Plot of the surface pressure coefficients for the probe, collapsed onto the  $C_{P1}$  curve using Equations 4.22–4.24. Mean pressure coefficients for tappings 1,2,3 and 4 are given by circle, square, triangle and diamond markers respectively. The median; 25th and 75th centiles; and 9th and 91st centiles are denoted by black, dark grey and light grey lines respectively, and are shown for clarity as the mean of centiles from all four tappings. Standard errors are smaller than the markers, and have been omitted.

differential micromanometer. These are connected in the configuration shown in the top right of Figure 4.17, where the positive pressure port is connected to the surface pressure tapping on the probe, and the negative pressure port is connected to the external reference pressure via a common distribution box.

If the probe is perfectly symmetrical, the pressure coefficients for each surface can be related to each other as follows:

$$C_{P2}(\alpha) \equiv C_{P1}(\alpha - 90) \quad (4.22)$$

$$C_{P3}(\alpha) \equiv C_{P1}(\alpha - 180) \quad (4.23)$$

$$C_{P4}(\alpha) \equiv C_{P1}(\alpha - 270) \quad (4.24)$$

where  $C_{P1}(\alpha)$  is symmetric about zero and 180 degrees, and periodic in 360 degrees.

Once the surface pressure coefficients have been measured, a curve is fit to describe the relationship between the surface pressure coefficient and the *façade* cross-flow direction. This is fit in the form of a Fourier series consistent with Section 4.3.1, which is periodic in 360 degrees and symmetric about an axis normal to the surface pressure tapping; see Appendix E.

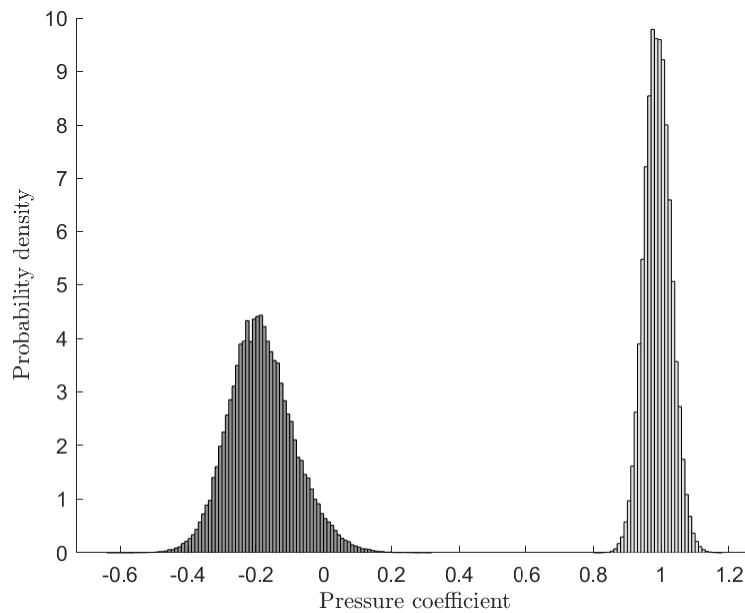
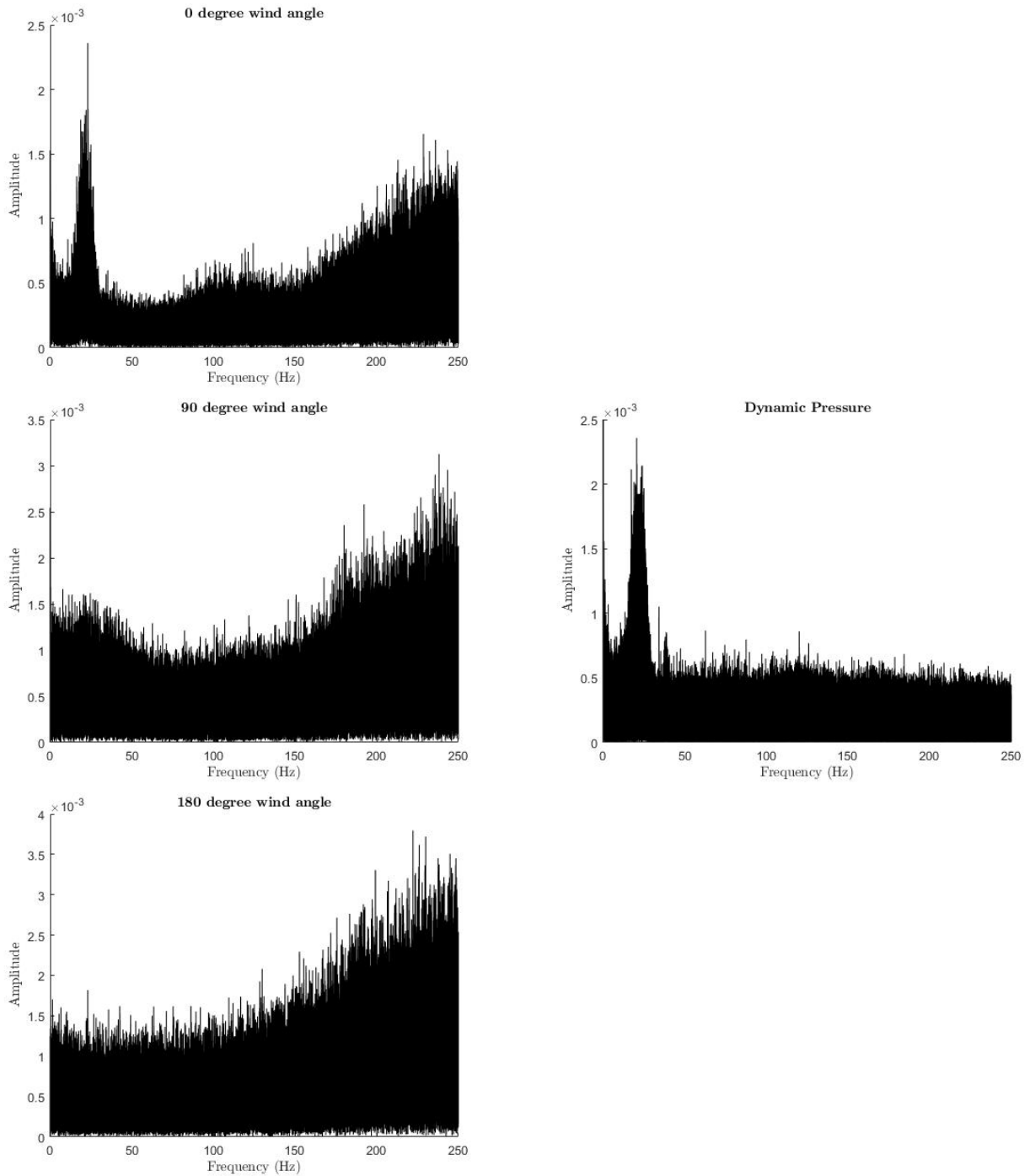


**Figure 4.20:** Probability density function of the pressure coefficient on the surface of the cross-flow probe. A *façade* cross-flow direction of 0 degrees is depicted in light grey (right), and a *façade* cross-flow direction of 180 degrees is depicted in dark grey (left).

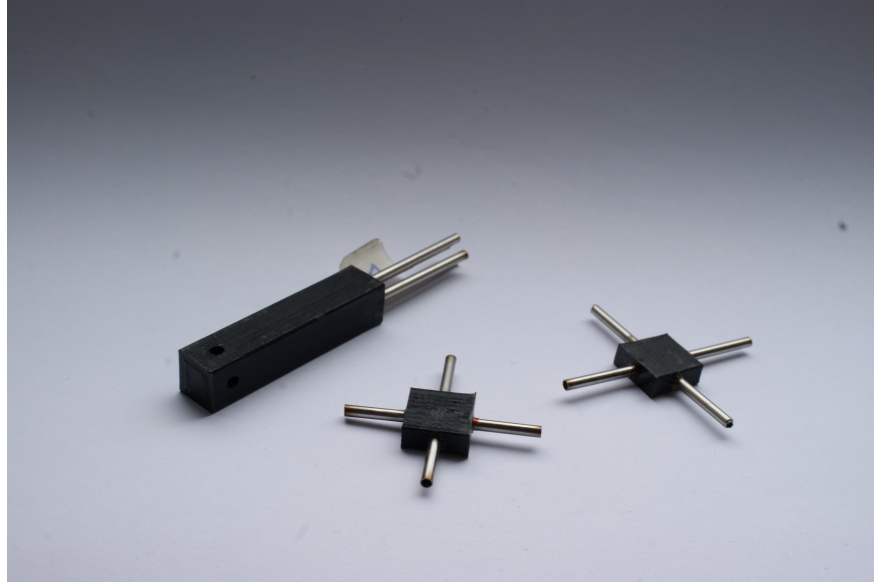
Figure 4.19 plots the measured surface pressure coefficients of the probe as a function of *façade* cross-flow direction. All four curves are shifted using Equations 4.22 to 4.24 to map onto the surface pressure coefficient of pressure tapping 1. After phase-shifting, the mean pressure coefficient values are close to identical for all four surfaces. This enables a single equation to be used to describe the surface pressure coefficients of the probe. The surface pressure coefficients on the probe reach a maximum close to 1. The surface pressure coefficients are relatively uniform in the lee of the probe.

Figure 4.20 depicts the probability distribution of surface pressure coefficients at *façade* cross-flow directions of 0 and 180 degrees. The surface pressure coefficients in the lee of the probe show a significantly greater spread than those on upstream surfaces.

Figure 4.21 plots the frequency decompositions of the probe surface pressure coefficients and the frequency decomposition of the directly measured dynamic pressure. The dynamic pressure measurements exhibit a peak frequency around 20 Hz, while the rest of the distribution is fairly uniform. The peak at 20 Hz measured in the dynamic pressure is transferred to the surface pressure coefficients at a *façade* cross-flow direction of zero degrees. The amplitude of oscillations is also increased at high frequencies. At the 90 and 180 degree *façade* cross-flow directions, the 20 Hz peak is no longer visible. The amplitude of all oscillations are increased for these angles.



**Figure 4.21:** Frequency decompositions of the probe surface pressure coefficients exposed to a *façade* cross-flow direction of 0, 90 and 180 degrees (top, middle, and bottom left), compared against the frequency decomposition of the dynamic pressure (right)



**Figure 4.22:** Image of the cross-flow probe and the splitters used to distribute the pressure from each pressure tapping.

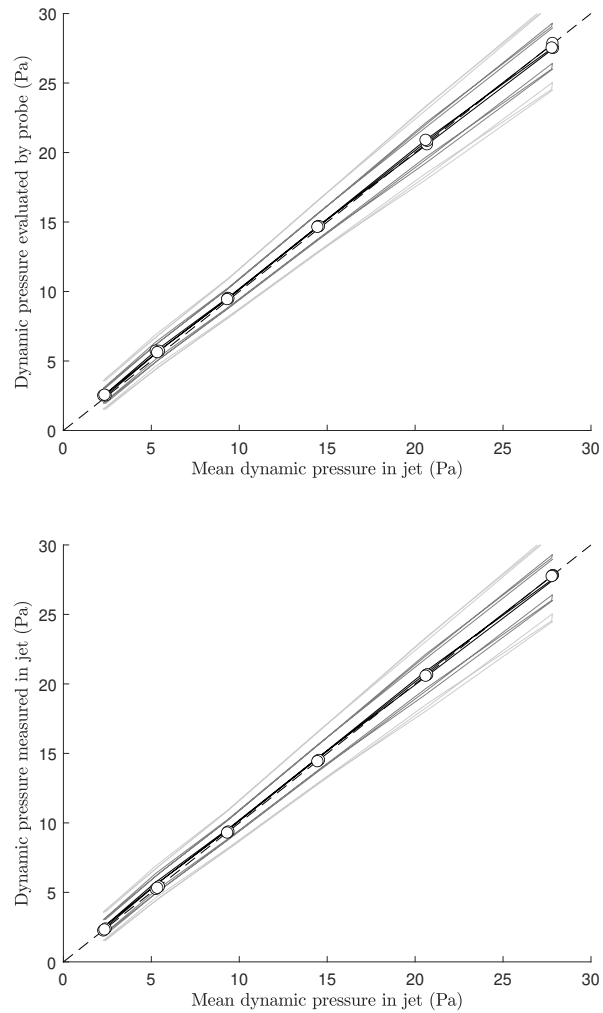
### Validation of probe output measurements

After calibration, the degree to which the cross-flow probe can measure the speed and direction of a notional cross-flow can be assessed. The probe is configured according to the bottom right of Figure 4.17, and mounted at 45 degrees to the calibration jet. The fan speed is varied to enable the dependence of measurement accuracy on dynamic pressure in the jet - and therefore Reynolds number - to be investigated.

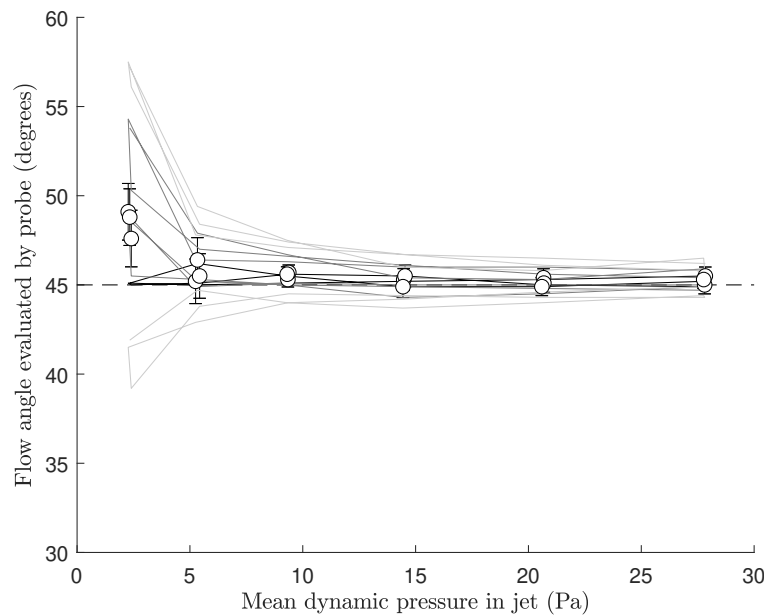
During operation, the probe measures the difference in pressure between different tappings on the probe surface; see Figure 4.17. This removes the need to specify a suitable reference pressure, which can be subject to ambiguity. The four surfaces yield six unique combinations of pressure differences that can be measured using differential manometers. This is achieved through the use of splitter boxes, which allow the output pressure from each pressure tapping to be connected to three different micro-manometers; see Figures 4.17 and 4.22.

Figure 4.23 compares the distributions in dynamic pressure measured by the cross-flow probe against those directly measured in the jet when the probe is mounted at a *façade* cross-flow direction of 45 degrees. The two distributions are not measurably different across the full range of dynamic pressures achieved in this test.

Figure 4.24 shows the distribution of predicted *façade* cross-flow directions for a range dynamic pressures in the jet when the probe is mounted at a *façade* cross-flow direction of 45 degrees. The precision of the probe is reasonable for dynamic pressures as low as 5 Pa, with a standard deviation in measured *façade* cross-flow direction of approximately 2 degrees. The precision improves at higher flow speeds, where standard



**Figure 4.23:** Range of dynamic pressures evaluated by the probe (top) compared against the range of dynamic pressures measured in the jet (bottom), plotted against the mean measured dynamic pressure in the jet. Mean values are denoted by circles. The 50th centile, 25th and 75th centiles, and 9th and 91st centiles are denoted by black, dark grey, and light grey lines respectively. Standard errors are smaller than the markers, and have been omitted.



**Figure 4.24:** Range of *façade* cross-flow directions evaluated by the probe against the mean measured dynamic pressure in the jet when the probe is mounted at a *façade* cross-flow direction of 45 degrees. Mean values are denoted by circles. The 50th centile, 25th and 75th centiles, and 9th and 91st centiles are denoted by black, dark grey, and light grey lines respectively. Error bars are shown to two standard errors.

deviations as low as 0.5 degrees are achieved. Figure 4.25 shows the frequency decomposition of the dynamic pressure and *façade* cross-flow direction evaluated by the probe. No clear peaks are visible for either metric.

### 4.6.3 Calculation of descriptive parameters

Descriptive parameters are evaluated from the output of the differential micro-manometers depicted in Figure 4.17. Techniques for evaluating the measured pressure from the voltage output of the micro-manometers are given in Section 4.4.8.

When calibrating the probe, the pressure in the jet and the surface pressure coefficients of the probe are evaluated as follows:

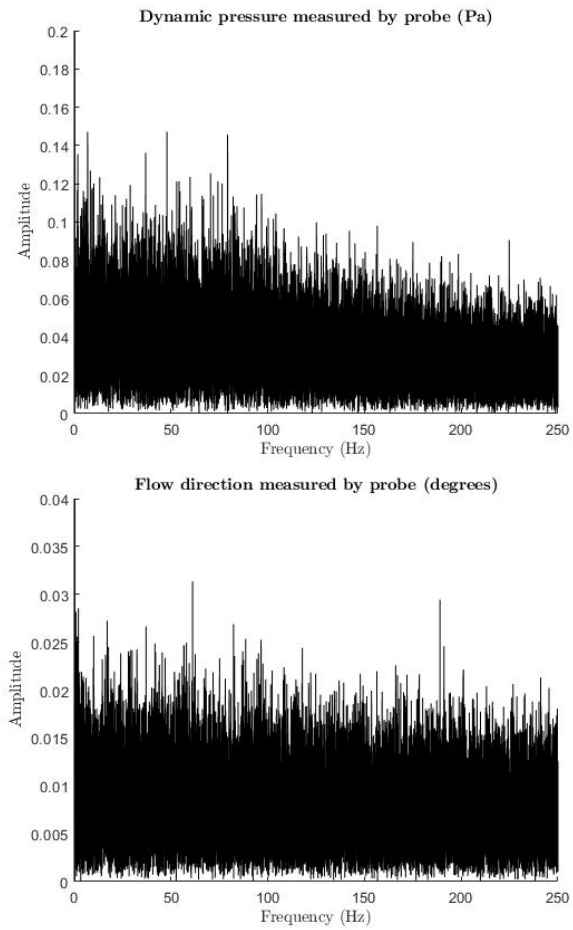


**Figure 4.25:** Frequency decomposition of dynamic pressure evaluated by the probe (top) and the *façade* cross-flow direction evaluated by the probe (bottom).

$$P_{d(jet)} = \Delta P_a \quad (4.25)$$

$$C_{P_1} = \frac{\Delta P_b}{\Delta P_a} \quad (4.26)$$

$$C_{P_2} = \frac{\Delta P_d}{\Delta P_a} \quad (4.27)$$

$$C_{P_3} = \frac{\Delta P_e}{\Delta P_a} \quad (4.28)$$

$$C_{P_4} = \frac{\Delta P_c}{\Delta P_a} \quad (4.29)$$

where  $P_{d(jet)}$  is the instantaneous dynamic pressure measured in the calibration jet;  $\Delta P_{a-e}$  are the pressure differentials measured by manometers  $4_{a-e}$  in Figure 4.17;  $C_{P_{1-4}}$  are the instantaneous surface pressure coefficients for each of the four faces of the cross-flow probe; and  $\overline{\Delta P_a}$  is the arithmetic mean of the pressure differential measured by manometer  $4_a$  in Figure 4.17 over the course of the sample reading.

#### 4.6.4 Evaluation of probe outputs

During operation, the crossflow probe measures six unique pressure differences using micro-manometers  $4_{f-k}$  in Figure 4.17. The output of these micro-manometers can be expressed as a function of the calibrated surface pressure coefficients:

$$\Delta P_f(\alpha) \equiv P_d (C_{P_1}(\alpha) - C_{P_4}(\alpha)) \quad (4.30)$$

$$\Delta P_g(\alpha) \equiv P_d (C_{P_1}(\alpha) - C_{P_3}(\alpha)) \quad (4.31)$$

$$\Delta P_h(\alpha) \equiv P_d (C_{P_3}(\alpha) - C_{P_4}(\alpha)) \quad (4.32)$$

$$\Delta P_i(\alpha) \equiv P_d (C_{P_1}(\alpha) - C_{P_2}(\alpha)) \quad (4.33)$$

$$\Delta P_j(\alpha) \equiv P_d (C_{P_2}(\alpha) - C_{P_4}(\alpha)) \quad (4.34)$$

$$\Delta P_k(\alpha) \equiv P_d (C_{P_2}(\alpha) - C_{P_3}(\alpha)) \quad (4.35)$$

where  $\Delta P_{f-k}(\alpha)$  are the instantaneous pressure differentials measured by micro-manometers  $4_{f-k}$  in Figure 4.17 at the unknown *façade* cross-flow direction  $\alpha$ ,  $P_d$  is the unknown dynamic pressure in the cross-flow, and  $C_{P_{1-4}}(\alpha)$  are the value of the surface pressure coefficients of the cross-flow probe at the unknown *façade* cross-flow direction  $\alpha$ , determined by calibration.

These measured pressure differences are used to evaluate fifteen unique pressure difference ratios. This



allows the unknown dynamic pressure to be eliminated.

$$\Delta P_{f/g}(\alpha) = \frac{\Delta P_f(\alpha)}{\Delta P_g(\alpha)} \equiv \frac{C_{P1}(\alpha) - C_{P4}(\alpha)}{C_{P1}(\alpha) - C_{P3}(\alpha)} \quad (4.36)$$

$$\Delta P_{f/h}(\alpha) = \frac{\Delta P_f(\alpha)}{\Delta P_h(\alpha)} \equiv \frac{C_{P1}(\alpha) - C_{P4}(\alpha)}{C_{P3}(\alpha) - C_{P4}(\alpha)} \quad (4.37)$$

$$\Delta P_{f/i}(\alpha) = \frac{\Delta P_f(\alpha)}{\Delta P_i(\alpha)} \equiv \frac{C_{P1}(\alpha) - C_{P4}(\alpha)}{C_{P1}(\alpha) - C_{P2}(\alpha)} \quad (4.38)$$

$$\Delta P_{f/j}(\alpha) = \frac{\Delta P_f(\alpha)}{\Delta P_j(\alpha)} \equiv \frac{C_{P1}(\alpha) - C_{P4}(\alpha)}{C_{P2}(\alpha) - C_{P4}(\alpha)} \quad (4.39)$$

$$\Delta P_{f/k}(\alpha) = \frac{\Delta P_f(\alpha)}{\Delta P_k(\alpha)} \equiv \frac{C_{P1}(\alpha) - C_{P4}(\alpha)}{C_{P2}(\alpha) - C_{P3}(\alpha)} \quad (4.40)$$

$$\Delta P_{g/h}(\alpha) = \frac{\Delta P_g(\alpha)}{\Delta P_h(\alpha)} \equiv \frac{C_{P1}(\alpha) - C_{P3}(\alpha)}{C_{P3}(\alpha) - C_{P4}(\alpha)} \quad (4.41)$$

$$\Delta P_{g/i}(\alpha) = \frac{\Delta P_g(\alpha)}{\Delta P_i(\alpha)} \equiv \frac{C_{P1}(\alpha) - C_{P3}(\alpha)}{C_{P1}(\alpha) - C_{P2}(\alpha)} \quad (4.42)$$

$$\Delta P_{g/j}(\alpha) = \frac{\Delta P_g(\alpha)}{\Delta P_j(\alpha)} \equiv \frac{C_{P1}(\alpha) - C_{P3}(\alpha)}{C_{P2}(\alpha) - C_{P4}(\alpha)} \quad (4.43)$$

$$\Delta P_{g/k}(\alpha) = \frac{\Delta P_g(\alpha)}{\Delta P_k(\alpha)} \equiv \frac{C_{P1}(\alpha) - C_{P3}(\alpha)}{C_{P2}(\alpha) - C_{P3}(\alpha)} \quad (4.44)$$

$$\Delta P_{h/i}(\alpha) = \frac{\Delta P_h(\alpha)}{\Delta P_i(\alpha)} \equiv \frac{C_{P3}(\alpha) - C_{P4}(\alpha)}{C_{P1}(\alpha) - C_{P2}(\alpha)} \quad (4.45)$$

$$\Delta P_{h/j}(\alpha) = \frac{\Delta P_h(\alpha)}{\Delta P_j(\alpha)} \equiv \frac{C_{P3}(\alpha) - C_{P4}(\alpha)}{C_{P2}(\alpha) - C_{P4}(\alpha)} \quad (4.46)$$

$$\Delta P_{h/k}(\alpha) = \frac{\Delta P_h(\alpha)}{\Delta P_k(\alpha)} \equiv \frac{C_{P3}(\alpha) - C_{P4}(\alpha)}{C_{P2}(\alpha) - C_{P3}(\alpha)} \quad (4.47)$$

$$\Delta P_{i/j}(\alpha) = \frac{\Delta P_i(\alpha)}{\Delta P_j(\alpha)} \equiv \frac{C_{P1}(\alpha) - C_{P2}(\alpha)}{C_{P2}(\alpha) - C_{P4}(\alpha)} \quad (4.48)$$

$$\Delta P_{i/k}(\alpha) = \frac{\Delta P_i(\alpha)}{\Delta P_k(\alpha)} \equiv \frac{C_{P1}(\alpha) - C_{P2}(\alpha)}{C_{P2}(\alpha) - C_{P3}(\alpha)} \quad (4.49)$$

$$\Delta P_{j/k}(\alpha) = \frac{\Delta P_j(\alpha)}{\Delta P_k(\alpha)} \equiv \frac{C_{P2}(\alpha) - C_{P4}(\alpha)}{C_{P2}(\alpha) - C_{P3}(\alpha)} \quad (4.50)$$

For a given set of instantaneous pressure measurements, a value of  $\alpha$  is found that minimises the sum of square residuals for the equivalence relations described by Equations 4.36 to 4.50. Where the pressure difference ratio is greater than one, the inverse equivalence relation is applied. This ensures that high magnitude residuals caused by a small denominator do not unduly affect the results of the minimisation. When the denominator and the numerator are both close to zero, small measurement errors can lead to large variations in the magnitude of the ratio. To reduce the impact of these errors on the result of the minimisation, residuals are weighted by the sum of the numerator and the denominator.

Once the *façade* cross-flow direction  $\alpha$  has been evaluated, Equations 4.30 to 4.35 can be re-arranged to

evaluate the coincident dynamic pressure in the cross-flow  $P_d$ . To minimise error, the pressure difference coefficient with the greatest magnitude at the measured flow approach angle is used to evaluate the dynamic pressure. Any wind angles that evaluate a negative dynamic pressure are given a weighting of zero in the least-squares minimisation.

A MATLAB script is written to find the best-fit *façade* cross-flow direction and cross-flow dynamic pressure for all instantaneous data points within a sample reading; see Appendix E.

## 4.7 Model building experiments - measurement of model inputs

To validate the characterisation experiments detailed in Section 4.4, it must be shown that the characterisation curves developed can be integrated into envelope flow models to improve ventilation rate predictions in a model building. To this end, a wind tunnel study on a model building is performed to measure the key input parameters required to predict ventilation rate: the surface pressure coefficients, and the speed and direction of the cross-flow at the location of each opening.

### 4.7.1 Experimental setup

The experimental setup consists of the open loop wind tunnel described in Section 4.4.1, with a model building in the form of a 200mm cube mounted on a turntable. The turntable can be rotated to simulate a range of different wind angles, which results in a maximum blockage ratio of 1.2%. The flow is preconditioned using spire-type turbulence structures in combination with the roughness elements described in Figure 4.5. The turbulence structures comprise a 250mm tall barrier across the width of the tunnel at its entrance, immediately followed by an array of five triangular spires, each measuring 1200mm in height and 200mm in width; see Figure 4.26. These create a turbulence structure and velocity profile that is *representative* of the types of flow that a building might encounter. A reference dynamic pressure in the atmospheric flow is measured using a pitot-static tube mounted 200mm above the surface of the wind tunnel, level with the building height, 450mm from the tunnel wall, and 1000mm upstream of the building centre. The dynamic pressure is measured by connecting the total pressure tapping and the static pressure tapping on the pitot-static tube to the positive and negative ports respectively of a SensorTechnics HCLA 02X5-B differential micromanometer, marked 7a) in Figure 4.28.

The model building consists of a 200mm hollow cube made from 6mm thick perspex with three exchangeable window openings. These openings allow a range of opening configurations to be achieved, and can be replaced with either a blank plate, a pressure tapping plate, a mounting plate for the cross-flow probe, a square orifice type window, or a hinged opening type window, see Figure 4.27. Both the square orifice and

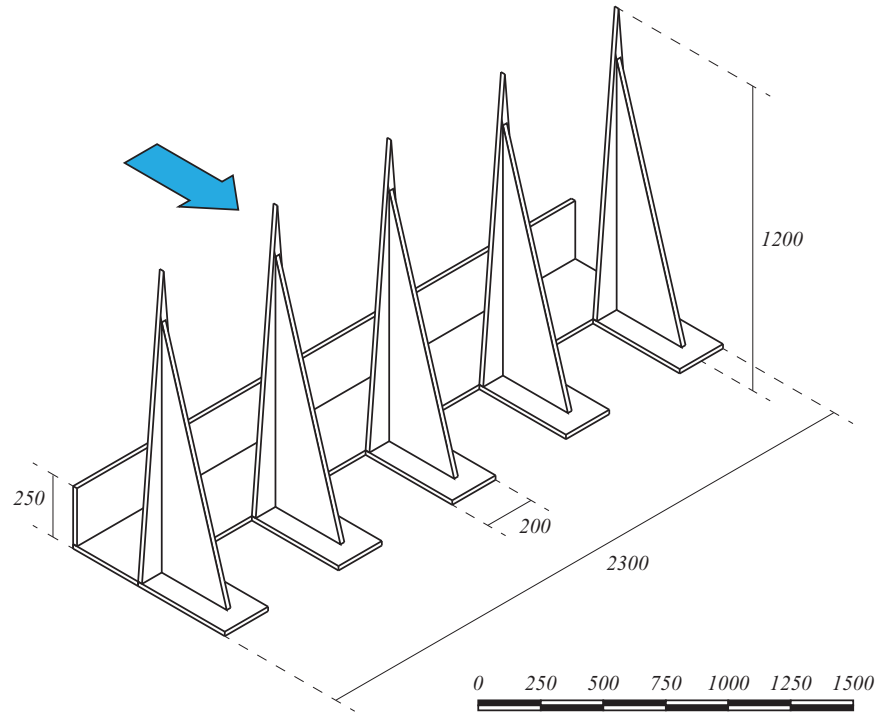


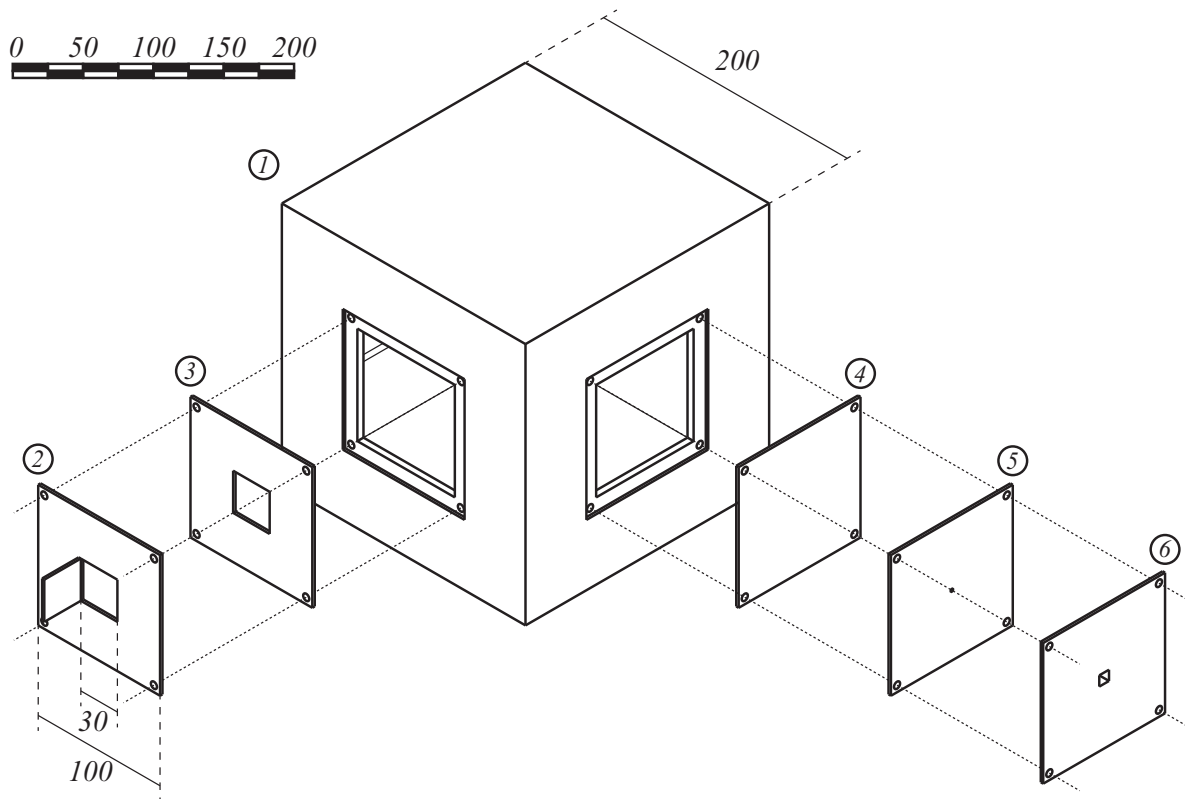
**Figure 4.26:** Isometric drawing of the spires used for velocity and turbulence profile preconditioning in the model building experiments. with dimensions given in millimeters. The direction of flow is denoted by the blue arrow.

the hinged windows are represented by a  $30\text{mm}$  square hole cut into a  $100\text{mm}$  square mounting plate made from  $2\text{mm}$  thick perspex. This corresponds to an opening porosity of  $2.25\%$ . This is well within the limits of  $10\%$  and  $23\%$  opening porosity identified by Seifert *et al.* [1] and Vickery and Karakatsanis [81] respectively, above which opening porosity is thought to have a significant effect on ventilation rates. The hinged window has a  $200\text{mm}$  square opening vane made from  $1\text{mm}$  thick aluminium, which projects at  $90$  degrees from the surface of the opening.

All window mounting plates are mounted flush with the building surface. A simple cube shaped building is chosen because of its symmetry. Here, the pressure and velocity profile on one surface can be phase-shifted to predict the pressure and velocity profile on the other three.

### 4.7.2 Error analysis

For the following experiments, a minimum of four repeats were conducted for each wind angle. Here the confidence in the mean is evaluated from the distribution in the mean of repeats according to Equation 4.19, as opposed to by propagation of error in measured variables. This better accounts for unknown sources of random error, but does not account for potential systematic errors.



- |                   |                   |                                    |
|-------------------|-------------------|------------------------------------|
| 1. Model building | 3. Square orifice | 5. Pressure tapping plate          |
| 2. Hinged window  | 4. Blank plate    | 6. Cross-flow probe mounting plate |

**Figure 4.27:** Isometric drawing of the model building with exchangeable opening plates. Key dimensions are given in millimeters.

Flow configurations that are symmetrically equivalent are aggregated as repeat measurements. Here the pressure coefficient measured using the square opening and the surface pressure tapping are symmetrical about 0 degrees; and the opening pressure coefficient measured with a left-mounted window is symmetrical to the opening pressure coefficient measured with a right mounted window about 0 degrees. The *cross-flow* dynamic pressure coefficient and the *façade* cross-flow direction are symmetrical about a wind angle of 0 degrees, where the *façade* cross-flow direction is also mirrored about the vertical on the façade. The equivalence relations can be given by

$$C_{P(i)}(\theta) \equiv C_{P(i)}(-\theta) \quad (4.51)$$

$$C_{P(Left)}(\theta) \equiv C_{P(Right)}(-\theta) \quad (4.52)$$

$$C_{P_{dc}}(\theta) \equiv C_{P_{dc}}(-\theta) \quad (4.53)$$

$$\alpha(\theta) \equiv -\alpha(-\theta) \quad (4.54)$$

where  $C_{P(i)}$  denotes the pressure coefficient measured with the square opening or the surface pressure tapping;  $\theta$  denotes the wind angle relative to the normal;  $C_{P(Left)}$  and  $C_{P(Right)}$  denote the pressure coefficients measured with the left mounted and right mounted hinged openings respectively;  $C_{P_{dc}}$  denotes the *cross-flow* dynamic pressure coefficient; and  $\alpha$  denotes the *façade* cross-flow direction relative to the vertical on the façade.

### 4.7.3 Surface pressure measurements

A key input to envelope flow models of wind driven ventilation is the surface pressure coefficient on the building facade at the location of each window opening. The surface pressure coefficient allows the static pressure on the surface of a building arising due to its interaction with atmospheric wind to be characterised. This is typically measured using wind tunnel experiments on model buildings with no openings in the façade. Window openings are assumed to be sufficiently small as to have a negligible impact on the pressure field around a building. However, when a window projects from the building, it has been shown to have a substantial impact on the pressure field close to the opening, even when the window is small compared to the size of the façade [136]. This has been hypothesised to have a substantial impact on ventilation rate [6]. Therefore, this Section develops techniques to directly measure the impact of window geometry on the surface pressure coefficients measured at the location of the window openings.

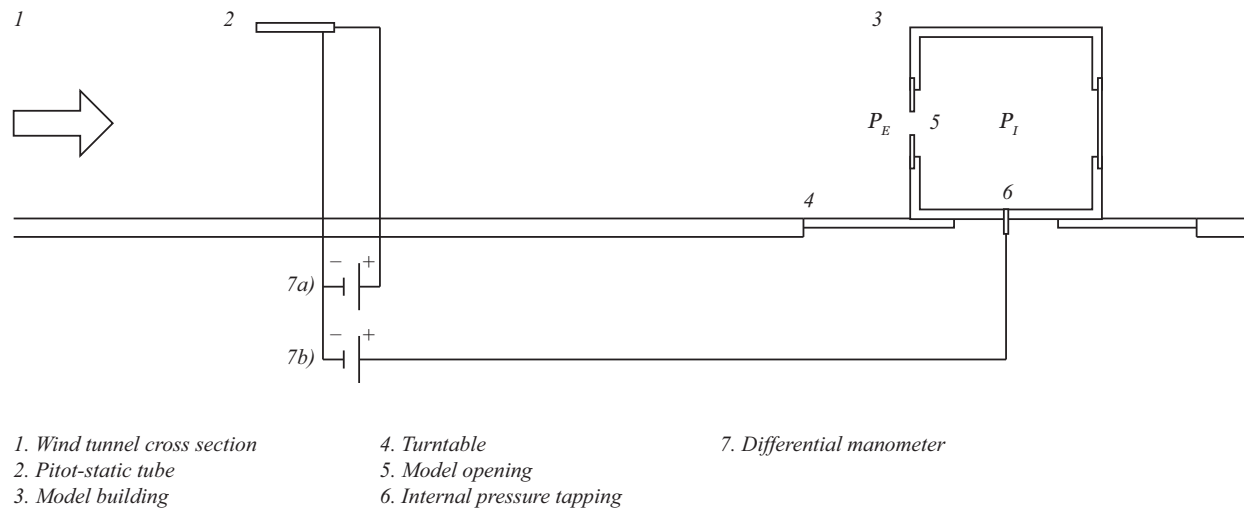


**Figure 4.28:** Diagram of instrumentation used to measure surface pressure coefficients on a model building. When the pressure tapping plate is used, the internal pressure tapping is connected directly to the surface pressure tapping on the plate.

### Instrumentation

The instrumentation used to measure surface pressure coefficients is detailed in Figure 4.28. The static pressure difference between the building interior and the free stream is measured by connecting the interior pressure tapping in the model building and the static pressure tapping on the pitot-static tube to the positive and negative ports respectively of differential manometer 7b) in Figure 4.28.

When measuring surface pressure on the model building, all openings are replaced with a blank plate except for one, which can be exchanged to measure the surface pressure that occurs with a range of different opening types. In this configuration, there is only one opening in the building. To preserve conservation of mass, the internal static pressure of the building equalises with the wind pressure acting on the surface of the opening. Therefore, the internal static pressure of the building can be used as a proxy to measure the surface pressure when the influence of opening geometry is included. When using the pressure tapping plate, the internal pressure tapping is connected directly to the pressure tapping on the mounting plate. This removes any influence from the building volume from the measurement of surface pressures.

### Experimental protocol

The surface pressure coefficient tests are divided into two categories: high Reynolds number tests and Reynolds number dependence tests.

The sharp edges of the building are expected to cause flow separation, which leads to pressure coefficients

that are relatively independent of Reynolds number above a critical value. To minimise the effect of zero-offset calibration error on the uncertainty in surface pressure coefficients, the high-Reynolds number pressure coefficient profiles are run at the maximum velocity of the tunnel. Different wind angles are simulated by rotating the turntable on which the model building is mounted. Surface pressure coefficient measurements are taken at 15 degree increments in wind angle, with zero offset calibration performed every 90 degrees. A five minute measurement period is employed for each wind angle, with a one minute wait each time the wind angle is changed to allow the flow pattern to settle.

To test whether the measured surface pressure coefficients exceeded the critical Reynolds number, Reynolds number dependence tests are performed at a few key wind angles. For the surface pressure tapping and the square opening, these are performed at 0 degrees and 255 degrees; see Figure 4.29. This corresponds to the highest and lowest measured value of the surface pressure coefficients respectively. For the hinged opening, Reynolds number dependence tests are performed at wind angles of 60, 105, 225, and 285 degrees; see Figure 4.30. This corresponds to the regions where the surface flow velocity is highest on the upstream and downstream faces of the building, and tests for Reynolds number independence at the window-scale. For both tests, Reynolds number independence is achieved above a mean Reynolds number of about  $4 \times 10^4$ . High measurement uncertainty at lower Reynolds numbers precludes means that no firm conclusions can be drawn about Reynolds number independence below this threshold.

### Calculation of descriptive parameters

The surface pressure coefficients and the Reynolds numbers in the atmospheric flow are evaluated using differential pressure measurements from the micromanometers described in Figure 4.28. These manometers must be calibrated using zero pressure measurements. Techniques for evaluating the measured pressure from the voltage output from the manometer are given in Section 4.4.8. The surface pressure coefficients and Reynolds number parameters are evaluated according to the following equations:

$$C_P = \frac{\Delta P_b}{\Delta P_a} \quad (4.55)$$

$$Re_T = \frac{H \sqrt{\frac{2}{\rho} \overline{\Delta P_a}}}{\nu} \quad (4.56)$$

where  $\Delta P_b$  is the static pressure difference between the building pressure tapping and the static pressure in the free stream, measured by manometer  $\tau_b$ ) in Figure 4.28;  $\overline{\Delta P_a}$  is the mean dynamic pressure in the atmospheric flow measured by manometer  $\tau_a$ ) in Figure 4.28;  $Re_T$  is the Reynolds number in the atmospheric

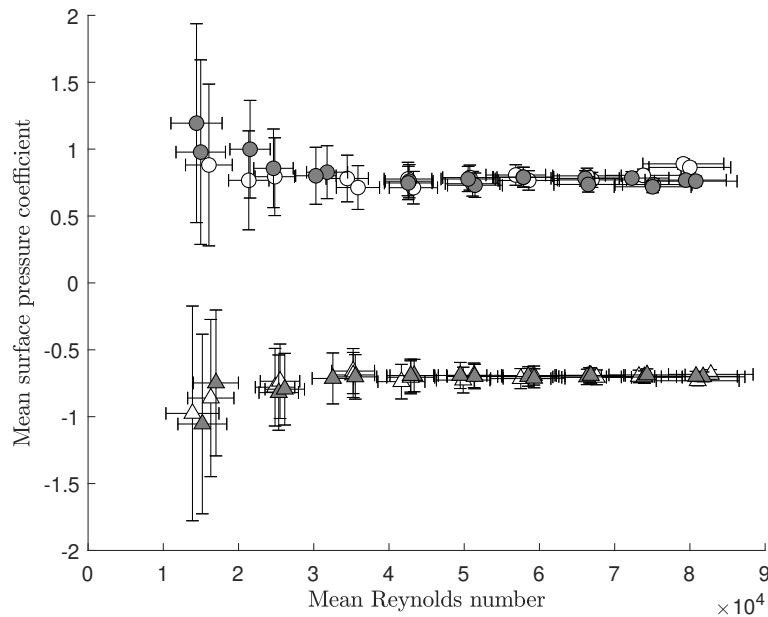


**Figure 4.29:** Relationship between the surface pressure coefficient on a model building with a surface pressure tapping or a square opening and Reynolds number. Wind angles of 0 and 255 degrees are denoted by circle and triangle markers respectively; results from the surface pressure tapping and the square opening are given by white and grey markers respectively. Error bars are shown to two standard errors.

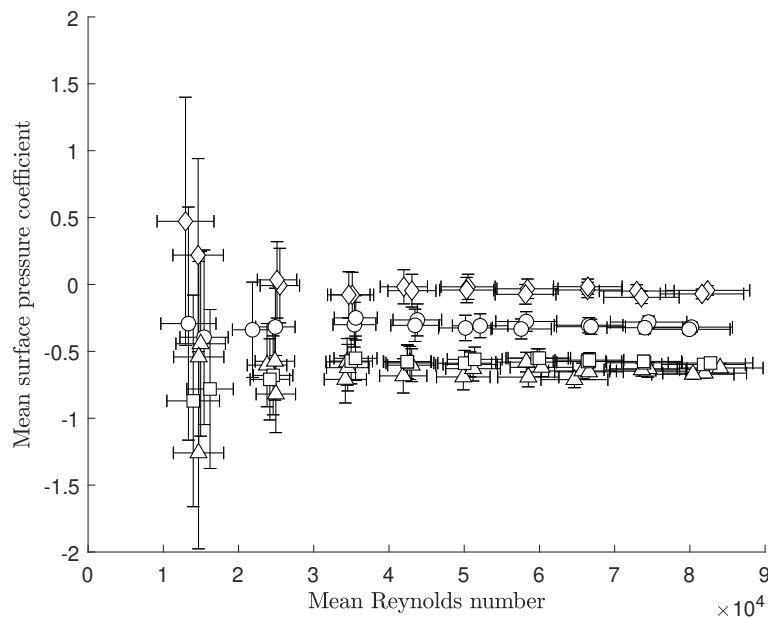


**Figure 4.30:** Relationship between the surface pressure coefficient on a model building with a hinged opening and Reynolds number. Wind angles of 60, 105, 225, and 285 degrees are denoted by circle, triangle, square, and diamond markers respectively. Error bars are shown to two standard errors.



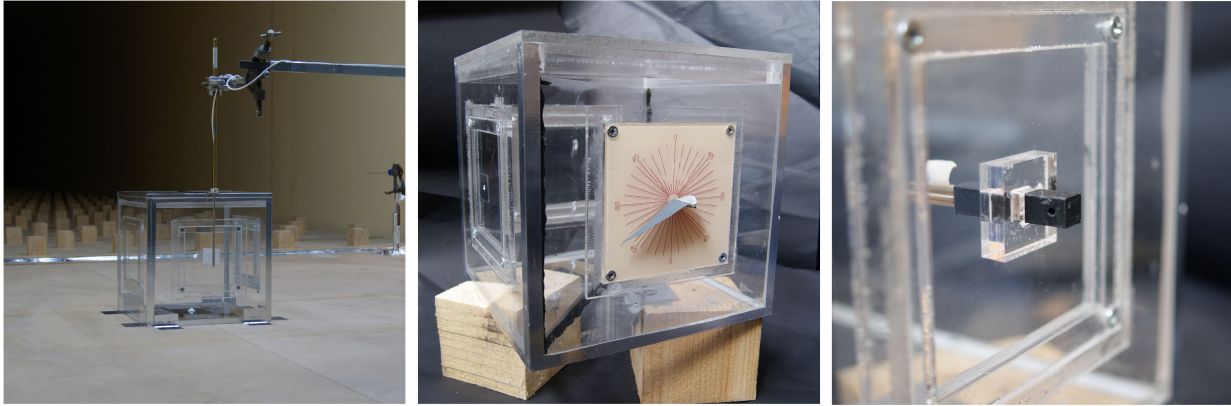


**Figure 4.31:** Image of the three techniques used to measure the speed and direction of the cross-flow: the hot wire anemometer used to measure flow speed (left), the weather-vane used to visualise flow direction (centre), and the cross-flow probe used to measure speed and direction of the cross-flow simultaneously (right).

flow, and  $H$  is the height of the model building. The values of air density and kinematic viscosity used are described in Section 4.4.8.

#### 4.7.4 Cross-flow velocity measurements

To integrate the cross-flow characterisation curves developed in Chapter 5 into envelope flow models, both the speed and direction of the cross-flow on a building surface must be measured.

##### Experimental techniques

To enable comparison and validation of measurement techniques, three approaches have been used to measure the speed and direction of the cross-flow; see Figure 4.31:

1. Hot-wire anemometer, used to measure the speed of the cross-flow
2. Weather-vane, used to visualise the direction of the cross-flow
3. Cross-flow probe, used to measure the speed and direction of the cross-flow simultaneously

The speed of the cross-flow is measured using a hot-wire anemometer mounted such that the wire is perpendicular to the surface of the building; see Figure 4.31. Here, flow in the plane parallel to the façade should be evaluated equivalently regardless of direction, yielding a measure of cross-flow speed. However, the perpendicular mounting of the wire is performed manually with visual measurement only. Results may be sensitive to the accuracy of this process. Furthermore, the geometry of the probe itself may present a blockage to flow. The probe has a cross-sectional area of  $600\text{mm}^2$  within the area of the façade, equivalent

to 1.5% of the façade area. This represents a barrier in the cross-flow above the probe, which could alter local flow behaviour. In addition to this, the mounting of the probe requires a large and robust mounting structure, which could interfere with the flow pattern around the wider building; see Figure 4.31. The need to mount the probe so that the mounting structure does not interfere with the flow leads to long structural lengths in the mounting structure. This is susceptible to significant vibration during wind tunnel operation, which is mitigated using a stabilising structure attached to the top of the building.

The direction of the cross-flow was visualised using a weather-vane mounted on the building façade: see Figure 4.31. This consists of a 50mm long paper flag, which is loosely wrapped around a 1.5mm diameter steel axle on an acrylic mounting plate. This mounting plate is exchangeable with those described in Figure 4.27. The flag is counter-weighted using adhesive putty such that it is free-spinning in the vertical plane. When located in the wind-tunnel, the flag spins to point in the direction of the cross-flow. This is filmed using a portable camera mounted on the turntable, facing the weather-vane. This may interfere with the dynamics of flow around the building, particularly when the camera is upstream of the building. The mounting plate has angles marked on it in 10 and 45 degree increments to facilitate visual analysis of the direction of the cross-flow.

The speed and direction of the cross-flow can be measured simultaneously by the cross-flow probe described in Section 4.6. This probe is mounted on the centre of the building façade at the same location as the surface pressure tappings using a mounting plate; see Figure 4.27. Here, the manometric tubing and micromanometers are concealed within the interior of the model building, so the cross-flow probe interacts minimally with the airflow over and around the building; see Figure 4.31. The probe is mounted at a fixed distance of 5mm from the façade; the characteristic distance identified during the hot-wire experiments. The probe presents a maximum blockage to the cross-flow of 84mm<sup>2</sup>, or 0.21% of the area of the façade, and does not interfere with the flow elsewhere in the wind tunnel. This is an improvement on the hot-wire anemometer, where the geometry of the probe and the mounting equipment can be expected to have a more significant effect on flow behaviour.

To minimise the measurement errors associated with low pressure differentials, the tunnel was run at its maximum speed, which corresponds to approximately 10ms<sup>-1</sup>. The dynamic pressure and tunnel velocity are measured at building height using a pitot-static tube and a hot wire anemometer respectively, according to the procedure described in Sections 4.7.1 and 4.5. A range of wind angles are simulated by rotating the turntable described in Section 4.7.1 in increments of 15 degrees, and the tunnel is stopped to take zero calibration measurements every 90 degrees.

### Calculation of descriptive parameters

The cross-flow speed and reference wind speed measured by the hot-wire anemometer are evaluated according to Section 4.5. The speed and direction of the cross-flow measured by the cross-flow probe are evaluated according to Section 4.6. An estimate of the mean flow direction is also made by visual analysis of the footage of the weather-vane. These measurements are used to evaluate the following descriptive parameters:

$$P_{dR} = \Delta P_a \quad (4.57)$$

$$C_{P_{d_c}} = \frac{P_{d_c}}{P_{dR}} \quad (4.58)$$

$$C_{P_{d_c}} = \left( \frac{U_c}{U_R} \right)^2 \quad (4.59)$$

$$C_{\Delta P_T} = \frac{P_{T_R} - P_{T_c}}{P_{d_c}} = 1 - C_{P_{d_c}} - C_P \quad (4.60)$$

where  $P_{dR}$  is the reference dynamic pressure in the atmospheric flow at building height, measured using a pitot-static tube;  $\Delta P_a$  is the pressure differential measured using manometer 7<sub>a</sub>) in Figure 4.28;  $C_{P_{d_c}}$  is the *cross-flow* dynamic pressure coefficient, which is equal to the square of the cross-flow velocity coefficient;  $P_{d_c}$  is the dynamic pressure in the cross-flow evaluated by the cross-flow probe;  $U_c$  is the cross-flow speed evaluated by the hot-wire anemometer;  $U_R$  is the reference wind speed at building height measured by the hot-wire anemometer;  $C_{\Delta P_T}$  is the total pressure loss coefficient, which characterises the loss in total pressure between a point in the atmospheric flow  $P_{T_R}$  and the cross-flow at the opening  $P_{T_c}$ ; and  $C_P$  is the surface pressure coefficient at the opening measured according to Section 4.7.3.

An estimate for the surface pressure coefficient measured with window geometry present can be evaluated using the surface pressure coefficient on an equivalent building without window geometry; the *cross-flow* dynamic pressure coefficient; the flow approach angle; and the *local* pressure coefficient curves evaluated according to Section 4.4. Here

$$C_{P_o} = C_{P_i} + C_{P_L}(\beta)C_{P_{d_c}} \quad (4.61)$$

Where  $C_{P_o}$  is the surface pressure coefficient with window geometry present;  $C_{P_i}$  is the surface pressure coefficient measured with an equivalent building without window geometry;  $C_{P_L}(\beta)$  is the *local* pressure coefficient for the window measured according to the procedure described in Section 4.4 at the flow approach angle  $\beta$ ; and  $C_{P_{d_c}}$  is the *cross-flow* dynamic pressure coefficient. This can be compared against the window-

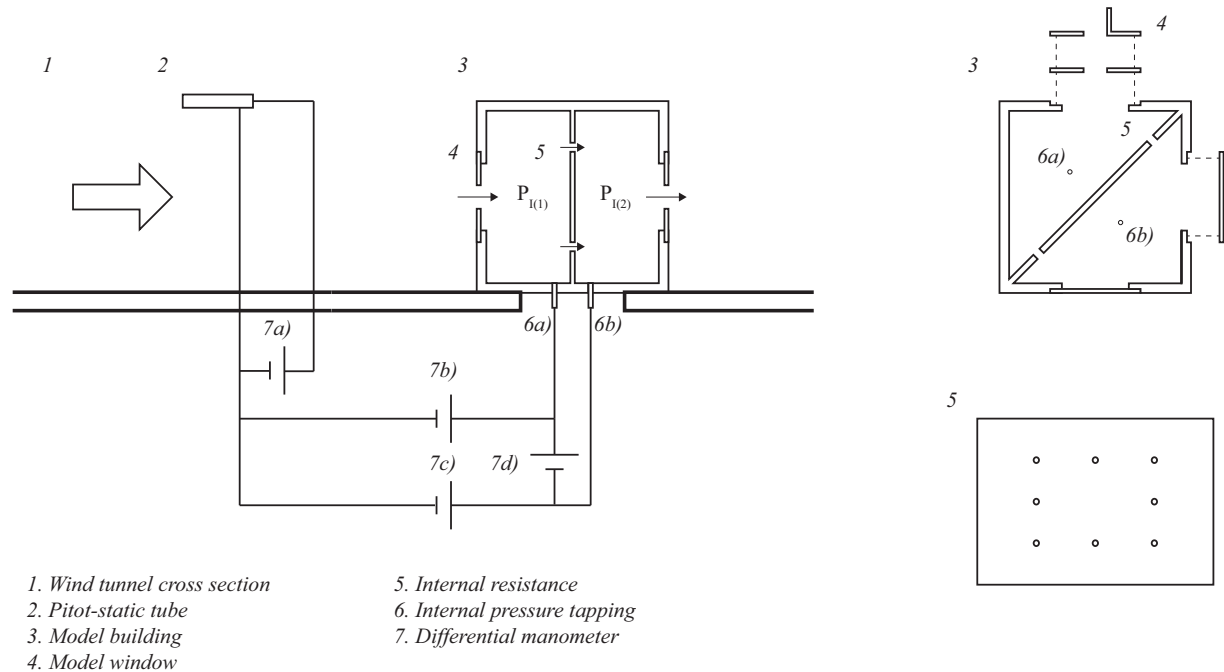


**Figure 4.32:** Diagram of the experimental setup used to measure volume flow rate through a model building, with the arrow denoting the direction of the airflow. A diagrammatic section is shown on the top left, and a diagrammatic plan is shown on the top right. An elevation of the internal resistance is shown on the bottom right.

integrated surface pressures that are measured directly.

## 4.8 Model building experiments - ventilation rate measurements

Measurements of ventilation rates in a model building are required to investigate the predictive capacity of the window performance characterisations detailed in Section 4.4. This Section describes experiments that measure the unidirectional component of ventilation in a model building. This is consistent with the requirement to validate steady-state envelope flow models, which only predict unidirectional flow rates. However, these tests provide an incomplete picture of pollutant removal rates as gas exchange rates in spaces are also dependent on unsteady and bidirectional mechanisms at the external openings. This is particularly true in the perimeter zones of buildings.

### 4.8.1 Experimental setup

The wind-tunnel setup is similar to that described in Section 4.7.1. However, here the model building is compartmentalised into two zones; see Figure 4.32.

A range of ventilation configurations can be investigated by exchanging the opening plates described in

Section 4.7.1. In each of these configurations, one window opening is located in each zone such that any flow between the two openings must pass through the internal partition; see Figure 4.32. The internal partition comprises a perspex dividing wall punctuated by eight circular orifices with a total area equal to one quarter of the reference area, or  $225\text{mm}^2$ . This forms a component in the ventilation network of known resistance; when the pressure drop across the partition is known, the volume flow rate through the partition can be evaluated. The circular orifices in the internal resistance are each assumed to have an *idealised* discharge coefficient equal to 0.61. The resistance of the internal partition is selected as a balance between the competing requirements to maximise the pressure drop across the partition, and thereby reduce measurement error, and to maximise the volume flow rate through the building. The circular orifices within the internal partition are distributed around the perimeter. This minimises the chance of conserved momentum from the inflow jet interfering with flow through the partition. To minimise the influence of wall effects on the aerodynamic properties of the orifices, each orifice is located at least five diameters away from the walls and from each other.

Pressure tappings are located in either zone to sample the internal pressure; see Figure 4.32. A pitot-static tube located at building height samples the reference static pressure and the total pressure in the atmospheric flow. Differential micro-manometers are used to measure the pressure drop across the internal partition, the pressure difference between each internal zone and the atmospheric pressure, and the dynamic pressure in the atmospheric flow; see micro-manometer  $7_d$ ), micro-manometers  $7_b$ ) and  $7_c$ ), and micro-manometer  $7_a$ ) respectively in Figure 4.32.

These experiments investigate the performance of a building under cross and corner ventilation configurations. Ventilation configurations are fitted with either simple, square openings or fully open hinged windows. Figure 4.33 illustrates the four ventilation configurations chosen for investigation. The specific configuration of hinged openings investigated are expected to result in the greatest difference in volume flow rate when compared to the rectangular opening configurations. This is evaluated by means of simple flow diagrams and the expected pressure interactions with a cross-flow. Figure 4.33 illustrates a wind angle where the windows are expected to increase surface pressures at the inlet and reduce surface pressures at the outlet, which would be expected to enhance ventilation flow rates. At other wind angles, the opposite effect is expected to occur, where the windows reduce surface pressures at the inlet and increase surface pressures at the outlet, which would be expected to suppress ventilation flow rates.

Ventilation configurations can be considered equivalent if they are symmetrical about an axis parallel to the direction of the wind.

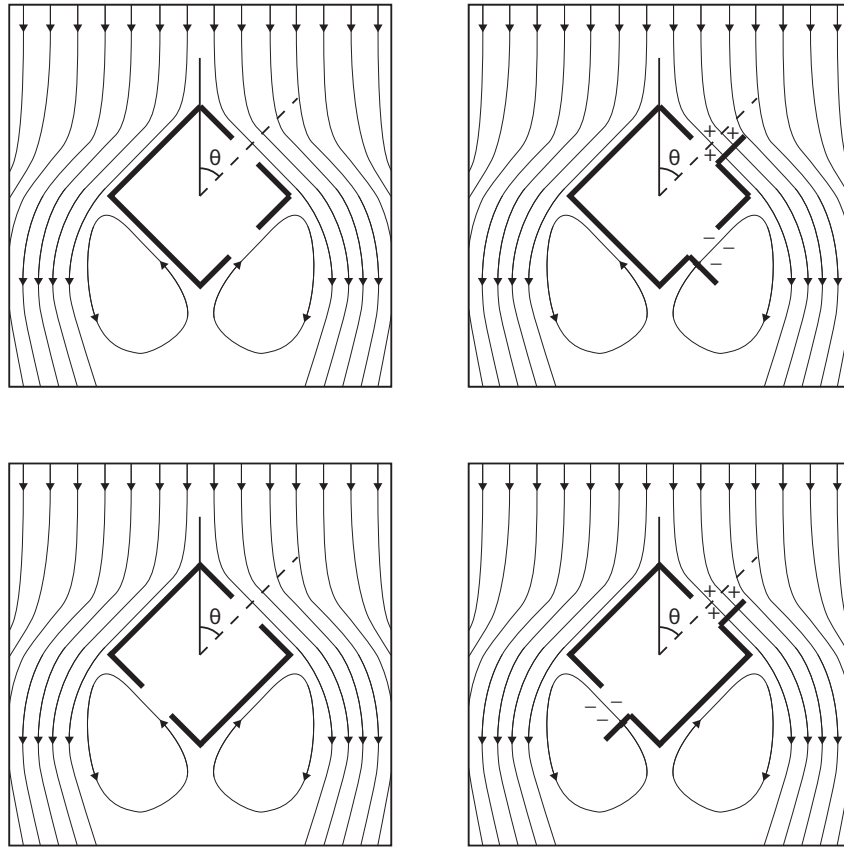


**Figure 4.33:** Diagram of the different ventilation configurations modelled, and how the wind angle is defined for each configuration. The dashed line passes through the primary opening in each configuration. Mean streamline patterns around the building are depicted following ASHRAE [16] and Wilson [52]

### 4.8.2 Characterising ventilation rate in the building

To provide a general description of the ventilation rate in the building, dimensionless parameters are used. Here, the ventilation rate in the model building is described by a dimensionless *building* flow rate, which is given by

$$Q_B^* = \frac{Q}{A_R U_R} \quad (4.62)$$

where  $Q$  is the volume rate through the building;  $A_R$  is a reference area, here taken to be the area of one window; and  $U_R$  is a reference wind speed measured at building height. Here both windows are the same size, and described by the area  $A_R = h \times w$ . The volume flow rate through the building is defined as positive when it flows from the primary opening - through which the dashed line passes in Figure 4.33 - to the secondary opening; and is defined as negative in the reverse direction. For ventilation rate calculations in a single zone, it is the *magnitude* of the volume flow rate that is important in determining pollutant removal rates.

### 4.8.3 Estimating volume flow rate through the model building

Prior to measuring the volume flow rate through the model building, it is necessary to evaluate predicted ventilation rate profiles using a range of different predictive models. This enables predicted and measured ventilation rates to be compared, and the suitability of different modelling techniques to be assessed. Here three prediction approaches are explored: the conventional orifice flow model; the orifice flow model corrected for variation in surface pressure caused by interaction between the window geometry and the cross-flow; and the cross-flow characterisation curves developed according to the methodology described in Section 4.4. These models require increasing levels on information to specify. Orifice flow models of wind-driven ventilation require measurements of surface pressure coefficients, and the area and *idealised* discharge coefficients of all window openings and internal resistances. The corrected orifice flow model requires knowledge of all the inputs of the orifice flow model, the *cross-flow* dynamic pressure coefficients at the location of each opening, and the relationship between *local* pressure coefficient and flow approach angle characteristic to each opening. Finally, the cross-flow characterisation models require knowledge of all the inputs to the orifice and corrected orifice flow models, and the relationship between *total* dimensionless volume flow rate, flow approach angle, and *local* dimensionless pressure characteristic to each opening. All these inputs can be acquired according to the methods described in Sections 4.3 to 4.7.

### Estimating volume flow rate using the orifice flow model

The orifice flow model is the simplest method of estimating volume flow rates, and requires only the surface pressure distribution to be known. For a two opening system separated by an internal resistance, the dimensionless *building* flow rate can be given by

$$Q_B^* = S_i \sqrt{\frac{|C_{P(1)} - C_{P(2)}|}{\left(\frac{A_R}{C_{d(1)}A_1}\right)^2 + \left(\frac{A_R}{C_{d(\Omega)}A_\Omega}\right)^2 + \left(\frac{A_R}{C_{d(2)}A_2}\right)^2}} \quad (4.63)$$

$$S_i = \frac{C_{P(1)} - C_{P(2)}}{|C_{P(1)} - C_{P(2)}|} \quad (4.64)$$

where the subscripts 1, 2, and  $\Omega$  refer to the primary opening, secondary opening, and internal resistance respectively,  $C_P$  is the surface pressure coefficient measured according to Section 4.7.3, and  $S_i$  is a directional indicator.

In the experimental configuration used for ventilation rate measurements, the hinged opening, square orifice, and internal resistance all have an equivalent *idealised* discharge coefficient, which is assumed to equal 0.61. The reference area for the primary and secondary openings are both equal to the reference area for the building, and the reference area of the internal partition is equal to 1/4 that of the reference area for the building. In this scenario, Equation 4.63 reduces to

$$Q_B^* = 0.61S_i \sqrt{\frac{|C_{P(1)} - C_{P(2)}|}{18}} \quad (4.65)$$

This corresponds to a 3 fold reduction in volume flow rate relative to an equivalent building with an internal resistance of zero.

### Correcting the orifice flow model for local pressure variations

Section 3.5.2 identifies that window geometry has the potential to alter surface pressures by interacting with the cross-flow. Section 4.7.3 describes techniques for directly measuring the window-integrated surface pressure coefficients that can be used to correct the orifice flow model. In the absence of direct measurements, Equation 4.61 can be used to estimate the window integrated surface pressure coefficients using the surface pressure coefficients measured without window geometry; the *cross-flow* dynamic pressure coefficient; the flow approach angle; and the *local* pressure coefficient curves evaluated according to Section 4.4. The latter approach is applied here for prediction purposes, as it is a more flexible approach consistent with its intended use in exploratory design. To correct the orifice flow model, the window-integrated surface pressure



coefficients thus derived are substituted for the surface pressure coefficients in Equation 4.63.

### Estimating volume flow rate using cross-flow characterisation curves

The cross-flow characterisation curves measured according to the techniques described in Section 4.4 aim to account for the influence of a cross-flow on the aerodynamic behaviour of window openings. However, the dimensionless *building* flow rate cannot be explicitly specified because the resistance of an opening is not constant. Here implicit solutions must be found that satisfy the following equations:

$$Q_{B(1)}^* = \frac{-Q_1}{A_R U_R} = -Q_{T(1)}^* A_1^* \sqrt{|C_{P_I(1)} - C_{P(1)}| + |C_{P_{d_c}(1)}|} \quad (4.66)$$

$$Q_{B(\Omega)}^* = \frac{Q_\Omega}{A_R U_R} = C_{d(\Omega)} A_\Omega^* S_{i(\Omega)} \sqrt{|C_{P_I(1)} - C_{P_I(2)}|} \quad (4.67)$$

$$S_{i(\Omega)} = \frac{C_{P_I(1)} - C_{P_I(2)}}{|C_{P_I(1)} - C_{P_I(2)}|} \quad (4.68)$$

$$Q_{B(2)}^* = \frac{Q_2}{A_R U_R} = Q_{T(2)}^* A_2^* \sqrt{|C_{P_I(2)} - C_{P(2)}| + |C_{P_{d_c}(2)}|} \quad (4.69)$$

$$Q_{B(1)}^* = Q_{B(\Omega)}^* = Q_{B(2)}^* \quad (4.70)$$

where the subscripts 1 and 2 refer to the primary and secondary opening respectively and their adjacent zones; the subscript  $\Omega$  refers to the internal resistance,  $Q_B^*$  is the dimensionless building flow rate evaluated through a given opening;  $Q_T^*$  is the *total* dimensionless volume flow rate through each opening, which is evaluated according to the characterisation experiments described in Section 4.4 as a function of *local* dimensionless pressure and flow approach angle; and  $A^*$  is the ratio of the reference area of the opening to the reference area used to evaluate the dimensionless *building* flow rate. The surface pressure coefficients, *cross-flow* dynamic pressure coefficients and flow approach angles are directly measured according to the experiments described in Sections 4.7.3 and 4.7.4. The *local* dimensionless pressure can be evaluated from the measured surface pressure coefficients and the implicitly-specified internal pressure coefficient according to the following equation:

$$P_L^* = \frac{C_{P(I)} - C_{P(i)}}{C_{P_{d_c}(i)}} - C_{P_L(i)} \quad (4.71)$$

Where the *local* pressure coefficient is determined from the results of the characterisation experiments described in Section 4.4 as a function of the measured flow approach angle.

### Estimating single-opening ventilation rates

Most models that describe cross ventilation predict zero ventilation rates when the mean pressure difference between the openings is zero. However, turbulence and other mixing mechanisms can drive gas exchange in buildings even where there is only one opening in the wall. Single opening ventilation rates driven by wind are included in the following analysis to give a minimum bound to predicted ventilation rates [61]. The equivalent dimensionless *building* flow rate attributable to single opening ventilation can be given by

$$|Q_B^*| = \sum 0.1A_i^*U_i^* \quad (4.72)$$

where the subscript  $i$  refers to an individual opening;  $A^*$  is the ratio between the opening area and the reference area, here equal to one; and  $U^*$  is the cross-flow velocity coefficient, which is described by ratio of the speed of the cross-flow at the opening to the reference wind speed.

### Estimating average ventilation capacity

For comparative purposes, it is convenient to evaluate an average ventilation capacity provided by a given ventilation configuration. This is defined as the average magnitude of the the dimensionless *building* flow rate for all wind angles. Here,

$$\overline{Q_B^*} = \frac{1}{N} \sum_{n=1}^{n=N} |Q_B^*(\theta_n)| \quad (4.73)$$

#### 4.8.4 Evaluation of measured results

Descriptive parameters are evaluated from the output of the differential micro-manometers depicted in Figure 4.32. Techniques for evaluating the measured pressure from the voltage output of the micro-manometers are given in Section 4.4.8.

The internal pressure coefficients in the two building zones and the dimensionless *building* flow rate can be evaluated according to the following equations:

$$C_{P_I(1)} = \frac{\Delta P_b}{\Delta P_a} \quad (4.74)$$

$$C_{P_I(2)} = \frac{\Delta P_c}{\Delta P_a} \quad (4.75)$$

$$C_{\Delta P_\Omega} = C_{P_I(1)} - C_{P_I(2)} = \frac{\Delta P_d}{\Delta P_a} \quad (4.76)$$

$$Q_B^* = C_{d(\Omega)} A_\Omega^* S_i \sqrt{|C_{\Delta P(\Omega)}|} \quad (4.77)$$

$$S_i = \frac{C_{\Delta P(\Omega)}}{|C_{\Delta P(\Omega)}|} \quad (4.78)$$

where  $\Delta P_{a-d}$  corresponds to the differential pressure measured by micro-manometers  $7_a-7_d$  in Figure 4.32; and  $C_{\Delta P_\Omega}$  is the differential pressure coefficient across the internal resistance. These measurements provide two techniques for estimating the differential pressure across the internal resistance, which enables the consistency of the results to be evaluated.

## 4.9 Conclusions

The methodologies described in this chapter describe the techniques required to characterise the aerodynamic performance of specific window geometries in the presence of a cross-flow, and to create empirical equations for use in design. The techniques required to implement these equations in building design are explored, and experiments described to measure the ventilation rate in a model building. This enables novel design equations to be developed, and their validity assessed.

## Part II

# Results



## Chapter 5

# Characterising airflow through windows in a cross-flow

### 5.1 Introduction

Chapter 2 identifies a lack of predictive models in the literature that describe the aerodynamic performance of common window geometries in a cross-flow. This chapter investigates the performance of simple, hinged openings (*iii - v* in Figure 2.7) under both still-air and wind driven conditions. Following analytical modelling in Chapter 3, the experimental techniques described in Section 4.4 are used to characterise the *idealised* discharge coefficient, the *local* pressure coefficient, and the *total* dimensionless volume flow rate of these openings. The approach flow used to simulate a wind-driven cross-flow over an opening is summarised in Section 5.2. The results of this investigation show how even simple window geometries can lead to behaviour that is incompatible with the behaviour of a simple, planar orifice.

### 5.2 Approach flow

As air flows over the surface of a building, skin friction results in the generation of a surface boundary layer [66]. The mean and fluctuating velocity profile in this flow will depend on the roughness characteristics of the façade, and the turbulence characteristics of the atmospheric flow prior to impingement on the façade. The local-scale experiments described here consider two boundary layer simulations: a notionally *thin* boundary layer grown over a roughness of smooth MDF boards, and a notionally *thick* boundary layer grown over a roughness of an array of blocks; see Section 4.4.2. This section summarises the mean and fluctuating velocity

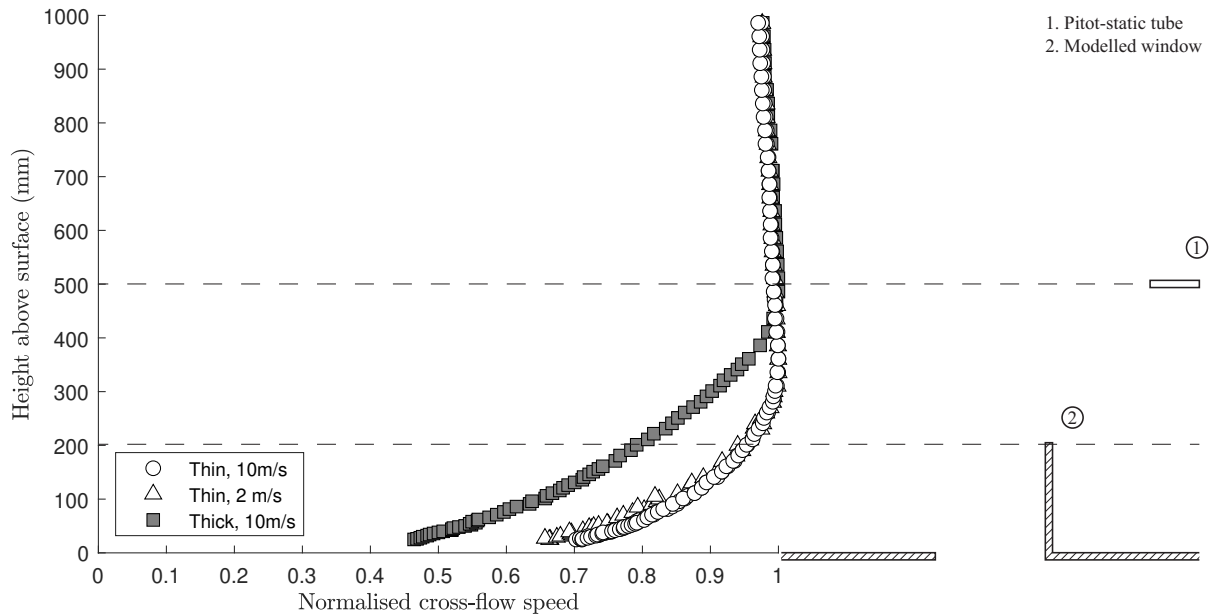


**Figure 5.1:** Plot of the surface boundary layer in the tunnel, normalised by peak flow velocity. Data from the *thin* boundary layer are denoted by white markers, and those from the *thick* boundary layer are denoted by grey markers. The heights of the pitot-static tube used to measure the reference velocity and the relative size of the window opening are denoted diagrammatically to the right of the plot.

profiles measured in the two simulated cross-flows.

### 5.2.1 Mean velocity profile

Figure 5.1 plots a normalised velocity profile in a vertical traverse of the cross-flow measured at operating speeds of approximately  $10 \text{ ms}^{-1}$  and  $2 \text{ ms}^{-1}$  - the maximum and minimum speeds achieved in the wind tunnel over the course of the dynamic tests. These show that the shape of the velocity profile is consistent across this range. Velocity measurements from a horizontal traverse indicate that velocity profile is uniform across the width of the tunnel the for both the *thick* and *thin* boundary layers.

It is clear from Figure 5.1 that the pitot-static tube used to sample the cross-flow velocity and the reference static pressure is located outside of the boundary layer and within the free stream for both boundary layer simulations. However, it is also clear that a significant boundary layer is present even in the *thin* boundary layer simulations, such that the projecting window geometry is entirely within the boundary layer.

The velocity profile displays the characteristics of *unbounded* boundary layers typical of flows on external walls, where the velocity increases to a peak with height, before decaying to the constant *free stream* value [259]. This differs from the *bounded* boundary layers that commonly occur in pipes, and allows the boundary layer thickness to be defined more simply by the height at which the peak velocity occurs - here approximately

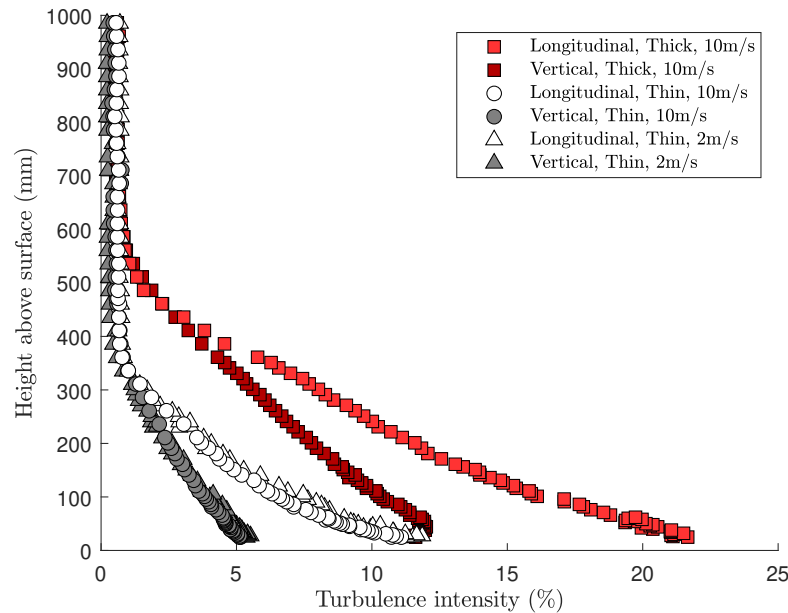


**Figure 5.2:** Plot of the turbulence intensity in the surface boundary layer in the wind tunnel. Data from the *thin* boundary layer are denoted by white and grey markers, and those from the *thick* boundary layer are denoted by light and dark red markers. Here, light and dark markers denote the longitudinal and vertical components of turbulence intensity respectively.

350mm for the *thin* boundary layer, and 500mm for the *thick* boundary layer. The normalised cross-flow velocity at one opening length from the surface is about 20% smaller in the *thick* boundary layer than in the *thin* boundary layer.

### 5.2.2 Turbulence intensity in the approach flow

Figure 5.2 plots the longitudinal and vertical components of the turbulence intensity in the cross-flow for the *thin* and *thick* boundary layer simulations, at reference wind speeds of 10 *m/s* and 2 *m/s*. Here, the turbulence intensity is at a maximum value close to ground level, and decays to a minimum value at the top of the surface boundary layer. Both the longitudinal and vertical components of the turbulence intensity in the simulated cross-flow are independent of Reynolds number over the range of measured wind speeds, with indistinguishable profiles presented at reference wind speeds of 10 *m/s* and 2 *m/s*.

The *thick* boundary layer achieves a higher turbulence intensity than the *thin* boundary layer over the majority of its height. A free stream turbulence of less than 1% is achieved for both the *thin* and *thick* boundary layer simulations.

In still-air tests, the wind tunnel is turned off and allowed to settle. Here it is assumed that the air in the wind tunnel is static, and the surface velocity profile and turbulence induced by flow through the window



opening in the plenum chamber can be neglected.

### 5.3 Aerodynamic resistance in still-air

The *idealised* discharge coefficient is considered to be a fundamental property of an opening, describing its resistance to flow under idealised, *still-air* conditions. Furthermore, Chapter 3 shows that this property represents an important limit to the *total* dimensionless volume flow rates achieved by openings in a cross-flow. These represent conditions where  $P_R^* \rightarrow -\infty$  for inflow and  $P_R^* \rightarrow +\infty$  for outflow.

Chapter 2 identifies a lack of predictive models in the literature that describe the aerodynamic performance of common window geometries in still-air. However, it is common in both academia and design practice to use *free-area* models to evaluate the aerodynamic performance of windows, whereby the unobstructed area presented by a window is specified as the reference area, and the *orifice* discharge coefficient is assumed to be a constant between 0.6 and 0.65; see Section 2.7.1. Ambiguity in the definition of *free area* results in different practitioners taking different approaches to estimating it, which, as this section shows, leads to a wide range of performance predictions for identical opening geometries. Furthermore, these predictions are seldom compared against experimental data, with practitioners assuming validity with no knowledge of anticipated errors.

This section examines the performance of simple hinged openings, as defined in Section 2.7.1. This family of openings is ubiquitous in naturally ventilated buildings. Empirical data describing the airflow characteristics of hinged openings in still-air have been identified in the literature for a wide range of opening angles and height to width ratios [124, 125, 108]. Here, these empirical data are used to develop a simple empirical model that allows *idealised* discharge coefficients for a family of hinged openings to be predicted as a function of characteristic geometric parameters [124, 125, 108]. The predictive capacity of this new model can then be assessed and compared against the predictions from a range of *free area* models. The results of experimental measurements characterising the *idealised* discharge coefficient of a square, hinged opening are then compared against the predictions of the EEAM model and the literature data used to fit it [124, 125, 108].

#### 5.3.1 Empirical Effective Area Model (EEAM)

The *idealised* discharge coefficient can be described as a dimensionless *effective* area determined by experiment, and can be expressed as a function of dimensionless parameters that describe the window geometry; see Section 2.7.1. The key parameters identified here are the opening angle  $\phi$  and the aspect ratio  $\sigma$ . Design equations are then statistically fitted to the empirical performance data presented by Baturin [108], Bot

[124], and Jong and Bot [125] as a function of these geometric parameters, to develop a Empirical Effective Area Model (EEAM).

The *idealised* discharge coefficient of a given opening geometry is independent of orientation with respect to gravity. Therefore, the same design equations can be used to describe top hung, bottom hung, side hung and horizontally mounted openings. This requires a definition of aspect ratio that is also independent of orientation. Here, the aspect ratio is defined as the ratio of the frame length perpendicular to the axis of opening, to the frame length parallel to the axis of opening. This definition is valid for all types of hinged or pivoted openings. For top and bottom hung windows, this is the height to width ratio of the opening; see Figure 2.7. For side hung windows, this is the width to height ratio of the opening.

The empirical modelling process is divided conceptually into primary and secondary modelling. Here, a common primary function is defined that can be used to describe the variation in the *idealised* discharge coefficient with a primary variable, here taken to be the opening angle, while the secondary variable is held constant, here taken to be the aspect ratio. This results in a family of curves, with fitted coefficients that can be expressed as a function of the secondary variable [256]. A secondary function can then be fitted to describe this variation, following the process described in Section 4.3. The selection of shape functions to fit the data results in the following expressions:

$$C_{d_I} = \frac{A_{eff}}{h w} = B (1 - e^{-M\phi}) \quad (5.1)$$

$$B = ae^{-b\sigma} + 0.611 \quad (5.2)$$

$$M = c\sigma + d \quad (5.3)$$

where  $\phi$  is the opening angle, and  $\sigma$  is the aspect ratio. The coefficients  $a, b, c$ , and  $d$  are fit using a least-squares minimisation; see Table 5.1. This expression preserves key analytical features expected to describe the *idealised* discharge coefficient of a hinged opening: the *idealised* discharge coefficient tends to zero as the opening angle tends to zero, and the *idealised* discharge coefficient tends to the analytical solution for a two dimensional slit as the aspect ratio tends to  $\infty$ .

**Table 5.1:** Fitted coefficients for the Empirical Effective Area Model

	<b>Coefficient</b>	<b>95% confidence interval</b>
<b>a</b>	0.25	0.18 , 0.33
<b>b</b>	1.4	1.1 , 1.8
<b>c</b>	0.016	0.014 , 0.018
<b>d</b>	0.016	0.014 , 0.019

As the uncertainty in the measurements is unknown, goodness-of-fit is evaluated using the coefficient of determination; see Section 4.3.2. Here a coefficient of determination of 0.98 is achieved. This means that 98% of the variance observed in data from the literature is explained by the fitted equation. The remaining 2% of unexplained variance includes contributions from measurement error, experimental differences between practitioners, and model error from the fitted equation. This corresponds to a standard deviation between predicted and measured *idealised* discharge coefficients of 0.023, or 7.7%.

### 5.3.2 Comparison with alternative models

Section 2.7.1 identified a wide range of models in the literature that are used to predict airflow through hinged openings, including analytical *free-area* models [121, 123, 126, 129, 116], semi-empirical models where measured data is used to calibrate a *free-area* model [125], and purely empirical models fit to proprietary data [2]. To assess the predictive capacity of the Empirical Effective Area Model described in Section 5.3.1, the regression statistics can be compared against those arising from the use of models presented in the literature.

The effective area predicted by *free area* models can be used to evaluate predictions of the *idealised* discharge coefficient, where

$$C_{dI} = 0.61 \frac{A_f}{hw} \quad (5.4)$$

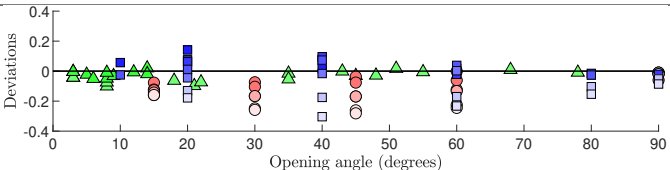
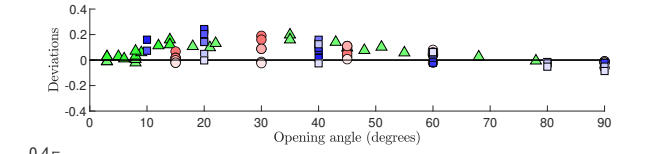
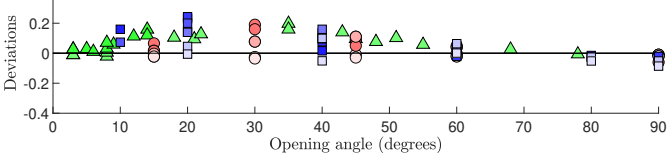
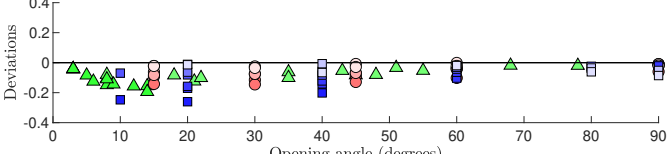
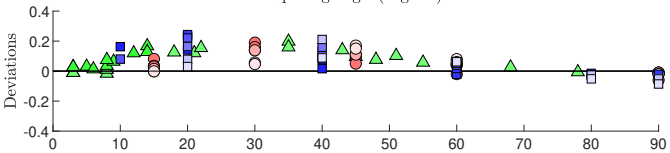
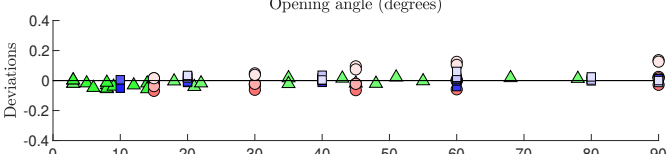
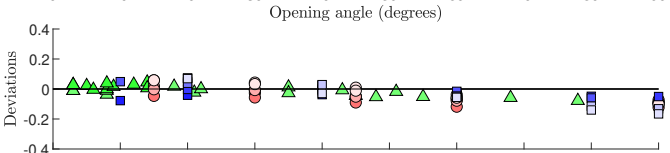
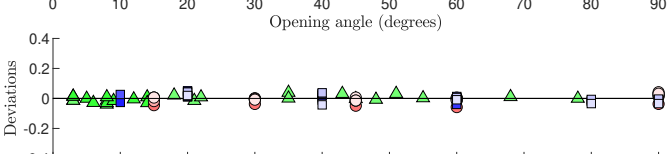
This enables a wide range of modelling techniques to be presented in a common form, and their predictive power compared. Table 5.2 presents the deviation between the *idealised* discharge coefficients predicted by a range of *free area* and empirical models, and values reported in the literature. Here, the mean deviation is used as an expression of skew: a negative value denotes a tendency of a given model to underestimate the *idealised* discharge coefficient, and a positive value denotes a tendency to overestimate the *idealised* discharge coefficient. The equations used to evaluate the predicted *idealised* discharge coefficients from each *free area* model are given in Appendix C.

In most *free area* models, the deviations between predicted and measured *idealised* discharge coefficients are exacerbated by large aspect ratios. In these models, increasing the aspect ratio results in the *side* areas representing a greater proportion of the total *free area*; see Figure 2.8. An exception to this is model A, where the greatest deviation occurs at low height to width ratios.

*Free area* models B, C and E tend to overestimate the *idealised* discharge coefficient. This effect is most substantial at opening angles of around 20-30 degrees.

*Free area* model A tends to underestimate the *idealised* discharge coefficient, although overestimation

**Table 5.2:** Deviation between predicted and measured *idealised* discharge coefficients for different modelling techniques as a function of opening angle. Markers are shaded based on the window aspect ratio, where white denotes an aspect ratio of zero, and fully saturated colour denotes an infinitely large aspect ratio. Data from Baturin is denoted by red circles [108], data from Bot are denoted by blue squares [124], and data from Jong and Bot are denoted by green triangles [125].

Model	Deviation in <i>idealised</i> discharge coefficients		$R^2$
	mean,	standard	
Free area (A, Figure 2.8)		-0.065, <b>0.11</b>	0.57
Free area (B, Figure 2.8)		0.054, <b>0.090</b>	0.73
Free area (C, Figure 2.8)		0.044, <b>0.083</b>	0.77
Free area (D, Figure 2.8)		-0.074, <b>0.092</b>	0.71
Free area (E, Figure 2.8)		0.066, <b>0.099</b>	0.67
Quasi-empirical (F, Figure 2.8)		0.001, <b>0.040</b>	0.95
Empirical (BB101)		-0.024, <b>0.057</b>	0.89
Empirical (EEAM)		-0.001, <b>0.023</b>	0.98

also occurs at high height to width ratios. *Free* area model D consistently underestimates *idealised* discharge coefficients for all aspect ratios and opening angles.

On average, empirical models provide a two fold reduction in standard deviation compared to *free* area models; see Table 5.2.

The *BB101* model tends to underestimate *idealised* discharge coefficients at large opening angles. Both EEAM and model F have small mean deviations, representing minimal systematic error over the range of available data.

The EEAM model has the lowest mean and standard deviation of all available models, with a standard deviation four times smaller than the average *free* area model, and two times smaller than the next best model.

### 5.3.3 Measurements of a square window

Section 4.4 describes an experimental setup use to measure the *idealised* discharge coefficient of a square orifice and a square hinged opening under both inflow and outflow conditions, over a range of Reynolds numbers. The *idealised* discharge coefficient of an opening is typically defined for flow rates great enough that the opening Reynolds number has an insignificant effect on the value of the *idealised* discharge coefficient.

In these experiments, slightly different values of the *idealised* discharge coefficient are evaluated for inflow and for outflow, both for the square orifice and the hinged opening. The square orifice has an *idealised* discharge coefficient of  $0.61 \pm 0.02$  for inflow, and an *idealised* discharge coefficient of  $0.57 \pm 0.02$  for outflow.

Figure 5.3 plots the measured *idealised* discharge coefficient of a square, hinged window as a function of opening angle, for both inflow and outflow. This agrees well with data from the literature [108, 124, 125], and with the predictions of the EEAM model developed in Section 5.3.1. For opening angles less than 30 degrees, *idealised* discharge coefficients corresponding to a common flow direction relative to the opening geometry (i.e. from the zone the window opens out of to the zone it opens into, or *vice versa*) are approximately equivalent. By contrast, at opening angles close to 90 degrees *idealised* discharge coefficients corresponding to a common flow direction relative to the experimental setup (i.e. inflow from the tunnel into the plenum, or outflow from the plenum into the tunnel) are approximately equivalent.

#### Dependence on Reynolds number

Figure 5.4 shows that the measured values of the *idealised* discharge coefficient are relatively independent of opening Reynolds number across the full range of measured conditions. This is true for square orifices, 90 degree openings and 5 degree openings. It is assumed that all intermediate opening angles are similarly

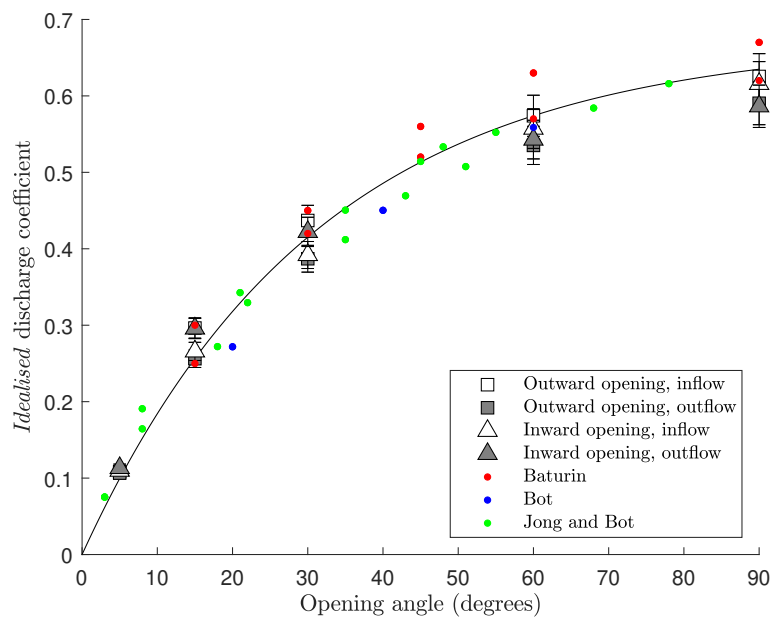


**Figure 5.3:** *Idealised* discharge coefficient of a square, butt hinged opening plotted against opening angle. Measured data is denoted by filled markers. Here, inflow and outflow through outward opening windows are denoted by white and grey squares respectively, and inflow and outflow through inward opening windows are denoted by white and grey triangles respectively. Data from Baturin [108], Bot [124], and Jong and Bot [125] are denoted by red, blue and green points respectively. The predictions of the EEAM model developed in Section 5.3.1 are given by a solid line. Error bars are shown to two standard errors.

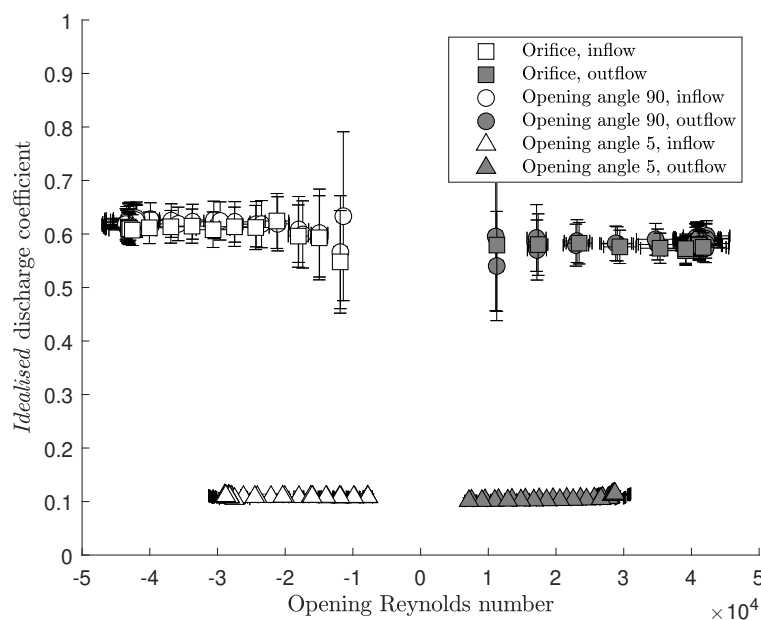


**Figure 5.4:** *Idealised* discharge coefficient plotted against opening Reynolds number. Data from a square orifice, and a butt hinged opening open to 90 degrees and 5 degrees are denoted by square, circular and triangular markers respectively. Inflow and outflow conditions are denoted by white markers and grey markers respectively. Error bars are shown to two standard errors.

**Table 5.3:** Models of *idealised* discharge coefficients in the form of Equation 5.1, their coefficients and the reduced chi squared value ( $\chi_v^2$ ) and coefficient of determination ( $R^2$ ) of their fit.

Model	B	M	$\chi_v^2$	$R^2$
EEAM	0.67	0.032	7.5	0.98
All configurations	0.61	0.039	4.6	0.99
Outward opening, inflow	0.65	0.038	1.8	0.998
Outward opening, outflow	0.59	0.039	1.9	0.996
Inward opening, inflow	0.62	0.037	4.0	0.99
Inward opening, outflow	0.59	0.043	1.3	0.997

independent of Reynolds number.

At low Reynolds numbers, the magnitude of the pressures being measured is not large compared to the zero error in the differential manometers, meaning substantial systematic errors are possible.

### Empirical modelling of measured data

With measured data, error analysis enables the use of the reduced chi squared value to assess the quality of fit. The EEAM model described in Section 5.3.1 has a reduced chi squared value of 7.5 when compared against measured data, a standard deviation between predicted and measured *idealised* discharge coefficients of 0.026, and a coefficient of determination of 0.98.

With measured data, the coefficients of Equation 5.1 can be refitted for specific opening configurations. Section 5.3.3 identified that values of the *idealised* discharge coefficient vary depending on the direction of flow through the opening, and whether the window opens into or out of the plenum chamber. Table 5.3 shows the reduced chi squared values achieved using the EEAM model, Equation 5.1 refitted using all measured data, and Equation 5.1 refitted for all ventilation configurations separately. The fitted values of the coefficients  $B$  and  $M$  are given in each case. The use of separate coefficients for each ventilation configuration significantly improves the quality of the fit in all cases. The fit quality is poorest for inflow through the inward opening window.

## 5.4 Local pressure phenomena in a cross-flow

The *local* pressure coefficient characterises the pressure evolved at the surface of an opening due to interaction with a cross-flow when no flow occurs through that opening; see Sections 3.5.2 and 4.4.7. This can be considered a fundamental aerodynamic property of an opening in the same manner as its *idealised* discharge coefficient. The *local* pressure coefficients used to characterise an opening are defined at flow rates great enough that the cross-flow Reynolds number has an insignificant effect on its value.

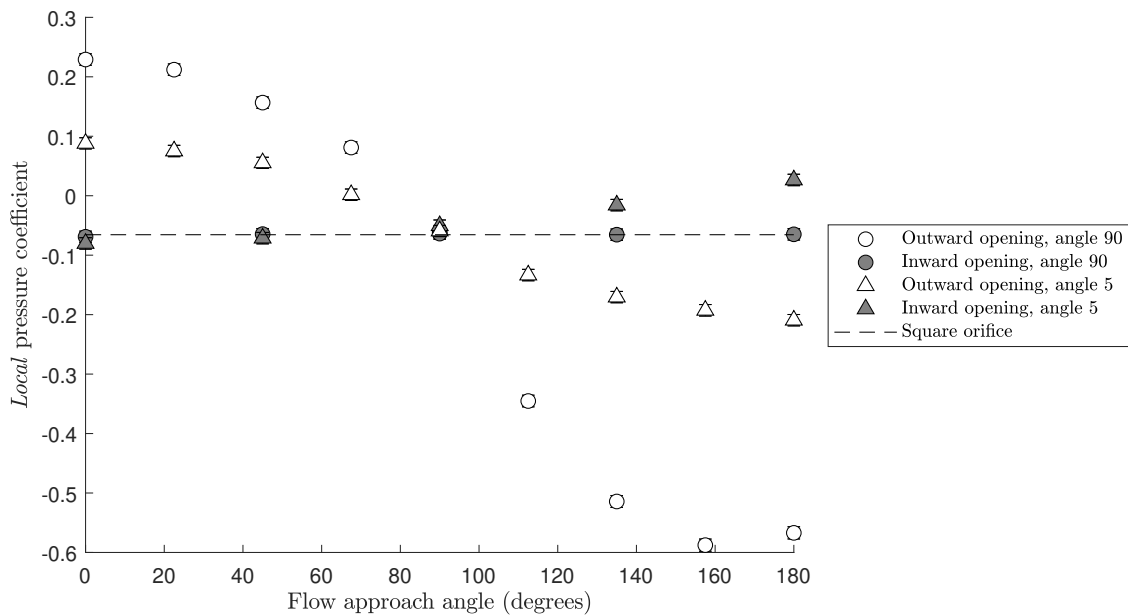


**Figure 5.5:** *Local* pressure coefficient plotted against the flow approach angle. Data from square, hinged openings open to 90 degrees and 5 degrees are denoted by circular and triangular markers respectively. Outward and inward opening windows are denoted by white markers and grey markers respectively, with the *local* pressure coefficient for a square orifice denoted by a dashed line. Error bars are shown to two standard errors. Error bars smaller than the markers have been omitted.

#### 5.4.1 Local pressure coefficients of a square window

Figure 5.5 plots the *local* pressure coefficient against flow approach angle for a range of opening angles, and Figure 5.6 plots the *local* pressure coefficient against opening angle for a range of flow approach angles.

The *local* pressure coefficient for a square orifice is independent of the direction of the cross-flow. As the geometry of the orifice does not project into the cross-flow, it might be expected to have a *local* pressure coefficient of zero. However, the *local* pressure coefficient of the square orifice has a measured value of  $-0.0655 \pm 0.005$ .

For outward opening windows, the *local* pressure coefficient of hinged openings is a function of the flow approach angle, and is positive where the opening is upstream of the projecting window geometry, and negative where the opening is in the lee of the projecting window geometry; see Figure 5.5. A flow approach angle of 90 degrees results in *local* pressure coefficients that are equivalent to that of the square orifice for all opening angles. The greatest measured value of the *local* pressure coefficient does not occur at an opening angle of 90 degrees, where the greatest projection occurs, but closer to 60 degrees; see Figure 5.6.

The dependence of the *local* pressure coefficient on flow approach angle is much less significant for inward opening windows than for outward opening windows. For flow approach angles between 0 and 90 degrees,



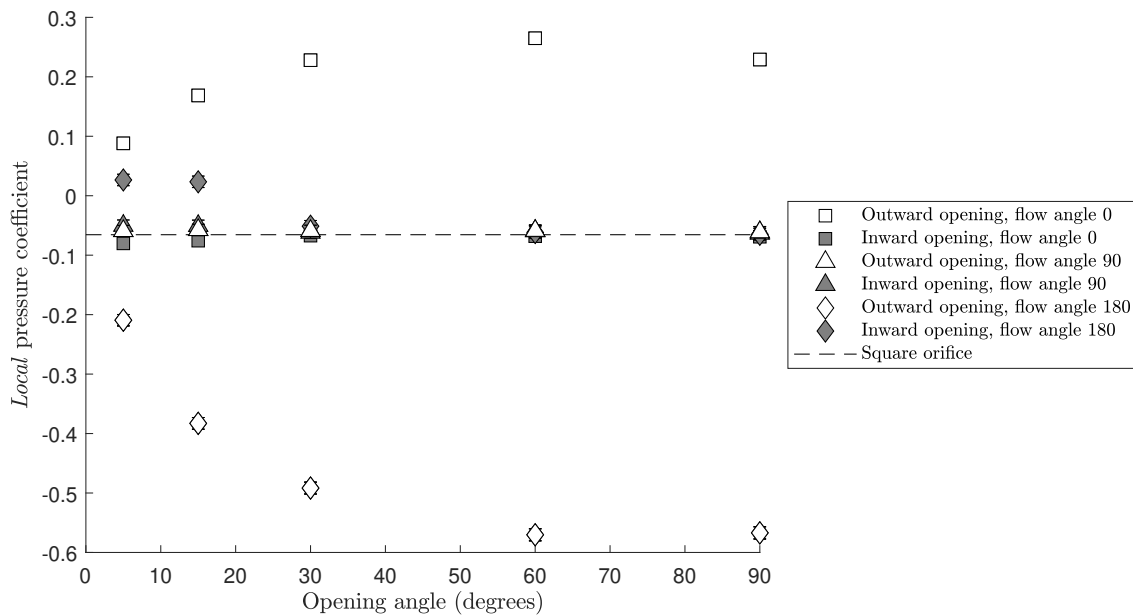


**Figure 5.6:** *Local* pressure coefficient plotted against opening angle. Data from flow approach angles of 0, 90 and 180 degrees are denoted by square, triangle and diamond shaped markers respectively. Outward and inward opening windows are denoted by white markers and grey markers respectively, with the *local* pressure coefficient for a square orifice denoted by a dashed line. Error bars are shown to two standard errors. Error bars smaller than the markers have been omitted.

where the opening vane is downstream of the opening, the *local* pressure coefficient is equivalent to that of the square orifice for all opening angles; see Figures 5.5 and 5.6. However, some dependence on opening angle is observed for flow approach angles between 90 and 180 degrees, where the opening vane is upstream of the opening; see Figure 5.5. This effect is only observed at small opening angles, and results in positive *local* pressure coefficients; see Figure 5.6.

#### 5.4.2 Dependence on Reynolds number

Figure 5.7 plots the *local* pressure coefficient against the Reynolds number in the cross-flow. For the square orifice and the hinged opening exposed to a flow approach angle of 0 degrees, the *local* pressure coefficient is not measurably dependent on Reynolds number, with variation typically being small compared to the size of the error. However, the *local* pressure coefficient of the hinged opening exposed to a flow approach angle of 180 degrees shows a weak dependence on Reynolds number. This dependence diminishes as the cross-flow Reynolds number increases.

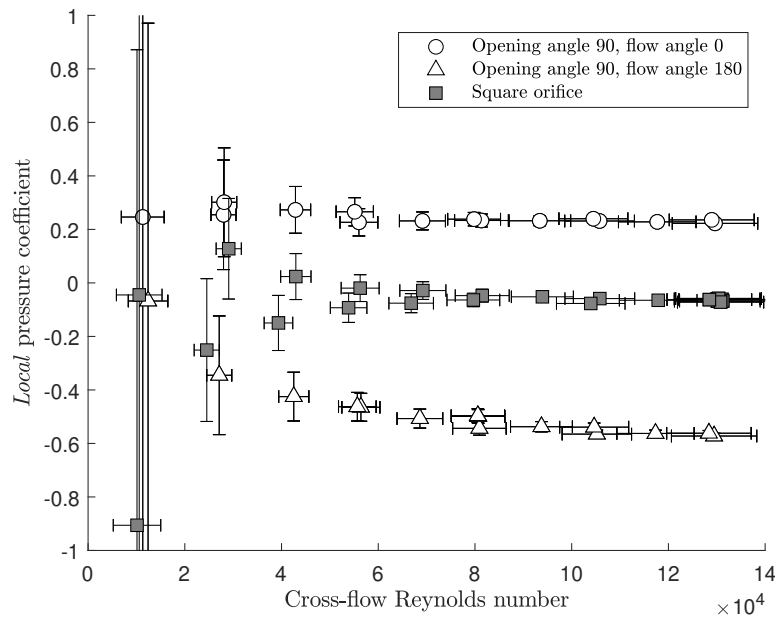


**Figure 5.7:** *Local* pressure coefficient plotted against cross-flow Reynolds number. Data from hinged windows open to 90 degrees exposed to flow approach angles of 0 and 180 degrees are denoted by white circles and triangles respectively. Data from square orifices are denoted by grey squares. Error bars are shown to two standard errors. Error bars smaller than the markers have been omitted.

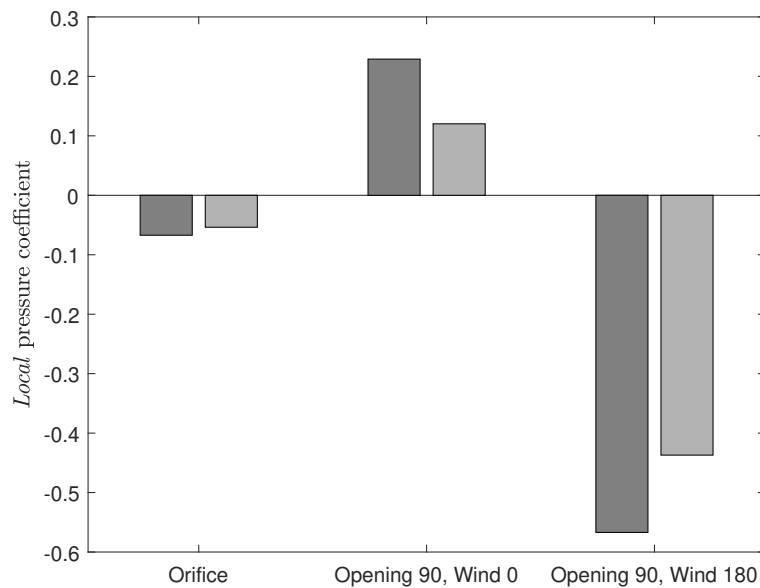


**Figure 5.8:** Comparison between the *local* pressure coefficients evaluated with the *thick* and *thin* boundary layers. Data from the *thin* boundary layer are denoted by dark grey bars, and data from the *thick* boundary layer are denoted by light grey bars.

### 5.4.3 Effect of boundary layer thickness

Figure 5.8 shows that the thicker surface boundary layer results in a 20% to 40% reduction in the magnitude of *local* pressure coefficients. The percentage reduction in *local* pressure coefficient resulting from the change in surface boundary layer is dependent on the flow approach angle, which shows that the selection of an appropriate location with which to measure the cross-flow velocity is not sufficient to account for this effect. Nevertheless, measuring the cross-flow velocity at a distance of one opening length above the surface of the opening reduces the change in *local* pressure coefficient attributable to the thicker surface boundary layer to between 10% and 15%. This is about 90% smaller than the variation in *local* pressure coefficient attributable to variation in flow approach angle.

### 5.4.4 Empirical modelling of local pressure coefficients

The *local* pressure coefficient of a square orifice is a constant, with a value of  $-0.0655 \pm 0.005$ ; see Section 5.4.1. However, the *local* pressure coefficient of hinged openings is a function of both opening angle and flow approach angle. To decompose the relationship into two single variable functions, a primary variable must be selected with which to create a family of curves; see Section 4.3. Limits on fitted *local* pressure coefficient values are easier to specify when considering the relationship between the *local* pressure coefficient and opening angle; see Section 4.3.1. Furthermore, the relationship between the *local* pressure coefficient and opening angle is formally simpler than its relationship with flow approach angle, and therefore should require fewer coefficients to characterise. For these reasons, the opening angle is selected as the primary variable, and the flow approach angle as the secondary variable.

The selection of shape functions to fit the data results in the following expressions:

$$C_{PL}(\phi) = a + C_1\phi^n + C_2\phi^2 \quad (5.5)$$

$$C_1 = b_1 + b_2\cos(\beta) \quad (5.6)$$

$$n = c_1 + c_2\cos(\beta) + c_3\cos(2\beta) + c_4\cos(3\beta) \quad (5.7)$$

$$C_2 = d_1 + d_2\cos(\beta) + d_3\cos(2\beta) \quad (5.8)$$

where the opening angle  $\phi$  is measured in degrees. The form of these equations preserve key theoretical behaviours: the predicted *local* pressure coefficient tends to a constant value independent of flow approach angle as the opening angle tends to zero, and predicted *local* pressure coefficients are symmetrical about a flow approach angle of zero degrees, and periodic in 360 degrees. The coefficients are fitted using an

**Table 5.4:** Fitted coefficients of Equations 5.5-5.8 and the resultant regression statistics.

<b>Coefficients</b>	
<b>a</b>	-0.051
<b>b<sub>1</sub></b>	$-0.42 \times 10^{-3}$
<b>b<sub>2</sub></b>	0.072
<b>c<sub>1</sub></b>	0.51
<b>c<sub>2</sub></b>	-0.073
<b>c<sub>3</sub></b>	-0.026
<b>c<sub>4</sub></b>	0.013
<b>d<sub>1</sub></b>	$2.8 \times 10^{-6}$
<b>d<sub>2</sub></b>	$-33 \times 10^{-6}$
<b>d<sub>3</sub></b>	$4.6 \times 10^{-6}$
<b><math>\chi_v^2</math></b>	<i>6.5</i>
<b>R<sup>2</sup></b>	0.98

error-weighted least-squares minimisation, and are given in Table 5.4. This results in a reduced chi-squared value of 6.5, and a coefficient of determination of 0.98.

Figure 5.9 plots the relationship between measured and predicted *local* pressure coefficients. Figure 5.10 plots the predicted and measured *local* pressure coefficient curves as a function of opening angle and flow approach angle. Here the visual agreement is good, and the robustness of interpolation is evident. Poorer agreement is evident for the flow approach angle of 112.5 degrees, where the predictive equation systematically underestimates the magnitude of *local* pressure coefficients.

## 5.5 Aerodynamic resistance in a cross-flow

Dynamic tests enable the characterisation of volume flow rates through openings in the presence of a cross-flow. Here, ventilation capacity is characterised as a function of the dimensionless room pressure. To reduce complexity, characterisation curves are defined only in the region where flow rates are sufficiently large that the ventilation capacity is relatively independent of Reynolds number. Here, the *idealised* discharge coefficients represent the asymptotes of the plot that occur where the dimensionless room pressure tends to  $\pm\infty$ . The *local* pressure coefficient represents the value of the dimensionless room pressure where net flow through the window transitions between inflow and outflow.

### 5.5.1 Comparison with literature data

The results presented in this chapter are measured for a square openings. This geometry was chosen due to its symmetry, formal simplicity, and the lack of ambiguity as to which edge the hinged window is mounted. However, data from the literature is restricted to rectangular orifices with an aspect ratio of 2:1 [66, 105]. These may be expected to behave similarly to the square orifice due to their planar nature, as neither the

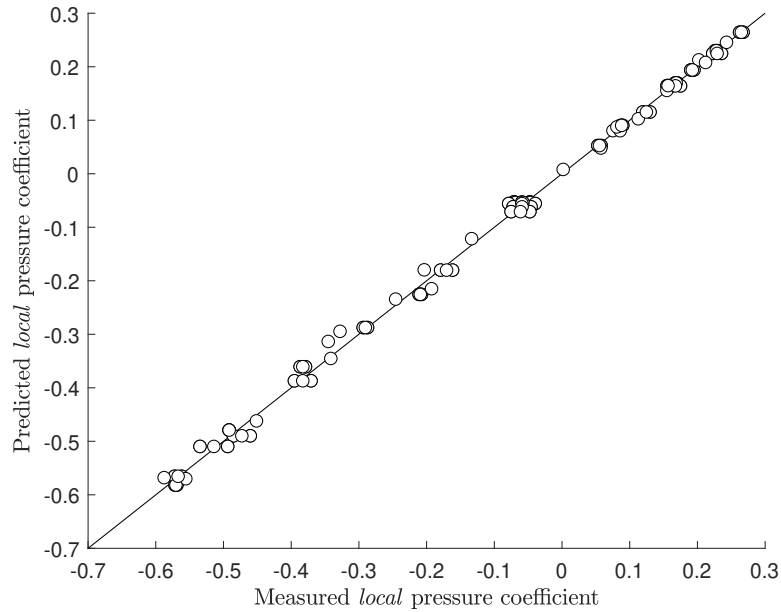


**Figure 5.9:** Comparison between measured values of the *local* pressure coefficient and those predicted using Equation 5.5.

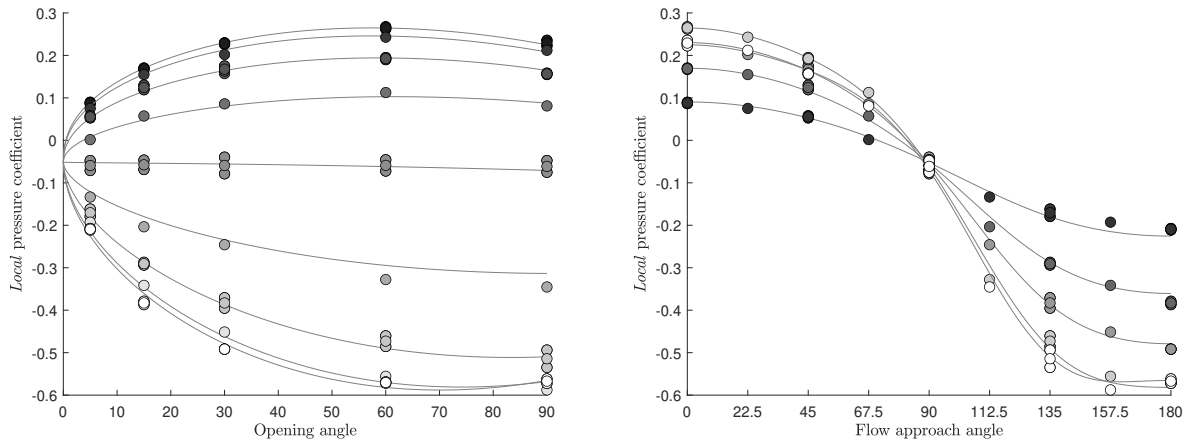


**Figure 5.10:** Plot of the measured and predicted *local* pressure coefficients as a function of opening angle (left), and flow approach angle (right). Measured values of the *local* pressure coefficient are denoted by circular markers, and the predictions of Equation 5.5 are denoted by grey lines. In the left plot, markers are coloured based on their corresponding flow approach angle, with a flow approach angle of 0 degrees denoted by black markers and a flow approach angle of 180 degrees denoted by white markers. Conversely, in the right plot, markers are coloured based on their corresponding opening angle, with an opening angle of 5 degrees denoted by black markers, and an opening angle of 90 degrees denoted by white markers.

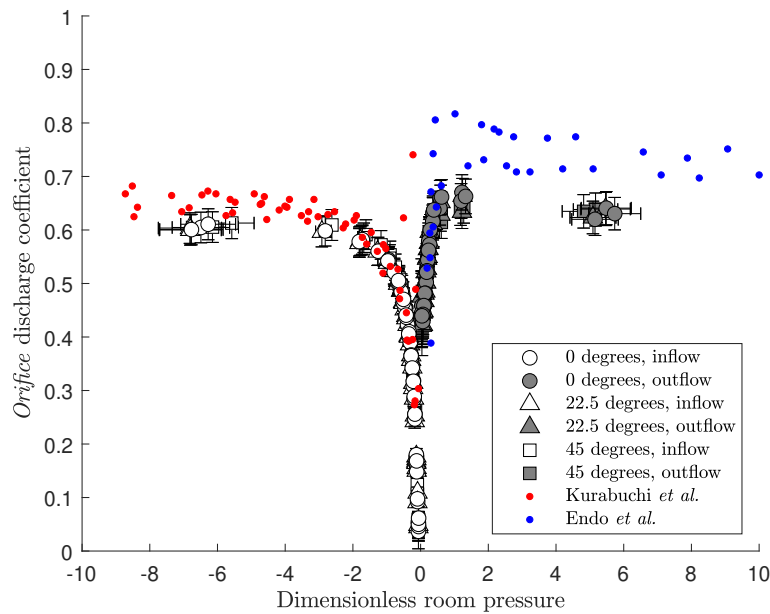


**Figure 5.11:** *Orifice* discharge coefficient of a square orifice plotted against dimensionless room pressure. Measured data for a square orifice is denoted by filled markers. Here, a flow approach angle of 0 degrees is denoted by circle markers, a flow approach angle of 22.5 degrees by triangle markers, and a flow approach angle of 45 degrees by square markers. Inflow conditions are denoted by white markers, and outflow conditions by grey markers. Error bars indicate two standard errors. Inflow measurements presented by Kurabuchi *et al.* are denoted by red dots [66], and outflow measurements presented by Endo *et al.* are denoted by blue dots [105]. All literature data represents measurements for a 2:1 aspect ratio rectangular orifice.

square or rectangular orifices interfere significantly with the horizontal component of streamline velocities. Furthermore, *idealised* discharge coefficients have been shown to exhibit only weak dependence on aspect ratio [124]. This allows the two sets of data to be compared.

Figure 5.11 compares the *orifice* discharge coefficient measured for a square opening in a cross-flow with data for rectangular orifices presented by Kurabuchi *et al.* and Endo *et al.* [66, 105]. For inflow, good agreement is found between the experimental results and those cited in the literature. This data extends the literature results to consider dimensionless room pressure values closer to zero, and suggests that the *orifice* discharge coefficient can be reduced completely to zero. The values of the *orifice* discharge coefficient measured here are slightly lower than those found in the literature. This is reflected in a difference in the measured value of the *idealised* discharge coefficient.

### 5.5.2 Choice of characteristic parameter

As discussed in Chapters 2 and 3, there are multiple methods of defining characteristic parameters with which to describe volume flow rates through openings. Figure 5.12 presents data for a hinged opening open to 90 degrees, exposed to a flow approach angle of 0 degrees, using a range of different characteristic parameters. In all cases, the *local* pressure coefficient corresponds to the value of the dimensionless room pressure where airflow transitions between inflow and outflow.

Here, the use of the *orifice* discharge coefficient results in calculated values that tend to  $\pm\infty$  as the dimensionless room pressure approaches zero. This effect can be eliminated by using the local pressure defined by the *local* pressure coefficient to specify the external pressure. Here, the corrected *orifice* discharge coefficient rises to a peak that is significantly greater than the *idealised* discharge coefficient asymptote. This peak occurs at relatively low values of the dimensionless room pressure.

The use of the *Bernoulli* discharge coefficient results in simpler curve behaviour, tending to zero as the *local* pressure coefficient is approached, and to the *idealised* discharge coefficient as the dimensionless room pressure tends to  $\pm\infty$ . All intermediate values of the *Bernoulli* discharge coefficient occur within this range. Similar behaviour is observed when using the *total* dimensionless volume flow rate. However, here inflow and outflow conditions can be readily differentiated by the sign of the *total* dimensionless volume flow rate. In addition, the curve reads as a single continuous function, as opposed to separate discontinuous performance curves for inflow and outflow. For these reasons, in addition to the generalisation benefits described in Section 3.2, the *total* dimensionless volume flow rate is henceforth used to describe airflow characteristics, as depicted in the bottom right of Figure 5.12.

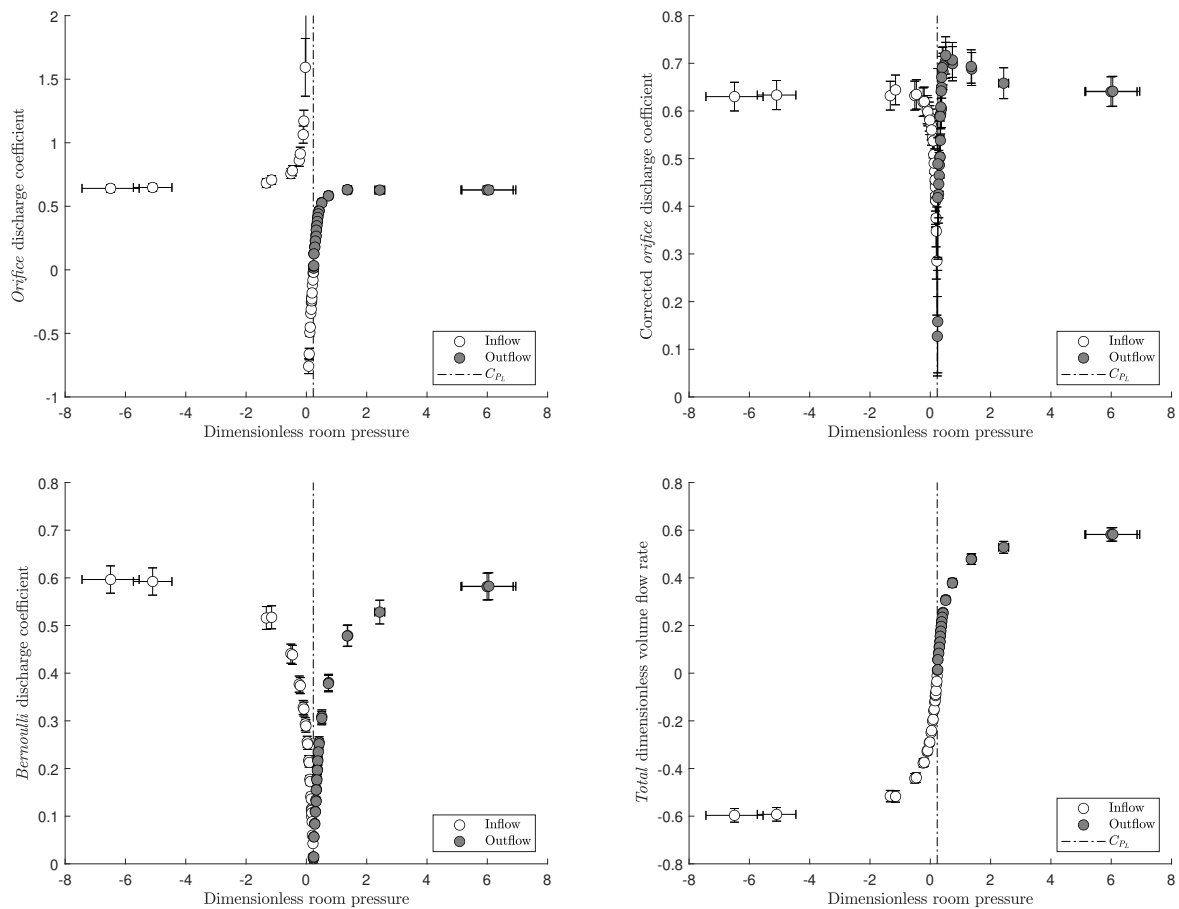


**Figure 5.12:** Alternative characteristic parameters for describing volume flow rate through openings, plotted against dimensionless room pressure. Data is presented for a square, hinged, outward opening window open to 90 degrees, exposed to a flow approach angle of 0 degrees. The top left utilises the *orifice* discharge coefficient; the top right corrects the *orifice* discharge coefficient to account for the effect of *local* pressure coefficients; the bottom left utilises the *Bernoulli* discharge coefficient; and the bottom right depicts the *total* dimensionless volume flow rate. Error bars are shown to two standard errors.



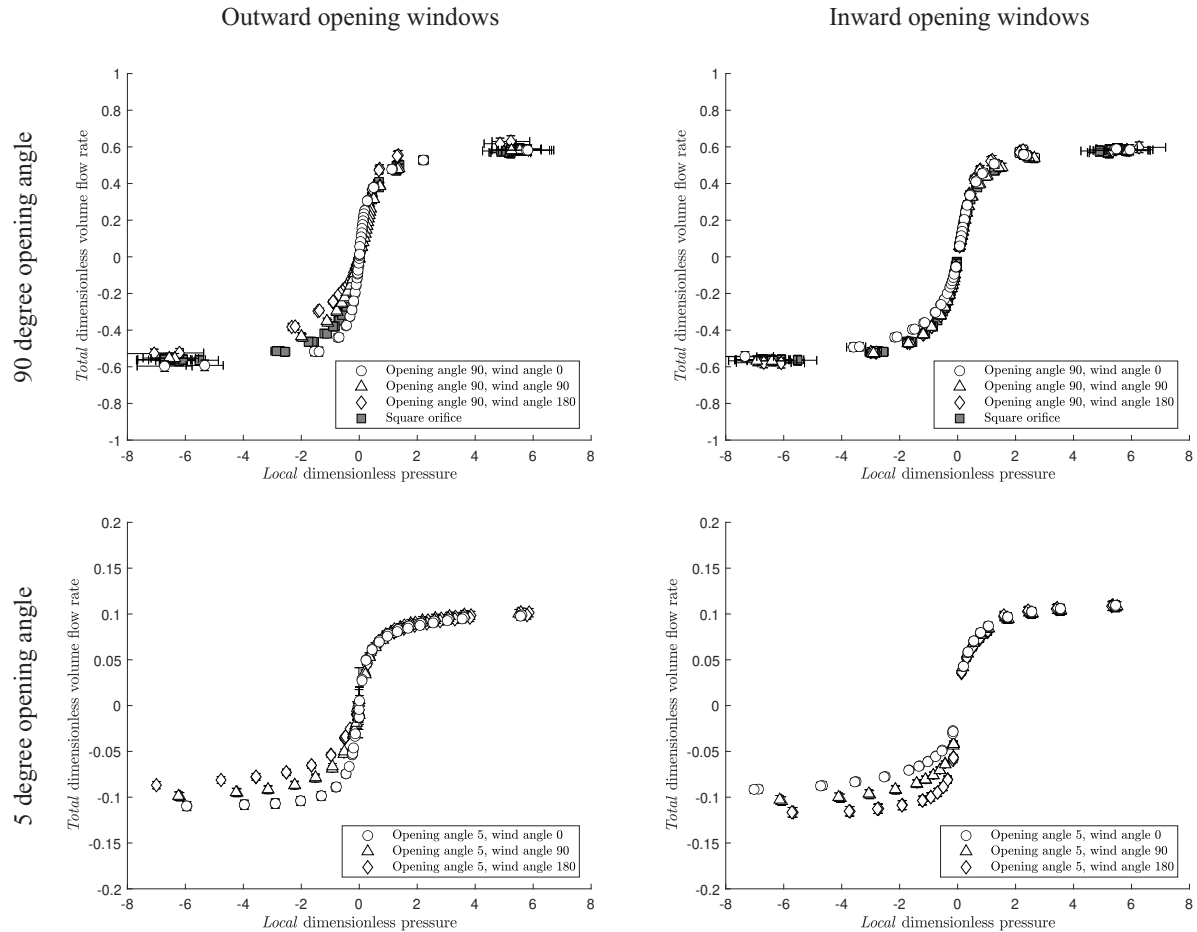


**Figure 5.13:** Plot of the *total* dimensionless volume flow rate against *local* dimensionless pressure. Data for windows open to 90 and 5 degrees are presented in the top and bottom rows respectively, and data for outward and inward opening windows are presented in the left and right columns respectively. Flow approach angles of 0, 90, and 180 degrees are denoted by circle, triangle and diamond markers respectively. All flow approach angles for the square orifice are denoted by grey squares. Error bars are shown to two standard errors.

### 5.5.3 Aerodynamic resistance of a square hinged opening

Figure 5.13 plots the relationship between *total* dimensionless volume flow rate and *local* dimensionless pressure for a range of different opening angles and flow approach angles, for both inward and outward opening windows. Here, outflow conditions hold positive values of both the *total* dimensionless volume flow rate and *local* dimensionless pressure, with negative values corresponding to inflow conditions. A *local* dimensionless pressure of zero corresponds to the no flow condition, where the dimensionless room pressure is equal to the *local* pressure coefficient for the window geometry and flow approach angle in question.

For all window configurations, the outflow performance curve appears to be significantly less dependent on flow approach angle than that for inflow.

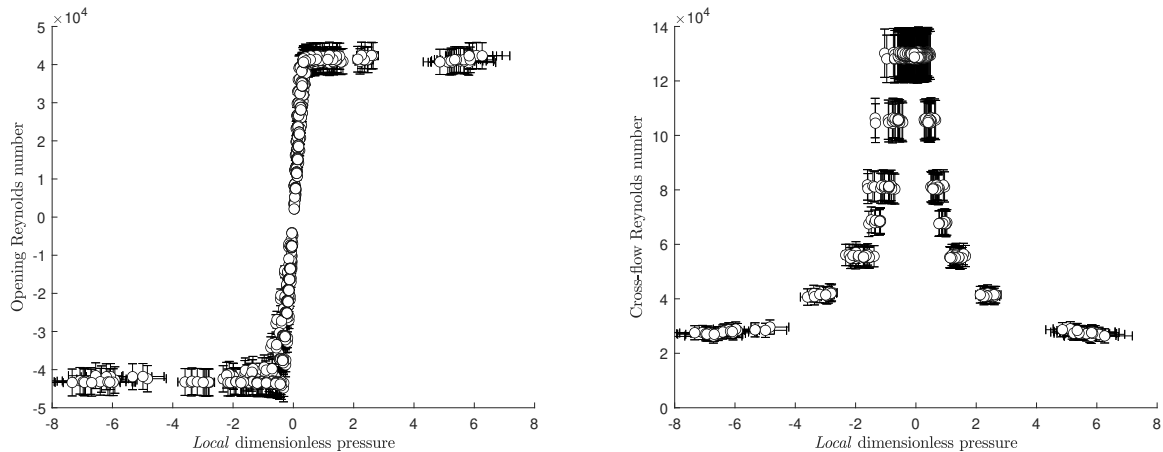


**Figure 5.14:** Reynolds number achieved during dynamic tests against *local* dimensionless pressure. Data are plotted for butt hinged windows open to 90 degrees, across the full range of flow approach angles tested. The left plot depicts the opening Reynolds number, and the right plot depicts the Reynolds number in the cross-flow. Error bars are shown to two standard errors.

For inflow through outward opening windows, openings exposed to flow approach angles closer to 180 degrees have a performance curve with a shallower gradient than those for openings exposed to flow approach angles closer to 0 degrees. For inflow through inward opening windows, performance curves closely match that of the square orifice for all wind angles when the opening angle is large. However, for small opening angles windows exposed to flow approach angles closer to 0 degrees have a performance curve with a shallower gradient than those for openings exposed to flow approach angles closer to 180 degrees.

Complete cross-flow characterisation curves are presented in Appendix F for all opening types tested, and all combinations of opening angle and flow approach angle measured.

#### 5.5.4 Dependence on Reynolds number

*Total* dimensionless volume flow rates at high magnitudes of the *local* dimensionless pressure are likely to be most strongly affected by the value of the *idealised* discharge coefficient, and therefore the Reynolds number of greatest interest here is the opening Reynolds number. Conversely, *total* dimensionless volume flow rates at low values of the *local* dimensionless pressure are likely to be most strongly affected by the value of the *local* pressure coefficient, and therefore the Reynolds number of greatest interest here is the cross-flow Reynolds number.

Figure 5.14 illustrates the Reynolds numbers achieved over the course of the experiments as a function of *local* dimensionless pressure. Here, the highest opening Reynolds numbers are achieved where the magnitude of the *local* dimensionless pressure is high, and lowest where the magnitude of the *local* dimensionless pressure is low. Conversely, the cross-flow Reynolds number is greatest where the magnitude of the *local* dimensionless

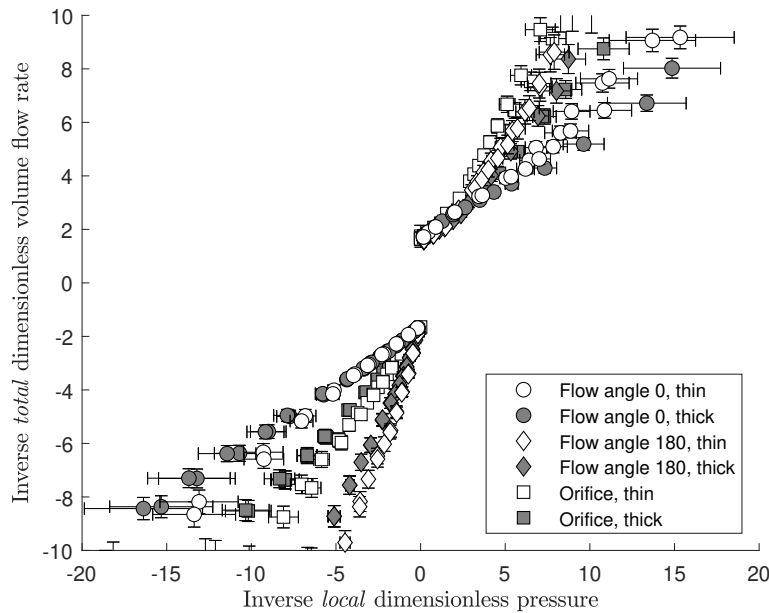


**Figure 5.15:** Plot of the inverse *total* dimensionless volume flow rate against the inverse *local* dimensionless pressure for a range of opening geometries exposed to a cross-flow with either a *thick* or *thin* boundary layer. Data from hinged openings open to 90 degrees and exposed to a flow approach angle of 0 and 180 degrees are denoted by circle and diamond markers respectively. Data from a square orifice are denoted by square markers, and data from *thin* and *thick* boundary layers are denoted by white and grey markers respectively. Error bars are shown to two standard errors.

pressure is small, and greatest when it is largest. Consequently, the relevant Reynolds numbers are maximised in the regions where they are most likely to have an impact on *total* dimensionless volume flow rates. This ensures that the measured *total* dimensionless volume flow rates are likely to be independent of Reynolds number across the measured *local* dimensionless pressure range.

### 5.5.5 Effect of boundary layer thickness

Figure 5.15 presents the plot of the inverse *total* dimensionless volume flow rate against the inverse of *local* dimensionless pressure for a range of opening geometries exposed to a cross-flow with either a *thick* or *thin* boundary layer. Here, the  $y$ -intercept denotes still-air conditions. Inflow and outflow conditions are denoted by negative and positive values respectively of both the inverse *local* dimensionless pressure and the inverse *total* dimensionless volume flow rate.

The thicker surface boundary layer results in a 15% to 40% reduction in gradient compared to data acquired using the *thin* boundary layer. When the change in *local* pressure coefficients is accounted for, openings of all types achieve higher *total* dimensionless volume flow rates in the *thick* boundary layer scenario than the *thin* boundary layer scenario. Measuring the cross-flow velocity at a distance of one opening length

above the surface of the opening reduces the change in gradient attributable to the thicker surface boundary layer to between 5% and 25%, with an average error of 10%. This is about 85% smaller than the variation in gradient that arises due to changes in opening geometry and flow approach angle.

### 5.5.6 Empirical modelling of *total* dimensionless volume flow rates

The *total* dimensionless volume flow rate is dependent on three parameters: the *local* dimensionless pressure; the opening angle, and the flow approach angle. The general approach described in Section 4.3 is used to decompose the relationship into a set of single variable functions.

The selection of shape functions to fit the data results in the following expressions:

$$\frac{C_{dI}}{Q_T^*} = S_i + C_1 \left| \frac{1}{P_L^*} \right|^n \quad (5.9)$$

$$S_i = \frac{|P_L^*|}{P_L^*} \quad (5.10)$$

$$C_1 = k_1 + k_2 \cos(\beta) \quad (5.11)$$

$$n = k_3 + k_4 \cos(\beta) \quad (5.12)$$

$$k_1 = a_0 + a_1 \phi + a_2 \phi^2 \quad (5.13)$$

$$k_2 = b_0 + b_1 \phi + b_2 \phi^2 \quad (5.14)$$

$$k_3 = c_0 + c_1 \phi \quad (5.15)$$

$$k_4 = d_0 + d_1 \phi \quad (5.16)$$

The form of these equations preserve key theoretical behaviours: the magnitude of the predicted *total* dimensionless volume flow rate tends to the *idealised* discharge coefficient as the *local* dimensionless pressure tends to  $\pm\infty$ ; the predicted *total* dimensionless volume flow rate tends to zero as the *local* dimensionless pressure tends to zero; and predicted *total* dimensionless volume flow rates are symmetrical about a flow approach angle of zero degrees, and periodic in 360 degrees. The coefficients are fitted using an error-weighted least-squares minimisation, and are given in Table 5.5.

In contrast to hinged openings, the aerodynamic characteristics of simple square orifices are independent of the direction of the cross-flow, and are not described by an opening angle. This makes empirical curve fitting considerably simpler; the primary function defined by Equation 5.9 is sufficient to characterise performance. Table 5.6 presents the fitted coefficients and regression statistics for square orifices. Here the reduced Chi squared values are close to one, suggesting that the error in the data is sufficient to explain the

**Table 5.5:** Fitted coefficients of Equations 5.9-5.16 for inflow and outflow through inward and outward opening hinged windows, and the resultant regression statistics.

Coefficients	Outward opening		Inward opening	
	Inflow	Outflow	Inflow	Outflow
$S_i$	-1	1	-1	1
$a_0$	-0.57	0.28	-0.33	0.31
$a_1$	-0.021	$2.3 \times 10^{-3}$	$-8.0 \times 10^{-3}$	$-0.79 \times 10^{-3}$
$a_2$	$0.19 \times 10^{-3}$	$-0.026 \times 10^{-3}$	$0.058 \times 10^{-3}$	$0.23 \times 10^{-15}$
$b_0$	0.40	$0.053 \times 10^{-9}$	-0.28	$3.4 \times 10^{-3}$
$b_1$	0.021	$2.3 \times 10^{-3}$	$-5.2 \times 10^{-3}$	$-0.018 \times 10^{-3}$
$b_2$	$-0.020 \times 10^{-3}$	$-0.014 \times 10^{-3}$	$0.077 \times 10^{-3}$	$5.0 \times 10^{-18}$
$c_0$	0.96	1.14	0.89	1.03
$c_1$	$0.25 \times 10^{-15}$	$1.3 \times 10^{-3}$	$1.2 \times 10^{-3}$	$4.7 \times 10^{-3}$
$d_0$	0.23	-0.36	-0.26	$0.082 \times 10^{-12}$
$d_1$	$-1.7 \times 10^{-3}$	$0.20 \times 10^{-15}$	$2.0 \times 10^{-3}$	$6.3 \times 10^{-18}$
$\chi_v^2$	9.3	5.9	5.2	3.6
$R^2$	0.975	0.980	0.981	0.984

**Table 5.6:** Fitted coefficients of Equation 5.9 for inflow and outflow through a simple square orifice, and the resultant regression statistics.

Coefficient	Inflow	Outflow
$S_i$	-1	1
$C_1$	-0.55	0.29
$n$	1.0	1.3
$\chi_v^2$	0.35	1.3
$R^2$	0.999	0.993

deviation between predicted and measured values.

Figure 5.16 plots the relationship between predicted and measured values of the *total* dimensionless volume flow rate, normalised against the *idealised* discharge coefficient. In still-air, the normalised *total* dimensionless volume flow rate is equal to -1 and 1 for inflow and outflow respectively. Reasonably good agreement between predicted and measured values is observed for all opening types. The standard deviation between predicted and measured values of the normalised *total* dimensionless volume flow rate is 0.016 for the square orifice, 0.040 for the inward opening window, and 0.045 for the outward opening window. This suggests that the empirical equations derived here can be used to predict *total* dimensionless volume flow rates with a confidence of around 5% of still-air values. Complete cross-flow characterisation curves with measured and predicted data are presented in Appendix F.

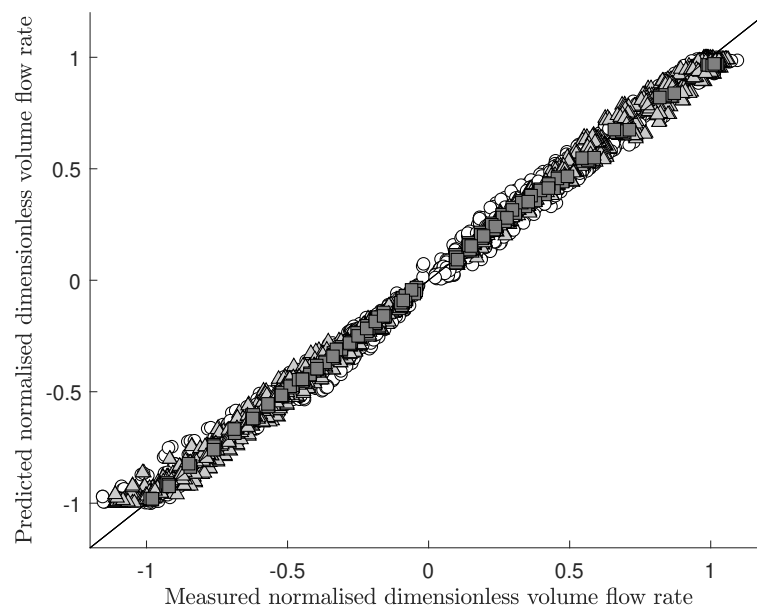


**Figure 5.16:** Plot of the relationship between measured values of the normalised *total* dimensionless volume flow rate against those predicted using the empirical equations derived in this chapter. Data for outward opening windows are denoted by white circles, data for inward opening windows are denoted by light grey triangles, and data for square orifices are denoted by dark grey squares.



## Chapter 6

# Surface flow field on a model building

### 6.1 Introduction

With conventional envelope flow models, knowledge of surface pressure coefficients are required to make estimates of volume flow rates through a building. However, the cross-flow characterisation models developed in Chapter 5 require additional environmental parameters to be specified; namely the speed and direction of the cross-flow at the location of the opening. The experiments described in this chapter measure the surface pressures and cross-flow velocities on the model building described in Section 4.7. The results of these experiments are applied in Chapter 7 to predict ventilation rates through a model building using the cross-flow characterisation models developed in Chapter 5, and compares the predictions against measured results to validate their application in natural ventilation design.

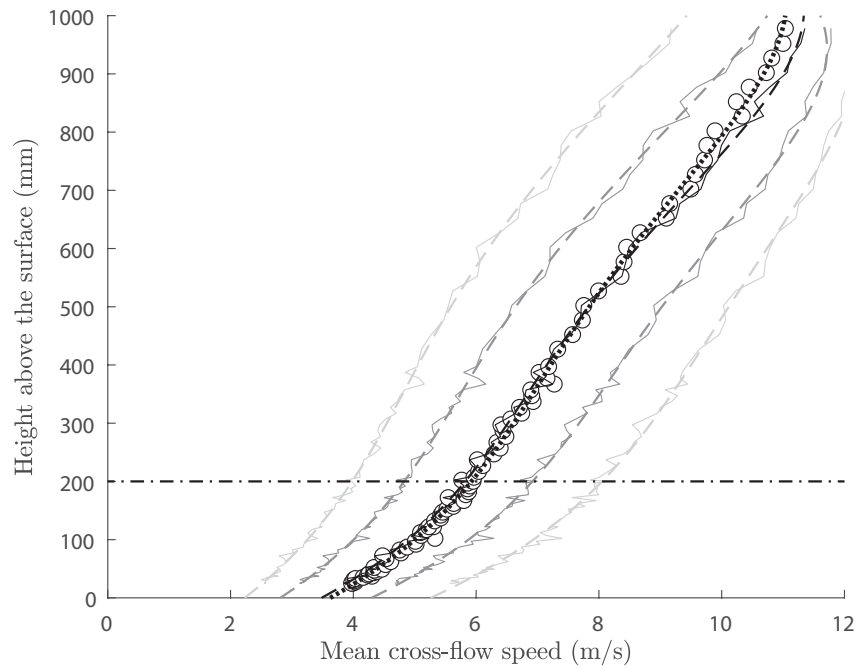
### 6.2 Approach flow

Section 2.9.3 identified the importance of generating a suitable atmospheric boundary layer in ensuring that wind tunnel studies on model buildings are representative. This Section describes the results of measurements of the ABL profile developed by the part-height barrier and mixing devices described in Section 4.7.1.

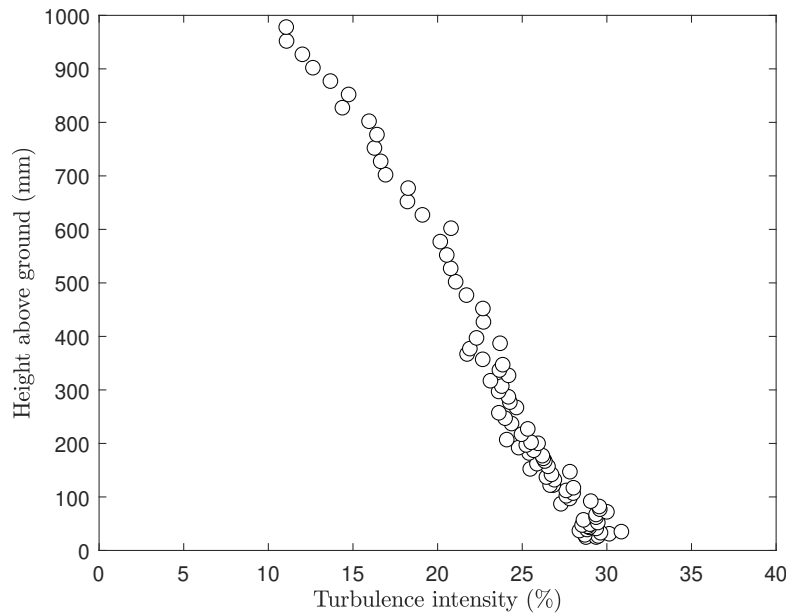
#### 6.2.1 Mean velocity profile

Figure 6.1 depicts the variation in wind velocity in the simulated atmospheric boundary layer with height. Turbulence in the flow can be seen to result in large variations in wind speed about the mean value. For design purposes, a reference velocity is defined at the height of the building, here equal to 200mm above the surface. To calculate explicit values for this, a curve is fitted to the velocity profile. Although atmospheric boundary





**Figure 6.1:** Plot of the velocity profile in the wind tunnel with height. The mean wind speed is denoted by circles. The median is denoted by a black line, the 25th and 75th centiles by a dark grey line, and the 9th and 91st centiles by a light grey line. A polynomial fit for the mean is denoted by a dotted line, and polynomial fits for the centiles are denoted by dashed lines. The height of the model building within the wind tunnel is denoted by a dashed and dotted line.



**Figure 6.2:** Plot of the turbulence intensity in the wind tunnel with height. The height of the model building within the wind tunnel is denoted by a dashed and dotted line.

layers are typically described using a power law model or log-law model [5], a fourth order polynomial is used here for accuracy of interpolation. This can then be used to evaluate a single mean velocity at any height in the tunnel. The same approach is taken to evaluate the velocity profile at a range of centiles so the temporal variation in velocity can be mapped.

A power law fit to the bottom 200mm of the surface boundary layer yields an exponent of *circa* 0.20. This is consistent with ABL profiles presented in the literature for suburban boundary layer flows, where flow exponents in the range of 0.09-0.25 are reported [61, 172, 57, 168].

### 6.2.2 Turbulence intensity in the approach flow

Figure 6.2 depicts the turbulence intensity in the atmospheric boundary layer with height. Here, the turbulence intensity is greatest close to ground level, and decays with height above the surface. Across the building height, turbulence intensities in the range of 24% – 31% are measured. This is consistent with part-height simulations of the atmospheric boundary layers over suburban terrain reported in the literature [168]. The average longitudinal turbulence intensity measured using the pitot-static tube mounted at building height is equal to 26.7%. This is slightly higher than the turbulence intensity measured using the hot-wire anemometer, which results in an average turbulence intensity at building height of 25.2%.

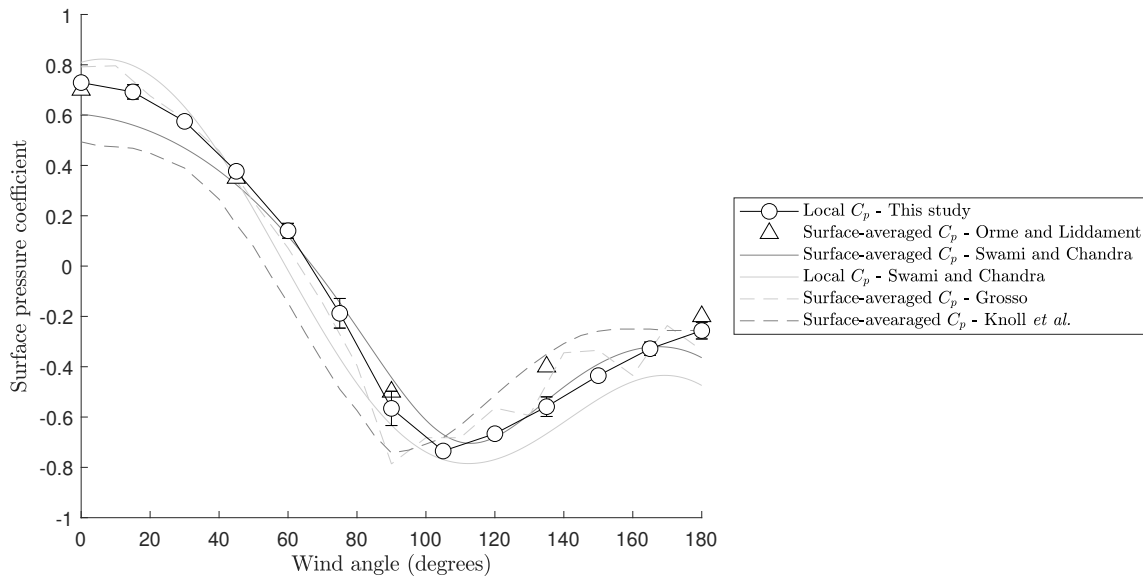


**Figure 6.3:** Comparison between measured surface pressure coefficients on the model building and surface pressure coefficients given in the literature. Surface pressure coefficients measured on the centre of a façade of the model building as depicted in Figure 4.27 are denoted by circular markers. Tabulated surface-averaged pressure coefficients collated by Orme and Liddament are denoted by triangular markers [94, 3]. Surface-averaged and local surface pressure coefficient correlations for the centre-point of a cube building presented by Swami and Chandra [84] are denoted by solid dark grey and light grey lines respectively, and surface pressure correlations presented by Grosso [91], and Knoll *et al.* [92] are denoted by dashed light and dark grey lines respectively. Error bars are shown to two standard errors. Error bars smaller than the markers have been omitted.

## 6.3 Surface pressure field

Both conventional envelope flow models and the window characterisation models developed in Chapter 5 require the measurement of surface pressure coefficients to predict ventilation rates. However, Section 2.4.1 identifies significant variation in surface pressure coefficients measured in the literature. Consequently, the selection of accurate surface pressure coefficients for validation studies requires wind-tunnel measurements. This section describes the measurements of surface pressure coefficients on a model cube, with and without opening windows present.

### 6.3.1 Surface pressure coefficients

Figure 6.3 presents the experimentally measured time-averaged surface pressure coefficient profile measured using a surface pressure tapping in the middle of the façade of the model building depicted in Figure 4.27, and compares the results with data and predictive models from the literature [95, 3, 84, 91, 92]. This shows good agreement between the surface pressure coefficients measured in this study and those derived from

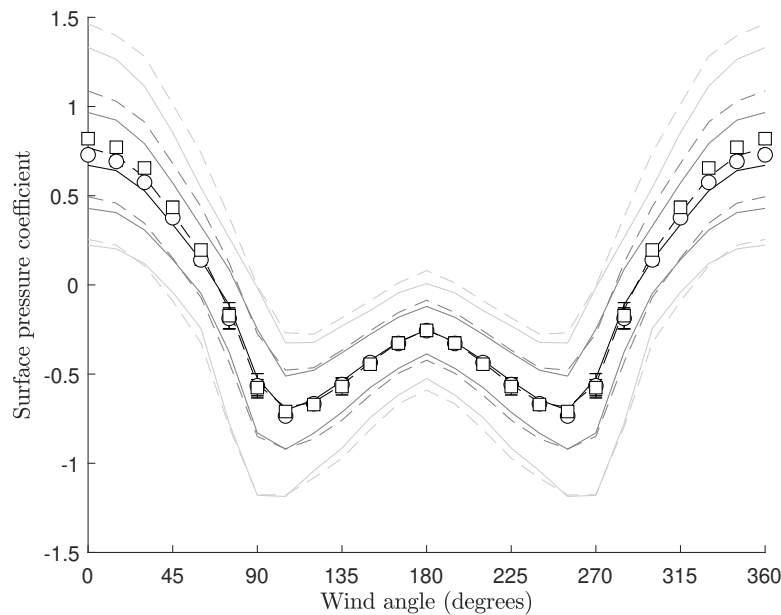


**Figure 6.4:** Plot of the measured surface pressure coefficients against wind angle for a surface pressure tapping (denoted by circle markers), and a square opening (denoted by square markers) on the centre of a façade; see Figure 4.27. The median; 25th and 75th centiles; and 9th and 91st centiles are denoted by black, dark grey and light grey lines respectively. A dashed line is used to represent the centiles for the square opening, and a solid line for those of the surface pressure tapping. Error bars are shown to two standard errors. Error bars smaller than the markers have been omitted.

literature data.

Figure 6.4 illustrates the surface pressure coefficient profile measured directly with a pressure tapping, and the opening pressure coefficient profile for a square opening, where the internal pressure of the space is measured as a proxy for the surface pressure; see Section 4.7.3. The two curves show good agreement. Here, the curves are periodic about 360 degrees, and symmetric about 180 degrees. At wind angles close to zero degrees the agreement between the two curves becomes worse. Here, the pressure coefficient measured with the square opening exceeds the surface pressure coefficient measurements by as much as 10%.

Figure 6.5 plots the standard deviation in instantaneous surface pressure coefficients measured with the surface pressure tapping and the square opening. This is a measure of the spread of the data, or how much the measured pressure varies. Here a general trend is observed where the greatest variance occurs on upwind surfaces near the stagnation zone, decreasing to a minimum in the building's wake. This trend is interrupted by a spike in variance that occurs near 90 degrees, where conditions at the opening might be expected to be affected by flow separation and vortex shedding as wind flows around the building. The standard deviation is generally greater for the square opening than for the surface pressure coefficients measured with the pressure tapping.

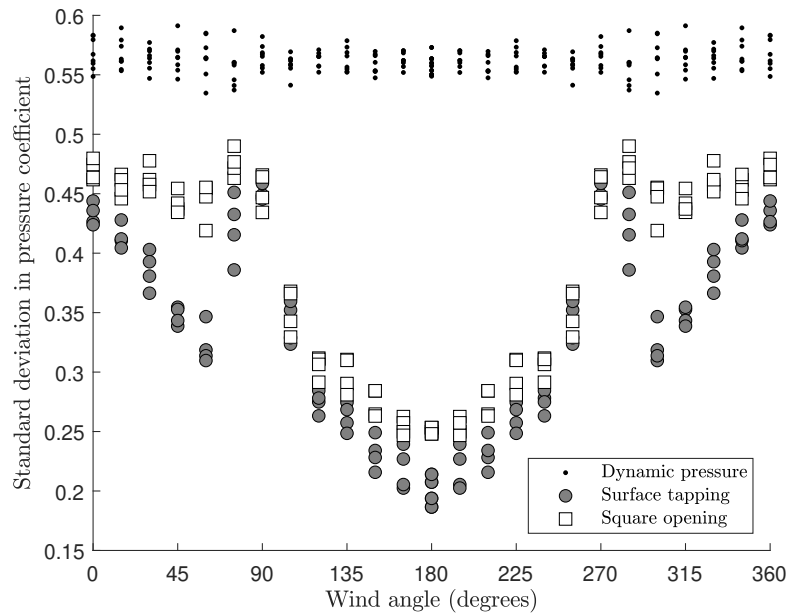


**Figure 6.5:** Plot of the standard deviation in measured surface pressure coefficients against wind angle. Values for the square opening are denoted by square markers, values for the surface pressure tappings are denoted by circle markers, and values for the dynamic pressure in the atmospheric flow are denoted by points.

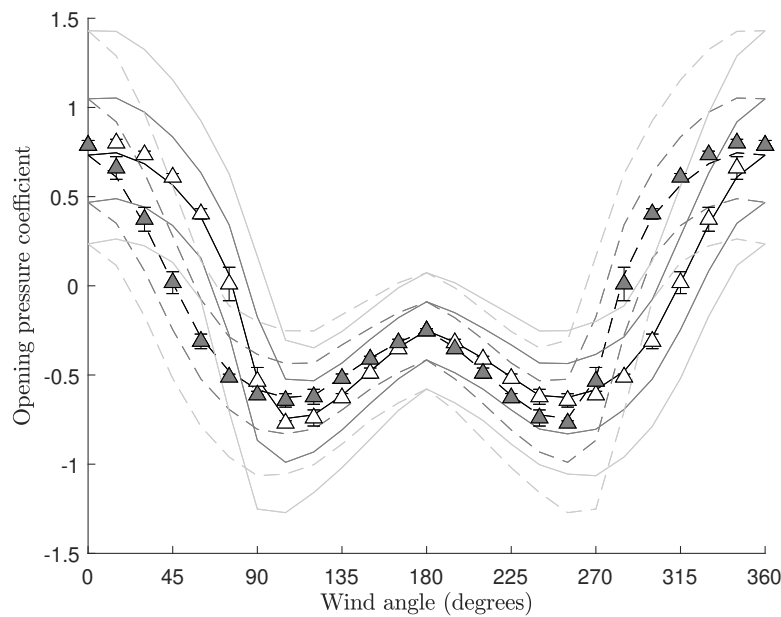
### 6.3.2 Window-integrated surface pressures

Figure 6.6 shows how the measured opening pressure coefficient varies with wind angle for left and right mounted side-hung windows. It is clear from this figure that the interaction between the opening geometry and the wind causes significant changes to the mean opening pressure coefficients. This interaction gives the opening pressure coefficient curve marked asymmetry. The opening pressure coefficients for the left-mounted opening can be related to those of the right-mounted opening according to Equation 4.52.

Figure 6.7 shows that hinged openings exhibit a similar degree of variation to that of the square opening. There are, however, a few differences. For the left-mounted opening, the variation is greatly increased around 90 degrees, and suppressed around 270 degrees. This relationship is inverted for the right-mounted opening.

## 6.4 Surface velocity field

In addition to measurements of surface pressure coefficients, the window characterisation models developed in Chapter 5 require measurements of the speed and direction of the cross-flow at the location of the opening. However, Chapter 2 identifies a lack of data in the literature that investigates either the steady or unsteady behaviour of a cross-flow near the surface of a building. This section describes the results of investigations



**Figure 6.6:** Plot of the measured opening pressure coefficients against wind angle for left mounted windows (denoted by white triangles) and right mounted windows (denoted by grey triangles). The median; 25th and 75th centiles; and 9th and 91st centiles are denoted by black, dark grey and light grey lines respectively. A dashed line is used to represent the centiles for the right mounted windows, and a solid line for those of the left mounted windows. Error bars are shown to two standard errors. Error bars smaller than the markers have been omitted.

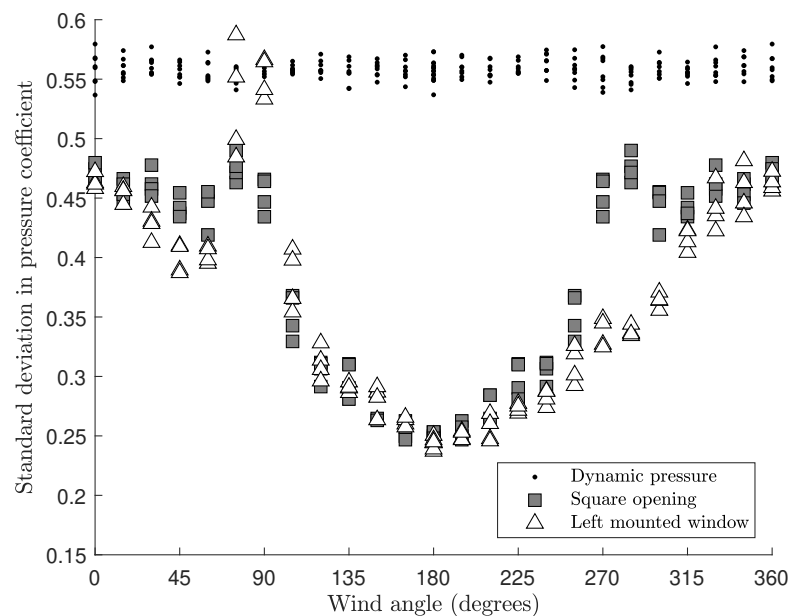


**Figure 6.7:** Plot of the standard deviation in measured opening pressure coefficients against wind angle. Left-mounted windows are denoted by white triangles, square openings by squares, and the dynamic pressure coefficient is denoted by points.

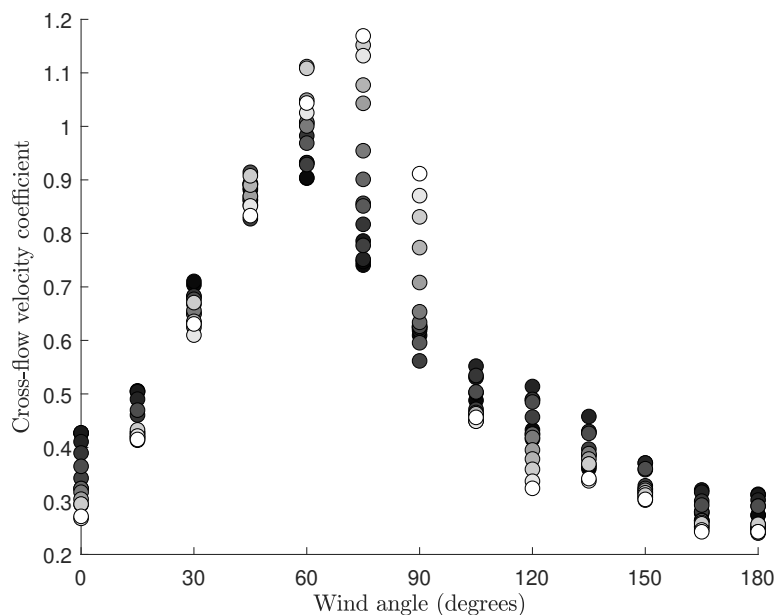


**Figure 6.8:** Plot of the cross-flow velocity coefficient measured with the hot-wire anemometer as a function of wind angle for measurements taken at relative distances from the building façade of 0.01 to 0.25 times the building length. The markers are colour weighted by distance from the building surface, where a point on the building surface is denoted by a black circle, and the point furthest from the surface is denoted by a white circle.

into the structure and distribution of the cross-flow occurring at the surface of the model cubic building described in Figure 4.27. Measurements of cross-flow speed are made with a hot-wire probe and the cross-flow probe developed in Section 4.6. This allows the accuracy of the cross-flow probe to be assessed, which is then used to provide detailed measurements of the instantaneous speed and direction of the cross-flow close to the surface of the façade.

#### 6.4.1 Cross-flow velocity profile

Section 2.4.2 identified that the cross-flow velocity might be expected to vary with distance from the façade as a result of surface friction [81, 104]. Therefore, measurement of the cross-flow velocity profile with distance from the façade is essential to ensure the selection of a suitable reference location that is outside the surface boundary layer at which to measure the cross-flow velocity.

Figure 6.8 shows how the mean cross-flow velocity coefficient measured with a hot-wire anemometer varies with wind angle at a range of distances from the building surface. This shows that, while wind direction is the dominant cause of variation in cross-flow speed, variation with distance from the façade is also significant. The trend between cross-flow velocity coefficient and distance from the façade also varies with wind angle:

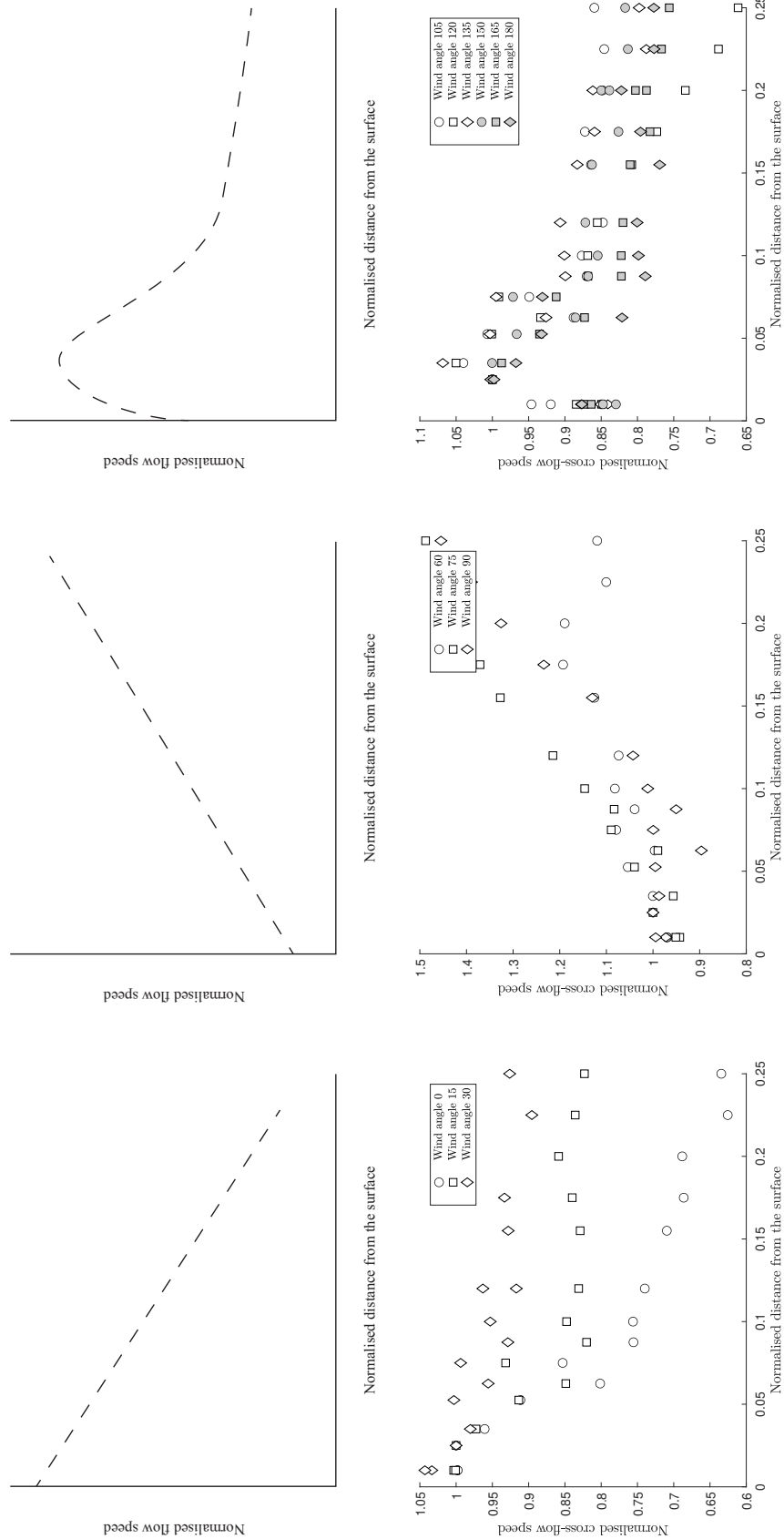


**Figure 6.9:** Illustrative diagrams of the three different patterns of velocity profile observed (top), and the measured data for different wind angles (bottom). Here the velocity is normalised by the cross-flow speed 5mm or 0.025 building lengths from the surface, and the distance from the surface is normalised by the building length. The wind angles are shown in the legend of each plot.



between 60 and 90 degrees the greatest velocity occurs furthest from the wall and the lowest occurs close to the surface; for other angles the reverse pattern is observed; see Figure 6.9.

In the lee of the building, between 105 and 180 degrees, relatively low velocities are measured close to the surface of the building. The measured cross-flow velocity rises rapidly to a peak at around 5-7mm from the surface of the building, or 0.025-0.035 times the building length. The velocity then decays with distance from the surface. A similar pattern occurs on the windward face of the building, between 0 and 30 degrees. Here, the speed of the cross-flow decays with distance from the surface. However, in contrast to the flow structure identified in the lee of the building, no reduction in cross-flow velocity close to the building surface is observed.

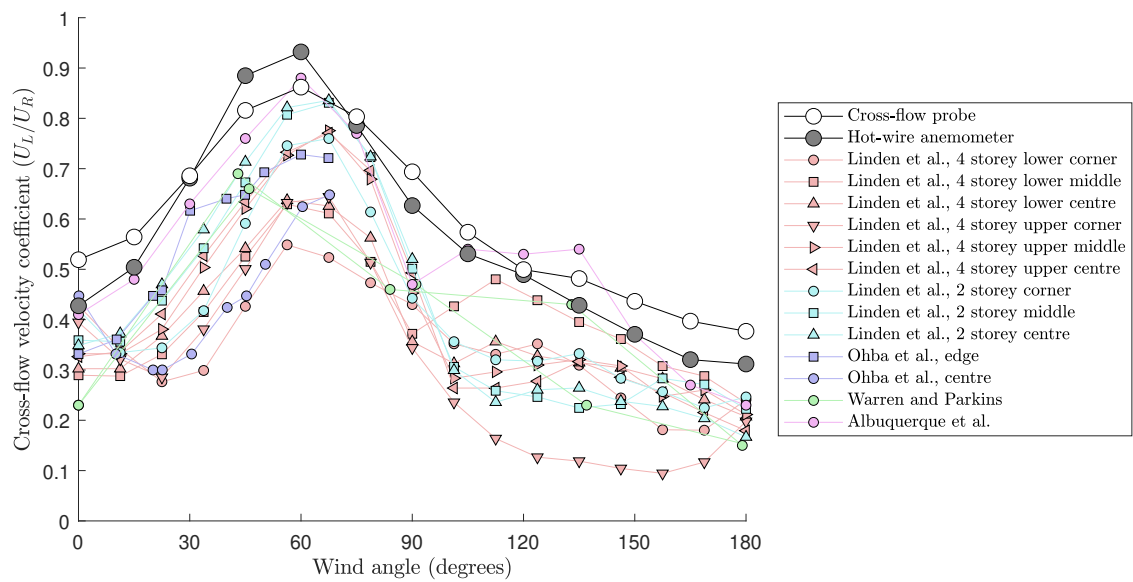
Between 60 and 90 degrees, a contrasting pattern is observed. Here, lowest speeds are measured close to the wall, and velocities increase as the distance from the surface increases.

#### 6.4.2 Cross-flow velocity coefficient

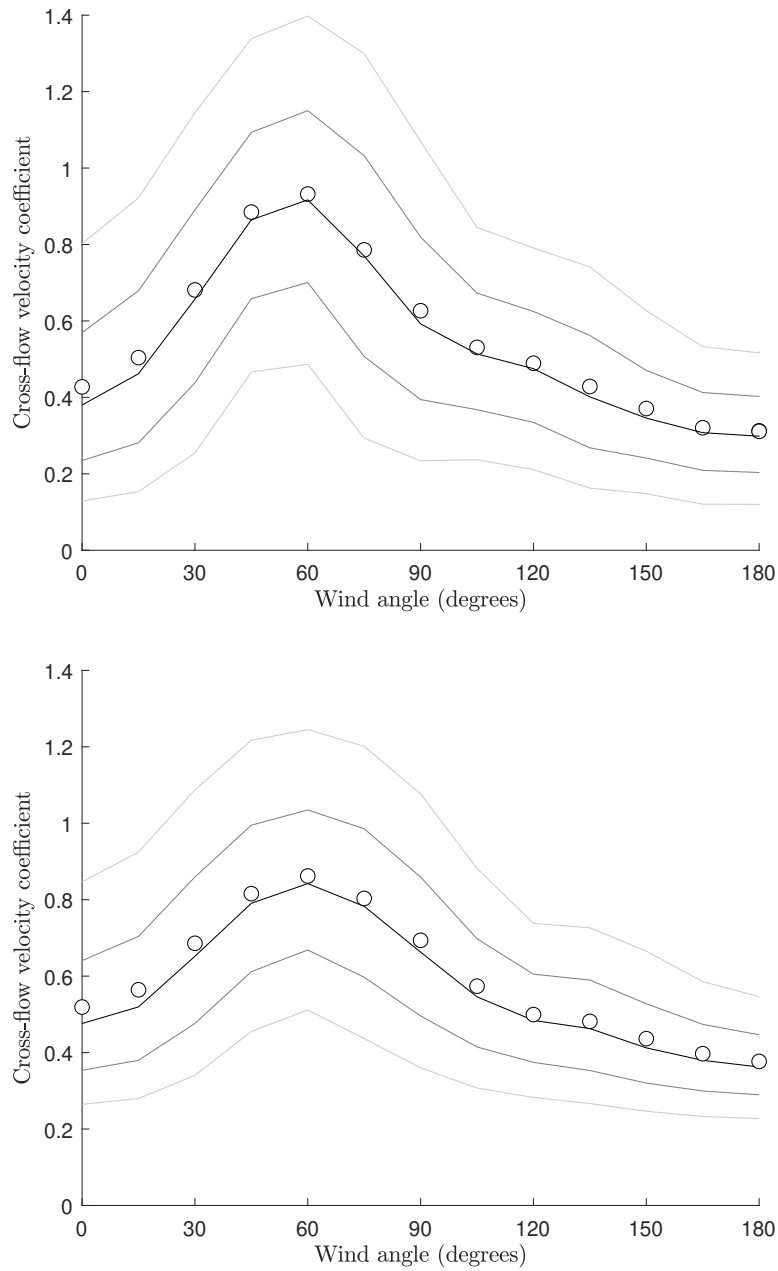
Figure 6.9 identifies that the minimum distance from the façade that is outside the surface boundary layer for all wind angles is 5mm, or 0.025 building lengths. This is chosen as the characteristic distance from the façade from which to measure the cross-flow velocity.

Figure 6.10 plots the mean cross-flow velocity coefficient measured by the hot wire anemometer and the cross-flow probe as a function of wind angle, and compares the results with data from the literature [85, 99, 61, 67]. This shows good agreement between the measurements of the hot-wire anemometer and the directional probe. The cross-flow velocity coefficients measured in this experiment show the same pattern as results from the literature - rising to a peak value at a wind angle of around 60 degrees and reducing to a minimum speed at a wind angle of about 180 degrees. However, the cross-flow velocity coefficients measured in this experiment are typically greater in magnitude than values found in the literature [85, 99, 61, 67].

Figure 6.11 compares the cross-flow velocity coefficient distribution measured using the hot-wire anemometer with that measured using the cross-flow probe. The results for both measurement techniques show a similar relationship between the cross-flow velocity coefficient and wind angle. Mean cross-flow velocity coefficients measured using the cross-flow probe are slightly lower than those measured by the hot-wire anemometer for wind angles between 30 and 75 degrees, and are slightly higher for all other wind angles. The variance in cross-flow velocity coefficient measured using the hot-wire anemometer is greater than that measured by the cross-flow probe across all wind angles.



**Figure 6.10:** Comparison between the cross-flow velocity coefficient measured at 0.025 building lengths from the facade using the hot wire anemometer, the cross-flow probe, and those measured in the literature. Measurements taken with the hot-wire anemometer are denoted by grey circles. Measurements taken with the cross-flow probe are denoted by white circles. Data from Linden *et al.* for a four storey building with an aspect ratio (W:H:L) of 2.6:1:1 are denoted by red markers [85]. Data from Linden *et al.* for a two storey building with an aspect ratio of 4.8:1:1.9 are denoted by cyan markers [85]. Data from Ohba *et al.* for a building with a 2:1:2 aspect ratio are denoted by blue markers [99]. Data from Warren and Parkins for a building with a 4.5:1:2 aspect ratio are denoted by green markers [61]. Finally, data from Albuquerque *et al.* for a building with an aspect ratio of 1.7:1:1.3 are denoted by magenta markers [67]. Error bars in the measured data are smaller than the markers, and have been omitted.



**Figure 6.11:** Plot of the cross-flow velocity coefficient measured using the hot-wire anemometer (above) and the cross-flow probe (below) as a function of wind angle. for measurements taken at 0.025 building lengths from the facade. Mean values are denoted by white circles. Median values are given by a black line, 25th and 75th centiles by a dark grey line, and 9th and 91st centiles by a light grey line. Error bars are smaller than the markers and have been omitted.

### 6.4.3 Component analysis of the cross-flow velocity

The use of the cross-flow probe allows the cross-flow velocity measurements to be decomposed into their components in the x and y direction. Here, an x-axis is defined in the horizontal plane parallel to the façade, running from left to right. Similarly, a y-axis is defined in the vertical plane, running from the bottom of the façade to the top; see Figure 4.2.

Figure 6.12 presents the distribution of the x and y components of the cross-flow velocity coefficient as a function of wind angle.

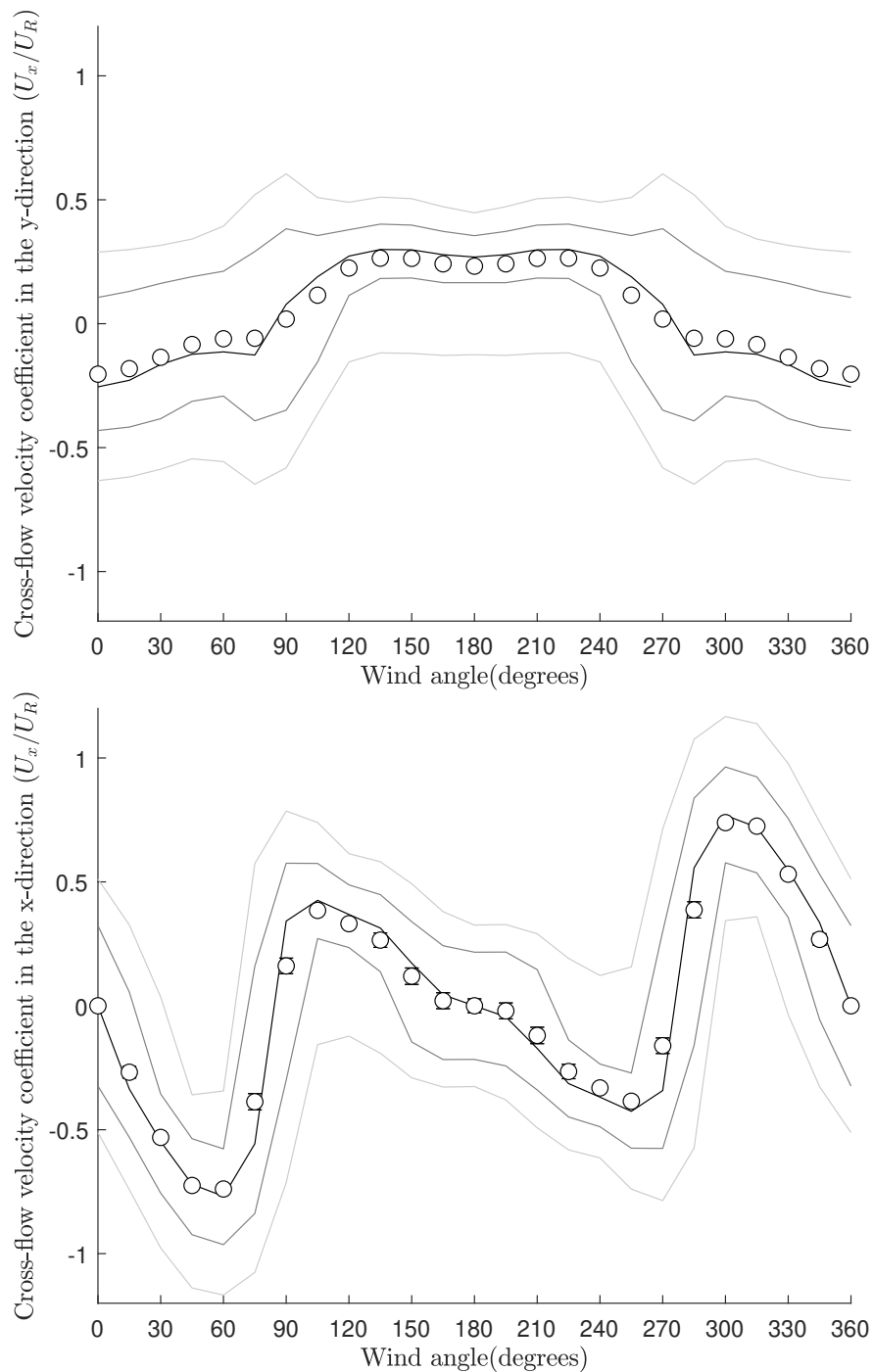
The y-component of the cross-flow velocity coefficient is symmetrical about a wind angle of 0 and 180 degrees. When the façade is on the windward side of the building, the cross-flow tends to occur in the negative direction, from the top to the bottom of the building. This pattern flips at a wind angle of around 90 and 270 degrees, resulting in a dominant cross-flow velocity coefficient in the positive direction in the lee of the building. The distribution in the y-component of the cross-flow velocity coefficient is widest close to wind angles of 90 and 270 degrees, and is wider upstream of the building than in the lee. However, transient flow reversal is not an uncommon feature at any wind angle.

The x-component of the cross-flow velocity coefficient is mirrored in both speed *and* direction about a wind angle of 0 and 180 degrees. Here, the mean x-component of the cross-flow velocity coefficient is zero at wind angles of 0 and 180 degrees, and rises to a maximum magnitude at wind angles of around 60 and 300 degrees. The direction of the cross-flow flips about a wind angle of 90 and 270 degrees, such that it occurs in an opposite direction in the lee of the building.

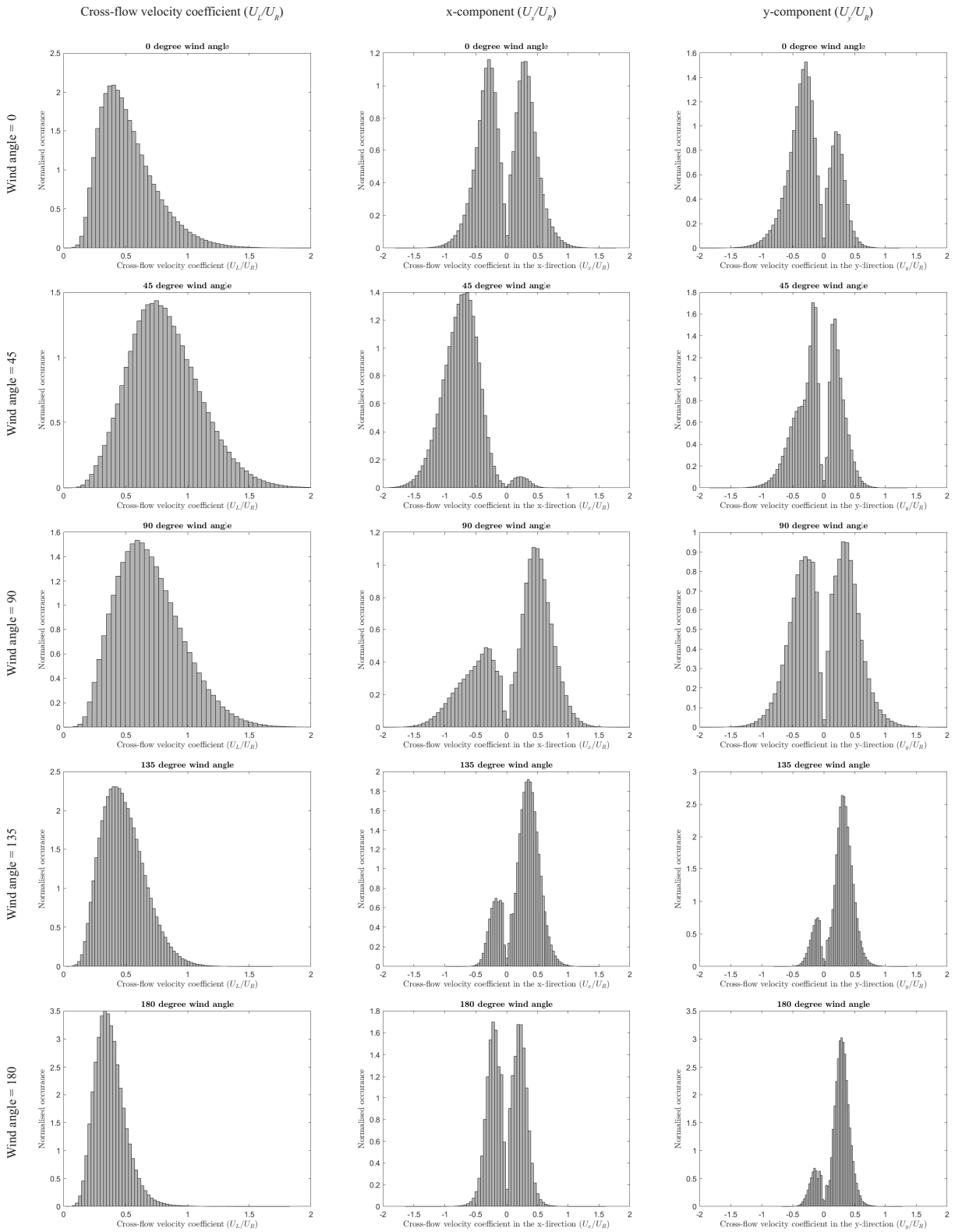
### 6.4.4 Frequency analysis of the cross-flow velocity coefficient distribution

Figure 6.13 presents the frequency distribution of the cross-flow velocity coefficient at a range of wind angles. The cross-flow speed exhibits a distribution with a single peak, that is skewed to low cross-flow speeds. However, the velocity components in both the x and y directions exhibit a clear bimodal distribution, regardless of wind direction. The shape, balance, and skew of these distributions change with wind direction. The distributions of the x-component of the cross-flow velocity coefficient are symmetrical about zero for wind angles of 0 and 180 degrees. Similarly, the distribution of the y-component of the cross-flow velocity coefficient is approximately symmetrical at a wind angle of 90 degrees.

Full distributions of the cross-flow velocity coefficient measured by the cross-flow probe are presented in Appendix G.



**Figure 6.12:** Component analysis of the cross-flow velocity coefficient measured using the cross-flow probe as a function of wind angle. The upper plot presents the velocity component in the y-direction, and the lower plot presents the velocity component in the x-direction. Mean values are denoted by white circles. Median values are given by a black line, 25th and 75th centiles by a dark grey line, and 9th and 91st centiles by a light grey line. Error bars are shown to two standard errors. Error bars smaller than the markers have been omitted.



**Figure 6.13:** Plot of distribution of the cross-flow velocity coefficient at wind angles of 0, 45, 90, 135, and 180 degrees (top to bottom). The distribution of the cross-flow speed is shown on the left, and the x and y components of the cross-flow velocity are shown on the middle and right respectively.

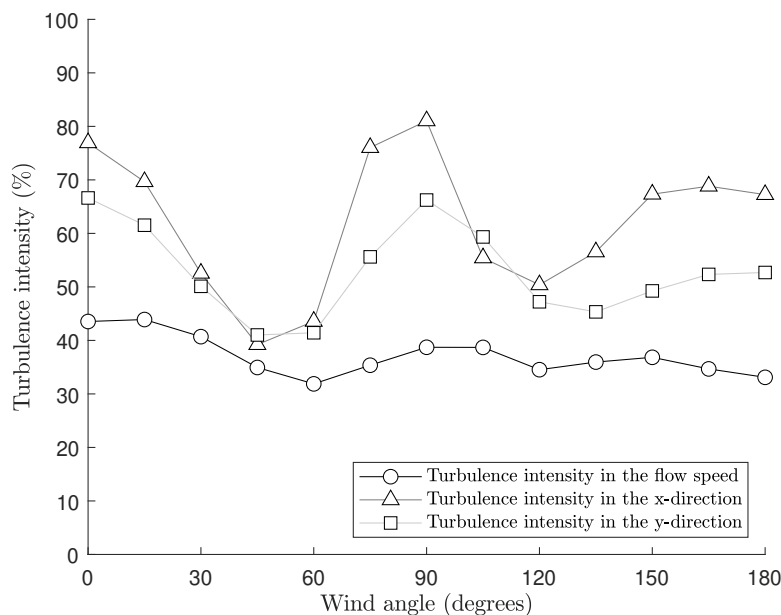


**Figure 6.14:** Plot of the turbulence intensity in the cross-flow as a function of wind angle. The turbulence intensity in the cross-flow speed is denoted by circle markers, and the turbulence intensity in the x and y components of the cross-flow velocity are denoted by triangle and square markers respectively.

#### 6.4.5 Turbulence in the cross-flow

Figure 6.14 presents the turbulence intensity in the cross-flow as a function of wind angle, for both the absolute flow speed and the x and y components of the cross-flow velocity. Here the turbulence intensity in the cross-flow speed is around 40%, and is typically greater in the upstream region than in the wake. This is greater than the turbulence intensity in the incident atmospheric flow.

The x and y components of the turbulence intensity are greater in magnitude than the turbulence intensity in the flow speed, and experience greater variation with wind direction. Here, local minima occur at wind angles of around 45-60 and 120-135 degrees, with local maxima occurring at wind angles of 0, 90, and 180 degrees. Turbulence intensity in the x-direction is typically greater than turbulence intensity in the y-direction.

#### 6.4.6 Mean *façade* cross-flow direction

The instantaneous *façade* cross-flow direction is measured using the cross-flow probe described in Section 4.6, and visualised using a flag mounted on the building surface. For all wind angles, the *façade* cross-flow direction is observed to exhibit temporal oscillations.

To increase ease of use a single mean *façade* cross-flow direction direction is evaluated. This is defined

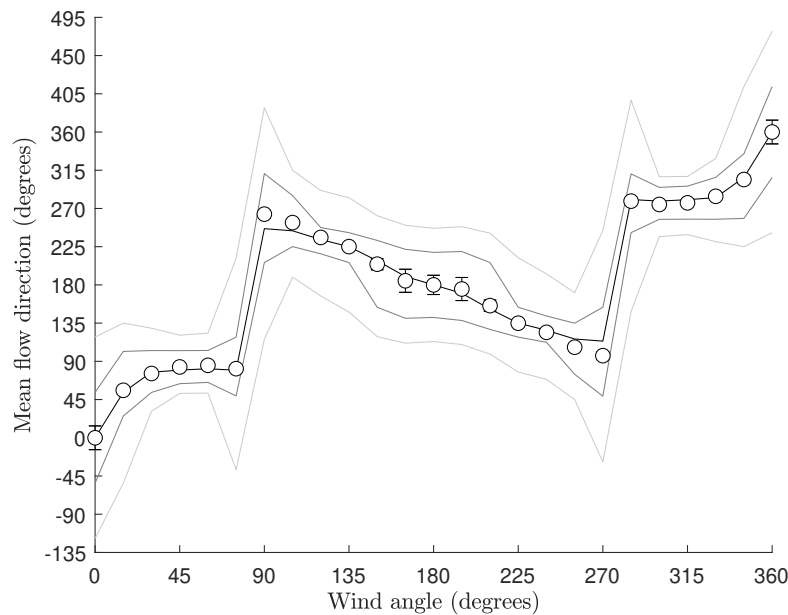


**Figure 6.15:** Plot of the mean *façade* cross-flow direction against wind angle. The 50th, 25th and 75th, and 9th and 91st centiles are denoted by black, dark grey and light grey lines respectively. Error bars are shown to two standard errors. Error bars smaller than the markers have been omitted

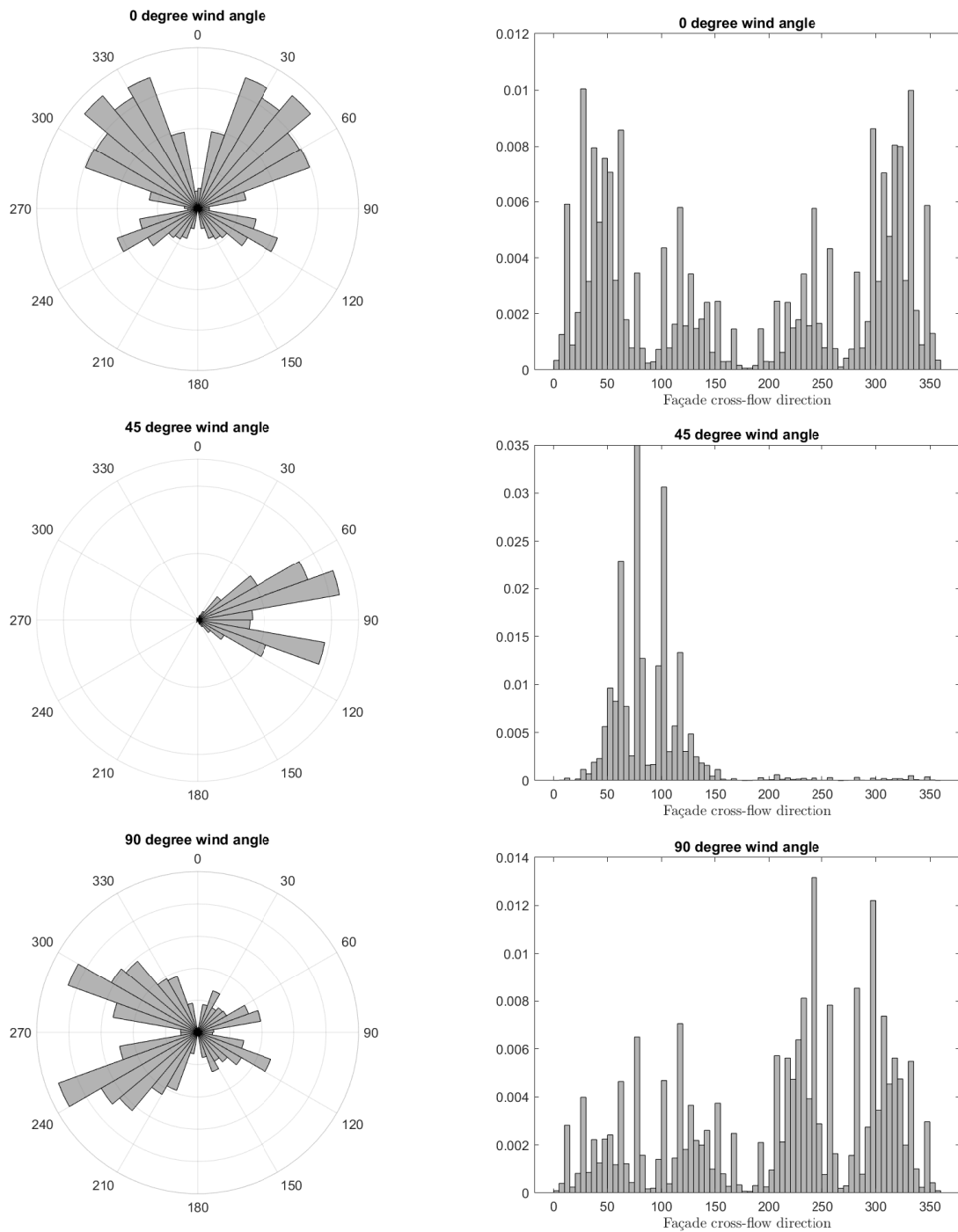
as the *façade* cross-flow direction that minimises the distance between mean and measured values. As a purely directional mean, no weighting is made for the dynamic pressure of the flow. Figure 6.15 shows how the mean *façade* cross-flow direction varies as a function of wind angle. Centiles are included based on their deviation from the mean value, and are allowed to extend below 0 degrees and above 360 degrees for clarity of representation.

The shape of the curve is very similar to that derived from visual observation of the tell-tales. When the windward *façade* is normal to the wind direction, the mean *façade* cross-flow direction is zero degrees, from the top to the bottom of the *façade*. As the wind angle deviates from zero, the *façade* cross-flow direction rapidly approaches 90 degrees, and the variance in the data reduces. The mean *façade* cross-flow direction flips from 90 to 270 degrees between wind angles of 75 and 90 degrees, where a large spike in variance is observed. The mean *façade* cross-flow direction then gradually moves round to 180 degrees as the wind angle approaches 180 degrees.

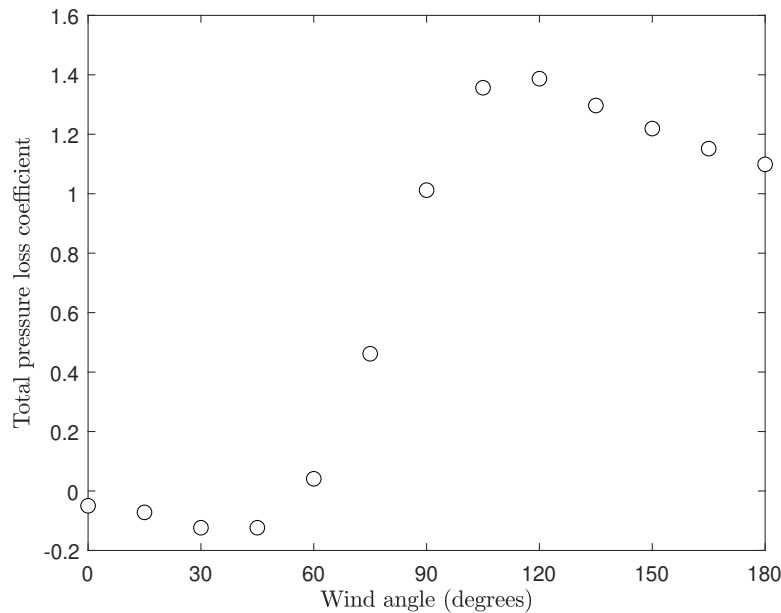
#### 6.4.7 Frequency analysis of the *façade* cross-flow direction distribution

Figure 6.16 depicts polar and linear histograms of *façade* cross-flow direction, normalised so that the total area of the bars is equal to one. These histograms clearly identify the importance of stochastic variation in *façade* cross-flow direction, where the direction of flow is frequently reversed. This is particularly true





**Figure 6.16:** Plot of distribution of *façade* cross-flow direction at wind angles of 0 degrees (top), 45 degrees (middle), and 90 degrees (bottom).



**Figure 6.17:** Plot of the mean total pressure loss coefficient against wind angle.

for wind angles close to 90 degrees. For each wind angle, the *façade* cross-flow direction is mapped by a probability distribution on which four key peaks can be identified. The position and relative sizes of these peaks vary with wind angle. Full distributions of the *façade* cross-flow direction measured by the cross-flow probe are presented in Appendix G.

## 6.5 Total pressure loss coefficient

An alternative parameter to characterise the cross-flow velocity is the *cross-flow* dynamic pressure coefficient, defined as the ratio of the dynamic pressure in the cross-flow to the reference dynamic pressure in the atmospheric flow. This is equivalent to the square of the cross-flow velocity coefficient. The *cross-flow* dynamic pressure coefficient and surface pressure coefficients can be used to calculate a total pressure loss coefficient, which characterises the loss in total pressure in the cross-flow at the opening relative to a point in the atmospheric flow at reference height.

Figure 6.17 shows how the total pressure loss coefficient varies with wind angle. The curve is periodic in 360 degrees, and symmetric about 0 and 180 degrees. Because the surface and dynamic pressure coefficients are not measured simultaneously, only mean values of the total pressure loss coefficient are depicted. Total pressure is well conserved on the upstream faces of the building up to a wind angle of around 60 degrees. Beyond this point, total pressure loss increases sharply. Significant total pressure losses are observed in the

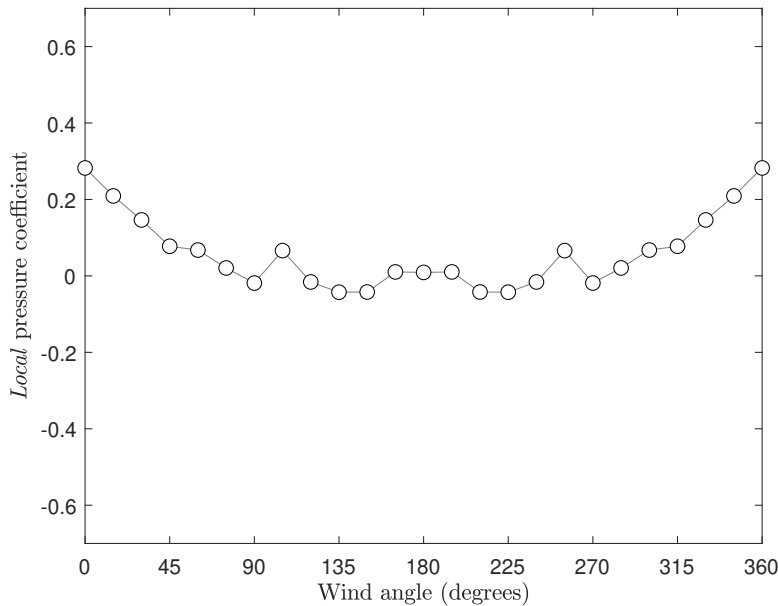


**Figure 6.18:** Plot of the *local* pressure coefficient of the square opening against wind angle.

lee of the building.

### 6.5.1 *Local* pressure coefficients

The *local* pressure coefficient is defined experimentally as the pressure increment local to the opening relative to that in the free stream, normalised by the dynamic pressure in the free stream. The pressure increment can be inferred from these experiments by comparing the pressure coefficients measured in different configurations; see Equation 4.61.

Figure 6.18 plots the calculated *local* pressure coefficient for the square orifice. *Local* pressure coefficients are close to zero most wind angles, apart from where the wind angle is close to zero. Here, the evaluated *local* pressure coefficient reaches unrealistically high values. This corresponds to the wind angles where the pressure coefficients measured with the square opening exceed those measured with the surface pressure tapping, identified in Figure 6.4. The cause of this deviation may be experimental, and the surface pressures measured with hinged openings more closely approximate the those measured with the square opening in this region. As such, pressure measurements for the square opening are used as a proxy for the surface pressure in the following analysis.

The *local* pressure coefficients calculated using this method can be compared against those directly measured in Section 5.4.1. Here, the mean *façade* cross-flow direction shown in Figure 6.15 is converted into a flow approach angle relative to the installed window opening. Figure 6.19 plots the calculated *local*

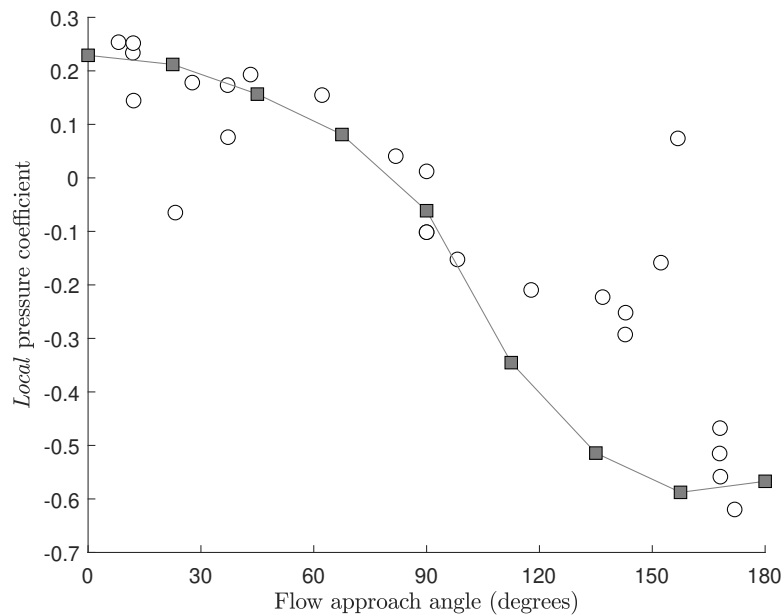


**Figure 6.19:** Plot of the *local* pressure coefficient of the hinged opening against the flow approach angle. The *local* pressure coefficients calculated from the surface pressure profiles are denoted by white circles. The *local* pressure coefficients measured by the characterisation experiments described in Chapter 5 are denoted by grey squares

pressure coefficients for the hinged openings and those measured in Section 5.4.1 against flow approach angle. Reasonable agreement is found between the two methods, considering the difference in shape and turbulence characteristics of the boundary layer profiles. Relatively poor agreement is found for negative *local* pressure coefficients.

An alternative method for estimating the *local* pressure coefficient is to apply a quasi-steady model to evaluate mean *local* pressure coefficients from the instantaneous probe data. Figure 6.20 plots the measured and predicted *local* pressure coefficients as a function of wind angle. Here, both the mean and instantaneous models track the measured *local* pressure coefficients reasonably well across most of the range of wind angles. However, both models significantly overestimate the magnitude of *local* pressure coefficients at wind angles between 90 and 135 degrees. The instantaneous model does not offer significant improvements relative to the mean model.

In conjunction with surface pressure and *cross-flow* dynamic pressure coefficients, the *local* pressure coefficients evaluated by either instantaneous or mean models can be used to predict the opening pressure coefficient profile for a given opening on a building. Figure 6.21 compares predicted and measured opening pressure coefficients for a left mounted opening. Good agreement is shown over a wide range of wind angles for both the instantaneous and mean models, which predict all the key features of the opening pressure

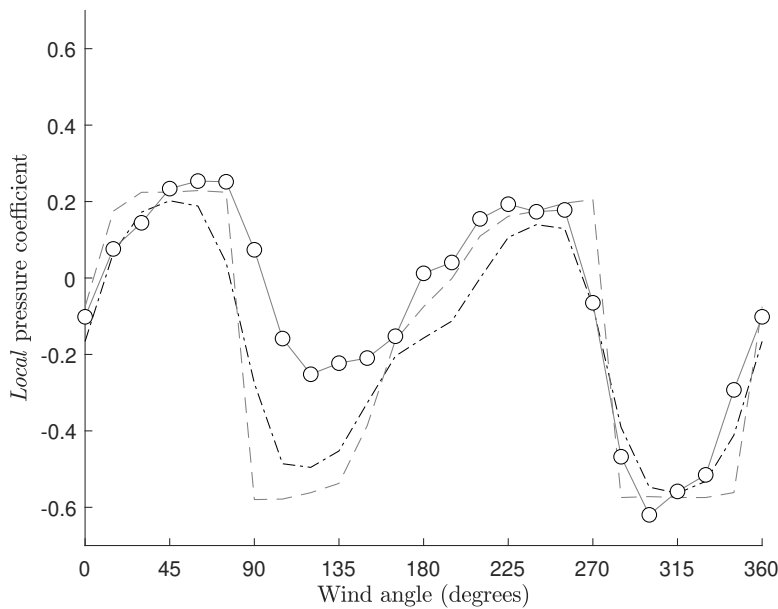


**Figure 6.20:** Plot of the *local* pressure coefficient occurring at a left mounted window opening against wind angle. Values evaluated from pressure measurements are denoted by white circles. The profile predicted using mean *façade* cross-flow direction data is denoted by a grey dashed line. The profile predicted using instantaneous *façade* cross-flow direction data is denoted by a black dashed and dotted line.

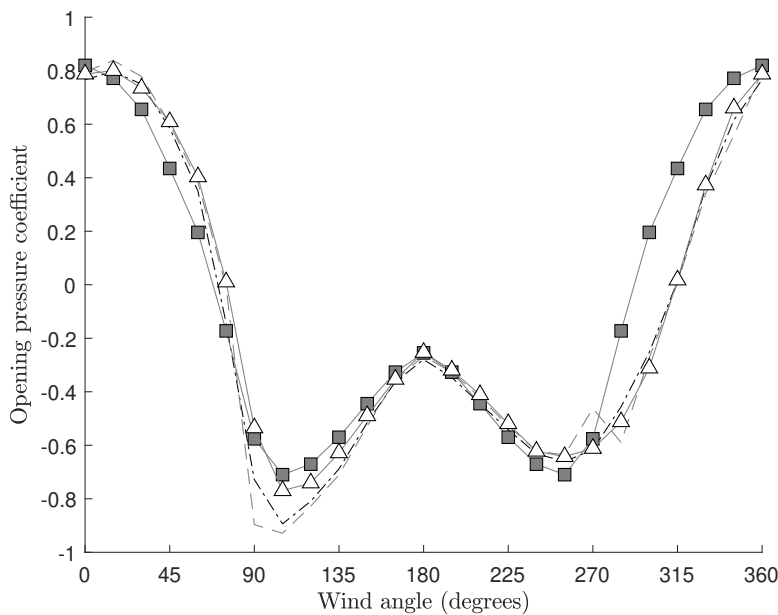


**Figure 6.21:** Plot of the opening pressure coefficients predicted using the characterisation data for a left-mounted window against wind direction alongside measured data for left-mounted and square openings. The measured left-mounted opening pressure coefficients are denoted by triangles, and those from square openings by squares. The profile predicted using mean *façade* cross-flow direction data is denoted by a grey dashed line. The profile predicted using instantaneous *façade* cross-flow direction data is denoted by a black dashed and dotted line.

coefficient curve. The *local* pressure coefficients derived from instantaneous probe data result in better agreement, and do not exhibit the erratic behaviour at a wind angle of 270 degrees observed when using *local* pressure coefficients evaluated using the mean *façade* cross-flow direction. Significant overestimation of the magnitude of wind pressures occur at wind angles between 90 and 135 degrees, which is consistent with the errors in the estimation of *local* pressure coefficient identified in Figure 6.20.



# Chapter 7

## Ventilation rate in a model building

### 7.1 Introduction

Chapter 5 described the results of novel experiments that characterise the ventilation rates through window openings exposed to a wind driven cross-flow. To apply the cross-flow characterisations thus developed to predict ventilation rate in a model building, measurements of surface pressure and cross-flow velocities are required. The results of these measurements were described in Chapter 6. This chapter applies the outcomes of Chapters 5 and 6 to predict ventilation rate through a model building, and compare the predictions against experimentally-measured ventilation rates. Furthermore, this chapter compares the predictive capacity of the novel cross-flow characterisation models against the simpler orifice flow model that is traditionally used to predict wind-driven natural ventilation rate.

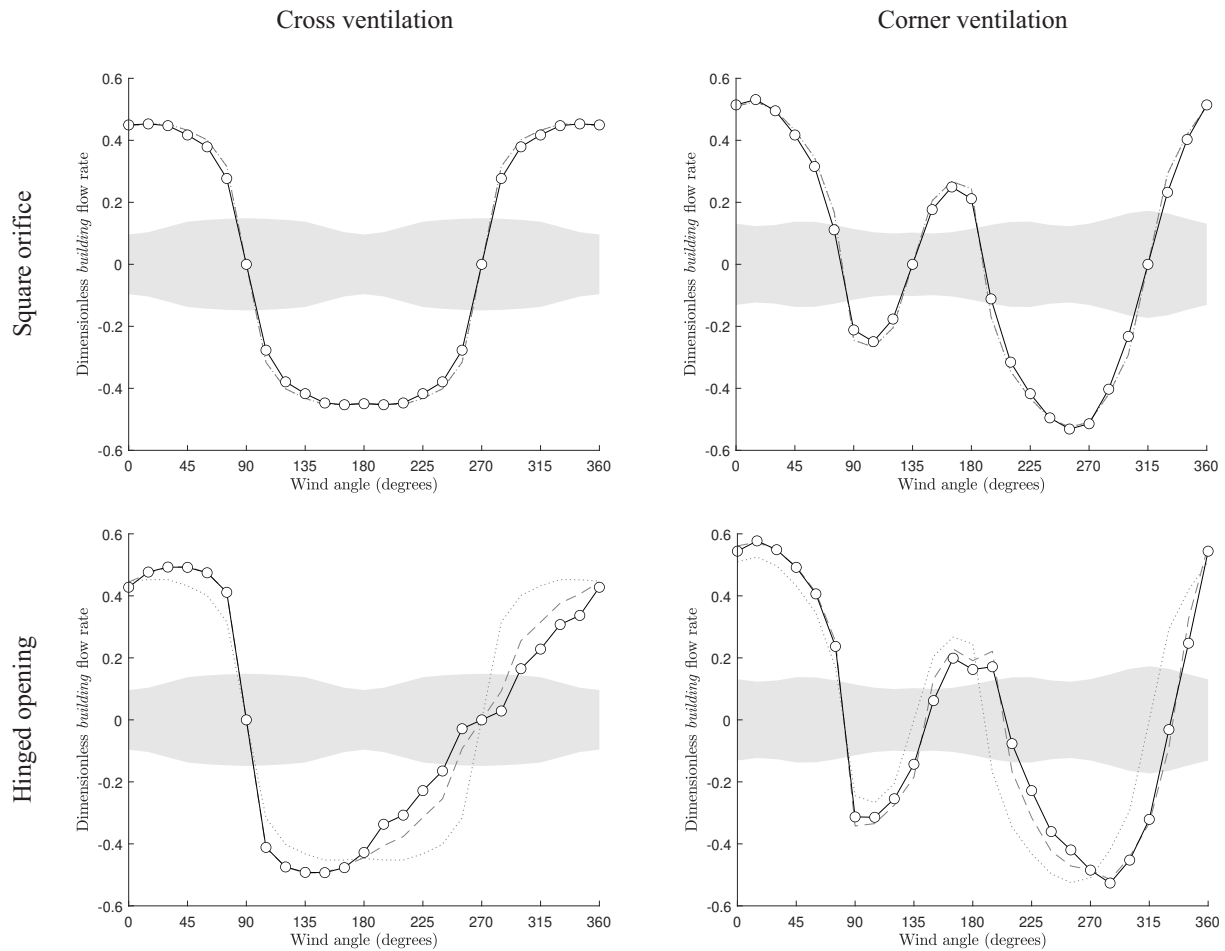
### 7.2 Ventilation rate predictions

The calculation methodologies described in Section 4.8.3 can be used to predict the dimensionless *building* flow rate that occurs in the ventilation configurations described by Figure 4.33 as a function of wind angle. These configurations are divided into two categories: cross ventilation and corner ventilation.

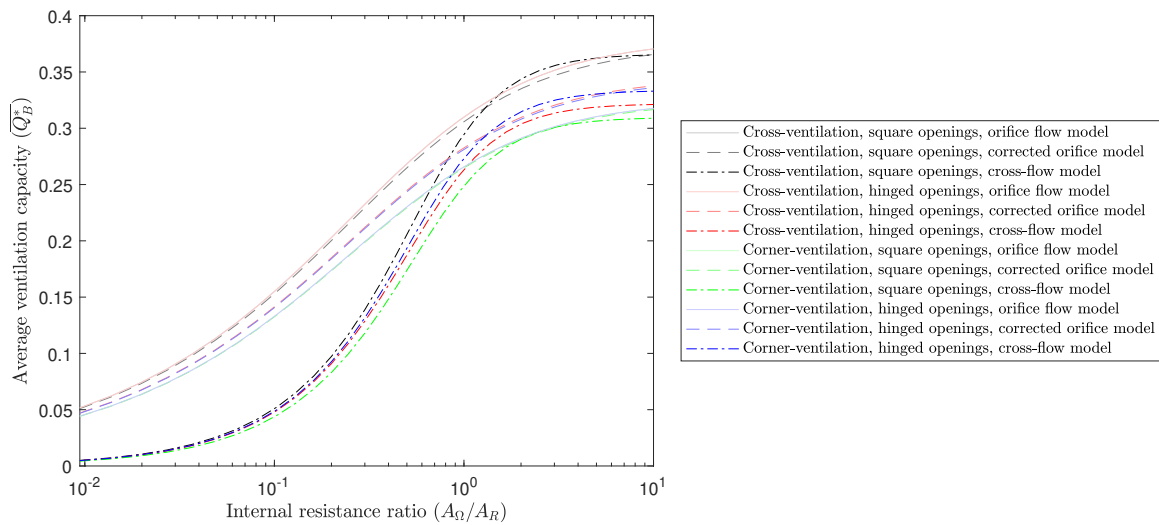
#### 7.2.1 Predictions for a single-zone building

Figure 7.4 presents the predicted dimensionless *building* flow rate through a single-zone building under the range of ventilation configurations described in Figure 4.33. For square orifices, the predictions of all three calculation methodologies described in Section 4.8.3 show close agreement. However, for outward opening windows, significant differences in ventilation rate predictions occur across a broad range of wind angles.





**Figure 7.1:** Plot of the predicted dimensionless *building* flow rate against wind angle for a range of ventilation configurations in a single-zone building. Cross ventilation configurations are shown on the left, and corner ventilation configurations are shown on the right. Square orifices and hinged openings are shown top and bottom respectively. Predictions using the cross-flow characterisation curves are denoted by circles, predictions made using the orifice flow equation are denoted by a dotted line, and the predictions of the corrected orifice flow model are denoted by a dashed line. The grey shaded region denotes the area where the single opening ventilation rate exceeds that attributable to the net volume flow rate.



**Figure 7.2:** Plot of the predicted wind-angle-averaged dimensionless *building* flow rate against the area ratio of the internal resistance. Predictions are shown for the orifice flow model (solid lines), the corrected orifice flow model (dashed lines), and the cross-flow characterisation model developed in Chapter 5 (dashed and dotted lines). Predictions for cross-ventilation and corner-ventilation configurations with square or hinged openings are depicted, according to the ventilation configurations shown in Figure 4.33.

Corner-ventilation configurations show greater variation with wind-angle than cross-ventilation configurations, but are also predicted to achieve higher ventilation rates at their optimum wind-angle. For cross-ventilation configurations, the minimum ventilation rate predicted by all unidirectional calculation methodologies coincides with the maximum ventilation rate predicted by bidirectional correlations for single-opening ventilation.

### 7.2.2 Impact of an internal resistance

In order to measure the volume flow rate through the building, an internal resistance is introduced in the form of a partition wall. This corresponds to a two zone building through which airflow is described using an airflow network model.

Figure 7.2 plots the predicted wind-angle-averaged dimensionless *building* flow rate as a function of the area ratio of the internal partition. For all models, this shows a reduction in ventilation rate as the opening area of the internal resistance increases. This reduction is typically predicted to be larger by the cross-flow characterisation model than that predicted by the orifice flow model or the corrected orifice flow model. Cross-ventilation configurations are typically predicted to perform better than corner ventilation across all internal resistance ratios. However, the cross-flow characterisation model predicts that the chosen configurations of hinged windows will result in slightly higher average ventilation rates for the corner ventilation model than

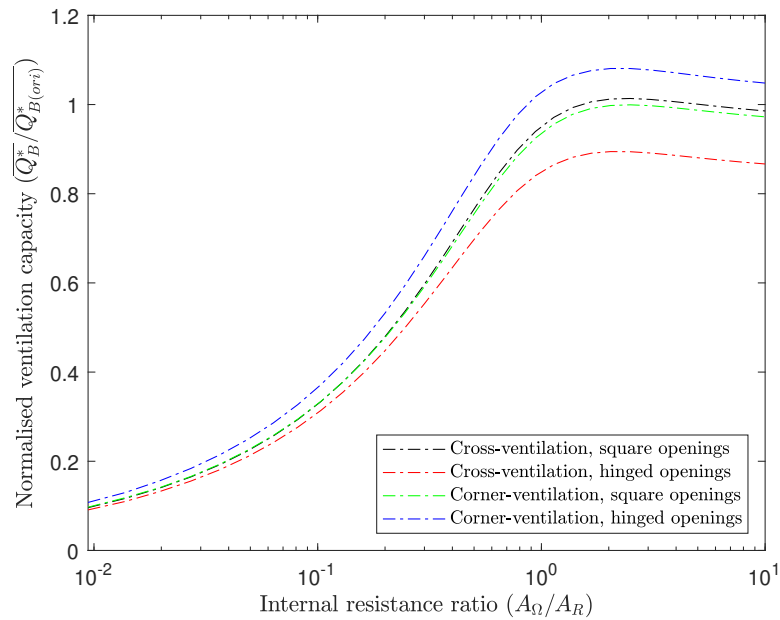


**Figure 7.3:** Ratio of the wind-angle-averaged dimensionless *building* flow rate predicted using the cross-flow characterisation model to that predicted by the orifice flow model, plotted against the area ratio of the internal resistance. Predictions for cross-ventilation and corner-ventilation configurations with square or hinged openings are depicted, according to the ventilation configurations shown in Figure 4.33.

the cross ventilation model.

Figure 7.3 presents the ratio of the average ventilation rate predicted by the cross-flow characterisation model to that predicted by the orifice equation for a range of different ventilation configurations. This shows that, for rectangular orifice type openings, the orifice equation and the cross-flow characterisation model show reasonable agreement when the opening area of the internal partition is equal to or greater than the area of the window opening. This agreement rapidly diminishes as the opening area of the internal resistance becomes smaller than the window openings, where the cross-flow characterisation model predicts smaller volume flow rates than the orifice flow model. For hinged windows, agreement is poor regardless of internal partition size. The cross-flow characterisation model predicts either higher or lower ventilation rates than those provided by square opening, depending on window orientation and the size of openings in the internal partition.

### 7.2.3 Predictions for a two-zone building

The measurements described in this chapter concern a building with an internal resistance in the form of a partition, punctuated with an opening that has a quarter of the area of the reference opening. Figure 7.4 shows the predicted dimensionless *building* flow rate profile as a function of wind-angle for the range of

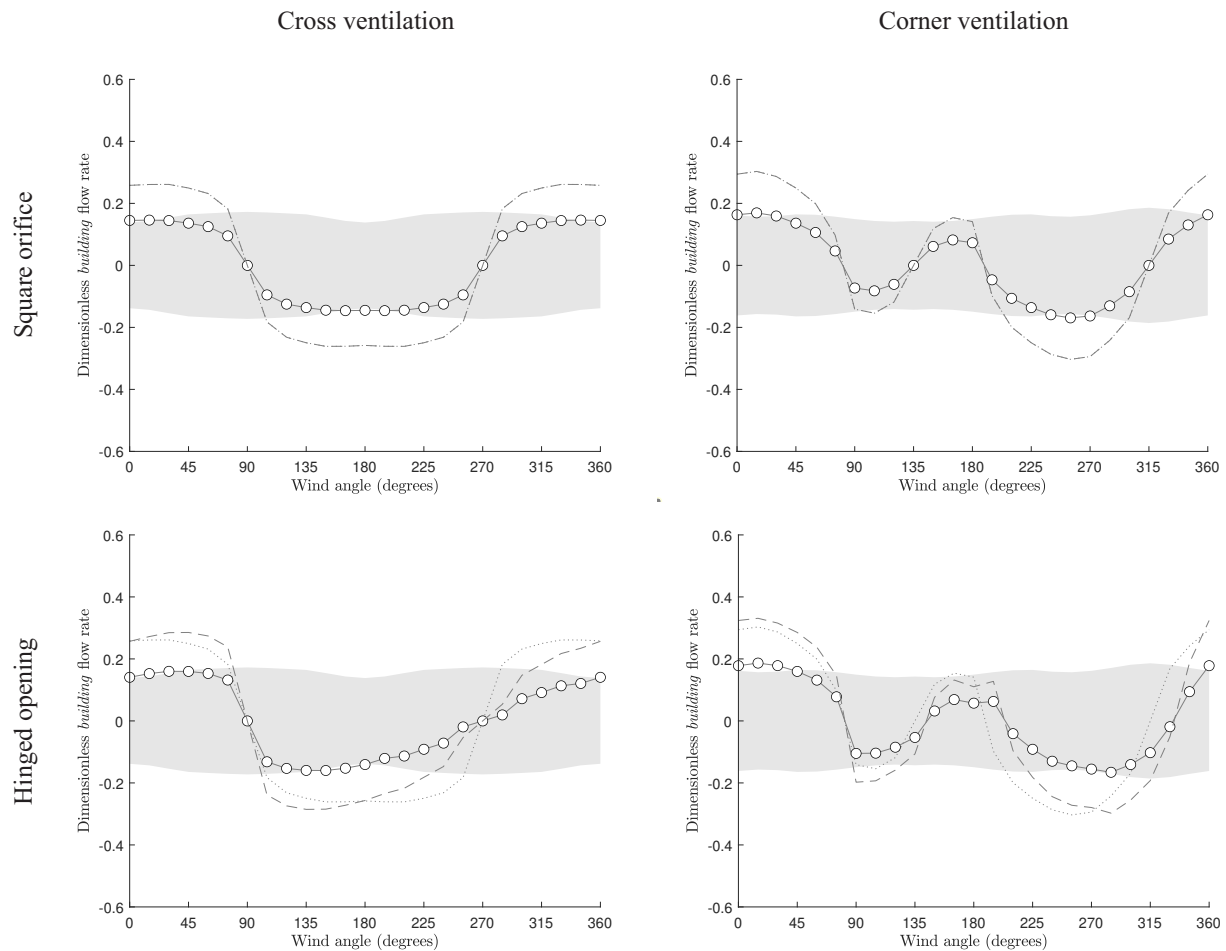


**Figure 7.4:** Plot of the predicted dimensionless *building* flow rate for a range of ventilation configurations against wind angle, with an internal resistance created by a partition with an opening  $1/4$  of the area of the external windows. Cross ventilation configurations are shown on the left, and corner ventilation configurations are shown on the right. Square orifices and hinged openings are shown top and bottom respectively. Predictions using the cross-flow characterisation curves are denoted by circles, predictions made using the orifice flow equation are denoted by a dotted line, and the predictions of the corrected orifice flow model are denoted by a dashed line. The grey shaded region denotes the area where the single opening ventilation rate exceeds that attributable to the net volume flow rate.

ventilation configurations depicted in Figure 4.33. Here, the difference in predictions between the three calculation methodologies described in Section 4.8.3 is more significant than for the single zone building. However, the ventilation rate predicted by the bidirectional single opening equation in the partitioned building often exceeds that predicted by the unidirectional cross ventilation equations.

## 7.3 Ventilation rate measurements

The data collected in these experiments enable graphs of dimensionless *building* flow rate against wind angle to be plotted. This data is used to provide a more detailed summary of the temporal dynamics of ventilation in the model building, in addition to enabling a comparison of the predictive capacity of different modelling techniques.

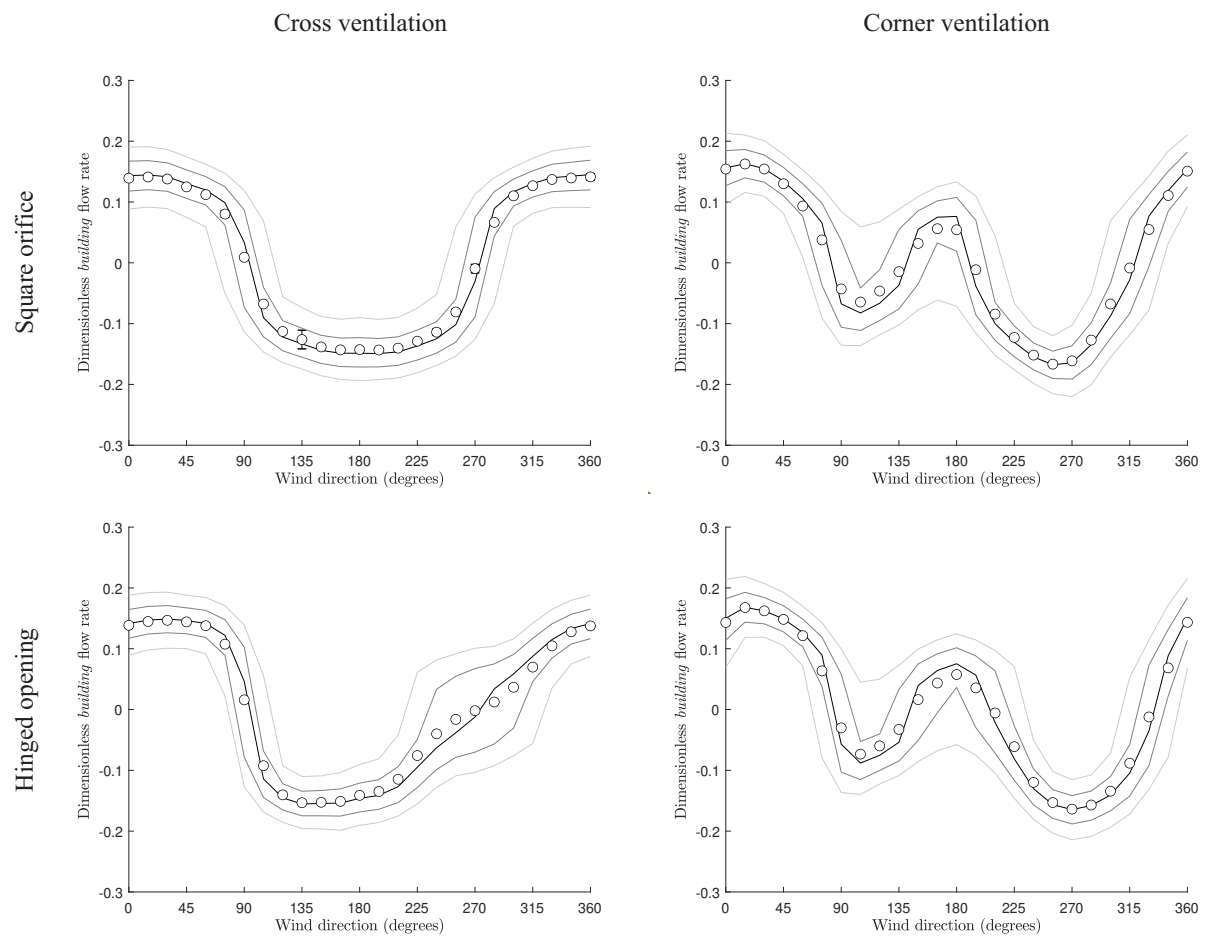
### 7.3.1 Dimensionless *building* flow rate

Figure 7.5 plots the measured dimensionless *building* flow rate against wind angle for all ventilation configurations measured. Here, the key features identified from the predictive modelling in Section 7.2 are clearly visible. Dimensionless *building* flow rates in the cross ventilation configuration with square orifices display clear symmetry; a symmetry that is broken with the inclusion of hinged openings. The use of outward opening windows has a measurable impact on building ventilation rates. This is particularly clear in the cross ventilation configuration.

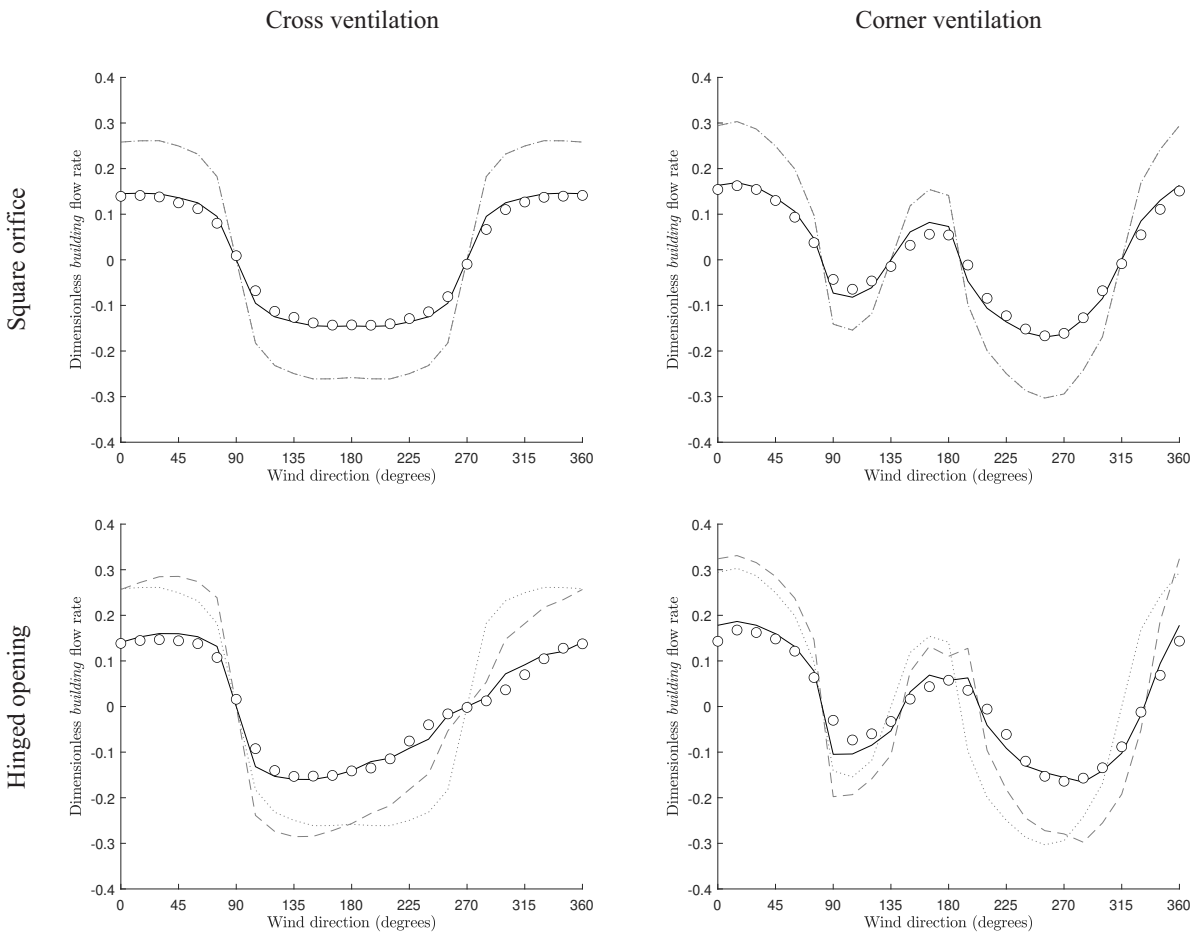
The centiles depicted in Figure 7.5 reveal the variation in dimensionless *building* flow rate. The standard deviation in dimensionless *building* flow rate is particularly high when the magnitude of mean dimensionless *building* flow rates is small. Here, changes in flow direction through the building are observed to occur. This effect is amplified when it coincides with wind angles close to 90 or 270 degrees.

Figure 7.6 compares the measured dimensionless *building* flow rate profile with the predictions made using the three calculation methods described in Section 7.2. The cross-flow characterisation curves developed in Chapter 5 show closer agreement with measured ventilation rates than either the orifice or corrected orifice flow equations across all measured wind angles.

Figure 7.7 plots the relationship between measured values of the dimensionless *building* flow rate and those predicted by the three calculation methods. The closest agreement between predicted and measured values occurs using the cross-flow characterisation model. Nevertheless, a tendency to overestimate mean flow rates is shown. This overestimation is largest when the mean volume flow rate is at its lowest. Agreement is less strong for the orifice and corrected orifice models. Both models tend to over-estimate volume flow rates through the building. In contrast to the cross-flow characterisation model, the magnitude of the



**Figure 7.5:** Plot of the measured dimensionless *building* flow rate against wind angle for a range of different ventilation configurations; with square orifices and hinged openings top and bottom respectively, and cross and corner ventilation configurations left and right respectively. Mean values are denoted by white circles. The 50th, 25th and 75th, and 9th and 91st centiles are denoted by black, dark grey, and light grey lines respectively. Error bars are shown to two standard errors. Error bars smaller than the markers have been omitted.



**Figure 7.6:** Plot of predicted and measured values of the dimensionless *building* flow rate against wind angle for a range of different ventilation configurations; with square orifices and hinged openings top and bottom respectively, and cross and corner ventilation configurations left and right respectively. Measured values are denoted by white circles. Predictions using the cross-flow characterisation curves are denoted by solid lines, and the predictions of the orifice and corrected orifice equations are denoted by the dotted and dashed lines respectively.

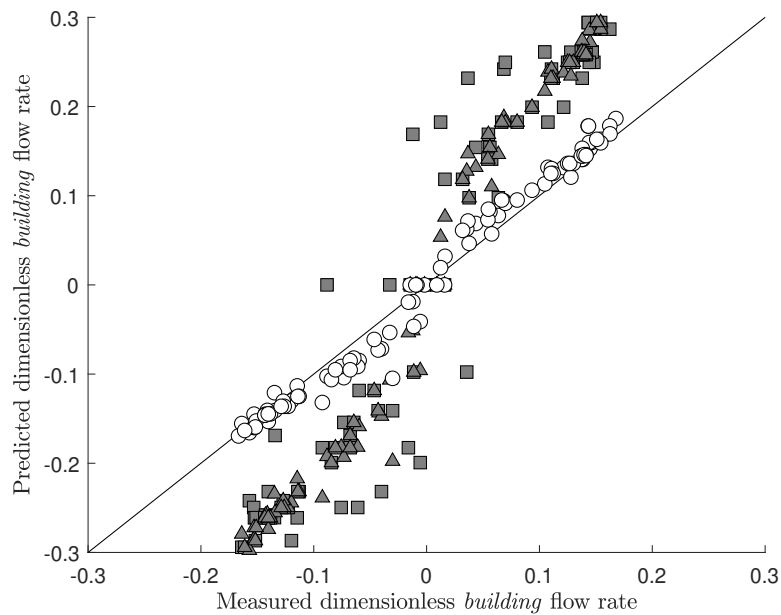


**Figure 7.7:** Plot of relationship between predicted and measured values of the dimensionless *building* flow rate for a range of different models. Predictions using the cross-flow characterisation curves are denoted by white circular markers, and the predictions of the orifice and corrected orifice equations are denoted by grey square and triangle markers respectively.

overestimation increases as the measured ventilation rate increases. The relationship between measured and predicted ventilation rate is more consistent with the corrected orifice flow model than the conventional orifice flow model, which shows more scatter.

Table 7.1 presents the regression statistics for ventilation rate predictions using the orifice equation, the corrected orifice equation, and the cross-flow characterisation models. Predictions made using the cross-flow characterisation models result in coefficients of determination between 0.94 and 0.99 depending on the ventilation configuration. This compares with coefficients of determination between -0.4 and 0.08 found when using models that do not consider the impact of a cross-flow on the aerodynamic resistance of openings. Agreement is generally better for cross ventilation configurations than corner ventilation configurations, and is generally better with square orifices than with hinged openings.

### 7.3.2 Absolute ventilation rates

Section 7.3.1 identified that when the mean value of the dimensionless *building* flow rate is close to zero, changes in flow direction through the building are observed to occur. This could result in pumping flow, which provides an alternative mechanism for driving gas exchange when mean volume flow rates are low. To investigate the impact of pumping flow on ventilation rates, the instantaneous mixing assumption common



	Coefficient of determination $R^2$		
	Orifice equation	Corrected orifice equation	Cross-flow characterisation model
<b>Cross ventilation, Square orifice</b>	0.08	0.08	0.99
<b>Cross ventilation, Hinged opening</b>	-0.30	0.02	0.98
<b>Corner ventilation, Square orifice</b>	-0.09	-0.09	0.97
<b>Corner ventilation, Hinged opening</b>	-0.40	-0.30	0.94

**Table 7.1:** Regression statistics for the ventilation rates predicted by the orifice equation, the corrected orifice equation, and the cross-flow characterisation models. Regression statistics are presented for cross-ventilation and corner-ventilation configurations with square or hinged openings, according to the ventilation configurations shown in Figure 4.33.

in studies of pumping or transient ventilation is applied [138, 25]. Here, air entering or leaving the building is assumed to mix instantaneously and perfectly. From this, the *magnitude* of the instantaneous volume flow rate through the building can be assumed to be the equivalent to the instantaneous *ventilation* rate in the building.

Figure 7.8 plots the absolute dimensionless *building* flow rate evaluated using this approach against wind direction for the range of opening configurations modelled. The peak absolute dimensionless *building* flow rate is very close to the mean dimensionless *building* flow rate under the same conditions. However, absolute dimensionless *building* flow rates do not drop below around half of their peak value. All ventilation configurations measured demonstrate absolute dimensionless *building* flow rates that are considerably more consistent with wind direction than would be expected from measurements of mean volume flow rate.

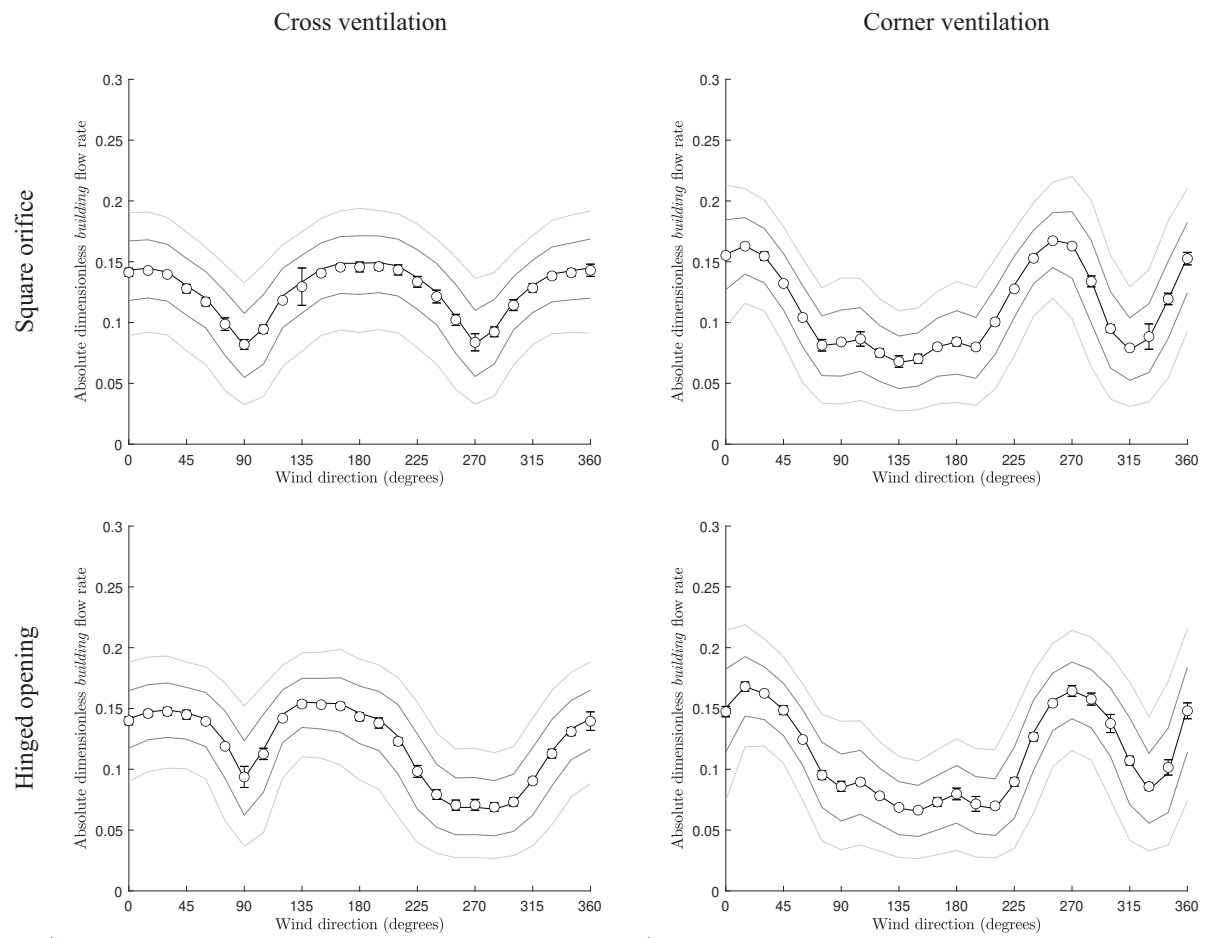


**Figure 7.8:** Plot of the measured absolute dimensionless *building* flow rate against wind angle for a range of different ventilation configurations; with square orifices and hinged openings top and bottom respectively, and cross and corner ventilation configurations left and right respectively. Mean values are denoted by white circles. The 50th, 25th and 75th, and 9th and 91st centiles are denoted by black, dark grey, and light grey lines respectively.



## Part III

# Discussion and conclusions



# Chapter 8

## Discussion

### 8.1 Introduction

The aim of this thesis is to develop techniques to *characterise* the influence of window geometry and the flow along a building façade on the ventilation rate through typical window openings. To achieve this aim, experimental measurements at the scale of an opening were performed to characterise the impact of a wind-driven cross-flow on ventilation rates. The results of these measurements are described in Chapter 5. The window-scale empirical characterisations developed in Chapter 5 were used to predict ventilation rate through a model building to validate its application to building design. This required the measurement of the surface pressure coefficients, and the development of a novel probe to measure the the speed and direction of the cross-flow on the surface of a model building, The results of these measurements are described in Chapter 6. Finally, measurement of the volume flow rate through a model building with a range of window configurations are described in Chapter 7. Measured results are compared against the predictions of the conventional orifice flow model and the window-scale empirical characterisations developed in Chapter 5.

This chapter discusses the results described in Chapters 5–7, and evaluates the degree to which the project aims have been achieved.

### 8.2 Characterising airflow through windows in a cross-flow

Chapter 5 develops techniques to characterise the performance of a notional window opening under wind-driven conditions, independently of the building in which it is located. Here, investigations focus on hinged openings, as an example of a common opening type that might be expected to perform differently to the ideal planar orifice that is ubiquitous in ventilation models.

These experiments aim to characterise the flow through window openings based on measurements of the local flow field. Here, an experimental setup was developed by which a wind tunnel is used to generate a steady cross-flow across the surface of a model window. This follows literature analysis presented in Section 2.4.2 that identifies the cross-flow configuration as characteristic of the local wind-driven flow field near window openings. The analysis in Chapter 3 identifies three characteristic properties that describe flow through window openings in wind-driven conditions: the *idealised* discharge coefficient; the *local* pressure coefficient; and the *total* dimensionless volume flow rate. Here the *idealised* discharge coefficient describes the ventilation capacity of the opening under *ideal*, still-air conditions, the *local* pressure coefficient characterises the pressure change that occurs due interaction between the window geometry and a cross-flow, and the *total* dimensionless volume flow rate describes the ventilation capacity of the opening as a function of the dimensionless room pressure.

### 8.2.1 Approach flow characteristics in the simulated cross-flow

The wind-tunnel velocity profile presented in Section 5.2 displays the characteristics of a classical surface boundary layer; see Figure 5.1. This is consistent with the mean velocity profile presented by Kurabuchi *et al.* for the cross-flow on an upstream surface of a model building. However, measurements of the cross-flow velocity performed in Section 6.4.1 identify that the shape of the mean cross-flow velocity profile varies considerably with wind angle. Furthermore, the temporal phenomena in the cross-flow on a model building identified in Section 6.4.7 are not replicated in the simulated cross-flow at a local scale. This suggests that both the mean and fluctuating components of the velocity field in the simulated cross-flow used in the local-scale characterisation experiments are not representative of those that occur on the surface of a building. Nevertheless, the simplified cross-flow represents a simplification of reality that is necessary to reduce the complexity of the characterisation process. The good agreement between predicted and measured ventilation rates in a model building described in Section 7.3 suggests that the simplification of the cross-flow velocity field applied in the local-scale characterisation experiments does not have a significant impact on the predictive capacity of the resulting empirical models.

The velocity profile present in a surface boundary layer introduces ambiguity in the location with which to measure the cross-flow velocity. In the local-scale experiments, this is resolved by choosing a location in the free-stream, outside the surface boundary layer. However, at the model building scale a free-stream outside the façade surface boundary layer cannot always be identified due to the influence of bluff body dynamics on the surface flow. An adequate solution to this problem has not been found in this thesis, and merits further research.

Section 5.2 describes the differences in the mean velocity profile and turbulence intensity profiles generated by the two roughness layers used to simulate the cross-flow in the characterisation experiments. As the MDF has a scaled surface roughness that is more representative of common building materials, experimental results measured in the notionally *thin* boundary layer are used to generate the empirical models described in Sections 5.4.4 and 5.5.6. However, many architectural treatments as well as surface protrusions such as downpipes, solar shading elements, and opening windows may be expected to generate a thicker boundary layer with a scaled surface roughness more consistent with the blocks.

Measurements with a thicker surface boundary layer are included to provide a qualitative assessment of the impact of the simulated cross-flow velocity profile on airflow through windows, in a controlled environment that is independent of other confounding variables that are present in model scale experiments. The principal effect of increasing the boundary layer thickness is to reduce the cross-flow velocity in the surface boundary layer from which airflow through the window is drawn, or into which the ventilation jet is discharged. Consequently, aerodynamic properties of window openings in a thicker boundary layer would be expected to behave closer to those measured in still-air conditions than those measured in the thinner surface boundary layer. The experimental measurements described in Sections 5.4.3 and 5.5.5 agree with this hypothesis: the magnitude of *local* pressure coefficients are lower for the thick boundary layer, and the *total* dimensionless volume flow rate approaches the *idealised* discharge coefficient more rapidly as the *local* dimensionless pressure is increased. The *idealised* discharge coefficient is measured in still-air, and is consequently independent of upstream surface treatment. This suggests that the experimental approach described by Kurabuchi *et al.* and Endo *et al.* [66, 105], which aims to generate a uniform velocity profile in the cross-flow, represents a *worst-case* scenario where the cross-flow velocity is overestimated and consequently the reduction in *total* dimensionless volume flow rate arising from the cross-flow is overestimated. However, a uniform velocity profile would also result in an overestimation of the *local* pressure coefficient, which could lead to either over or underestimations of ventilation rate depending on the ventilation configuration.

If the main impact of boundary layer thickness is to reduce the cross-flow velocity over the height of the opening, then it might be expected that the effect can be accounted for by the selection of a suitable reference height. However, the relative change in the magnitude of *local* pressure coefficients that occurs due to boundary layer thickness is not constant, and varies with flow approach angle. This suggests that measured aerodynamic properties cannot be corrected through the simple selection of a suitable reference height, and may be influenced by factors such as the shape of the mean velocity profile or the turbulence characteristics in the approach flow. Selection of a reference height at one opening length from the façade at which to measure the cross-flow velocity reduces, but does not eliminate, the impact of the velocity profile on the measured aerodynamic properties in the cross-flow. However, this approach introduces complications



when selecting a suitable distance at which to measure the cross-flow on a model building, where the size of windows may not be known, or may vary across the façade.

Complete characterisation of the impact of the cross-flow velocity profile on aerodynamic performance is prohibitively complex, and would not be able to account for the range of approach flows that occur on building façades. Furthermore, it has no impact on *idealised* discharge coefficients, and therefore is only significant when the cross-flow plays a significant role in reducing ventilation capacity. For these reasons, the characterisations of ventilation capacity developed in Chapter 5 are used in Chapter 7 to predict ventilation rates in a model building, without alterations to account for the impact of the surface boundary layer on aerodynamic performance.

### 8.2.2 *Idealised* discharge coefficient of hinged windows

The *idealised* discharge coefficient is considered to be a fundamental property of an opening. The *idealised* discharge coefficient describes the ventilation capacity of an opening under *idealised* conditions: where air flow through the opening is steady and unidirectional, and occurs between two reservoirs of uniform pressure and equal density. Furthermore, Chapter 3 shows that this property represents an important limit to the *total* dimensionless volume flow rates achieved by openings in a cross-flow. These represent conditions where  $P_R^* \rightarrow -\infty$  for inflow and  $P_R^* \rightarrow +\infty$  for outflow.

In the absence of empirical data, the use of *free area* models are ubiquitous in both industry and academia to estimate the ventilation capacity of window openings [121, 123, 126, 129, 124, 125, 116]. *Free area* models are analytically flawed, and ambiguous in application. Section 5.3.2 compares the *idealised* discharge coefficients predicted using a range of different *free area* models with academic data identified in the literature for hinged openings with a range of aspect ratios and opening angles [108, 124, 125]. This analysis shows that commonly used *free area* models cannot be used with confidence to predict the measured *idealised* discharge coefficients of simple hinged windows. Many of these models systematically overestimate volume flow rates through openings. Applying these models in design could result in under-sized openings, which in turn increases the risk of under-ventilation and overheating in occupied spaces.

Section 5.3.1 develops an Empirical Effective Area Model (EEAM) to predict the *idealised* discharge coefficient of simple hinged windows as a function of aspect ratio and opening angle. This model is fitted using academic data identified in the literature [108, 124, 125]. The EEAM model provides a significantly better fit to the empirical data than any existing models: the standard percentage deviation between measured and predicted *idealised* discharge coefficients is 7.7%, compared to an average of 28% for *free area* models. Furthermore, the use of statistical models based on empirical data can help to eliminate the systematic error

associated with the use of free area models. The EEAM model has a coefficient of determination of 0.98, which means that 98% of the variation in measured data is explained by the design equation. The remaining 2% comprises measurement error, differences in experimental design and measurement between authors, and modelling error in the descriptive equation. This is likely to be sufficient for engineering accuracy, particularly when compared against other sources of error such as the prediction of wind and buoyancy forces.

Empirical modelling techniques inevitably require large volumes of data to produce useful design equations. Measurement data is not widely available for many of the common window geometries identified in Figure 2.7. Empirical models also lack the flexibility offered by analytical *free area models*. Consequently, these models cannot be applied to novel window geometries without the use of physical or numerical modelling, which requires high levels of expertise and expense to perform. No techniques exist to adapt empirical models where other building elements such as sills and reveals restrict volume flow rates. Consequently, designers must ensure that opening windows are designed so that sills and reveals do not restrict the opening area to ensure reliable application of empirical models. Alternatively, minimal *free area* models such as model 'd' in Figure 2.7, where the *free area* is measured in one plane only, can be used. These models consistently underestimate *idealised* discharge coefficients for all aspect ratios and opening angles. When applied in ventilation design, this is expected to result in over-sizing of window openings as opposed to under-sizing. This reduces the risk of under-ventilation and overheating risk in naturally ventilated buildings.

Experimental characterisation of the *idealised* discharge coefficient of a simplified hinged opening is performed in Section 5.3.3. Measured data agree well with the EEAM model developed in Section 5.3.1. The coefficient of determination of 0.98 is consistent with the fit to literature data. However, the EEAM model has a reduced chi squared value of 7.5 when compared against measured data. This suggests that the difference between the predictions of the EEAM model and measured data is greater than can be explained by measurement error. Here *idealised* discharge coefficients are identified to be dependent on both the flow direction through the opening, and the flow direction through the experimental apparatus. Similar phenomena are observed in the literature for flow through windows and flow in pipes [108, 38, 139]. Section 5.3.3 shows how the EEAM model can be optimised for a specific window, and develops separate statistical models that describe the *idealised* discharge coefficients for inflow and outflow as a function of opening angle.

Experimental measurements of the *idealised* discharge coefficient of a square orifice performed in Section 5.3.3 evaluate different discharge coefficients for inflow and for outflow. As the square orifice is symmetrical, this difference must be associated with the flow direction through the experimental equipment as opposed to the flow direction through the opening. In the dynamic flow tests, both inflow and outflow through the orifice appear to approach the same value of the *idealised* discharge coefficient as the dimen-

sionless room pressure tends to  $\pm\infty$ . This suggests that the source of the discrepancy does not arise from metering error in the orifice flow meter, and must be related to flow conditions near the window opening in either the plenum or wind tunnel.

### 8.2.3 *Local* pressure coefficients of hinged windows

Section 2.8.4 identifies that wind can interact with window geometry to alter the pressure near its surface. Existing methods of measuring the pressure at the surface of a window rely on measuring the surface pressure at a number of fixed points around the frame, and use an averaging process to find an estimate of the mean pressure acting on the opening [88, 136]. However, this technique is ambiguous, and does not measure the pressure acting over the majority of the opening.

A novel technique to independently measure the *local* pressure coefficient is developed in Section 4.4.7. This technique is simple and unambiguous, and describes *local* pressure coefficients for a given opening geometry using a single differential pressure measurement, under a fixed set of conditions. The design of the experimental setup ensures that the measured *local* pressure coefficient has a specific physical meaning: it corresponds to the dimensionless room pressure where the net flow rate through the opening transitions between inflow and outflow. However, this measurement technique does not permit measurement of the local pressure when there is a net flow through the opening. Consequently, it cannot identify any phenomena whereby the cross-flow interacts with an outflow jet to alter the local pressure field [105]. While this may not be important for characterisation purposes, it does not permit the application of the measurement technique to more detailed studies of flow mechanisms.

The *local* pressure coefficients derived from these experiments are a function of both opening angle and the direction of the cross-flow relative to the opening, which is described by a flow approach angle. Experimental results for outward opening, hinged windows show that window openings can interact with the cross-flow to either increase or decrease pressures acting on the opening, depending on the flow approach angle. Generally, Section 5.4.1 identifies that a positive *local* pressure coefficient occurs when window geometry projects into the flow downstream from the opening. Here, the cross-flow above the opening is slowed due to interaction with the opening vane, resulting in a local increase in static pressure. Conversely, a negative *local* pressure coefficient is shown to occur when window geometry projects into the flow upstream from the opening. Here, the opening lies within the turbulent wake of the opening vane, and is therefore exposed to a local reduction in pressure. These pressure changes can reinforce or inhibit the intended ventilation pattern, depending on whether the opening is operating as an inlet or an outlet.

Section 5.4.1 identifies that the opening angle influences the magnitude of the *local* pressure coefficient,

where smaller opening angles are typically associated with lower *local* pressure coefficients. The maximum magnitude of the *local* pressure coefficient does not occur at an opening angle of 90 degrees, where the opening vane projects furthest into the cross-flow. Instead, the magnitude of the *local* pressure coefficient peaks at an opening angle of around 60 degrees. Here the opening vane is better oriented to direct incident flow towards the opening, as opposed to flowing around. This hypothesis is backed up by smoke visualisations, which show smoke moving down the vane and recirculating in the opening plane. This pattern of smoke variation also suggests that the pressure field near the opening vane is spatially varied, with a higher pressure region close to the opening vane driving flow into the opening. Here, a smaller opening angle would be expected to localise the region of static pressure increase closer to the window opening. Conversely, a smaller opening angle presents a smaller cross-sectional area to the cross-flow, and intercepts a lower-velocity region of the surface boundary layer. The balance of these mechanisms likely contributes to the observed relationship between the *local* pressure coefficient and opening angle.

Inward opening windows are also shown to be capable of generating pressure effects despite containing no elements that project into the cross-flow. Significant pressure effects are only observed at opening angles of 15 degrees or less. Here, an increase in *local* pressure coefficient is observed at flow approach angles between 90 and 270 degrees. This may be associated with the Coanda effect redirecting the cross-flow along the surface of the opening vane and into the plenum chamber. Similar mechanisms have been identified as important in single-opening ventilation [67].

The *local* pressure coefficient for a square orifice is independent of the direction of the cross-flow. As the geometry of the orifice does not project into the cross-flow, it might be expected to have a *local* pressure coefficient of zero. However, the *local* pressure coefficient of the square orifice has a measured value of  $-0.0655 \pm 0.005$ . This may be an artefact of the experimental setup, or could alternatively be caused by the generation of turbulence as the cross-flow interacts with the static air inside the plenum.

While *local* pressure coefficients tend to be relatively independent of Reynolds number, a weak dependence on Reynolds number was identified where the window opening lies in the wake of the opening vane. This is consistent with literature observations concerning flow around buildings, which find that the size of the wake region behind a bluff body is dependent on Reynolds number [70]. Variations in wake size around the opening vane would affect the distribution of the low pressure region over the opening, and consequently affect the measured *local* pressure coefficient.

Section 5.4.4 develops empirical models to describe the *local* pressure coefficient as a function of opening angle and flow approach angle. These models are shown to predict the *local* pressure coefficient well, with a coefficient of determination of 0.98. Here, the poorest agreement is evident for a flow approach angle of 112.5 degrees, where the predictive equation systematically underestimates the magnitude of *local* pressure

coefficients. However, this is the steepest part of the curve between the *local* pressure coefficient and flow approach angle, and small errors in the flow approach angle might be expected to result in large differences in the *local* pressure coefficient. Prediction errors arising from the quality of the curve fit are small compared to the variation that occurs due to Reynolds number dependency, and changes in the surface boundary layer.

#### 8.2.4 Aerodynamic resistance in a cross-flow

The dynamic performance describes the ventilation capacity of an opening as a function of dimensionless room pressure. The *idealised* discharge coefficient and the *local* pressure coefficient describe the limits to this relationship, and are determined through independent experiments. Here, the *idealised* discharge coefficient represents the ventilation capacity in *still-air*, as the dimensionless room pressure tends to  $\pm\infty$ . The *local* pressure coefficient represents the value of the dimensionless room pressure where the net flow through the opening transitions from inflow to outflow. This defines a *local* dimensionless pressure that is the difference between the dimensionless room pressure and the *local* pressure coefficient. Here, a negative *local* dimensionless pressure corresponds to inflow through the openings, and a positive *local* dimensionless pressure corresponds to outflow.

The characterisation curve for a square orifice that is measured in Section 5.5 is consistent with those found in the literature [66, 105]. These experiments confirm that, for a square orifice, the characterisation curve describing ventilation rates in a cross-flow is independent of the direction of the cross-flow [66]. For the square orifice, the presence of a cross-flow is shown to result in a reduction in ventilation capacity, which is consistent with literature observations. The data presented in Section 5.5 extends the range of measurements identified in the literature, and suggests that a cross-flow is capable of reducing the *orifice* discharge coefficient to zero.

Evaluated values of the *orifice* discharge coefficient for outflow through a square orifice are noticeably lower than those given in the literature. However, there is reason here to doubt the accuracy of the literature values. The outflow values present in the literature come from simulations of directional flow from an inlet, which find that, particularly for windows aligned with wind direction, the dynamic pressure in the jet from the inlet increases flow through the opening, resulting in an increased measure of the *orifice* discharge coefficient. The experimental setup described in Section 4.4.7 aims to ensure a uniform static pressure field inside the chamber, which would result in a lower value of the *orifice* discharge coefficient.

Chapters 2 and 3 identify a range of dimensionless parameters that can be used to describe the ventilation capacity of an opening: the *orifice* discharge coefficient, the *Bernoulli* discharge coefficient, and the *total* dimensionless volume flow rate. Section 5.5.2 compares the use of these dimensionless parameters to describe

the ventilation capacity of hinged openings in a cross-flow. Here, openings with a non-zero *local* pressure coefficient evaluate an *orifice* discharge coefficient that tends to  $\pm\infty$  as the dimensionless room pressure tends to zero. Here, the interaction between the window geometry and the cross-flow evolves driving pressures that are not accounted for in the definition of the *orifice* discharge coefficient. This identifies the cause of similar observations in the literature [6, 105]. This effect can be eliminated by using the local pressure defined by the *local* pressure coefficient to specify the external pressure. Where the opening is upstream of projecting window geometry, the corrected *orifice* discharge coefficient for outflow rises to a peak that is significantly greater than the *idealised* discharge coefficient asymptote, and occurs at relatively low values of the *local* dimensionless pressure - typically less than 0.5. This could be explained by a local pressure coefficient that is more negative under outflow conditions due to interaction with an outflow jet. Here, the outflow jet may act to direct the cross-flow away from the opening vane, reducing the magnitude of static pressures evolved near the opening. A similar effect is observed for outflow through a square orifice. The increase in the corrected *orifice* discharge coefficient above the *idealised* discharge coefficient asymptote is less pronounced for square orifices than for hinged openings. Similarly, this behaviour could be explained by a local pressure coefficient that is more negative under outflow conditions due to interaction with an outflow jet, consistent with wind tunnel and CFD experiments by Endo *et al.* [105].

The presence of a local maxima in the corrected *orifice* discharge coefficient at certain flow approach angles poses challenges to empirical curve fitting. The use of either the *Bernoulli* discharge coefficient or the *total* dimensionless volume flow rate provides a potential solution to this problem, where the measured *Bernoulli* discharge coefficient and *total* dimensionless volume flow rate are below the asymptote for all flow approach angles and opening angles. The definition of the *total* dimensionless volume flow rate also contains information as to the direction of flow through the opening, whereby a negative *total* dimensionless volume flow rate corresponds to inflow, and a positive *total* dimensionless volume flow rate corresponds to outflow. Furthermore, the use of the *total* dimensionless volume flow rate ensures compatibility with the general empirical models of ventilation described in Section 3.2. For these reasons, the use of the *total* dimensionless volume flow rate is proposed to characterise the ventilation capacity of windows in a cross-flow.

The pressures evolved due to interaction between the cross-flow and opening geometry can act either to reinforce or inhibit flow through openings, depending on the direction of flow. The reduction in *ventilation capacity* attributable to the influence of the cross-flow can be separated from the change in *driving pressure* attributable to the influence of the cross-flow through the use of a *local* dimensionless pressure, described in Section 3.5.3.

The measured characterisation curves for hinged openings reveal that the ventilation capacity is dependent on the direction of the cross-flow. This effect cannot be entirely explained by the *local* pressure

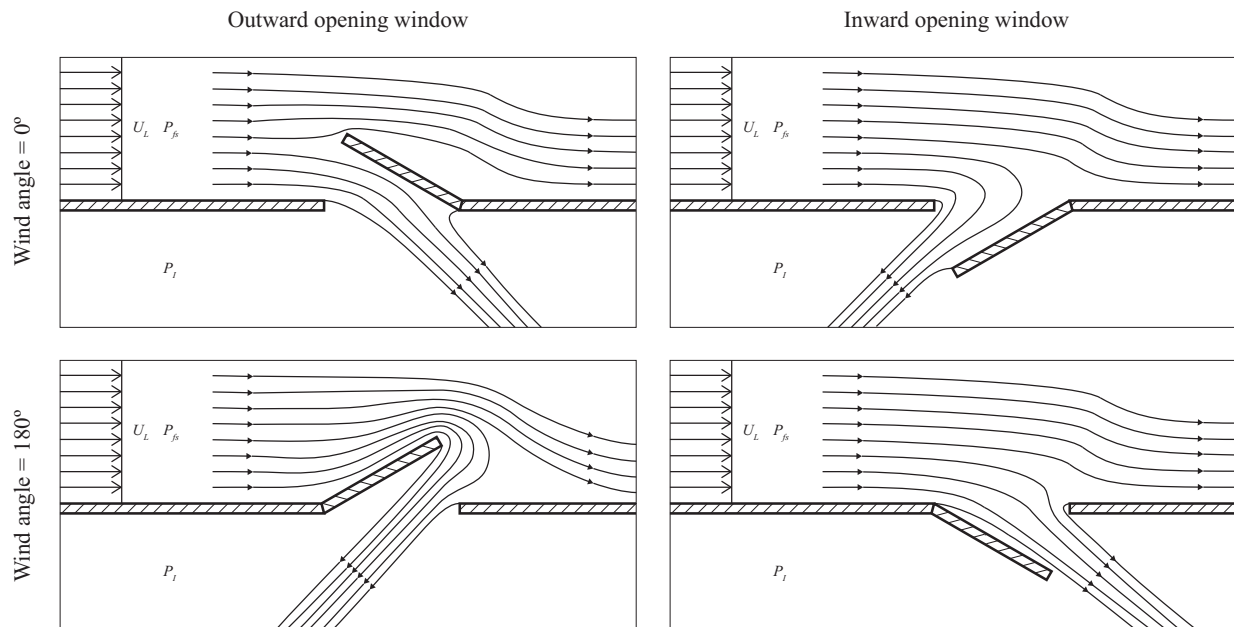


**Figure 8.1:** Diagram of inflow through inward and outward opening windows at wind directions of 0 and 180 degrees.

coefficient: even inward opening windows, which do not directly interact with the cross-flow, show a dependence of ventilation capacity on flow approach angle. This effect is stronger for inflow than for outflow, and refutes the assertion prevalent in the existing literature that the independence from cross-flow direction identified for rectangular orifices applies to other opening geometries [99]. These experiments identify that the independence from cross-flow direction identified for rectangular orifices is in fact a feature unique to openings that are approximately axisymmetric in section.

For inflow through outward opening windows, openings exposed to flow approach angles closer to 180 degrees have a performance curve with a shallower gradient than those for openings exposed to flow approach angles closer to 0 degrees. This shows that, for outward opening windows the inflow performance is more dependent on the cross-flow when the flow approach angle is close to 180 than zero degrees, and provides a greater resistance to flow even when the change in local pressure has been accounted for. This corresponds to conditions where the opening is in the turbulent wake of the projecting window geometry. Here, streamlines that originate in the cross-flow must flow around the projecting window geometry before passing through the opening; see Figure 8.1. The required contortion of the streamlines would be expected to increase resistance to flow through the opening.

Inward opening windows do not extend into the cross-flow, and therefore it might be expected that their performance curves may be less dependent on flow approach angle. This is true for fully open windows, where performance curves match closely with those of the square orifice for a wide range of flow approach

angles. However, this is not true for partially open windows. Here, openings exposed to flow approach angles closer to 0 degrees have a performance curve with a shallower gradient than those for openings exposed to flow approach angles closer to 180 degrees. This is opposing behaviour to that observed for outward opening windows. However, the increased resistance can be explained by the same mechanism, whereby streamlines originating in the cross-flow must flow around the opening vane before entering the space; see Figure 8.1.

Section 5.5.6 develops empirical models that describe the *total* dimensionless volume flow rate for square hinged openings and a square orifice as a function of opening angle, flow approach angle, and *local* dimensionless pressure. Separate fitted expressions are derived for inflow and outflow, which are expressed as single, continuous functions. This is an improvement on existing models, which use piece-wise expressions to model the characterisation curves [99]. Furthermore, the functional relationship with flow approach angle is symmetric about 0 and 180 degrees, and periodic in 360 degrees. This increases its robustness for use in design.

The reduced chi squared value for the empirical models of *total* dimensionless volume flow rate through hinged openings are significantly greater than one. This suggests that the fitted empirical equations are not sufficient to explain the variation in the data. However, the reduced chi squared values are within one order of magnitude of unity, which is not unreasonable for a purely empirical model that describes the interaction between three independent variables. Furthermore, the coefficients of determination are all in excess of 0.97. This is a sufficient level of engineering accuracy to improve on current models, particularly when compared against the error in other variables, such as weather data.

For a simple square orifice, the reduced chi squared value of the fit is close to one, which suggests that the error in the data is sufficient to explain the deviation between predicted and measured values. However, the reduced chi squared value for the inflow fit is significantly lower than unity. This represents a fit that is better than can be explained by the error in the data, and suggests that the error in the measured data may have been overestimated. To some extent this is expected, as potential sources of systematic error have been incorporated into the evaluated measurement uncertainty. The coefficient of determination remains a better metric for establishing whether a design equation is suitable for making engineering predictions. The coefficient of determination for the empirical models of *total* dimensionless volume flow rate through a simple square orifice is equal to 0.999, which suggests that it can be used confidently to predict ventilation rates in the simulated cross-flow conditions.



### 8.3 Surface flow field on a model building

To apply the novel characterisations of aerodynamic performance developed in Chapter 5 to predict volume flow rates through a notional building, measurements of the surface pressure coefficients and the speed and direction of the cross-flow are required. Section 4.7 describes experiments to measure these parameters on the façade of a simple cube building. While an atmospheric boundary layer was simulated, no specific roughness scale or model scale was targeted. As these experiments target the validation application of wind tunnel modelling, the similarity requirements in the approach flow are less strenuous than those for design purposes. The mean velocity profiles and turbulence profiles are not inconsistent with part-height simulations of atmospheric boundary layers presented in the literature [61, 172, 57, 168]. Therefore, the simulated atmospheric boundary layer is considered to be adequate for validation purposes.

Temporal variation is identified as a defining feature of surface pressures, cross-flow speed, and cross-flow direction. Standard deviations in the measured values of all these parameters are not small compared to their mean values. This can cause issues when propagating mean values through non-linear functions, whereby the mean value of a function is not the same as the value evaluated using the mean of its constituent variables. This problem directly affects ventilation calculations, where volume flow rate is not linearly related to pressure differentials, and is also important when converting between dimensionless parameters.

#### 8.3.1 Cross-flow probe

While the measurement of surface pressure coefficients is well understood, no simple techniques for measuring the speed and direction of a cross-flow have been identified. To that end, a cross-flow probe is developed in Section 4.6 that is capable of providing instantaneous measurements of both the speed and direction of a cross-flow. This probe is easy to make, and utilises the same measurement equipment required for surface pressure measurements.

To calibrate the cross-flow probe, the probe was placed in a jet of known speed and direction, and surface pressure coefficients evaluated. The calibration of the cross-flow probe evaluated mean surface pressure coefficients on the upstream face of the probe that were close to one, suggesting a stagnation zone is achieved near the tapping and that minimal energy has been lost in the calibration jet. The surface pressure coefficients in the lee of the probe show a significantly greater spread than those on upstream surfaces. This may be a result of turbulence induced in the probe's wake, and may be associated with vortex shedding processes. This may interfere with measurement accuracy of the probe, particularly if these fluctuations occur at similar frequencies to those in the wider flow.

The dynamic pressure of the calibration jet exhibited a peak frequency around 20 Hz, which is likely

associated with the rotational speed of the fan providing the air supply for the jet. The rest of the distribution is fairly uniform, which suggests that the source of this variation is random. The peak at 20 Hz measured in the dynamic pressure is transferred to the surface pressure coefficients at a *façade* cross-flow direction of zero degrees. The amplitude of oscillations in the surface pressure is also increased at high frequencies, and is suggestive of turbulence forming in the calibration jet. At the 90 and 180 degree *façade* cross-flow directions, the 20 Hz peak is no longer visible. This is likely a result of interference from the turbulence generated in the wake of the probe. The amplitude of all oscillations are increased for these angles. This is likely associated with the turbulent wake region that would be expected to form behind the probe. The absence of a clear amplitude spike at a specific frequency suggests periodic vortex shedding is not a significant driver of the variation in pressure coefficients compared to random turbulence or sensor noise.

Testing the calibrated probe in a jet of known speed and direction reveals that dynamic pressure can be measured with good accuracy over the assessed range - between  $2Pa$  and  $28Pa$ . Here no evidence of Reynolds number sensitivity was observed. By contrast, a substantial reduction in precision and accuracy in the assessed flow direction was observed to occur at dynamic pressures below about  $5Pa$ . The low measurement precision that occurs at small dynamic pressures may be caused by an increased influence of small random errors and zero errors on results, or could be caused by slower moving turbulent vortices interfering with the dynamics of flow around the probe. The frequency decomposition of the dynamic pressure and *façade* cross-flow direction evaluated by the probe yields no clear peaks for either metric, suggesting periodic behaviour such as vortex shedding is not a significant effect affecting the probe output. The absence of the 20 Hz peak that is measured in the dynamic pressure suggests that the cross-flow probe may not be sensitive to high frequency variations in flow properties.

Calibration tests indicate that the probe can provide precise measurements of both the speed and direction of a cross-flow over a wide range of flow speeds. This is supported by good agreement between the mean cross-flow velocities measured with the cross-flow probe and those measured with the hot-wire probe on the model building. However, the distribution of flow velocities measured by the cross-flow probe is significantly less broad than that measured by the hot-wire probe. This suggests that the hot-wire probe is more sensitive to fluctuations in flow velocity than the cross-flow probe, which is consistent with frequency decomposition results observed during calibration. This is not unexpected: while the sensing element of the hot-wire probe is small and thin, with a high spatial resolution and frequency response, the sensing element of the cross-flow probe is significantly larger, and resolving a flow velocity requires the presence of bluff body flow dynamics in the flow field around the whole probe. Consequently, the cross-flow probe would be expected to have a lower spatial and temporal resolution than the hot-wire anemometer. However, the potential to simultaneously resolve speed scalars and directional vectors in the flow, and the reduced obstruction to the

local flow presented by the wider probe geometry and supports, represent significant benefits. Furthermore, the use of a square hole cut within the façade to mount the probe mitigates alignment issues, which can be a significant source of error when using a hot-wire anemometer.

### 8.3.2 Surface pressure field

The surface pressure coefficients measured on the model building agree well with those aggregated from literature data [84, 91, 92]. This agreement suggests that the experimental setup and approach flow is sufficiently representative of an atmospheric boundary layer for the proposed validation studies.

The surface pressure coefficients on the surface of the model building are smaller in magnitude than those measured on the cross-flow probe, and less uniform in the wake region. This might be explained by differences in approach flow: the jet used to calibrate the probe has a more uniform mean velocity profile, whereas the ABL approach flow has a lower velocity at window height than at reference height. Furthermore, the jet used to calibrate the probe provided flow with a uniform direction, whereas the model building is presented with an ABL flow with turbulence generated by spires. Where the scale of turbulent eddies is large compared to the building scale, these eddies present as fluctuations in wind direction, which would act to reduce the mean surface pressure measured on the upstream surface, and more evenly distribute surface pressure fluctuations around the building.

Surface pressure coefficients measured with a surface pressure tapping and with a square window opening show good agreement across most window angles. However, at wind angles close to zero higher surface pressure coefficients are measured with the square opening than are measured using the surface pressure tapping. It is unclear why the square opening might cause an increase in measured pressure relative to the pressure tapping case. These pressure effects may have occurred due to variations in the flush mounting of the window plates, or due to irregularities in the surface of the pressure tapping. Another possibility is that it is caused by resonant effects with the building volume. However, the lowest resonant frequency of the space is around 850Hz, and is unlikely to be responsible for the effects seen here.

If the compressibility of the air in the space volume can be neglected, the variance in the wind pressure coefficients of the square opening and surface pressure tapping should be the same. If it cannot be neglected, the compressibility would be expected to act to damp any variations in pressure, which would result in a reduction in the standard deviation of the square opening pressure coefficients. However, it can be seen from Figure 6.5 that the standard deviation is generally greater for the square opening than for the surface pressure coefficients. This suggests the compressibility of the internal volume can be neglected, and another factor is responsible for the increased pressure variation. This may be caused by separation at the edge of

the square opening, leading to greater turbulent fluctuations over the opening area.

### 8.3.3 Window-integrated surface pressures

The methodology described in Section 4.7.3 represents an effective method of directly measuring the impact of window geometry on the surface pressure coefficients on a model building. The advantage of this method is that it reduces the number of calculation steps required to evaluate the local pressure, and implicitly integrates a representative cross-flow velocity distribution. However, its use in design requires simultaneous resolution of the building geometry and ventilation strategy, and a fixed set of window opening angles. Consequently, the wind-tunnel measurement of window-integrated surface pressures at model building scale offers a lower degree of flexibility for use in design than the application of local pressure coefficients characterised at window scale with measured cross-flow velocities.

The measured window-integrated surface pressure coefficients show a marked asymmetry for left-mounted and right-mounted, outward opening hinged windows open to an angle of 90 degrees. Some regions of the curve show substantial differences in mean opening pressure coefficients between left and right-mounted windows. This suggests that the use of two counter-mounted openings in the same façade may enable significant steady-state pressure differences to be harnessed. This has potential improve the performance of single-sided ventilation schemes that are commonly considered to be limited in terms of ventilation potential.

It might be anticipated that interaction with the opening vane may result in local turbulence that would increase the variability in the measured wind pressures. However, Figure 6.7 shows that hinged openings exhibit a similar degree of variation to that of the square opening. There are, however, a few differences. For the left-mounted opening, the standard deviation in surface pressure is increased around 90 degrees, and suppressed around 270 degrees. This relationship is inverted for the right-mounted opening. This can be explained by considering the anticipated local flow patterns when turbulent eddies flow past the building that are sufficiently large to manifest as fluctuations in wind direction; see Figure 8.2. When the wind swings clockwise, the façade at 90 degrees to the mean wind direction experiences a positive pressure variation, and cross-flow is directed from right to left. A left-mounted window interacts with the left-moving cross-flow to increase pressure, reinforcing the positive pressure swing. When the wind swings counterclockwise, the façade experiences a negative pressure variation, and the cross-flow is directed from left to right. A left-mounted window interacts and with a right-moving cross-flow to reduce pressure, reinforcing the negative pressure swing. Consequently, both positive and negative changes in surface pressure are enhanced by the interaction between the window and the cross-flow. This would result in an increased variance in measured pressures. By contrast, a right-mounted opening interacts with left-moving cross-flow to reduce pressure,

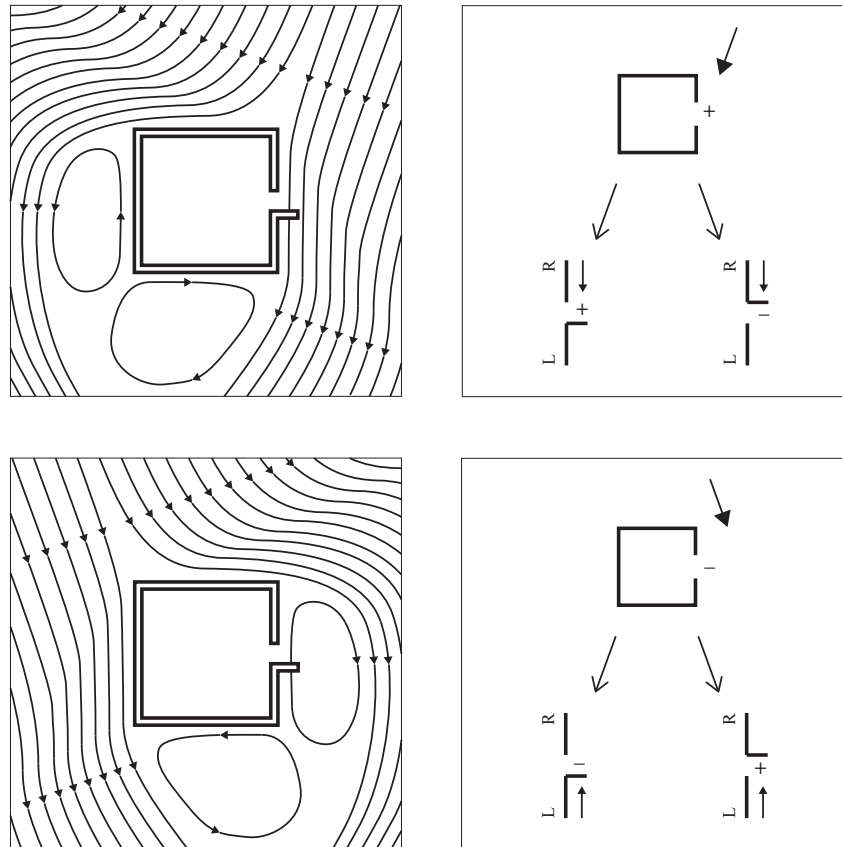


**Figure 8.2:** Diagram of the mechanism by which interaction between hinged openings and the cross-flow can reinforce or inhibit surface pressure variations generated by an oscillating wind direction.

suppressing the positive pressure swing; and with right-moving cross-flow to increase pressure, suppressing the negative pressure swing. This would result in reduced variance in measured pressures. This effect is reversed at a wind angle of 270 degrees. While this proposed mechanism adequately explains the measured phenomena, more detailed measurements are required to verify this hypothesis.

### 8.3.4 Cross-flow velocity profile

Hot-wire anemometry of the cross-flow velocity profile on the façade of a model building reveals that the shape of the boundary layer on the façade of a building exposed to wind is non-classical, with features that vary depending on the angle of exposure. Here, the selection of a suitable location to measure the cross-flow is ambiguous. However, within the first 0.1 building lengths from the façade the variation in cross-flow velocity with distance from the façade is less than 7% on average. This is about 90% smaller than the variation in cross-flow velocity with wind angle. Nevertheless, the variation of cross-flow velocity with distance from the façade could be a factor that contributes the variation between measurements in the literature [67].

A common pattern in the mean cross-flow velocity profile is observed in the lee of the building, between 105 and 180 degrees. Here, relatively low velocities are measured close to the surface of the building, rising rapidly to a peak at around 5-7mm from the surface of the building, or 0.025-0.035 times the building length. The velocity then decays with distance from the surface. The increase in cross-flow speeds between 0 and 7mm corresponds to the surface boundary layer arising from skin friction. The subsequent reduction in velocity may be a result of the rotating vortices that are characteristic of flow in recirculation zones. As the distance from the surface of the building is increased the speed of flow in the vortice reduces as the centre of rotation is approached. In addition, any non-parallel components to the flow are not measured by the hot-wire, resulting in a reduction in measured flow speed further from the surface.

A similar pattern is observed on the windward face of the building, between 0 and 30 degrees. Here, however, the surface boundary layer attributable to skin friction is too thin to be detectable. This is likely because increased levels of turbulence results in greater momentum transport into the surface boundary layer. The measured cross-flow velocity decreases with distance from the façade. This may reflect streamlines that are increasingly non-parallel with distance from the façade, or a cross-flow that is accelerated close to the building surface by surface pressure variations.

Between 60 and 90 degrees, a contrasting pattern is observed. Here, lowest speeds are measured close to the wall, and velocities increase as the distance from the surface increases. This may be an artefact of flow separation and turbulent variation in the wind angle. High velocity flow separates at the leading edge of the building. A streamline drawn from this edge separates a region of fast moving, accelerated atmospheric flow from a relatively slow velocity field in the recirculation zone. Turbulent fluctuations in the wind angle can be expected to cause the distance between this boundary and the façade to fluctuate. As the distance between the sensor and the building surface increases, the proportion of time the sensor spends in the accelerated atmospheric flow region would increase. While this proposed mechanism adequately explains the measured phenomena, more detailed measurements are required to verify this hypothesis.

### 8.3.5 Cross-flow velocity coefficient

Section 6.4.2 presents the cross-flow velocity coefficients measured at a distance of 0.025 building lengths from the façade as a function of wind angle. Reasonably good agreement is found between the mean measurements of the hot-wire anemometer and the cross-flow probe in this range, which suggests that the cross-flow probe is a suitable measurement technique. While the measured cross-flow velocity coefficients show the same pattern as results from the literature, the cross-flow velocity coefficients measured here are typically greater in magnitude than values found in the literature. However, the available data presented in the literature

concerns flow around rectangular buildings of a range of different proportions, with measurements taken at different points on the façade. Much of the literature data do not specify a distance from the façade at which the cross-flow velocity is measured. Furthermore, the data in the literature are applied with different ABL conditions in the approach flow. This limits the validity of direct comparison. There are also good reasons to expect that many of the literature measurements underestimate the mean cross-flow velocity. Linden *et al.* use a hot film anemometer to evaluate the speed of the cross-flow on the façade of two and four storey buildings [85]. The hot film is mounted on a circular disk, so that it is sensitive to the component of air velocity in the plane of the disk, and relatively insensitive to the component of air velocity in the axis perpendicular to the disk. This is mounted such that the plane of the disk is perpendicular to the façade and parallel to the ground. Therefore, the sensor will be insensitive to the vertical component of the cross-flow, and will consequently underestimate the speed of the cross-flow. Warren and Parkins orient a hot-wire probe to be perpendicular to the mean flow direction determined by a wool tuft [61]. Similarly, this method is insensitive to velocity fluctuations in directions that do not align with the mean flow, and the results are dependent on alignment accuracy. The most similar results in the literature are those presented by Albuquerque *et al.* [67]. Here a cross-wire anemometer is used to capture both velocity components in the plane of the wall. Consequently, these measurements have the highest magnitude of all the literature data presented, and are the most consistent with the measurements presented in this thesis.

The use of the cross-flow probe allows the cross-flow velocity measurements to be decomposed into their components in the x and y direction. A thorough literature review did not identify any data measuring the cardinal velocity components in the cross-flow with which to compare the data. Consequently, this analysis constitutes a novel contribution to the literature.

### 8.3.6 Mean *façade* cross-flow direction

The use of the cross-flow probe allows the instantaneous and mean *façade* cross-flow direction to be evaluated. A thorough literature review did not identify any data measuring *façade* cross-flow direction in the cross-flow on a model building as a function of wind angle. Consequently, this analysis constitutes a novel contribution to the literature. However, the lack of literature data limits the potential for validation.

Here, *façade* cross-flow direction measured using the cross-flow probe was compared against those evaluated visually through the observation of tell-tales. Similar mean flow directions and temporal effects were observed to those measured by the cross-flow probe, which lends credibility to the quantitative measurements provided by the probe. Nevertheless, replication of these measurements with alternative quantitative techniques such as PIV or LDA would be necessary to properly evaluate the accuracy of the cross-flow probe

measurements.

### 8.3.7 Temporal variation in the cross-flow

Frequency analysis of the cross-flow velocity reveals that the cross-flow speed has a distribution with a single peak, whereas the *façade* cross-flow direction is represented by a tetra-modal distribution with four distinct peaks. These features are present in the cross-flow at all measured wind angles. This suggests that the tetra-modal distribution is a general feature of flow around the building, and may be associated with vortex shedding and bluff-body flow dynamics. Often, the evaluated *mean façade* cross-flow direction occurs at a direction that is significantly under represented by the instantaneous cross-flow on the building surface. The rapid changes in *façade* cross-flow direction that occur may introduce chaotic jetting at the inlet, which could enhance mixing within the space. This may have implications for both thermal comfort and pollutant removal.

Decomposition of the flow velocity into the  $x$  and  $y$  components reveals a bimodal distribution in both of these planes. A similar bimodal distribution has been identified by PIV and CFD studies in the vertical component of flow velocities in the horseshoe vortex that forms upstream of a cube [73, 74]. While these were measured in a different point in the flow, the ubiquity of this distribution in cross-flow velocities measured at all points around a cube suggests that this may be a general feature of bluff body flow dynamics. The cross-flow measurements in this thesis suggest that the bimodal distribution in flow velocity arise from variations in flow direction rather than flow speed. Furthermore, the presence of this distribution in the wake region suggests that the source of this distribution may be associated with bluff-body vortex shedding behaviour, as opposed to interaction between the horseshoe vortex and the region of positive vorticity in front of the cube, as has been previously hypothesised [73, 74].

The turbulence intensity in the  $x$ -component of the cross-flow velocity is larger than the turbulence intensity in the  $y$ -component. This is consistent with the hypothesis that the tetra-modal distribution in flow distribution is associated with vortex shedding behaviour, as the strength of vortices shed from the two free walls of a rectangular body is greater than those shed from the top [53].

### 8.3.8 Total pressure loss in the cross-flow

Measurements of the surface pressure coefficients and *cross-flow* dynamic pressure coefficients allow the total pressure loss in the cross-flow at the opening to be evaluated, relative to a point in the atmospheric flow at building height. Two regimes can be broadly identified: the windward regime where total pressure losses are approximately zero, and the leeward regime where the total pressure loss coefficient is approximately 1.2.



This could be used by practitioners to find a first order estimate of the dynamic pressure in the cross-flow based on available surface pressure coefficient data and simple flow diagrams.

For some wind angles a negative total pressure loss coefficient is measured. This could be caused by the cross-flow stream acquiring total pressure from other parts of the flow. Alternatively, it could be an artefact of pressure variations between the surface pressure tapping and the cross-flow velocity measurement point 5mm above it.

## 8.4 Ventilation rates in a model building

Chapter 7 uses the pressure and velocimetry data gathered in Chapter 6, in conjunction with the characterisation curves developed in Chapter 5, to predict ventilation rates in a model building. This model building is set up in either a cross ventilation or a corner ventilation configuration, with a range of different opening types. Direct wind-tunnel measurements of volume flow rate through the model buildings were made to validate the models used to predict ventilation rate, and compare them against current techniques.

These predictions suggest that, for simple, single zone buildings with simple, orifice-type openings, the reduction in ventilation rate associated with a cross-flow is small for a wide range of wind directions. Good agreement between the predictions of the orifice flow model and the novel cross-flow characterisations for orifice-type openings exists when the internal resistance of the space is equal to or lower than the resistance of either opening. The agreement between the two models occurs because both the cross and corner ventilation configurations achieve a large pressure differential across the openings, which results in high values of the dimensionless room pressure. Here the cross-flow characterisation curves flatten, approaching the asymptote in still-air that is equivalent to flow described by the conventional orifice equation. In addition to this, a reduction in flow through one opening causes the internal pressure to shift, increasing the pressure drop across it. This forms a balancing mechanism that reduces the impact of a cross-flow on ventilation performance.

The good agreement between the two models in this region does not justify the additional complexity involved in the use of the cross-flow characterisation curves developed in this thesis, which require detailed characterisations of specific window types in addition to measurement of the speed and direction of the cross-flow. However, the impact of the *local* pressure coefficients associated with outward opening windows results in significant changes to the shape of the volume flow rate profile. This can either increase or reduce the mean ventilation rate through a model building, depending on the opening configuration. This suggests that cross-flow phenomena need to be accounted for when outward opening windows form a part of the ventilation strategy.

As the internal resistance becomes larger than the resistance of the window openings, the agreement

between the two models becomes rapidly worse, and the cross-flow characterisation model predicts lower ventilation rates than the conventional orifice flow model. This occurs because the internal resistance reduces the pressure drop across either opening, resulting in smaller values of the dimensionless room pressure. This suggests that the reduction in ventilation rate associated with a cross-flow could be an important phenomena in airflow network models, where natural ventilation air moves between multiple different spaces through ventilation grilles. This phenomena could also be important where two ventilation openings are located on the same façade, and consequently smaller static pressure differentials are available. However, the ventilation rate predicted by the bidirectional single opening equation in the partitioned building often exceeds that predicted by the unidirectional cross ventilation equations. This suggests that bidirectional exchange and mixing mechanisms may play an important role in gas exchange through window openings under these conditions - a phenomena which is not described by the cross-flow characterisation models presented in this thesis.

The predicted ventilation rate profile for cross ventilation is relatively consistent with wind angle. Where the dimensionless *building* flow rate attributed to the net volume flow is at its lowest point, the dimensionless *building* flow rate attributed to single opening ventilation is close to its highest. This is because the cross-flow velocity coefficient is close to its maximum at this point. This mechanism may boost the resilience of the cross ventilation configuration, enabling high ventilation rates to be achieved across all wind angles. In addition, transient flow patterns such as pumping flow might be expected to occur [78], which would increase the magnitude of the ventilation rate achieved in practice.

The net volume flow rates through the model building are directly measured in Chapter 7. Measured volume flow rate profiles are very close to those predicted using the cross-flow characterisation curves, and measurably different to those predicted using the orifice flow model. This demonstrates that cross-flow characterisation curves developed from independent wind tunnel measurements on openings can confidently be applied using *mean* surface pressure and velocity data to predict *mean* net volume flow rates through buildings.

The corrected orifice flow equation can be seen to consistently overestimate the magnitude of dimensionless *building* flow rates. Data points are well grouped, however, suggesting that it correctly describes the character of ventilation if not the numerical magnitude. By contrast, the conventional orifice equation is considerably more scattered. This is because the orifice flow equation fails to account for pressure changes that occur when outward opening windows interact with the cross-flow. Nevertheless, a clear tendency to overestimate the magnitude of dimensionless *building* flow rates is observed. The use of cross-flow characterisation curves can be seen to greatly reduce the tendency to overestimate ventilation rates, and provide consistently accurate estimates of building performance.

Good agreement between dimensionless *building* flow rates predicted by the cross-flow characterisation model and those measured by experiment is achieved despite substantial differences in the shape of the cross-flow velocity profile on the model building compared to that in the independent characterisations, and the use of *mean* cross-flow speeds and directions that do not account for temporal variation. This suggests these phenomena do not substantially alter the accuracy of predictions of mean volume flow rates for a range of ventilation configurations.

As with the pressure and velocimetry measurements, measurements of volume flow rate through the building show a strong temporal element. For some wind angles, this results in significant pumping ventilation, where volume flow rate through the building changes in direction as well as in magnitude. This creates exchange flows that could result in average ventilation rates that exceed the mean volume flow rate through the building. This standard deviation in measured ventilation rates is amplified when it coincides with wind angles close to 90 or 270 degrees. This coincides with a peak in the standard deviation in surface pressure coefficients observed in Section 6.3.1.

An estimate of the impact of pumping mechanisms on *mean* ventilation rates can be found by evaluating the mean of the instantaneous absolute volume flow rate. This assumes instantaneous and perfect mixing of the indoor air, and that the building acts as a single zone space. While these assumptions are unlikely to hold true for the partitioned building, this analysis provides insights that may be applicable to single zone spaces. The peak absolute dimensionless *building* flow rate is very close to the mean dimensionless *building* flow rate under the same conditions, suggesting that flow reversal is rare at optimal wind angles. However, absolute dimensionless *building* flow rates do not drop below around half of their peak value. This is indicative of the robustness of the cross ventilation strategy, whereby significant ventilation rates are possible even for non-optimal angles as a result of pumping ventilation. Furthermore, this model does not account for turbulent mixing mechanisms, which might be expected to further increase gas exchange rates under this regime.

The data collected in these experiments enable graphs of dimensionless *building* flow rate against wind angle to be plotted. These can be considered to be characterisation curves for the natural ventilation of the building, and can be useful tools for design in their own right [141]. Future researchers could apply this approach to create generative design data for common ventilation strategies, using tracer gas techniques to evaluate measured gas exchange rates in each zone.

## 8.5 Limitations of this thesis

- All empirical characterisations presented here apply to specific window geometries. No techniques exist to analytically extend results to other window geometries, or cases where wall build-ups such as sills and reveals cause flow restrictions.
- The building-scale measurements and cross-flow velocity distributions are specific to the model building and the atmospheric boundary layer used in the simulation. As this was created for model validation purposes and not ventilation design, the simulated ABL is not representative of a specific terrain type or model scale.
- The cross-flow configuration used for the window-scale characterisations assume streamlines parallel to the façade, and a uniform static pressure. While this may be valid for windows that are small compared to the size of the façade and far from the building edges, these assumptions break down when the opening is not small, or is located close to the edge of buildings.
- All model openings that are characterised in this thesis are mounted flush with the surface of the façade. In practice, many window openings are recessed within deep wall-build-ups.
- All model openings simulated in this thesis are set within notionally thin wall plates. This is unlikely to be true in real buildings, particularly as increasingly stringent building regulations push towards thicker insulation and deeper wall build-ups.
- All model openings that are characterised in this thesis are treated in isolation, with a well developed and uniform approach flow. Any nearby windows or projections from the façade on which the building is located could affect the dynamics of flow through the opening. The potential impact of these effects has not been investigated.
- The empirical correlations presented in this thesis describe the steady, net volume flow rate through window openings. They do not describe or characterise any bidirectional or unsteady ventilation mechanisms, which can be an important driver of gas exchange in naturally ventilated buildings. Consequently, the empirical correlations presented in this thesis cannot be applied to improve performance predictions of single-opening ventilation configurations.
- The empirical correlations presented in this thesis concern wind-driven ventilation only, and do not consider the influence of thermal buoyancy on flow dynamics. These conditions may be expected to occur only transiently in building operation.

## 8.6 Alternative applications

The framework shown in Figure 2.1 can be used to rank the complexity of a ventilation problem. Here, simplifying assumptions to the left of the framework are assigned a value of zero, and more complex conditions to the right of the framework are assigned a value of one. The complexity ranking is found by summing the values of the physical conditions represented within the framework, and takes values between zero and eight. Here, a complexity ranking of zero denotes idealised orifice flow, which is represented by the *idealised* discharge coefficients of planar openings. This level of complexity is common in simple envelope flow models. Much of the literature does not exceed a complexity ranking of one [66, 100]. Where the complexity ranking is greater than three, descriptive equations developed in the literature are typically limited to statistical correlations [117, 142]. Section 5.3.1 describes *idealised* discharge coefficients of a family of hinged openings, and has a complexity ranking of one. Sections 5.4 and 5.5 describe the ventilation capacity of square orifices and hinged openings in a cross-flow, and have complexity rankings of one and two respectively. No higher levels of complexity are considered in this thesis.

## 8.7 Suggestions for future work

The literature review identifies a large number of potential avenues for future work. There is very little characterisation data describing the performance of common window geometries under any set of environmental conditions. Fundamental studies into the interaction between wind and buoyancy forces in flows through openings are also lacking. In addition to this, no studies have been identified that investigate wind driven flow when mixing through turbulent shear occurs concurrently with net flow through the opening. This regime is expected to occur in the experiments described in Chapter 7, and is hypothesised to be a mechanism that could contribute to the measured reduction in volumetric flow capacity that occurs when a window opening is exposed to a cross-flow.

One of the most important determinants of ventilation rate in a building remains the *idealised* discharge coefficient of the specified windows. Lack of knowledge of this variable is likely to be the most significant source of design error identified in this thesis. However, there is a general lack of empirical data for common window geometries, and consequently a lack of empirical models for use in design. Expanding the empirical models developed in Section 5.3.1 to other common window types would therefore be a useful avenue for future research. However, empirical tests can be time consuming and expensive, and the resulting statistical models do not allow for the influence of building geometry such as sills and reveals on *idealised* discharge coefficients to be accounted for. Therefore, the development of simple CFD tools to predict the still-air

characteristics of arbitrary opening geometries installed in an arbitrary façade system would be of great practical use to designers. Ideally, performance data would be collected directly by providers of PPOs, enabling their integration into envelope models and providing confidence to designers.

Further characterisation experiments are required to determine the influence of opening aspect ratio on the aerodynamic characteristics of hinged openings in a cross-flow. This may impact both the magnitude of the *local* pressure coefficients, and the gradient of the dynamic characterisation curves. Furthermore, the measurement of cross-flow characterisation curves for other common opening geometries are required. As these experiments are time consuming and expensive, the development of CFD simulation tools to generate and model these performance curves would be very useful. This could enable customisation to specific designs, and the integration of façade buildup into performance predictions. CFD studies also have the potential to investigate the mechanisms behind the flow characteristics identified in this thesis, and provide richer measurements of the pressure and velocity fields near the opening. This would enable the characterisation of other flow parameters that could be useful for building design: knowledge of the speed and direction of the inflow jet from an open window could help designers ensure contact with thermal mass, and understand thermal comfort implications.

In addition to measures of net volume flow rates identified in these experiments, it is also important to characterise the rates of exchange flow that occur through open windows. This could be achieved by integrating tracer gas measurements into the experimental setup described in Chapter 5.

The strong temporal variation in ventilation characteristics - in volume flow rate terms, as well as speed and direction of inflow jets - makes wind driven natural ventilation fundamentally different in quality to mechanical ventilation. As the façade surface flow field represents the boundary conditions for indoor air studies, the speed, direction, and temporal variation in the cross-flow could potentially impact on pollutant mixing and distribution in occupied spaces, and may disrupt the formation of displacement flow regimes. Furthermore, the temporal variation in airflow characteristic to natural ventilation could contribute to a perception of air freshness. Therefore, computational and physical indoor environment studies using realistic distributions of cross-flow velocity may prove to be an interesting avenue of further study.

Chapter 6 describes patterns of statistical variation in surface pressures, cross-flow speeds and *façade* cross-flow directions. Further research is required to characterise these phenomena, to identify the statistical relationship between these variables, and to validate the measurements of the cross-flow probe using alternative experimental techniques. This conception raises the potential for statistical models of natural ventilation to be developed, whereby both inputs and outputs are specified by probability distributions. This could represent an improvement on mechanistic ventilation models currently in use, as it would provide designers with an idea of the confidence in building performance predictions.

## 8.8 Advice for practitioners

The novel techniques and performance characterisations developed in this thesis require considerably more data to implement in design than the use of the conventional orifice flow equation. Detailed information about the speed and direction of the cross-flow on building façades is required, in addition to cross-flow characterisation curves for specific windows. In the absence of this data, it is useful to provide practical advice to designers to minimise the influence of a cross-flow on ventilation performance.

The interaction between window geometry and a cross-flow can generate pressure variations that are capable of significantly altering ventilation rates through openings. These pressure variations are primarily associated with window elements that project out into a cross-flow. Therefore, the specification of inward opening windows would reduce the uncertainty associated with the use of conventional orifice flow models.

Furthermore, the reduction in ventilation capacity caused by the influence of a cross-flow can be minimised by maximising the pressure drop across the windows. This can be achieved by locating the inlet and outlet on different façades, where the maximum difference in surface pressure is achieved. In addition to this, it is important to minimise the internal resistance of the building; ideally it should operate as a single zone. For cross-ventilation through simple square openings of equal size, the *effective* area of the internal partition should be greater than the *effective* area of either opening to keep the systematic error associated with the cross-flow within 5%. Rules of thumb describing the total pressure loss coefficient can be used to make first order estimates of the dimensionless pressure at an opening using available surface pressure coefficients and simple flow diagrams to identify the upstream and wake regions. This can be used to determine whether conventional envelope flow models are sufficient to describe ventilation rates or whether more complex cross-flow characterisation models are required.

If these areas of advice are followed, then the volume flow rate through the building should be expected to behave similarly to that predicted by envelope flow models. Here, attention should be focused on ensuring adequate characterisation of the *idealised* discharge coefficients of specified openings, and the surface pressure coefficients on the building façades.

## Chapter 9

# Conclusions

The experimental and analytical work in this thesis allow the following conclusions to be drawn, which represent novel contributions to knowledge and advancements in the field of natural ventilation design:

- Conventional *free area* models are inadequate for predicting volume flow rates through window openings in still air, and can lead to the substantial overestimation of ventilation capacity.
- Empirical models of *idealised* discharge coefficients can significantly improve the predictions of volume flow rate through window openings in still air, but require large empirical data sets for fitting.
- The interaction between a wind-driven cross-flow and window geometry can alter the pressure field near the opening. This can be characterised using a *local* pressure coefficient that can be directly measured by experiment.
- The *local* pressure coefficient is a function of opening geometry and the direction of the cross-flow relative to the opening, described by a flow approach angle. This relationship can be well characterised using empirical models fitted to experimental data.
- In addition to local pressure effects, the cross-flow can reduce the ventilation capacity of window openings. This effect can be characterised as using a *local* dimensionless pressure, with characterisation curves measured in wind tunnel experiments.
- Empirical models can be used to describe the *total* dimensionless volume flow rates through simple window geometries as a function of their opening angle, flow approach angle, and the *local* dimensionless pressure.



- A novel cross-flow probe is developed to successfully measure the instantaneous speed and direction of the cross-flow on a model building.
- The velocity profile of a cross-flow measured on building façades is not consistent with wind angle, and is consequently poorly represented by *window-scale* wind tunnel characterisation studies.
- Significant temporal variation is identified in the cross-flow, where a tetra-modal distribution in the flow approach angle and a uni-modal distribution in the flow speed result in a bi-modal distribution of the x and y velocity components at all measured wind angles. This temporal variation is poorly represented by *window-scale* wind tunnel characterisation studies.
- Conventional orifice flow models are shown to significantly over-predict ventilation rates through a model building with an internal resistance, over a range of wind angles and ventilation configurations.
- For a two-zone building where both windows are of equal size, conventional orifice flow models are predicted to be sufficiently accurate for initial design calculations providing that the internal resistance of the space is lower than that of either opening, and opening geometry does not project into the cross-flow.
- Despite unrepresentative simulated cross-flows at the window scale, empirical models developed to characterise the aerodynamic performance of window openings in a cross-flow can be used to accurately predict *mean* volume flow rates through a model building using *mean* values of surface pressure, cross-flow speed, and *façade* cross-flow direction. This represents an improvement over current methods.

# Bibliography

- [1] Joachim Seifert, Yuguo Li, James Axley, and Markus Rösler. Calculation of wind-driven cross ventilation in buildings with large openings. *Journal of Wind Engineering and Industrial Aerodynamics*, 94(12):925–947, 2006.
- [2] Department for Education and Skills (DfES). Building bulletin (bb) 101, 2018: A design guide: Ventilation of school buildings, 2018.
- [3] Guide A CIBSE. Environmental design. *The Chartered Institution of Building Services Engineers, London*, 2016.
- [4] Pawel Wargocki, Jan Sundell, W Bischof, G Brundrett, Povl Ole Fanger, F Gyntelberg, SO Hanssen, P Harrison, A Pickering, O Seppänen, et al. Ventilation and health in non-industrial indoor environments: report from a european multidisciplinary scientific consensus meeting (euroven). *Indoor air*, 12(2):113–128, 2002.
- [5] AM10 CIBSE. Natural ventilation in non-domestic buildings. *The Chartered Institution of Building Services Engineers, London*, 2005.
- [6] David W Etheridge and Mats Sandberg. *Building ventilation: theory and measurement*, volume 50. John Wiley & Sons Chichester, UK, 1996.
- [7] HM Government. Approved document F - ventilation. *London, UK*, 2010.
- [8] CIBSE. TM40 Health and wellbeing in building services, 2020.
- [9] Carrie A Redlich, Judy Sparer, and Mark R Cullen. Sick-building syndrome. *The Lancet*, 349(9057):1013–1016, 1997.
- [10] Brian Crook and Nancy C Burton. Indoor moulds, sick building syndrome and building related illness. *Fungal Biology Reviews*, 24(3-4):106–113, 2010.

- [11] Hua Qian, Yuguo Li, WH Seto, Patricia Ching, WH Ching, and HQ Sun. Natural ventilation for reducing airborne infection in hospitals. *Building and Environment*, 45(3):559–565, 2010.
- [12] Paul Roelofsen. A new methodology for the evaluation of the perceived air quality depending on the air pollution, caused by human bioeffluents, the temperature, the humidity as well as the air velocity. *Intelligent Buildings International*, 10(3):154–161, 2018.
- [13] Nigel Oseland and Adrian Burton. Quantifying the impact of environmental conditions on worker performance for inputting to a business case to justify enhanced workplace design features. *Journal of Building Survey, Appraisal & Valuation*, 1(2):151–165, 2012.
- [14] Olli A Seppanen and William J Fisk. Summary of human responses to ventilation. *Indoor air*, 2004.
- [15] CIBSE. Covid-19 ventilation guidance, 2020.
- [16] ASHRAE. *ASHRAE handbook fundamentals - SI edition*. American Society of Heating, Refrigeration and Air-Conditioning Engineers, 2017.
- [17] Michael Humphreys, Fergus Nicol, and Susan Roaf. *Adaptive thermal comfort: foundations and analysis*. Routledge, 2015.
- [18] Poul O Fanger et al. Thermal comfort. analysis and applications in environmental engineering. *Thermal comfort. Analysis and applications in environmental engineering.*, 1970.
- [19] CIBSE. TM52 The limits of thermal comfort: avoiding overheating, 2017.
- [20] CIBSE. TM59 Design methodology for the assessment of overheating risk in homes, 2017.
- [21] C Alan Short. *The recovery of natural environments in architecture: Air, comfort and climate*. Routledge, 2017.
- [22] HM Government England. Requirement 01 of the building regulations 2010: Overheating mitigation, 2021.
- [23] Greater London Authority. Energy assessment guidance: Greater London Authority guidance on preparing energy assessments as part of planning applications (june 2022), 2022.
- [24] HM Government England. Requirement 11 of the building regulations 2010: Conservation of fuel and power, 2023.
- [25] David Etheridge. *Natural ventilation of buildings: theory, measurement and design*. John Wiley & Sons, 2012.

- [26] Guide B2 CIBSE. Ventilation and ductwork. *The Chartered Institution of Building Services Engineers, London*, 2016.
- [27] Zahid H Ayub. Plate heat exchanger literature survey and new heat transfer and pressure drop correlations for refrigerant evaporators. *Heat transfer engineering*, 24(5):3–16, 2003.
- [28] Yinping Zhang, Jinhua Mo, Yuguo Li, Jan Sundell, Pawel Wargocki, Jensen Zhang, John C Little, Richard Corsi, Qihong Deng, Michael HK Leung, et al. Can commonly-used fan-driven air cleaning technologies improve indoor air quality? a literature review. *Atmospheric Environment*, 45(26):4329–4343, 2011.
- [29] William J Fisk. Health benefits of particle filtration. *Indoor air*, 23(5):357–368, 2013.
- [30] R De Dear, J Xiong, J Kim, and B Cao. A review of adaptive thermal comfort research since 1998. *Energy and Buildings*, 214:109893, 2020.
- [31] Yongchao Zhai, Anoop Honnekeri, Margaret Pigman, Marc Fountain, Hui Zhang, Xiang Zhou, and Edward Arens. Use of adaptive control and its effects on human comfort in a naturally ventilated office in alameda, california. *Energy and Buildings*, 203:109435, 2019.
- [32] Lisa Collins, Sukumar Natarajan, and Geoff Levermore. Climate change and future energy consumption in uk housing stock. *Building Services Engineering Research and Technology*, 31(1):75–90, 2010.
- [33] Department of the Environment and Energy. *Heating, Ventilation and Air-Conditioning High Efficiency Systems Strategy - HVAC energy breakdown*. Australian Government, 2013.
- [34] Benjamin Jones and Ray Kirby. Indoor air quality in uk school classrooms ventilated by natural ventilation windcatchers. *International Journal of Ventilation*, 10(4):323–337, 2012.
- [35] M Santamouris, Afroditi Synnefa, Margarita Assimakopoulos, I Livada, K Pavlou, M Papaglastra, Niki Gaitani, Denia Kolokotsa, and Vassilis Assimakopoulos. Experimental investigation of the air flow and indoor carbon dioxide concentration in classrooms with intermittent natural ventilation. *Energy and Buildings*, 40(10):1833–1843, 2008.
- [36] P Karava, T Stathopoulos, and AK Athienitis. Wind driven flow through openings—a review of discharge coefficients. *International journal of ventilation*, 3(3):255–266, 2004.
- [37] Benjamin M Jones, Malcolm J Cook, Shaun D Fitzgerald, and Christopher R Iddon. A review of ventilation opening area terminology. *Energy and Buildings*, 118:249–258, 2016.

- [38] Per Heiselberg and Mats Sandberg. Evaluation of discharge coefficients for window openings in wind driven natural ventilation. *International journal of ventilation*, 5(1):43–52, 2006.
- [39] David Etheridge. A perspective on fifty years of natural ventilation research. *Building and Environment*, 91:51–60, 2015.
- [40] Bert Blocken, Ted Stathopoulos, and JPAJ Van Beeck. Pedestrian-level wind conditions around buildings: Review of wind-tunnel and cfd techniques and their accuracy for wind comfort assessment. *Building and Environment*, 100:50–81, 2016.
- [41] Hemant Mittal, Ashutosh Sharma, and Ajay Gairola. A review on the study of urban wind at the pedestrian level around buildings. *Journal of Building Engineering*, 18:154–163, 2018.
- [42] Rubina Ramponi, Bert Blocken, B Laura, and Wendy D Janssen. Cfd simulation of outdoor ventilation of generic urban configurations with different urban densities and equal and unequal street widths. *Building and Environment*, 92:152–166, 2015.
- [43] YW Dai, Cheuk Ming Mak, and ZT Ai. Computational fluid dynamics simulation of wind-driven inter-unit dispersion around multi-storey buildings: Upstream building effect. *Indoor and Built Environment*, 28(2):217–234, 2019.
- [44] Yaxing Du, Bert Blocken, and Stefan Pirker. A novel approach to simulate pollutant dispersion in the built environment: Transport-based recurrence cfd. *Building and Environment*, 170:106604, 2020.
- [45] Yu-Heng Tseng, Charles Meneveau, and Marc B Parlange. Modeling flow around bluff bodies and predicting urban dispersion using large eddy simulation. *Environmental science & technology*, 40(8):2653–2662, 2006.
- [46] Ricardo Forgiarini Rupp, Natalia Giraldo Vásquez, and Roberto Lamberts. A review of human thermal comfort in the built environment. *Energy and buildings*, 105:178–205, 2015.
- [47] Noël Djongyang, René Tchinda, and Donatien Njomo. Thermal comfort: A review paper. *Renewable and sustainable energy reviews*, 14(9):2626–2640, 2010.
- [48] William W Nazaroff. Indoor particle dynamics. *Indoor air*, 14(Supplement 7):175–183, 2004.
- [49] Xiaodong Cao, Junjie Liu, Nan Jiang, and Qingyan Chen. Particle image velocimetry measurement of indoor airflow field: A review of the technologies and applications. *Energy and Buildings*, 69:367–380, 2014.

- [50] Jianshun Jensen S Zhang. Combined heat, air, moisture, and pollutants transport in building environmental systems. *JSME International Journal Series B Fluids and Thermal Engineering*, 48(2):182–190, 2005.
- [51] Chadi Younes, Caesar Abi Shdid, and Girma Bitsuamlak. Air infiltration through building envelopes: A review. *Journal of Building physics*, 35(3):267–302, 2012.
- [52] D.J. Wilson. Flow patterns over flat roofed buildings and application to exhaust stack design. *ASHRAE transactions*, 2(82):284–295, 1979.
- [53] Stefan Becker, Hermann Lienhart, and F Durst. Flow around three-dimensional obstacles in boundary layers. *Journal of Wind Engineering and Industrial Aerodynamics*, 90(4-5):265–279, 2002.
- [54] William V Burton. *Wind tunnel simulation of an atmospheric boundary layer*. PhD thesis, Texas Tech University, 2001.
- [55] Jack E Cermak et al. ASCE manuals and reports on engineering practice no.67: Wind tunnel studies of buildings and structures. Technical report, American Society of civil engineers Reston, VA, USA, 1999.
- [56] Emil Simiu and Robert H Scanlan. *Wind effects on structures: fundamentals and applications to design*, volume 688. John Wiley New York, 1996.
- [57] Hrvoje Kozmar. Wind-tunnel simulations of the suburban abl and comparison with international standards. *Wind and Structures, An International Journal*, 14(1):15–34, 2011.
- [58] DA Spera and TR Richards. Modified power law equations for vertical wind profiles. In *Proceedings of the Conference and Workshop on Wind Energy Characteristics and Wind Energy Siting; 19-21 June 1979; Portland, Oregon (USA)*, pages 47–58, 1979.
- [59] OG Sutton. The application to micrometeorology of the theory of turbulent flow over rough surfaces. *Quarterly journal of the Royal meteorological society*, 75(326):335–350, 1949.
- [60] NJ Cook. Wind-tunnel simulation of the adiabatic atmospheric boundary layer by roughness, barrier and mixing-device methods. *Journal of Wind Engineering and Industrial Aerodynamics*, 3(2-3):157–176, 1978.
- [61] PR Warren and LM Parkins. Single-sided ventilation through open windows. In *Windows in building design and maintenance*, pages 209–228, 1984.

- [62] BSI. BS EN 1991-1:2005 eurocode 1: actions on structures - part 1-4: General actions - wind actions. Technical standards, British standards institute, 2005.
- [63] Hrvoje Kozmar. Influence of spacing between buildings on wind characteristics above rural and suburban areas. *Wind Struct*, 11(5):413–426, 2008.
- [64] John D Holmes. *Wind loading of structures*. CRC press, 2018.
- [65] JO Counihan. Adiabatic atmospheric boundary layers: a review and analysis of data from the period 1880–1972. *Atmospheric Environment (1967)*, 9(10):871–905, 1975.
- [66] Takashi Kurabuchi, Masaaki Ohba, Tomoyuki Endo, Yoshihiko Akamine, and Fumihiro Nakayama. Local dynamic similarity model of cross-ventilation part 1-theoretical framework. *International Journal of Ventilation*, 2(4):371–382, 2004.
- [67] Daniel P Albuquerque, Paul D O’Sullivan, and Guilherme Carrilho da Graça. Effect of window geometry on wind driven single sided ventilation through one opening. *Energy and Buildings*, 245:111060, 2021.
- [68] HW Tieleman and RE Akins. Effects of incident turbulence on pressure distributions on rectangular prisms. *Journal of Wind Engineering and Industrial Aerodynamics*, 36:579–588, 1990.
- [69] Henry W Tieleman. Wind tunnel simulation of the turbulence in the surface layer. *Journal of Wind Engineering and Industrial Aerodynamics*, 36:1309–1318, 1990.
- [70] R Jason Hearst, Guillaume Gomit, and Bharathram Ganapathisubramani. Effect of turbulence on the wake of a wall-mounted cube. *Journal of Fluid Mechanics*, 804:513–530, 2016.
- [71] IP Castro and AG Robins. The flow around a surface-mounted cube in uniform and turbulent streams. *Journal of fluid Mechanics*, 79(2):307–335, 1977.
- [72] Andreas Schröder, Chris Willert, Daniel Schanz, Reinhard Geisler, Tobias Jahn, Quentin Gallas, and Benjamin Leclaire. The flow around a surface mounted cube: a characterization by time-resolved piv, 3d shake-the-box and lbm simulation. *Experiments in Fluids*, 61(9):189, 2020.
- [73] Alexander Yakhot, Tomer Anor, Heping Liu, and Nikolay Nikitin. Direct numerical simulation of turbulent flow around a wall-mounted cube: spatio-temporal evolution of large-scale vortices. *Journal of Fluid Mechanics*, 566:1–9, 2006.
- [74] Alexander Yakhot, Heping Liu, and Nikolay Nikitin. Turbulent flow around a wall-mounted cube: A direct numerical simulation. *International journal of heat and fluid flow*, 27(6):994–1009, 2006.

- [75] S Depardon, JJ Lasserre, LE Brizzi, and J Borée. Instantaneous skin-friction pattern analysis using automated critical point detection on near-wall piv data. *Measurement Science and Technology*, 17(7):1659, 2006.
- [76] R Martinuzzi. Experimentelle untersuchungen der umströmung wandgebundener, rechteckiger, prismatischer hindernisse dissertation lstm. *Universität Erlangen-Nürnberg*, 1992.
- [77] Robert Martinuzzi and Cameron Tropea. The flow around surface-mounted, prismatic obstacles placed in a fully developed channel flow (data bank contribution). *Journal of Fluids Engineering*, 1993.
- [78] Nicholas Charles Daish, G Carrilho da Graça, Paul Frederick Linden, and D Banks. Impact of aperture separation on wind-driven single-sided natural ventilation. *Building and Environment*, 108:122–134, 2016.
- [79] Vincenz Strouhal. *Über eine besondere Art der Tonerregung*. Stahel, 1878.
- [80] ER Meinders and K Hanjalić. Vortex structure and heat transfer in turbulent flow over a wall-mounted matrix of cubes. *International Journal of Heat and fluid flow*, 20(3):255–267, 1999.
- [81] BJ Vickery and C Karakatsanis. External wind pressure distributions and induced internal ventilation flow in low-rise industrial and domestic structures. *ASHRAE transactions*, 93:2198–2213, 1987.
- [82] Daniel Costola, Bert Blocken, and JLM Hensen. Overview of pressure coefficient data in building energy simulation and airflow network programs. *Building and environment*, 44(10):2027–2036, 2009.
- [83] Nicolas Heijmans and Peter Wouters. Impact of the uncertainties on wind pressures on the prediction of thermal comfort performances. Technical report, International Energy Agency, Energy Covervation in Buildings and Community Systems, 2002.
- [84] MV Swami and S Chandra. Correlations for pressure distribution on buildings and calculation of natural-ventilation airflow. *ASHRAE transactions*, 94(1):243–266, 1988.
- [85] Paul Linden, David Banks, Nick Daish, Marc Fountain, Greg Gross, Anoop Honnekeri, Margaret Pigman, Ronnie Thomas, Kyle Adams, Sam Brunswick, et al. *Natural ventilation for energy savings in California Commercial Buildings*. Center for the built environment, 2016.
- [86] Robert E Akins. *Wind pressures on buildings*. PhD thesis, Colorado State University. Libraries, 1976.
- [87] Mohammadreza Shirzadi, Parham A Mirzaei, and Mohammad Naghashzadegan. Development of an adaptive discharge coefficient to improve the accuracy of cross-ventilation airflow calculation in building energy simulation tools. *Building and Environment*, 127:277–290, 2018.



- [88] Ahsan Iqbal, Alireza Afshari, Hans Wigö, and Per Heiselberg. Discharge coefficient of centre-pivot roof windows. *Building and Environment*, 92:635–643, 2015.
- [89] Annamaria Belleri, Roberto Lollini, and Spencer M Dutton. Natural ventilation design: An analysis of predicted and measured performance. *Building and Environment*, 81:123–138, 2014.
- [90] PJ Richards, RP Hoxey, and LJ Short. Wind pressures on a 6 m cube. *Journal of Wind engineering and industrial aerodynamics*, 89(14-15):1553–1564, 2001.
- [91] Mario Grosso. Wind pressure distribution around buildings: a parametrical model. *Energy and Buildings*, 18(2):101–131, 1992.
- [92] B Knoll. Implementing the results of ventilation research. In *Proceedings of the 16th AIVC Conference, Palm Springs, USA 19-22 September, 1995*, 1995.
- [93] Pekka Tuomaala et al. *Implementation and evaluation of air flow and heat transfer routines for building simulation tools*. VTT Technical Research Centre of Finland, 2002.
- [94] Malcolm Orme, Martin W Liddament, and Andrew Wilson. *Numerical data for air infiltration and natural ventilation calculations*. Air Infiltration and Ventilation Centre Bracknell, 1998.
- [95] Martin W Liddament. *Air infiltration calculation techniques: An applications guide*. Air infiltration and ventilation centre Berkshire, UK, 1986.
- [96] W Liddament Martin. *A guide to energy efficient ventilation*. AIVC, Coventry, UK, 1996.
- [97] Subrato Chandra and Muthusamy V Swami. Procedures for calculating natural ventilation airflow rates in buildings. 03-87. Technical report, Florida Solar Energy Center, 1987.
- [98] Helmut E Feustel. Comis—an international multizone air-flow and contaminant transport model. *Energy and Buildings*, 30(1):3–18, 1999.
- [99] Masaaki Ohba, Takashi Kurabuchi, Endo Tomoyuki, Yoshihiko Akamine, Motoyasu Kamata, and Aya Kurahashi. Local dynamic similarity model of cross-ventilation part 2-application of local dynamic similarity model. *International Journal of Ventilation*, 2(4):383–394, 2004.
- [100] YH Chiu and DW Etheridge. External flow effects on the discharge coefficients of two types of ventilation opening. *Journal of Wind Engineering and Industrial Aerodynamics*, 95(4):225–252, 2007.
- [101] S Depardon, JJ Lasserre, JC Boueilh, LE Brizzi, and J Borée. Skin friction pattern analysis using near-wall piv. *Experiments in Fluids*, 39(5):805–818, 2005.

- [102] Yong Cao, Tetsuro Tamura, Dai Zhou, Yan Bao, and Zhaolong Han. Topological description of near-wall flows around a surface-mounted square cylinder at high reynolds numbers. *Journal of Fluid Mechanics*, 933:A39, 2022.
- [103] Yong Cao, Tetsuro Tamura, and Hidenori Kawai. Investigation of wall pressures and surface flow patterns on a wall-mounted square cylinder using very high-resolution cartesian mesh. *Journal of wind engineering and Industrial Aerodynamics*, 188:1–18, 2019.
- [104] Takashi Kurabuchi, Masaaki Ohba, Tomonobu Goto, Yoshihiko Akamine, Tomoyuki Endo, and Motoyasu Kamata. Local dynamic similarity concept as applied to evaluation of discharge coefficients of cross-ventilated buildings—part 1 basic idea and underlying wind tunnel tests; part 2 applicability of local dynamic similarity concept; part 3 simplified method for estimating dynamic pressure tangential to openings of cross-ventilated buildings. *International Journal of Ventilation*, 4(3):285–300, 2005.
- [105] Tomoyuki Endo, Takashi Kurabuchi, Masaaki Ohba, Yoshihiko Akamine, and Motoyasu Kamata. A fundamental study on the air flow structure of outflow openings. *International Journal of Ventilation*, 2(4):439–446, 2004.
- [106] PF Linden, GF Lane-Serff, and DA Smeed. Emptying filling boxes: the fluid mechanics of natural ventilation. *Journal of Fluid Mechanics*, 212:309–335, 1990.
- [107] Rajesh K Bhagat, MS Davies Wykes, Stuart B Dalziel, and PF Linden. Effects of ventilation on the indoor spread of covid-19. *Journal of Fluid Mechanics*, 903, 2020.
- [108] Vladimir Vasil'evič Baturin. *Fundamentals of industrial ventilation*. Pergamon Press Ltd Headington Hill Hall, Oxford., 1972.
- [109] Mats Sandberg. An alternative view on the theory of cross-ventilation. *International journal of ventilation*, 2(4):409–418, 2004.
- [110] H Shetabivash. Investigation of opening position and shape on the natural cross ventilation. *Energy and Buildings*, 93:1–15, 2015.
- [111] Paul F Linden. The fluid mechanics of natural ventilation. *Annual review of fluid mechanics*, 31(1):201–238, 1999.
- [112] Monika Hall. Untersuchungen zum thermisch induzierten luftwechselfpotential von kippfenstern. *Bau-physik*, 26(3):109–115, 2004.

- [113] Per Heiselberg, Kjeld Svidt, and Peter V Nielsen. Characteristics of airflow from open windows. *Building and Environment*, 36(7):859–869, 2001.
- [114] F Flourentzou, J Van der Maas, and C-A Roulet. Natural ventilation for passive cooling: measurement of discharge coefficients. *Energy and buildings*, 27(3):283–292, 1998.
- [115] BSI. BSEN 13141-1:2019 ventilation for buildings - performance testing of components/products for residential ventilation. Technical standards, British standards institute, 2019.
- [116] Smoke Control Association et al. Guidance on smoke control to common escape routes in apartment buildings (flats and maisonettes). *SCA, London*, 2015.
- [117] Tine S Larsen and Per Heiselberg. Single-sided natural ventilation driven by wind pressure and temperature difference. *Energy and Buildings*, 40(6):1031–1040, 2008.
- [118] Chia-Ren Chu, Y-H Chiu, Yi-Ting Tsai, and Si-Lei Wu. Wind-driven natural ventilation for buildings with two openings on the same external wall. *Energy and Buildings*, 108:365–372, 2015.
- [119] Gian Vincenzo Fracastoro, Guglielmina Mutani, and Marco Perino. Experimental and theoretical analysis of natural ventilation by windows opening. *Energy and Buildings*, 34(8):817–827, 2002.
- [120] Chia-Ren Chu and Bo-Fan Chiang. Wind-driven cross ventilation in long buildings. *Building and environment*, 80:150–158, 2014.
- [121] Marcello Caciolo, Pascal Stabat, and Dominique Marchio. Full scale experimental study of single-sided ventilation: analysis of stack and wind effects. *Energy and Buildings*, 43(7):1765–1773, 2011.
- [122] Hildebrando Cruz and João Carlos Viegas. On-site assessment of the discharge coefficient of open windows. *Energy and Buildings*, 126:463–476, 2016.
- [123] Haojie Wang, Panagiota Karava, and Qingyan Chen. Development of simple semiempirical models for calculating airflow through hopper, awning, and casement windows for single-sided natural ventilation. *Energy and Buildings*, 96:373–384, 2015.
- [124] Gerardus PA Bot. *Greenhouse climate: from physical processes to a dynamic model*. Thesis, Landbouwhogeschool te Wageningen, 1983.
- [125] T De Jong and GPA Bot. Flow characteristics of one-side-mounted windows. *Energy and buildings*, 19(2):105–112, 1992.

- [126] Jörn von Grabe. Flow resistance for different types of windows in the case of buoyancy ventilation. *Energy and Buildings*, 65:516–522, 2013.
- [127] Benjamin M Jones and Ray Kirby. Quantifying the performance of a top-down natural ventilation windcatcher™. *Building and Environment*, 44(9):1925–1934, 2009.
- [128] MA Serag-Eldin. Prediction of performance of a wind-driven ventilation device. *Journal of Wind Engineering and Industrial Aerodynamics*, 97(11-12):560–572, 2009.
- [129] DJ Wilson and DE Kiel. Gravity driven counterflow through an open door in a sealed room. *Building and Environment*, 25(4):379–388, 1990.
- [130] Maria Kolokotroni and Per Kvols Heiselberg. Ventilative cooling: State-of-the-art review. Technical report, International Energy Agency Energy Energy in Communities and Buildings Programme, 2015.
- [131] Peter Holzer and Theofanis Ch Psomas. Ventilative cooling sourcebook: Energy in buildings and communities programme. march 2018. Technical report, International Energy Agency Energy Energy in Communities and Buildings Programme, 2018.
- [132] British Standards Institute. BSEN 13141-5:2019 ventilation for buildings - performance testing of components/products for residential ventilation - part 5: Cowls and roof outlet terminal devices. Technical standards, British standards institute, 2019.
- [133] BJ Bailey, JI Montero, J Perez Parra, AP Robertson, E Baeza, and R Kamaruddin. Airflow resistance of greenhouse ventilators with and without insect screens. *Biosystems Engineering*, 86(2):217–229, 2003.
- [134] K K. Syrios and GR Hunt. Design considerations for roof-mounted ventilation systems. *International Journal of Ventilation*, 3(2):89–104, 2004.
- [135] M Sherman. A power-law formulation of laminar flow in short pipes. *Journal of Fluids Engineering*, 114(4), 1992.
- [136] Ahsan Iqbal, Hans Wigo, Per Heiselberg, and Alireza Afshari. Effect of opening the sash of a centre-pivot roof window on wind pressure coefficients. *International Journal of Ventilation*, 13(3):273–284, 2014.
- [137] HK Malinowski. Wind effect on the air movement inside buildings. In *Tokyo Conference of Wind Loads, Tokyo, Japan*, 1971.

- [138] JP Cockroft and Peter Robertson. Ventilation of an enclosure through a single opening. *Building and Environment*, 11(1):29–35, 1976.
- [139] Isaak E Idelchik. Handbook of hydraulic resistance. *Washington*, 1986.
- [140] Chia R Chu, Y-H Chiu, Yan-Jhih Chen, Yu-Wen Wang, and C-P Chou. Turbulence effects on the discharge coefficient and mean flow rate of wind-driven cross-ventilation. *Building and Environment*, 44(10):2064–2072, 2009.
- [141] DW Etheridge. Nondimensional methods for natural ventilation design. *Building and environment*, 37(11):1057–1072, 2002.
- [142] W De Gids and H Phaff. Ventilation rates and energy consumption due to open windows: a brief overview of research in the netherlands. *Air infiltration review*, 4(1):4–5, 1982.
- [143] W S Dols and B J Polidoro. Contam user guide and program documentation version 3.2. Technical report, NIST, 2015.
- [144] Integrated Environmental Solutions Limited. Macroflo user guide. Technical report, IES Virtual Environment, 2014.
- [145] Guilherme Carrilho da Graça. A technical note on simplified modeling of turbulent mixing in wind-driven single sided ventilation. *Building and Environment*, 131:12–15, 2018.
- [146] FH Champagne, YH Pao, and IJ Wygnanski. On the two-dimensional mixing region. *Journal of Fluid Mechanics*, 74(2):209–250, 1976.
- [147] Stephen B Pope and Stephen B Pope. *Turbulent flows*. Cambridge university press, 2000.
- [148] Shinsuke Kato, Ryohei Kono, Takamasa Hasama, Ryoza Ooka, and Takeo Takahashi. A wind tunnel experimental analysis of the ventilation characteristics of a room with single-sided opening in uniform flow. *International Journal of Ventilation*, 5(1):171–178, 2006.
- [149] Toshio Yamanaka, M Narasaki, Ryuji Satoh, and K Iwamoto. Wind-forced ventilation of the room with a single opening-ventilation based on mixing layer caused by the airflow along opening plane. *JOURNAL OF ARCHITECTURE PLANNING AND ENVIRONMENTAL ENGINEERING*, pages 37–44, 1999.
- [150] Toshio Yamanaka, Hisashi Kotani, Kiyotaka Iwamoto, and Masahiro Kato. Natural, wind-forced ventilation caused by turbulence in a room with a single opening. *International Journal of Ventilation*, 5(1):179–187, 2006.

- [151] BSI. BSEN 16798-7:2017 energy performance of buildings - ventilation for buildings - part 7: Calculation methods for the determination of air flow rates in buildings including infiltration. Technical standards, British standards institute, 2017.
- [152] Petri Majander and Timo Siikonen. Large-eddy simulation of a round jet in a cross-flow. *International Journal of Heat and Fluid Flow*, 27(3):402–415, 2006.
- [153] Richard J Margason. Fifty years of jet in cross flow research. *In AGARD*, 1993.
- [154] Yasuhiro Kamotani and Isaac Greber. Experiments on a turbulent jet in a cross flow. *AIAA journal*, 10(11):1425–1429, 1972.
- [155] WP Jones and M Wille. Large-eddy simulation of a plane jet in a cross-flow. *International journal of heat and fluid flow*, 17(3):296–306, 1996.
- [156] R Camussi, G Guj, and A Stella. Experimental study of a jet in a crossflow at very low reynolds number. *Journal of fluid mechanics*, 454:113–144, 2002.
- [157] Fariborz Haghghat, Jiwu Rao, and Paul Fazio. The influence of turbulent wind on air change rates—a modelling approach. *Building and environment*, 26(2):95–109, 1991.
- [158] Toshio Yamanaka, Hisashi Kotani, Kiyotaka Iwamoto, and Masahiro Kato. Natural, wind-forced ventilation caused by turbulence in a room with a single opening. *International Journal of Ventilation*, 5:1:179–187, 2006.
- [159] PS Carey and DW Etheridge. Direct wind tunnel modelling of natural ventilation for design purposes. *Building Services Engineering Research and Technology*, 20(3):131–142, 1999.
- [160] Tomás Norton, Da-Wen Sun, Jim Grant, Richard Fallon, and Vincent Dodd. Applications of computational fluid dynamics (cfd) in the modelling and design of ventilation systems in the agricultural industry: A review. *Bioresource technology*, 98(12):2386–2414, 2007.
- [161] R Everett. Rapid thermal calibration of houses. Technical report, Open University, 1985.
- [162] Thierry Boulard and S Wang. Experimental and numerical studies on the heterogeneity of crop transpiration in a plastic tunnel. *Computers and Electronics in agriculture*, 34(1-3):173–190, 2002.
- [163] A Shklyar and A Arbel. Numerical model of the three-dimensional isothermal flow patterns and mass fluxes in a pitched-roof greenhouse. *Journal of Wind Engineering and Industrial Aerodynamics*, 92(12):1039–1059, 2004.

- [164] Jack E Cermak. Laboratory simulation of the atmospheric boundary layer. *Aiaa Journal*, 9(9):1746–1754, 1971.
- [165] Edgar Buckingham. On physically similar systems; illustrations of the use of dimensional equations. *Physical review*, 4(4):345, 1914.
- [166] WD Curtis, J David Logan, and WA Parker. Dimensional analysis and the pi theorem. *Linear Algebra and its Applications*, 47:117–126, 1982.
- [167] Ain A Sonin. A generalization of the  $\pi$ -theorem and dimensional analysis. *Proceedings of the National Academy of Sciences*, 101(23):8525–8526, 2004.
- [168] ME De Bortoli, B Natalini, MJ Paluch, and MB Natalini. Part-depth wind tunnel simulations of the atmospheric boundary layer. *Journal of Wind Engineering and Industrial Aerodynamics*, 90(4-5):281–291, 2002.
- [169] XX Cheng, J Dong, Y Peng, L Zhao, and YJ Ge. Full-scale/model test comparisons to validate the traditional abl wind tunnel simulation technique: a literature review. *Preprints*, 2017.
- [170] Claës Dyrbye and Svend Ole Hansen. *Wind loads on structures*. Wiley (John) & Sons, Limited, 1997.
- [171] J Armit and J Counihan. The simulation of the atmospheric boundary layer in a wind tunnel. *Atmospheric Environment (1967)*, 2(1):49–71, 1968.
- [172] J Counihan. An improved method of simulating an atmospheric boundary layer in a wind tunnel. *Atmospheric Environment (1967)*, 3(2):197–214, 1969.
- [173] NM Standen. *A spire array for generating thick turbulent shear layers for natural wind simulation in wind tunnels*. National Aeronautical Establishment, Low Speed Aerodynamics Section, 1972.
- [174] NJ Cook. On simulating the lower third of the urban adiabatic boundary layer in a wind tunnel. *Atmospheric Environment (1967)*, 7(7):691–705, 1973.
- [175] HPAH Irwin. The design of spires for wind simulation. *Journal of wind engineering and industrial aerodynamics*, 7(3):361–366, 1981.
- [176] RA Wooding, Edward F Bradley, and JK Marshall. Drag due to regular arrays of roughness elements of varying geometry. *Boundary-Layer Meteorology*, 5(3):285–308, 1973.
- [177] Hamlyn Peter Anthony Hugh Irwin. Design and use of spires for natural wind simulation. *National Aeronautical Establishment, Laboratory Technical Report*, 1979.

- [178] Cesar Farell and Arun KS Iyengar. Experiments on the wind tunnel simulation of atmospheric boundary layers. *Journal of wind engineering and industrial aerodynamics*, 79(1-2):11–35, 1999.
- [179] Hakki Ergun Cekli and Willem van de Water. Tailoring turbulence with an active grid. *Experiments in fluids*, 49:409–416, 2010.
- [180] A Nishi, H Kikugawa, Y Matsuda, and D Tashiro. Active control of turbulence for an atmospheric boundary layer model in a wind tunnel. *Journal of wind engineering and industrial aerodynamics*, 83(1-3):409–419, 1999.
- [181] R Jason Hearst and Philippe Lavoie. The effect of active grid initial conditions on high reynolds number turbulence. *Experiments in Fluids*, 56:1–20, 2015.
- [182] Patrick J Roache. Quantification of uncertainty in computational fluid dynamics. *Annual review of fluid Mechanics*, 29(1):123–160, 1997.
- [183] Joel H Ferziger, Milovan Perić, and Robert L Street. *Computational methods for fluid dynamics*, volume 3. Springer, 2002.
- [184] GJ Maslach. A precision differential manometer. *Review of Scientific Instruments*, 23(7):367–369, 1952.
- [185] Thomas E Piemme. Pressure measurement: Electrical pressure transducers. *Progress in Cardiovascular Diseases*, 5(6):574–594, 1963.
- [186] Robert T Eckenrode and Howard A Kirshner. Measurement of pressure transients. *Review of Scientific Instruments*, 25(1):33–40, 1954.
- [187] Tokihiko Kobata and Douglas A Olson. Accurate determination of differential pressure between two pressure balances using a pressure transducer. In *SICE 2003 Annual Conference (IEEE Cat. No. 03TH8734)*, volume 2, pages 2125–2130. IEEE, 2003.
- [188] John C Lilly. The electrical capacitance diaphragm manometer. *Review of Scientific Instruments*, 13(1):34–37, 1942.
- [189] JM Los and JA Morrison. A sensitive differential manometer. *Review of Scientific Instruments*, 22(11):805–809, 1951.
- [190] Harry Matheson and Murray Eden. A highly sensitive differential manometer. *Review of Scientific Instruments*, 19(8):502–506, 1948.



- [191] V Graeger, R Kobs, and M Liehr. A ceramic differential-pressure transducer. *Philips Tech. Rev.*, 43(4):86, 1987.
- [192] M Kojima, K Saitou, and T Kobata. Study on calibration procedure for differential pressure transducers. In *IMEKO 20th TC3, 3rd TC16 and 1st TC22 International Conference Cultivating metrological knowledge, Merida, Mexico, 2007*.
- [193] MJ Morris, JF Donovan, JT Kegelman, SD Schwab, RL Levy, and RC Crites. Aerodynamic applications of pressure sensitive paint. *AIAA journal*, 31(3):419–425, 1993.
- [194] Christian Klein, Rolf H Engler, Ulrich Henne, and Werner E Sachs. Application of pressure-sensitive paint for determination of the pressure field and calculation of the forces and moments of models in a wind tunnel. *Experiments in Fluids*, 39(2):475–483, 2005.
- [195] Masayuki Anyoji, Daju Numata, Hiroki Nagai, and Keisuke Asai. Pressure-sensitive paint technique for surface pressure measurements in a low-density wind tunnel. *Journal of Visualization*, 18:297–309, 2015.
- [196] JW Gregory, K Asai, M Kameda, T Liu, and JP Sullivan. A review of pressure-sensitive paint for high-speed and unsteady aerodynamics. *Proceedings of the Institution of Mechanical Engineers, Part G: Journal of Aerospace Engineering*, 222(2):249–290, 2008.
- [197] Tomohide Niimi, Masaki Yoshida, Makoto Kondo, Yusuke Oshima, Hideo Mori, Yasuhiro Egami, Keisuke Asai, and Hiroyuki Nishide. Application of pressure-sensitive paints to low-pressure range. *Journal of thermophysics and heat transfer*, 19(1):9–16, 2005.
- [198] James Bell. Applications of pressure-sensitive paint to testing at very low flow speeds. In *42nd AIAA Aerospace Sciences Meeting and Exhibit*, page 878, 2004.
- [199] Nikolaos-Petros Pallas and Demetri Bouris. Calculation of the pressure field for turbulent flow around a surface-mounted cube using the simple algorithm and piv data. *Fluids*, 7(4):140, 2022.
- [200] James Carvill. *Mechanical engineer's data handbook*. Butterworth-Heinemann, 1994.
- [201] BSI. BS EN ISO 3966:2020 measurement of fluid flow in closed conduits - velocity area method using pitot static tubes. Technical standards, British standards institute, 2020.
- [202] Rex Klopfenstein Jr. Air velocity and flow measurement using a pitot tube. *ISA transactions*, 37(4):257–263, 1998.

- [203] NM Guirguisa, AA Abd El-Aziz, and MM Nassief. Study of wind effects on different buildings of pitched roofs. *Desalination*, 209(1-3):190–198, 2007.
- [204] Niels Franck. *Model Law and Experimental technique for determination of Wind Loads on Buildings*. National Physical Laboratory, 1963.
- [205] Roger Legg. *Air conditioning system design*. Butterworth-Heinemann, 2017.
- [206] John Owen Bird and PJ Chivers. *Newnes engineering and physical science pocket book*. Newnes, 2014.
- [207] Edward Lewis Houghton and Peter William Carpenter. *Aerodynamics for engineering students*. Elsevier, 2003.
- [208] PC Stainback and KA Nagabushana. Review of hot-wire anemometry techniques and the range of their applicability for various flows. *a a*, 1:4, 1993.
- [209] B Session, B Knobloch, and S Mierzwinski. Comparatory tests of omnidirectional and hot wire anemometers. *Room-vent*, 1990.
- [210] Narinder K Tutu and Rene Chevray. Cross-wire anemometry in high intensity turbulence. *Journal of Fluid Mechanics*, 71(4):785–800, 1975.
- [211] ARG Lang and R Leuning. New omnidirectional anemometer with no moving parts. *Boundary-Layer Meteorology*, 20(4):445–457, 1981.
- [212] MGLC Loomans and AWM v Schijndel. Simulation and measurement of the stationary and transient characteristics of the hot sphere anemometer. *Building and Environment*, 37(2):153–163, 2002.
- [213] JGj Olin and RB Kiland. Split-film anemometer sensors for three-dimensional velocity-vector measurement. In *Aircraft Wake Turbulence and Its Detection*, pages 57–79. Springer, 1971.
- [214] Bruce W Spencer and BG Jones. Turbulence measurements with the split-film anemometer probe. *Symposia on turbulence in Liquids*, 1971.
- [215] HPAH Irwin. A simple omnidirectional sensor for wind-tunnel studies of pedestrian-level winds. *Journal of wind engineering and industrial aerodynamics*, 7(3):219–239, 1981.
- [216] Hanqing Wu and Theodore Stathopoulos. Further experiments on irwin’s surface wind sensor. *Journal of wind engineering and industrial aerodynamics*, 53(3):441–452, 1994.
- [217] M Moravej, P Irwin, I Zisis, A Gan Chowdhury, and B Hajra. Effects of roof height on local pressure and velocity coefficients on building roofs. *Engineering Structures*, 150:693–710, 2017.

- [218] Charles P Wang. Laser doppler velocimetry. *Journal of Quantitative Spectroscopy and Radiative Transfer*, 40(3):309–319, 1988.
- [219] JB Abbiss, TW Chubb, and ER Pike. Laser doppler anemometry. *Optics & Laser Technology*, 6(6):249–261, 1974.
- [220] Angelo Algieri, Sergio Bova, and Carmine De Bartolo. Experimental and numerical investigation on the effects of the seeding properties on lda measurements. *Journal of Fluids Engineering*, 2005.
- [221] DA Lyn and W Rodi. The flapping shear layer formed by flow separation from the forward corner of a square cylinder. *Journal of fluid Mechanics*, 267:353–376, 1994.
- [222] Dennis A Lyn, S Einav, W Rodi, and J-H Park. A laser-doppler velocimetry study of ensemble-averaged characteristics of the turbulent near wake of a square cylinder. *Journal of Fluid Mechanics*, 304:285–319, 1995.
- [223] Marcel Bottema. *Wind climate and urban geometry*. PhD thesis, Technische Universiteit Eindhoven, 1993.
- [224] Richard D Keane and Ronald J Adrian. Theory of cross-correlation analysis of piv images. *Applied scientific research*, 49:191–215, 1992.
- [225] Fulvio Scarano. Tomographic piv: principles and practice. *Measurement Science and Technology*, 24(1):012001, 2012.
- [226] Panagiota Karava, Ted Stathopoulos, and AK Athienitis. Airflow assessment in cross-ventilated buildings with operable façade elements. *Building and environment*, 46(1):266–279, 2011.
- [227] Bert Blocken, WD Janssen, and Twan van Hooff. Cfd simulation for pedestrian wind comfort and wind safety in urban areas: General decision framework and case study for the eindhoven university campus. *Environmental Modelling & Software*, 30:15–34, 2012.
- [228] Yongling Zhao, Haiwei Li, Aytac Kubilay, and Jan Carmeliet. Buoyancy effects on the flows around flat and steep street canyons in simplified urban settings subject to a neutral approaching boundary layer: Wind tunnel piv measurements. *Science of the Total Environment*, 797:149067, 2021.
- [229] Yoshihide Tominaga, Shin-ichi Akabayashi, Takuya Kitahara, and Yuki Arinami. Air flow around isolated gable-roof buildings with different roof pitches: Wind tunnel experiments and cfd simulations. *Building and Environment*, 84:204–213, 2015.

- [230] Sang-Joon Lee, Cheol-Woo Park, and Jong-Hoon Kang. Evaluation of wind environment around a residential complex using a piv velocity field measurement technique. *Environmental fluid mechanics*, 9:655–668, 2009.
- [231] Zhixiang Liu, Zhixiang Yu, Xiaoxiao Chen, Ruizhou Cao, and Fu Zhu. An investigation on external airflow around low-rise building with various roof types: Piv measurements and les simulations. *Building and Environment*, 169:106583, 2020.
- [232] Renata Gnatowska, Marcin Sosnowski, and Václav Uruba. Cfd modelling and piv experimental validation of flow fields in urban environments. In *E3S Web of Conferences*, volume 14, page 01034. EDP Sciences, 2017.
- [233] Bubryur Kim, KT Tse, Akihito Yoshida, Yukio Tamura, Zengshun Chen, Pham Van Phuc, and Hyo Seon Park. Statistical analysis of wind-induced pressure fields and piv measurements on two buildings. *Journal of Wind Engineering and Industrial Aerodynamics*, 188:161–174, 2019.
- [234] Boris Conan, Jeroen van Beeck, and Sandrine Aubrun. Sand erosion technique applied to wind resource assessment. *Journal of Wind Engineering and Industrial Aerodynamics*, 104:322–329, 2012.
- [235] Renate Teppner, Bernd Langensteiner, Walter Meile, Günter Brenn, and Sybill Kerschbaumer. Air change rates driven by the flow around and through a building storey with fully open or tilted windows: An experimental and numerical study. *Energy and buildings*, 76:640–653, 2014.
- [236] WJ Beranek and H Van Koten. Visual techniques for the determination of wind environment. *Journal of Wind Engineering and Industrial Aerodynamics*, 4(3-4):295–306, 1979.
- [237] F Livesey, D Incelet, N Isyumov, and AG Davenport. A scour technique for the evaluation of pedestrian winds. *Journal of Wind Engineering and Industrial Aerodynamics*, 36:779–789, 1990.
- [238] Jason CR Hunt, Christopher J Abell, Jozef A Peterka, and H Woo. Kinematical studies of the flows around free or surface-mounted obstacles; applying topology to flow visualization. *Journal of Fluid Mechanics*, 86(1):179–200, 1978.
- [239] Carlos Pinho. The positive displacement method for calibration of gas flow meters. the influence of gas compressibility. *Applied thermal engineering*, 41:111–115, 2012.
- [240] D Jones. Positive displacement gas meters are durable servants. *Pipe line & gas industry*, 80(12):31–33, 1997.

- [241] Josue Marc Jeannon. *Pulsations from rotary positive displacement gas meters*. University of Leicester (United Kingdom), 1975.
- [242] BSI. BS EN ISO 5167-1:2003 measurement of fluid flow by means of pressure differential devices inserted in circular cross-section conduits running full - part 1: General principles and requirements. Technical standards, British standards institute, 2003.
- [243] BSI. BS EN ISO 5167-2:2003 measurement of fluid flow by means of pressure differential devices inserted in circular cross-section conduits running full - part 2: Orifice plates. Technical standards, British standards institute, 2003.
- [244] BSI. BS EN ISO 5167-3:2003 measurement of fluid flow by means of pressure differential devices inserted in circular cross-section conduits running full - part 3: Nozzles and venturi nozzles. Technical standards, British standards institute, 2003.
- [245] BSI. BS EN ISO 5167-4:2003 measurement of fluid flow by means of pressure differential devices inserted in circular cross-section conduits running full - part 4: Venturi tubes. Technical standards, British standards institute, 2003.
- [246] BSI. BS EN ISO 5167-5:2003 measurement of fluid flow by means of pressure differential devices inserted in circular cross-section conduits running full - part 5: Cone meters. Technical standards, British standards institute, 2003.
- [247] Max H Sherman. Tracer-gas techniques for measuring ventilation in a single zone. *Building and Environment*, 25(4):365–374, 1990.
- [248] S Van Buggenhout, Andres Van Brecht, S Eren Özcan, Erik Vranken, W Van Malcot, and Daniel Berckmans. Influence of sampling positions on accuracy of tracer gas measurements in ventilated spaces. *Biosystems Engineering*, 104(2):216–223, 2009.
- [249] Hiroyasu Okuyama, Yoshinori Onishi, Shin-ichi Tanabe, and Seiichi Kashihara. Statistical data analysis method for multi-zonal airflow measurement using multiple kinds of perfluorocarbon tracer gas. *Building and Environment*, 44(3):546–557, 2009.
- [250] Jessica Few and Clifford Elwell. Measuring the ventilation rate in occupied buildings and adapting the co2 tracer gas technique. In *Proceedings of the 40th AIVC–8th TightVent–6th venticool Conference, Ghent, Belgium*, pages 15–16, 2019.

- [251] Gabriel Remion, Bassam Moujalled, and Mohamed El Mankibi. Review of tracer gas-based methods for the characterization of natural ventilation performance: Comparative analysis of their accuracy. *Building and Environment*, 160:106180, 2019.
- [252] Jörn von Grabe, Petr Svoboda, and Armin Bäumler. Window ventilation efficiency in the case of buoyancy ventilation. *Energy and Buildings*, 72:203–211, 2014.
- [253] MH Sherman. Uncertainty in air flow calculations using tracer gas measurements. *Building and Environment*, 24(4):347–354, 1989.
- [254] Jihong Wang, Shugang Wang, Tengfei Zhang, and Francine Battaglia. Assessment of single-sided natural ventilation driven by buoyancy forces through variable window configurations. *Energy and buildings*, 139:762–779, 2017.
- [255] Hannah Gough, T Sato, Christos Halios, CSB Grimmond, Zhiwen Luo, Janet F Barlow, Adam Robertson, Roger Hoxey, and Andrew Quinn. Effects of variability of local winds on cross ventilation for a simplified building within a full-scale asymmetric array: Overview of the silsoe field campaign. *Journal of Wind Engineering and Industrial Aerodynamics*, 175:408–418, 2018.
- [256] John Mandel and Frank L McCrackin. Analysis of families of curves. *Journal of Research of the National Bureau of Standards. Section A, Physics and Chemistry*, 67(3):259, 1963.
- [257] MATLAB. *version 7.10.0 (R2010a)*. The MathWorks Inc., Natick, Massachusetts, 2010.
- [258] Ifan G. Hughes and Thomas P.A. Hase. *Measurements and their uncertainties - a practical guide to modern error analysis*. Oxford University Press, 2010.
- [259] David Weyburne. The unbounded and bounded boundary layer models for flow along a wall. Technical report, Air Force Research Laboratory/RYDH Wright-Patterson AFB United States, 2020.
- [260] Gary R Hunt and Joanne M Holford. The discharge coefficient—experimental measurement of a dependence on density contrast. In *Proc. 21st AIVC Conference, The Hague, Netherlands*, 2000.
- [261] Tine Steen Larsen, Christoffer Plesner, Valérie Leprince, François Rémi Carrié, and Anne Kirkegaard Bejder. Calculation methods for single-sided natural ventilation: Now and ahead. *Energy and Buildings*, 177:279–289, 2018.



# Appendix A

## Derivations of the orifice equation

The orifice equation relates the volume flow rate of fluid through an orifice to the pressure drop across it. In general, this can be derived by applying Bernoulli analysis to a streamline between a point upstream of the opening and a point within the *vena contracta* to evaluate the flow velocity, and integrating over the contracted area of the jet at this point. The *vena contracta* represents the location in the jet where all the available pressure differential has been converted into momentum, and has the same static pressure as the surrounding air. The standard derivation relies on a range of assumptions:

- Incompressible flow
- Irrotational flow
- Inviscid flow
- Uniform density
- Negligible variation in static pressure with height
- Still air in both upstream and downstream reservoirs
- Uniform velocity profile in the *vena contracta*
- Negligible entrainment between the opening and the *vena contracta*

### A.1 Standard derivation

The standard derivation applies the Bernoulli equation to streamlines of constant height, or where the variation in static pressure with height can be neglected. Here, equating the total pressure between a point



in the static reservoir upstream of the opening and a point in the *vena contracta* yields

$$P_{T(1)} = P_{T(2)} \quad (\text{A.1})$$

$$P_1 = P_2 + \frac{1}{2}\rho U_2^2 \quad (\text{A.2})$$

$$U_2 = \sqrt{\frac{2}{\rho}(P_1 - P_2)} \quad (\text{A.3})$$

To account for frictional losses, a loss factor  $C_f = U/U_2$  is included, where  $U$  is the flow velocity achieved in reality, and  $U_2$  is the flow velocity predicted by the Bernoulli equation. When the pressure difference across the opening is uniform, this can be integrated over the area of the *vena contracta* to yield

$$Q = \int^{A_{vc}} C_f U_2 dA \quad (\text{A.4})$$

$$Q = A_{vc} C_f \sqrt{\frac{2}{\rho}(P_1 - P_2)} \quad (\text{A.5})$$

$$C_c = \frac{A_f}{A_{vc}} \quad (\text{A.6})$$

$$Q = A_f C_c C_f \sqrt{\frac{2}{\rho}(P_1 - P_2)} \quad (\text{A.7})$$

$$Q = A_f C_{d_o} \sqrt{\frac{2}{\rho}(P_1 - P_2)} \quad (\text{A.8})$$

where  $C_c$  is the contraction coefficient,  $A_f$  is the reference area used to define the contraction coefficient, and  $C_{d_o}$  is the *orifice* discharge coefficient.

## A.2 Non-uniform streamline height

The impact of a non-uniform streamline height can be considered by applying the Bernoulli analysis between an arbitrary point in the upstream reservoir to a point in the *vena contracta*. Here, still air of uniform density in both the upstream and downstream reservoirs is assumed. The total pressure balance yields the following relation:

$$P_1 + \rho g z_1 = P_2 + \rho g z_2 + \frac{1}{2}\rho U_2^2 \quad (\text{A.9})$$

$$U_2 = \sqrt{\frac{2}{\rho}(P_1 - P_2 + (\rho g z_1 - z_2))} \quad (\text{A.10})$$

If the density of the reservoir on the inlet side is uniform, the static pressure in the streamline  $P_1$  can be expressed in terms of the measured pressure in the upstream reservoir at the height of the *vena contracta*. This yields

$$P_1 + \rho g z_1 = P_{1(z_2)} + \rho g z_2 \quad (\text{A.11})$$

$$P_1 = P_{1(z_2)} - \rho g (z_1 - z_2) \quad (\text{A.12})$$

$$U_2 = \sqrt{\frac{2}{\rho} (P_{1(z_2)} - P_2)} \quad (\text{A.13})$$

where  $P_{1(z_2)}$  is the static pressure in the upstream reservoir at the height of the *vena contracta*  $z_2$ . This yields the same expression for velocity as that derived from the assumption of constant streamline height. Therefore, where the fluid density is uniform, an expression based on uniform streamline heights presents a valid description of flow behaviour regardless of the shape of upstream streamlines.

### A.2.1 Flow from a reservoir of non-uniform density

Let us consider a case where the inlet reservoir represents a stratified space. Here, the window sits within a zone of well-mixed air of uniform density. At a distance above the top of the window, a boundary exists between this air and a stratified layer of well mixed air at a lower density.

Let us consider a streamline that passes through the opening, and originates within the stratified layer. Equating total pressures along the streamlines yields

$$P_1 + \rho_s g z_1 = P_2 + \rho_s g z_2 + \frac{1}{2} \rho U_2^2 \quad (\text{A.14})$$

$$U_2 = \sqrt{\frac{2}{\rho_s} (P_1 - P_2 + \rho_s g (z_1 - z_2))} \quad (\text{A.15})$$

where  $\rho_s$  is the density of the air in the stratified layer. If the air density is uniform in the stratified layer and is also uniform in the inlet reservoir beneath it, the static pressure in the streamline  $P_1$  can be expressed in terms of the static pressure at the boundary of the stratified layer  $P_s$ , which can in turn be expressed in terms of the static pressure in the inlet reservoir air at the height of the outlet  $P_{I(z_2)}$ .

$$P_1 + \rho_s g z_1 = P_s + \rho_s g z_s \quad (\text{A.16})$$

$$P_s + \rho_I g z_s = P_{I(z_2)} + \rho_I g z_2 \quad (\text{A.17})$$

$$P_1 = P_{I(z_2)} + \rho_I g (z_2 - z_s) + \rho_s g (z_s - z_1) \quad (\text{A.18})$$

$$U_2 = \sqrt{\frac{2}{\rho_s} (P_{I(z_2)} - P_2 - (\rho_I - \rho_s) g (z_s - z_2))} \quad (\text{A.19})$$

where  $z_s$  is the height of the boundary of the stratified layer, and  $\rho_I$  is the density of the air in the inlet reservoir. The velocity of a streamline originating within the stratified layer relative to one originating within the inlet reservoir can be given by

$$\frac{U_{2(s)}}{U_{2(I)}} = \sqrt{\frac{\frac{2}{\rho_s} (P_{I(z_2)} - P_2 - (\rho_I - \rho_s) g (z_s - z_2))}{\frac{2}{\rho_I} (P_{I(z_2)} - P_2)}} \quad (\text{A.20})$$

$$\frac{U_{2(s)}}{U_{2(I)}} = \sqrt{\frac{\rho_I}{\rho_s} \left( 1 - \frac{(\rho_I - \rho_s) g (z_s - z_2)}{P_{I(z_2)} - P_2} \right)} \quad (\text{A.21})$$

$$\frac{U_{2(s)}}{U_{2(I)}} = \sqrt{\frac{\rho_I}{\rho_s} (1 - P_s^*)} \quad (\text{A.22})$$

Here, the dimensionless stratification pressure  $P_s^*$  represents the ratio of the flow resistance caused by the buoyancy of the stratified layer to the pressure drop available to drive flow. Streamlines originating from the stratified layer would inevitably have a lower velocity than those originating from the layer within which the opening resides. If the dimensionless stratification pressure is greater than one, then no streamlines originating within the stratified layer are capable of passing through the opening.

It follows from this analysis that, in reservoirs of non-uniform density, the velocity in the outlet cannot be described independently of the origin of the streamlines. However, in these conditions it is energetically favourable for streamlines to follow flatter paths through the media, reducing the degree to which streamline velocities may be reduced. In the case of stratified, well mixed layers, all streamlines that pass through the opening can be regarded as independent of the origin of the jet when the dimensionless stratification pressure is greater than one.

The impact of this effect may not be straightforward. Flows originating from stratified layers would reduce the velocity at the outlet, and therefore might be expected to reduce volume flow rates. However, the presence of these buoyancy forces would change the shapes of the streamlines. In the limiting case, the stratified layer acts as a solid wall, restricting the size of the internal space. Studies of flow in pipes

have shown that this can increase the *orifice* discharge coefficient of openings [38], and therefore result in increased volume flow rates. As such, general models of volume flow rate through openings in stratified flows are likely to be too complex for practical use.

### A.2.2 Flow between zones of different density

A common condition in natural ventilation occurs where air flows through ventilation openings between zones of different density. When a jet leaves an opening, it is subject to buoyancy forces in the zone it enters. This can cause the jet to either accelerate or decelerate, potentially altering both the speed and direction of resulting flows.

Let us consider a horizontally mounted opening between two zones of different density. Equating total pressures along the streamline yields

$$P_1 + \rho_I g z_1 = P_2 + \rho_I g z_2 + \frac{1}{2} \rho_I U_2^2 \quad (\text{A.23})$$

$$U_2 = \sqrt{\frac{2}{\rho_I} (P_1 - P_2 + \rho_I g (z_1 - z_2))} \quad (\text{A.24})$$

where the static pressure  $P_2$  equates to the static pressure in the outlet reservoir at the height of the streamline in the *vena contracta*,  $P_{O(z_2)}$ . Where both the air in the inlet reservoir and air in the outlet reservoir are of uniform density, the pressures  $P_1$  and  $P_2$  can be expressed in terms of measured at a common reference height, here chosen to be the height of the window  $z_w$

$$P_1 + \rho_I g z_1 = P_{I(z_w)} + \rho_I g z_w \quad (\text{A.25})$$

$$P_2 + \rho_O g z_2 = P_{O(z_w)} + \rho_O g z_w \quad (\text{A.26})$$

$$U_2 = \sqrt{\frac{2}{\rho_I} (P_{I(z_w)} - P_{O(z_w)} + (\rho_O - \rho_I) g (z_2 - z_w))} \quad (\text{A.27})$$

The velocity of a streamline between two zones of different density relative to that occurring between two zones of equal density can be given by

$$\frac{U_{2(B)}}{U_{2(O)}} = \sqrt{\frac{P_{I(w)} - P_{O(w)} + (\rho_O - \rho_I) g (z_2 - z_w)}{P_{I(w)} - P_{O(w)}}} \quad (\text{A.28})$$

$$\frac{U_{2(B)}}{U_{2(O)}} = \sqrt{1 + \frac{(\rho_O - \rho_I) g (z_2 - z_w)}{P_{I(w)} - P_{O(w)}}} \quad (\text{A.29})$$

$$\frac{U_{2(B)}}{U_{2(O)}} = \sqrt{1 + \frac{1}{P_P^*}} \quad (\text{A.30})$$

$$(\text{A.31})$$

where the dimensionless plume pressure  $P_P^*$  represents the ratio of the static pressure difference that occurs at uniform density relative to the pressure increment due to buoyancy in the outgoing plume. Where the dimensionless plume pressure is positive, the streamline velocity would be greater than that predicted using the orifice equation. If it is negative, streamline velocities would be lower.

The impact on volume flow rate, however, is more complex. Jets reinforced by buoyancy forces have a higher velocity at the *vena contracta*, and therefore might be expected to have higher volume flow rates. However, studies on buoyancy reinforced flows through horizontal openings has shown that buoyancy forces result in a reduced area of the *vena contracta* as the plume contracts [260]. A thorough review of the literature identified no studies that have been undertaken to investigate the impact an adverse density gradient would have on volume flow rates.

The contraction effect of plumes may also have an effect on volume flow rates through vertically mounted windows, as inflow jets are deflected by buoyancy forces [113]. Volume flow rates through openings across a density gradient have been shown to be lower than those that occur between zones of equal density [113]. The mechanism behind this effect, however, is not clear, and is confounded by the presence of a pressure gradient across the height of the opening.

For characterisation purposes, the dimensionless plume pressure can be used to characterise any flow scenario between two zones of uniform but different densities. However, as the height of the *vena contracta* is seldom known *a priori*, a characteristic dimensionless plume pressure needs to be defined based on measurable characteristic dimensions. This can be given by

$$P_{P_c}^* = \frac{\Delta P}{\frac{1}{2} \Delta \rho g L_c} \quad (\text{A.32})$$

### A.3 Non-uniform pressure profile

When deriving the orifice flow equation, it is commonly assumed that the pressure profile is uniform across the opening. This simplifies the integration of the streamline velocity over the area of the *vena contracta*. It is useful to investigate the implication of common scenarios where this assumption is violated.

Here, the case where both the upstream and downstream reservoirs are still, and are of uniform, but different densities, is considered. Uniform streamline height is assumed, which implies that the pressure difference driving flow is large compared to the pressure increment due to buoyancy of the outgoing jet.

In general, the volume flow rate through the opening can be expressed as

$$Q = \int^{A_{vc}} \sqrt{\frac{2}{\rho_I} \Delta P} dA_{vc} \quad (\text{A.33})$$

$$Q = \int^{w_{vc}} \int^{h_{vc}} \sqrt{\frac{2}{\rho_I} \Delta P} dz dx \quad (\text{A.34})$$

Where  $\Delta P$  is a function of height  $z$ ;  $x$  lies in the direction parallel to the opening plane and perpendicular to the height;  $h_{vc}$  is the height of the *vena contracta*; and  $w_{vc}$  is the width of the *vena contracta* measured in the  $x$  direction. Where the pressure is uniform in the  $x$  direction, this evaluates to

$$Q = \int^{h_{vc}} w_{vc} \sqrt{\frac{2}{\rho_I} \Delta P} dz \quad (\text{A.35})$$

For flow through a rectangular opening, it is assumed that the width of the *vena contracta* is invariant with height. When the upstream and downstream reservoirs are static and of uniform density, the pressure difference can be expressed as a function of distance from the neutral pressure level, This yields

$$Q = \int^{h_{vc}} w_{vc} \sqrt{\frac{2}{\rho_I} (\rho_I - \rho_O) g (z_n - z)} dz \quad (\text{A.36})$$

$$Q = w_{vc} \sqrt{2g \frac{(\rho_I - \rho_O)}{\rho_I}} \int_{z_n - z_{vc(t)}}^{z_n - z_{vc(b)}} \sqrt{z_{\Delta n}} dz_{\Delta n} \quad (\text{A.37})$$

$$Q = \frac{2}{3} w_{vc} \sqrt{2g \frac{\rho_I - \rho_O}{\rho_I}} \left( \sqrt{(z_n - z_{vc(b)})^3} - \sqrt{(z_n - z_{vc(t)})^3} \right) \quad (\text{A.38})$$

where  $z_{vc(t)}$  is the height of the top of the *vena contracta*,  $z_{vc(b)}$  is the height of the bottom of the *vena contracta*, and  $z_n$  is the height of the neutral pressure level. This equation yields real values only when unidirectional flow occurs through the opening. This occurs when the neutral height is either above the top of the opening or below the bottom of the opening. To simplify the equation, a few dimensionless parameters

are created, given by

$$z_n^* = \frac{2(z_n - z_{vc(c)})}{h_{vc}} \quad (\text{A.39})$$

$$h_{vc}^* = \frac{h_{vc}}{h} \quad (\text{A.40})$$

where  $z_n^*$  is the dimensionless neutral height,  $z_{vc(c)}$  is the vertical centre of the *vena contracta*, and  $h^*$  is the dimensionless height of the *vena contracta*. When the dimensionless neutral height is greater than one or less than negative one, unidirectional flow occurs through the opening. This yields

$$Q = \frac{1}{3} w_{vc} h_{vc} \sqrt{g \frac{\rho_I - \rho_O}{\rho_I} h_{vc}} \left( \sqrt{(z_n^* + 1)^3} - \sqrt{(z_n^* - 1)^3} \right) \quad (\text{A.41})$$

$$Q = \frac{1}{3} C_d A \sqrt{hg \frac{\rho_I - \rho_O}{\rho_I} h_{vc}^*} \left( \sqrt{(z_n^* + 1)^3} - \sqrt{(z_n^* - 1)^3} \right) \quad (\text{A.42})$$

Assuming equivalent contraction coefficients, the ratio of air flow through the opening relative to that which occurs when a uniform pressure differential is specified equal to that occurring at the centre of the opening can be given by

$$\frac{Q}{Q_O} = \frac{1}{3} \left( \sqrt{(z_n^* + 1)^3} - \sqrt{(z_n^* - 1)^3} \right) \sqrt{\frac{1}{z_n^*}} \quad (\text{A.43})$$

This equation is valid only when unidirectional flow occurs through the opening, and tends rapidly to one as the dimensionless neutral height exceeds one. The minimum value achieved during unidirectional flow regimes is around 0.94, suggesting that for simple, rectangular openings, the effect of this pressure gradient can usually be neglected.

When the neutral height occurs within the area of the opening, the descriptive equation needs to be evaluated piecewise to separate the components of the flow occurring in each direction. This yields the following equations

$$Q_1 = \frac{1}{3} C_d A \sqrt{hg \frac{\rho_H - \rho_L}{\rho_L} h_{vc}^* (1 - z_n^*)^3} \quad (\text{A.44})$$

$$Q_2 = \frac{1}{3} C_d A \sqrt{hg \frac{\rho_H - \rho_L}{\rho_H} h_{vc}^* (z_n^* + 1)^3} \quad (\text{A.45})$$

$$Q_{net} = Q_1 - Q_2 \quad (\text{A.46})$$

$$Q_{net} = \frac{1}{3} C_d A \sqrt{hg \frac{\rho_H - \rho_L}{\bar{\rho}} h_{vc}^*} \left( \sqrt{\frac{\bar{\rho}}{\rho_L} (1 - z_n^*)^3} - \sqrt{\frac{\bar{\rho}}{\rho_H} (z_n^* + 1)^3} \right) \quad (\text{A.47})$$

$$\frac{Q_{net}}{Q_O} = \frac{1}{3} \left( \sqrt{\frac{\bar{\rho}}{\rho_L} (1 - z_n^*)^3} - \sqrt{\frac{\bar{\rho}}{\rho_H} (z_n^* + 1)^3} \right) \sqrt{\frac{1}{z_n^*}} \quad (\text{A.48})$$

where the subscripts  $H$  and  $L$  refer to the high and low density fluids respectively;  $Q_1$  refers to flow through the top of the opening and occurs in the direction of low to high density;  $Q_2$  refers to flow through the bottom of the opening and occurs in the direction of high to low density; and  $\bar{\rho}$  is the mean density of the two fluids. This regime occurs when  $z_n^* h_{vc}^*$  is between positive and negative one.

Most derivations of this equation assume uniform streamline height, and therefore that  $h_{vc}^*$  is equal to one. A further simplification occurs when the neutral height occurs in the centre of the opening, and the Boussinesq assumption is applied to the density term. Here

$$Q_1 = Q_2 = \frac{1}{3} C_d A \sqrt{hg \frac{\Delta\rho}{\rho}} \quad (\text{A.49})$$

This situation arises where buoyancy drives flow through a single opening, and is widely used to model single-sided ventilation [61, 3, 5, 16, 261].





## Appendix B

# Modelling the impact of flow connection on driving pressures and ventilation efficiency

### B.1 Introduction

Chapter 2 identified evidence of increases in bulk airflow rate that occur when inflow and outflow openings are closely aligned. This effect may be caused by conservation of kinetic energy between the inflow jet and the outlet, or it may be associated with a change in streamline shape in the approach to the outlet. Moreover, it is unclear whether this effect is beneficial, as it is possible that this flow connection inhibits the removal of pollutants from the wider space.

### B.2 Analytical model

A simplified analytical approach to this question is developed by considering a stream tube that forms between two aligned openings in a large space; see Figure B.1. In this model, the inflow air is treated as a free jet, which expands as it entrains air on its journey towards an outlet located on the opposite wall. When the inlet is small, the inflow jet mixes thoroughly with the room air before being extracted and so the extracted air can be considered to be made up entirely of room air. The kinetic energy is also completely dissipated, resulting in still-air conditions at the surface of the outflow opening. Conversely, when the inlet is large, much of the fresh air leaves via the outlet without mixing with the room air, and the jet reaches the

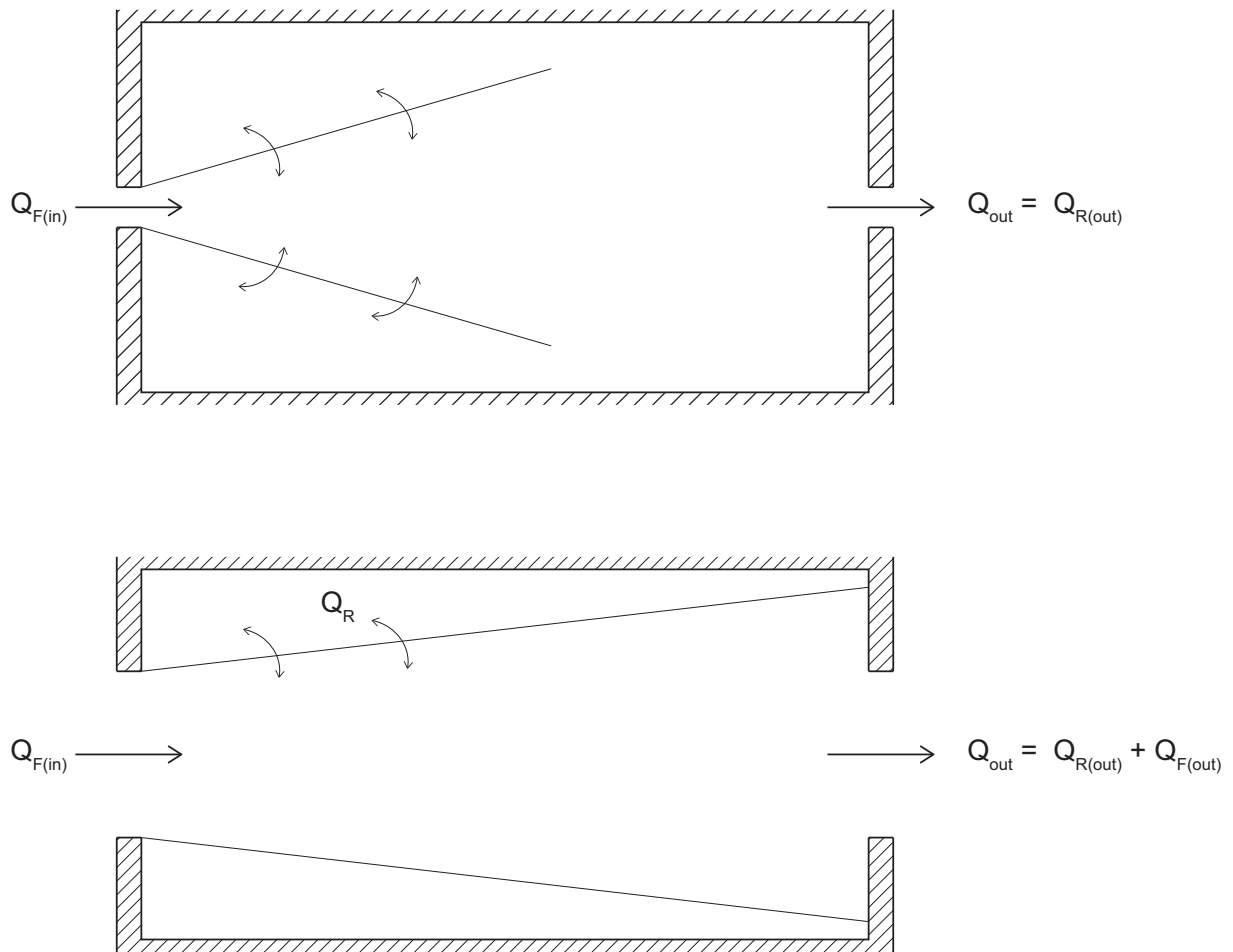


**Figure B.1:** An illustration of the difference between an expanding jet from a small opening (top) and a large opening (bottom).

outlet with a significant velocity. Room air can be removed from the space only by entrainment into the jet.

The effect of flow connection on a natural ventilation strategy can be broken down into two key phenomena; the increase in bulk airflow rate due to conservation of kinetic energy and the reduction in ventilation effectiveness [3],  $E_v$ , caused by short circuiting of fresh air.

A simple model for estimating bulk airflow rates can be made using a modified envelope flow model, which allows a proportion of the dynamic pressure in the inflow jet to be conserved to drive air through the outflow opening. The dynamic pressure in the jet available to drive airflow can be evaluated using the entrainment equations for ideal free jets [6]. Assuming the contraction coefficients of the openings are unchanged by the altered streamlines, a dimensionless volume flow rate can be evaluated

$$\frac{Q}{Q_E} \sqrt{\frac{1 + A^{*2}}{1 + A^{*2} - 16 \frac{A_{eff(1)}}{x^2}}} \quad (\text{B.1})$$

where  $Q_E$  is the volume flow rate predicted by conventional envelope flow models,  $A^*$  is the ratio of the *effective* area of the inlet  $A_{eff(1)}$  to the *effective* area of the outlet  $A_{eff(2)}$ , and  $x$  is the distance between the two openings.

The ventilation effectiveness [3] can be defined as the proportion of room air in the jet at the outlet. Similarly, this can be evaluated using the entrainment equations for free jets [6], giving

$$E_v = \frac{Q_{R(out)}}{Q_{out}} = 1 - 4 \frac{\sqrt{A_{eff(1)}}}{x} \quad (\text{B.2})$$

where  $Q_{R(out)}/Q_{out}$  is the proportion of room air extracted from the space. The effective ventilation rate of room air can be calculated as the product of the ventilation effectiveness and the volume flow rate. Equations B.1 and B.2 suggest that the relevant dimensionless parameter is the ratio  $\sqrt{A_{eff}}/x$ , rather than the commonly favoured opening porosity [38].

### B.3 Comparison with literature data

The predictions of these equations can be compared against the data presented by Seifert *et al.* [1]. They present a CFD study of a 6m cube, where the area of the inlet and outlet are gradually increased. By applying the model to this data, the mass flow rate of room and fresh air can be plotted as opening area is increased; see Figure B.2. Once flow connection has been formed, the rate at which room air is removed drops and is not sufficiently offset by increasing flow rate of fresh air. This contrasts with conventional wisdom that larger airflow rates imply higher pollutant dilution rates and provide more effective ventilative cooling. It also demonstrates the continuous predictions made by combining free jet and envelope flow models agree

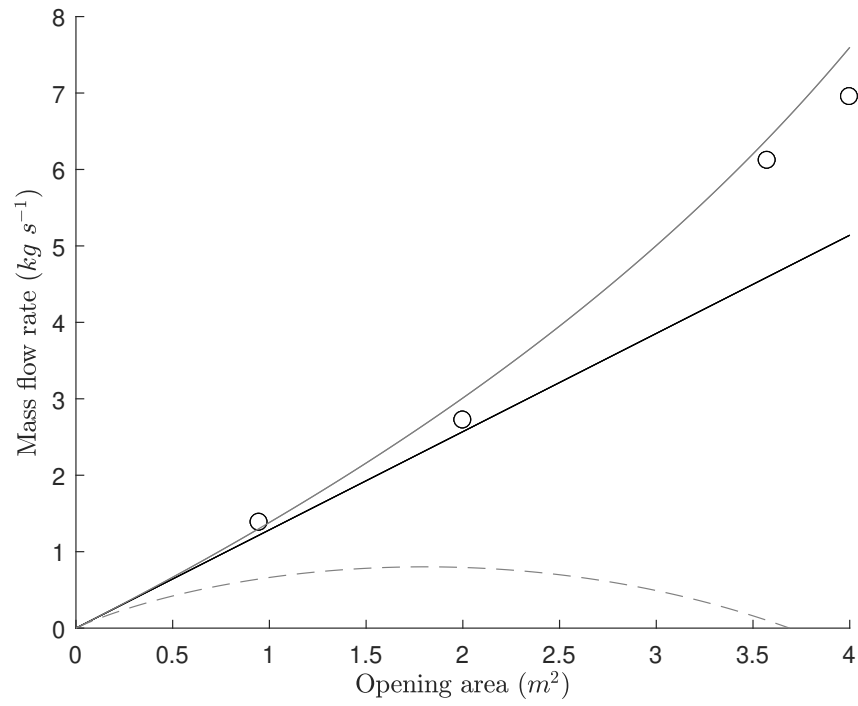


**Figure B.2:** Comparison between CFD data presented by Seifert *et al.* [1] and the predictions of Equations B.1 and B.2. The fresh air supply rate predicted by CFD data are denoted by circular markers, and the predictions of a conventional orifice flow model and Equation B.1 are denoted by solid black and grey lines respectively. The ventilation rate of room air predicted using Equation B.2 is denoted by a dashed grey line.

well with the discrete data points produced by the CFD. This suggests that the increase in volume flow rate is caused primarily by transmission of dynamic pressure in the jet, and not by a reduction in the contraction coefficient. The agreement is surprising given the scale of the difference in complexity and computation time between the two models.

## B.4 Implications for design

Counter-intuitively, this model suggests that, under certain circumstances, increasing the open area can reduce pollutant removal from a space. Ventilation strategies should be designed to prevent flow contact between the inflow jet and the outflow opening. This can either be achieved by interfering with the transmission of the jet through the space, or by manipulating the openings to adjust the size, velocity and direction of the inflow jet. These parameters represent a set of aerodynamic properties that need to be characterised for different opening types, beyond merely their resistance to airflow. Knowledge of these properties would be useful when designing for thermal comfort, as well as ensuring contact with thermal mass.

In real buildings, the reduction in pollutant removal rates is likely to be less severe than predicted by the model, as three-dimensional opening geometry, buoyancy, and internal obstacles will interfere with the clean propagation of the jet and encourage mixing. However, formation of a wall jet caused by locating openings near ceilings would reduce the entrainment coefficient [6], which could cause pollutant removal rates to be lower than predicted.



# Appendix C

## Evaluation of *Free area* models

### C.1 Introduction

Section 2.7.1 identifies a range of different *free area* models, which are illustrated in Figure 2.8. Section 5.3.2 then compares the predictions of these *free area* models against empirical data collected by Baturin [108], Bot [124], and Jong and Bot [125]. This appendix describes how the predictions of the various *free area* models are evaluated and compared.

### C.2 Common method of evaluating different techniques

To enable comparison between different models, the ventilation capacity of all openings must be described in a common way. Here the ventilation predictions of all *free area* models are expressed as an *idealised* discharge coefficient, described by Equations 2.21 and 2.22.

$$C_{d_I} = \frac{A_{eff}}{h w} \quad (C.1)$$

$$C_{d(free)} = \frac{0.61A_f}{h w} \quad (C.2)$$

### C.3 *Free area* models

This section describes the derivation of equations describing the *idealised* discharge coefficients predicted by *free area* models a-f in Figure 2.8. Here, the *idealised* discharge coefficient of model a can be given by:



$$A_{f(a)} = \min(hw ; A_1 + A_2 + A_3) \quad (C.3)$$

$$A_{f(a)} = \min(hw ; h^2 \sin(\phi) \cos(\phi) + w((h - h \cos(\phi))) \quad (C.4)$$

$$\sigma = \frac{h}{w} \quad (C.5)$$

$$A_{f(a)} = \min(hw ; hw\sigma \sin(\phi) \cos(\phi) + hw((1 - \cos(\phi))) \quad (C.6)$$

$$C_{d(a)} = 0.61 \times \min(1 ; \sigma \sin(\phi) \cos(\phi) + 1 - \cos(\phi)) \quad (C.7)$$

The *idealised* discharge coefficient of model b can be given by:

$$A_{f(b)} = \min(hw ; A_1 + A_2 + A_3) \quad (C.8)$$

$$A_{f(b)} = \min\left(hw ; 2h^2 \sin\left(\frac{\phi}{2}\right) \cos\left(\frac{\phi}{2}\right) + 2hw \sin\left(\frac{\phi}{2}\right)\right) \quad (C.9)$$

$$A_{f(b)} = \min\left(hw ; 2hw\sigma \sin\left(\frac{\phi}{2}\right) \left(\sigma \cos\left(\frac{\phi}{2}\right) + 1\right)\right) \quad (C.10)$$

$$C_{d(b)} = 0.61 \times \min\left(1 ; 2\sigma \sin\left(\frac{\phi}{2}\right) \left(\sigma \cos\left(\frac{\phi}{2}\right) + 1\right)\right) \quad (C.11)$$

The *idealised* discharge coefficient of model c can be given by:

$$A_{f(c)} = \min(hw ; A_1 + A_2 + A_3) \quad (C.12)$$

$$A_{f(c)} = \min(hw ; h^2 \sin(\phi) \cos(\phi) + hws \sin(\phi)) \quad (C.13)$$

$$A_{f(c)} = \min(hw ; hws \sin(\phi) (\sigma \cos(\phi) + 1)) \quad (C.14)$$

$$C_{d(c)} = 0.61 \times \min(1 ; \sin(\phi) (\sigma \cos(\phi) + 1)) \quad (C.15)$$

The *idealised* discharge coefficient of model d can be given by:

$$A_{f(d)} = \min(hw ; A_1) \quad (C.16)$$

$$A_{f(d)} = \min(hw ; hws \sin(\phi)) \quad (C.17)$$

$$C_{d(d)} = 0.61 \times \min(1 ; \sin(\phi)) \quad (C.18)$$

The *idealised* discharge coefficient of model e can be given by:

$$A_{f(e)} = \min(hw ; A_1 + A_2 + A_3 + A_4) \quad (C.19)$$

$$A_{f(e)} = \min(hw ; h^2 \sin(\phi) \cos(\phi) + w((h - h \cos(\phi)) +) + h w \sin(\phi) \quad (C.20)$$

$$A_{f(e)} = \min(hw ; h w \sigma \sin(\phi) \cos(\phi) + h w ((1 - \cos(\phi)) + h w \sin(\phi)) \quad (C.21)$$

$$C_{d(e)} = 0.61 \times \min(1 ; \sigma \sin(\phi) \cos(\phi) + 1 - \cos(\phi) + \sin(\phi)) \quad (C.22)$$

Finally, model *f* applies a *free area* model with a fictitious discharge coefficient determined as a function of aspect ratio, following measurements on rectangular openings by Bot [124]. In addition to this, the *side areas* are multiplied by an empirical coefficient to improve the agreement between the *free area* model and measured data. The *idealised* discharge coefficient of model *f* can then be given by:

$$C_{d(f)} = \frac{C_{d(free)} A_{f(f)}}{h w} \quad (C.23)$$

$$C_{d(free)} = \frac{1}{\sqrt{1.75 + 0.7e^{\frac{-\max(\sigma \sin(\phi) ; \frac{1}{\sigma \sin(\phi)})}{32.5}}}} \quad (C.24)$$

$$A_{f(f)} = A_1 + 0.6(A_2 + A_3) \quad (C.25)$$

$$A_{f(f)} = h w \sin(\phi) + 0.6 \left( h^2 \sin(\phi) \cos(\phi) - \frac{90 - \phi}{180} \pi h^2 \sin^2(\phi) \right) \quad (C.26)$$

$$A_{f(f)} = h w \sin(\phi) + 0.6 \left( h w \sigma \sin(\phi) \cos(\phi) - \frac{90 - \phi}{180} \pi h w \sigma \sin^2(\phi) \right) \quad (C.27)$$

$$A_{f(f)} = h w \sin(\phi) \left( 1 + 0.6 \sigma \left( \cos(\phi) - \frac{90 - \phi}{180} \pi \sin(\phi) \right) \right) \quad (C.28)$$

$$C_{d(f)} = \left( \frac{1}{\sqrt{1.75 + 0.7e^{\frac{-\max(\sigma \sin(\phi) ; \frac{1}{\sigma \sin(\phi)})}{32.5}}}} \right) \left( \sin(\phi) \left( 1 + 0.6 \sigma \left( \cos(\phi) - \frac{90 - \phi}{180} \pi \sin(\phi) \right) \right) \right) \quad (C.29)$$

## C.4 BB101 model

Building Bulletin 101 (BB101) presents a discharge coefficient calculator tool for evaluating the *idealised* discharge coefficient of hinged windows [2]. This describes the *idealised* discharge coefficient using the following empirical equation:

$$C_{d(BB101)} = B (1 - e^{-M\phi}) \quad (C.30)$$

where  $B$  and  $M$  are coefficients drawn from analysis of proprietary data for hinged windows with a range of different aspect ratios, and take the values given in Table C.1.

Aspect ratio	B	M
$\sigma > 2$	0.612	0.06
$1 < \sigma \leq 2$	0.589	0.048
$0.5 < \sigma \leq 1$	0.563	0.04
$\sigma \leq 0.5$	0.548	0.038

**Table C.1:** Coefficients of Equation C.30 presented in the BB101 discharge coefficient calculator [2].

# Appendix D

## Interpretation of literature data

### D.1 Introduction

To enable comparison between different sources of literature data, all data describing a given phenomena must be expressed in the same form. However, many different authors use different conventions to define parameters such as surface pressure coefficients and cross-flow velocity coefficients. Consequently, some post-processing is required to convert literature data into a common form to enable cross comparison.

Much of the literature data presented in this thesis has been interpreted from graphical plots as opposed to tabulated data. While digital techniques have been utilised to improve measurement accuracy, some reading error can be expected.

### D.2 Surface pressure coefficients

This thesis adopts the convention where the reference velocity at building height is used to define surface pressure coefficients. This is consistent with much of the literature data: the tabulated pressure coefficients presented by Orme and Liddament [94], and the surface pressure correlations presented by Grosso [91] and Knoll *et al.* [92] are all defined in this way. Consequently, data from these sources can all be taken directly from tabulated data or read from graphical plots, without subsequent manipulation.

The surface-averaged surface pressure correlation presented by Swami and Chandra for low rise buildings defines a normalised surface pressure coefficient, where the measured surface pressure coefficient at a given wind angle is normalised by the surface pressure coefficient measured at a wind angle of zero degrees [84]. In this formulation, the reference velocity cancels, which allows literature data with different or unknown reference velocities to be compared. Swami and Chandra give a typical surface pressure coefficient at a wind

angle of zero degrees of 0.6 to use with the normalised surface pressure coefficient correlation, defined with a reference velocity at building height. The predictions of the surface-averaged surface pressure correlation presented by Swami and Chandra for low rise buildings can consequently be converted to the common convention applied in this thesis by multiplying the predictions by a factor of 0.6 [84].

The local surface pressure coefficient correlation presented by Swami and Chandra for high-rise buildings describes surface pressure coefficients with a reference velocity at opening height [84]. This can be converted to a surface pressure coefficient with a reference velocity measured at building height according to the following relations:

$$C_{P(B)} = \frac{P_i - P_R}{\frac{1}{2}\rho U_B^2} \quad (\text{D.1})$$

$$C_{P(w)} = \frac{P_i - P_R}{\frac{1}{2}\rho U_w^2} \quad (\text{D.2})$$

$$C_{P(B)} = C_{P(w)} \frac{C_{P(B)}}{C_{P(w)}} = C_{P(w)} \frac{U_w^2}{U_B^2} \quad (\text{D.3})$$

where  $C_{P(B)}$  and  $C_{P(w)}$  are the pressure coefficients measured with a reference velocity at building height and window height respectively, and  $U_B$  and  $U_w$  are the wind speed measured at building height and window height respectively. The local surface pressure coefficient correlation presented by Swami and Chandra for high-rise buildings is fitted to data from a wind tunnel study by Atkins and Cermak [86]. Atkins and Cermak investigate 15 different building geometries in four different boundary layers. Detailed tabulated boundary layer data are provided, which allows correction factors to be derived for a window at the building centre. Depending on the combination of boundary layer and building geometry, these correction factors vary from 0.58 to 0.88, with a mean correction factor of 0.7. The mean correction factor is typical of boundary layer 2 presented in the paper [86]. Therefore, the local surface pressure coefficients for high-rise buildings predicted by the correlations presented by Swami and Chandra are multiplied by a factor of 0.7 to convert from surface pressure coefficients referenced at the building centre to those referenced at building height [84, 86].

### D.3 Cross-flow velocity coefficient data

This thesis adopts the convention where the reference velocity at building height is used to define cross-flow velocity coefficients. This is consistent with the approach used to define surface pressure coefficients, and simplifies their measurement through the selection of a fixed reference location. However, numerous authors use different conventions for measuring the reference velocity. This introduces challenges in converting

literature data to a consistent format. In general, the cross-flow velocity coefficient defined using the wind speed measured at building height can be converted from values of the cross-flow velocity coefficient defined at an arbitrary reference height according to the following relations:

$$U_B^* = \frac{U_L}{U_B} \quad (\text{D.4})$$

$$U_R^* = \frac{U_L}{U_R} \quad (\text{D.5})$$

$$U_B^* = U_R^* \frac{U_R}{U_B} \quad (\text{D.6})$$

where  $U_B^*$  and  $U_R^*$  are the cross-flow velocity coefficients defined using the wind speed at building height and at an arbitrary reference height respectively,  $U_L$  is the cross-flow velocity, and  $U_B$  and  $U_R$  are the wind speed measured at building height and reference height respectively.

Warren and Parkins present measurements of cross-flow velocity coefficient defined using a reference velocity at a height of 10m above the ground [61]. To convert these measurements to a cross-flow velocity coefficient defined at building height, knowledge of the building height and the boundary layer profile are required. Here the building height is inferred from measurements of photographic data, and is taken to be 3.25m, and the atmospheric boundary layer is described in the paper as consistent with a 1/7 power law model. Here, measured values of cross-flow velocity coefficient defined with a reference velocity at a height of 10m are converted to cross-flow velocity coefficients defined with a reference velocity at building height by multiplying by a factor of 1.17.

Linden *et al.* present measurements of cross-flow velocity coefficient defined using a reference velocity at window height [85]. A lack of reported data concerning the boundary layer makes conversion to building reference height difficult. As the results presented by Linden *et al.* are intended for compatibility with EnergyPlus software, it has been assumed here that an ABL consistent with the EnergyPlus default boundary layer profiles has been simulated. This corresponds to a 0.14 power law model, and results in a conversion factor of 0.95 for the two storey building measurements; 0.87 for the four storey, low windows measurements; and 0.97 for the four storey, high windows measurements.

Albuquerque *et al.* and Ohba *et al.* both define cross-flow velocity coefficient using a reference velocity at building height [67, 99]. Consequently, data from these sources can all be taken directly from tabulated data or read from graphical plots, without subsequent manipulation.

## D.4 *Idealised* discharge coefficient data

Empirical data measured by Baturin [108] are already in a format consistent with the definition of the *idealised* discharge coefficient, whereby the reference area for the opening is taken as the product of its height and width. Consequently, this data can be read directly from the tabular data presented in the source without further interpretation.

However, Bot [124] and Jong and Bot [125] present performance data in terms of an area metric  $f_2$ , which is given by

$$f_2 = \frac{Q}{A} \sqrt{\frac{1}{2\rho} \frac{1.75 + 0.7e^{-\frac{\max(\sigma \sin(\phi); \frac{1}{\sigma \sin(\phi)})}{32.5}}}{\Delta P}} \quad (\text{D.7})$$

Consequently, the performance data reported by Bot [124] and Jong and Bot [125] can be converted into an *idealised* discharge coefficient value by

$$C_{d_I} = \frac{f_2}{\sqrt{1.75 + 0.7e^{-\frac{\max(\sigma \sin(\phi); \frac{1}{\sigma \sin(\phi)})}{32.5}}}} \quad (\text{D.8})$$

# Appendix E

## Matlab code for the cross-flow probe

### E.1 Introduction

Section 4.6 describes the development of a novel probe that measures the simultaneous speed and direction of the cross-flow on the surface of a model building. This appendix summarises the MATLAB code used to convert the raw data measured by the pressure transducers into cross-flow speed and direction measurements.

### E.2 Master Routine

The master routine arranges the subroutines to ensure all inputs are available to convert measured manometer outputs into cross-flow dynamic pressure and *façade* cross-flow direction measurements. These evaluated outputs are then saved to a results file.

```
1 clear
2 %% Input information to identify raw data collected in a given session
3 Date = '03082021';
4 Case = 'Case1';
5
6 %% Extract wind angle, and evaluate pressure measurements from voltage data
7 [Wind_Angle, pressure, testno] = Data_collate(Date, Case);
8
9 %% Evaluate probe calibration predictions at the desired precision in surface
   flow direction
```



```

10 [Angrange , dCp , rCp , weights ,PdIndex] = Data_format();
11
12 %% Evaluate surface flow direction and crossflow dynamic pressures measured by
    the probe
13 [Flow_Angle ,Dynamic_Pressure] = Calculate_surface_flow(Wind_Angle , pressure ,
    Angrange , dCp , rCp , weights ,PdIndex);
14
15 %% Evaluate the dynamic pressure in the atmospheric flow
16 Wind_Pressure = pressure(:,7);
17
18 save('Results','Flow_Angle','Dynamic_Pressure','Wind_Angle','Wind_Pressure','
    testno')

```

### E.3 Subroutine Data collate

The *data collate* subroutine converts the raw voltages output by the manometers into pressure differential measurements in Pascals, and collates them ready for interpretation by other routines.

```

1 function [flow_direction ,pressure ,testno] = Data_collate(Date ,Case)
2
3 %%Total number of differential manometers used
4 sensor_number = 7;
5
6 %% Load log file
7 log = load(['logFileDate' Date Case '.csv']);
8
9 % identify run number corresponding to pressure measurement files
10 runs = log(:,2);
11 % identify run number corresponding to zero calibration measurements
12 zeroruns = runs( log(:,4)==0);
13
14 % identify measurement frequency
15 Hz = log(:,4);

```

```

16
17 % identify measured wind angles
18 angles = log(:,5);
19
20 %% Evaluate measured pressures from output voltages
21
22 for i = 1:length(zeroruns)-1
23     if zeroruns(i+1)-zeroruns(i)>1
24         %% Calculate zero offset voltage
25         % average the zero offset voltage from calibration measurements taken
                before and after each set of data collection
26         zerovolt = mean([ mean(load(['PressureVoltage' Case '_' num2str(zeroruns
                (i)) '.csv'])) ; mean(load(['PressureVoltage' Case '_' num2str(
                zeroruns(i+1)) '.csv']))]);
27         zerovolt = zerovolt(:,[1:sensor_number]);
28
29         %% Convert pressure (V) to pressure (Pa)
30         % identify run number corresponding to measurements taken between zero
                calibration measurements
31         pressure_runs = runs(runs<zeroruns(i+1) & runs>zeroruns(i));
32
33         for j = 1:length(pressure_runs)
34             % load pressure measurements in voltage outputs
35             pressurevolt = load(['PressureVoltage' Case '_' num2str(pressure_runs(
                j)) '.csv']);
36             pressurevolt = pressurevolt(:,[1:sensor_number]);
37             % convert pressure (V) to pressure (Pa) using measured zero offset
38             pressureval = (pressurevolt - zerovolt).*125;
39
40             %store corresponding measurement frequency, run number, and wind angle
                for each test measurement
41             Hztest = (pressureval(:,1).*0) + Hz(runs==pressure_runs(j));

```

```

42     num = Hztest.*0 + pressure_runs(j);
43     angtest = Hztest.*0 + angles(runs==pressure_runs(j));
44
45     % concatenate into single array
46     if j == 1 && i == 1
47         pressure = pressureeval;
48         flow_direction = angtest;
49         testno = num;
50     else
51         pressure = [pressure ; pressureeval];
52         flow_direction = [flow_direction ; angtest];
53         testno = [testno;num];
54     end
55
56     end
57
58     end
59 end
60
61 %% Save evaluated pressures, and corresponding wind direction and test numbers
62 save('Data', 'flow_direction', 'pressure', 'testno')
63
64
65 end

```

## E.4 Subroutine Data format

The *data format* subroutine evaluates the predictions of the calibrated probe surface pressure coefficients for pressure coefficient differentials and pressure coefficient difference ratios at a range of possible *façade* cross-flow directions. These will be compared against measured data in the *calculate surface flow* subroutine to identify the best-fit surface direction. The *data format* subroutine also identifies suitable weightings for the subsequent curve fitting, and an index for the best pressure differential measurement to evaluate cross-flow

dynamic pressure at each possible *façade* cross-flow direction measurement.

```

1 function [Angrange , dCp , rCp , weights ,PdIndex] = Data_format(~)
2
3 % Load function describing surface pressure coefficient as a function of flow
   angle
4 load('curvefit.mat')
5
6 %define potential flow angles with suitable precision
7 Angrange = 0:0.1:359.9;
8
9 %calculate range of potential surface pressure coefficient differentials
   between probe ports across potential flow angles
10 dCp = [ fp(Angrange) - fp(Angrange + 90) , fp(Angrange) - fp(Angrange + 180) ,
        fp(Angrange) - fp(Angrange + 270) , fp(Angrange+90) - fp(Angrange + 180)
        , fp(Angrange + 90) - fp(Angrange + 270) , fp(Angrange + 180) - fp(
        Angrange + 270)];
11
12 %calculate range of potential surface pressure coefficient differential ratios
   across potential flow angles
13 rCp = [ dCp(:,2)./dCp(:,1) , dCp(:,3)./dCp(:,1) , dCp(:,4)./dCp(:,1) , dCp
        (:,5)./dCp(:,1) , dCp(:,6)./dCp(:,1) , dCp(:,3)./dCp(:,2) , dCp(:,4)./dCp
        (:,2) , dCp(:,5)./dCp(:,2) , dCp(:,6)./dCp(:,2) , dCp(:,4)./dCp(:,3) , dCp
        (:,5)./dCp(:,3) , dCp(:,6)./dCp(:,3) , dCp(:,5)./dCp(:,4) , dCp(:,6)./dCp
        (:,4) , dCp(:,6)./dCp(:,5)];
14
15 %Separately evaluate numerator and denominator of pressure differential ratio
   to facilitate weighting
16 numerator = [dCp(:,(2:6)) , dCp(:,(3:6)) , dCp(:,(4:6)) , dCp(:,(5:6)) , dCp
        (:,6)];
17 denominator = [ repmat(dCp(:,1),1,5) , repmat(dCp(:,2),1,4) , repmat(dCp(:,3)
        ,1,3) , repmat(dCp(:,4),1,2) , dCp(:,5)];
18

```

```

19 %evaluate suitable weights for curvefit that minimise influence of high-error
    zero pressure measurements on results
20 weights = numerator.^2 + denominator.^2;
21 weights = weights./sum(weights,2);
22 weights(weights<0.01) = 0;
23 weights = weights./sum(weights,2);
24
25 Angrange = Angrange.';
26
27 % Identify set of pressure differentials with the greatest absolute pressure
    difference at each potential flow angle, used to minimise error in dynamic
    pressure evaluation.
28 absdCp = abs(dCp);
29 [~,PdIndex] = max(absdCp,[],2);
30
31
32 save('Calibration_curves' , 'Angrange' , 'dCp' , 'rCp' , 'weights' , 'PdIndex')
33
34 end

```

## E.5 Subroutine Calculate surface flow

The *calculate surface flow* subroutine evaluates the best-fit *façade* cross-flow direction from the instantaneous pressures measured by the differential manometers and the calibration predictions. The best fit *façade* cross-flow direction is then used in conjunction with the measured pressures and calibrated surface pressure coefficients to evaluate a cross-flow dynamic pressure, based on the surface pressure coefficient of the largest magnitude at the evaluated *façade* cross-flow direction.

```

1 function [Flow_Angle,Dynamic_Pressure] = Calculate_surface_flow(flow_direction
    ,pressure,Angrange , dCp , rCp , weights,PdIndex)
2
3 % Load differential pressure measurements
4 dp = pressure(:,[1:6]);

```

```

5 % Calculate measured instantaneous pressure coefficient difference ratios
6 rp = [ pressure(:,2)./pressure(:,1) , pressure(:,3)./pressure(:,1) , pressure
      (:,4)./pressure(:,1) , pressure(:,5)./pressure(:,1) , pressure(:,6)./
      pressure(:,1) , pressure(:,3)./pressure(:,2) , pressure(:,4)./pressure
      (:,2) , pressure(:,5)./pressure(:,2) , pressure(:,6)./pressure(:,2) ,
      pressure(:,4)./pressure(:,3) , pressure(:,5)./pressure(:,3) , pressure
      (:,6)./pressure(:,3) , pressure(:,5)./pressure(:,4) , pressure(:,6)./
      pressure(:,4) , pressure(:,6)./pressure(:,5) ] ;
7 % evaluate inverse pressure coefficient difference ratios (calibration
      predictions)
8 irCp = 1./rCp;
9 % evaluate inverse pressure coefficient difference ratios (measured pressures
      )
10 irp = 1./rp;
11
12 % evaluate linear index to locate optimum pressure measurement to evaluate
      dynamic pressure at each potential surface flow direction
13 idx = sub2ind(size(dCp) ,[1:length(Angrange)],PdIndex. ');
14
15 % identify total number of measured data points to analyse
16 testlength = length(flow_direction);
17
18 % Create arrays for storing sum of square residuals , and all output
      measurements
19 Sres = zeros(size(rCp));
20 Flow_Angle = zeros(testlength,1);
21 Dynamic_Pressure = Flow_Angle;
22
23 %% Evaluate best-fit surface direction and crossflow dynamic pressure
24 for t = 1:testlength
25     % extract measured instantaneous pressure coefficient difference ratios
      and their inverses for the given instant

```

```

26     rptest = rp(t,:);
27     irptest = irp(t,:);
28
29     % calculate the sum of square residuals based on pressure coefficient
        difference ratios and based on their inverse values
30     Sres1 = (rCp - rptest).^2;
31     Sres2 = (irCp - irptest).^2;
32
33     % Where the predicted pressure coefficient difference ratio is less than
        one, apply the residuals based on the pressure difference coefficient
        ratio. Otherwise, apply the residuals based on the inverse pressure
        difference coefficient ratio.
34     Sres(rCp<1&rCp>-1) = Sres1(rCp<1&rCp>-1);
35     Sres(rCp>=1|rCp<=-1) = Sres2(rCp>=1|rCp<=-1);
36
37     % Calculate the predicted dynamic pressure at all possible crossflow
        directions
38     Pdref = dp(t,:)./dCp;
39     Pdref1 = Pdref(idx).';
40
41     % Apply evaluated weightings to sum of square residuals to reduce
        influence of large errors when the numerator or denominator are close
        to zero
42     SSres = sum(Sres.*weights,2);
43     % Give a high weighting to exclude any non-physical evaluations of
        crossflow dynamic pressure (where crossflow dynamic pressure is
        negative)
44     SSres(Pdref1<0) = 500000;
45
46     % Identify location of best-fit flow direction
47     [~,Indexmin] = min(SSres);
48

```

```

49     % Extract surface flow direction and crossflow dynamic pressure from best
        fit location
50     Flow_Angle(t) = Angrange(Indexmin);
51     Dynamic_Pressure(t) = Pdref1(Indexmin);
52
53 end
54
55 %% save evaluated probe outputs
56 save('analysed_data2','Flow_Angle','Dynamic_Pressure')
57 end

```

## E.6 Calibration curve fit

The evaluation of probe outputs is dependent on a calibration curve of probe surface pressure coefficients. This is evaluated as a function of a curve fit to empirical measurements. This program shows how this curve was fit, relating mean surface pressure coefficients to *façade* cross-flow direction. To ensure a closer agreement to measured data without the risk of common over-fitting errors, linear interpolation of the measured data points was performed prior to curve fitting. This program runs multiple iterations of the curve fit to identify the impact of number of terms on fit quality.

```

1 clear
2
3 %Load surface pressure coefficient data
4 load('meanCp.mat')
5
6 x = Angle_range;
7 y = meanCp;
8
9 xorig = x;
10 yorig = y;
11
12 figure(1)
13 hold on

```



```

14 plot(x,y, 'Marker', 'o', 'MarkerSize', 7, 'MarkerEdgeColor', 'black', '
    MarkerFaceColor', 'white', 'LineStyle', 'none', 'color', [0.5 0.5 0.5])
15 axis([0,360,-1,1])
16
17 %% add linear interpolation to data
18 for count = 1:(length(Angle_range)-1)
19 xrag = x(count):((x(count+1)-x(count))/100):x(count+1);
20 yrag = y(count):((y(count+1)-y(count))/100):y(count+1);
21
22 xrag = xrag.';
23 yrag = yrag.';
24
25 x = [x;xrag];
26 y = [y;yrag];
27 end
28
29 %% compile and test example equations
30
31 equation = 'a';
32
33 letters = 'abcdefghijklmnopqrstuvwz';
34 term_no = 2:22;
35
36 R2 = 0.*term_no;
37
38 for i = term_no
39
40 equation = [equation '+ (' letters(i) '.* (cos(' num2str(i - 1) '.* (x.*pi
    ./180))))'];
41
42
43

```

```
44
45 fiti = fit(x,y,equation);
46
47 x1 = 0:0.1:360;
48 plot(x1,fiti(x1))
49
50 R2(i-1) = 1 - (sum( (y - fiti(x)).^2 ) ./ sum( (y- mean(y)).^2 ) );
51
52 end
53
54 figure(2)
55 plot(term_no,R2,'Marker','o','MarkerSize',7,'MarkerEdgeColor','black','
    MarkerFaceColor','white','LineStyle','none','color',[0.5 0.5 0.5])
56
57 figure(3)
58 hold on
59 plot(xorig,yorig,'Marker','o','MarkerSize',7,'MarkerEdgeColor','black','
    MarkerFaceColor','white','LineStyle','none','color',[0.5 0.5 0.5])
60 axis([0,360,-1,1])
61 plot(x1,fiti(x1))
62
63 fp = fiti;
64
65 save('curvefit','fp')
```



## Appendix F

# Cross-flow characterisation curves of simple window geometries

### F.1 Introduction

The measured data that is collected in Section 5.5.3 for the development of cross-flow characterisation curves is presented alongside the empirical modelling predictions described by Equation 5.9. Data is presented that relates the *total* dimensionless volume flow rate to the dimensionless room pressure. In the following plots, the dimensionless room pressure is plotted in the range  $-1 \leq P_R^* \leq 1$ , and its inverse is plotted in the range  $-1 \leq 1/P_R^* \leq 1$ . This enables the full range of data, where the dimensionless room pressure varies from  $-\infty$  to  $+\infty$ , to be plotted on a single graph. For reference, the mathematical definitions of *total* dimensionless volume flow rate and dimensionless room pressure are reproduced here:

$$Q_T^* = \frac{Q}{L_c^2 \sqrt{\frac{2}{\rho} (|\Delta P| + |\frac{1}{2} \Delta \rho g L_c| + |\frac{1}{2} \rho U_L^2|)}}}$$
$$P_R^* = \frac{P_I - P_E}{P_{d(c)}}$$

## F.2 Square orifice

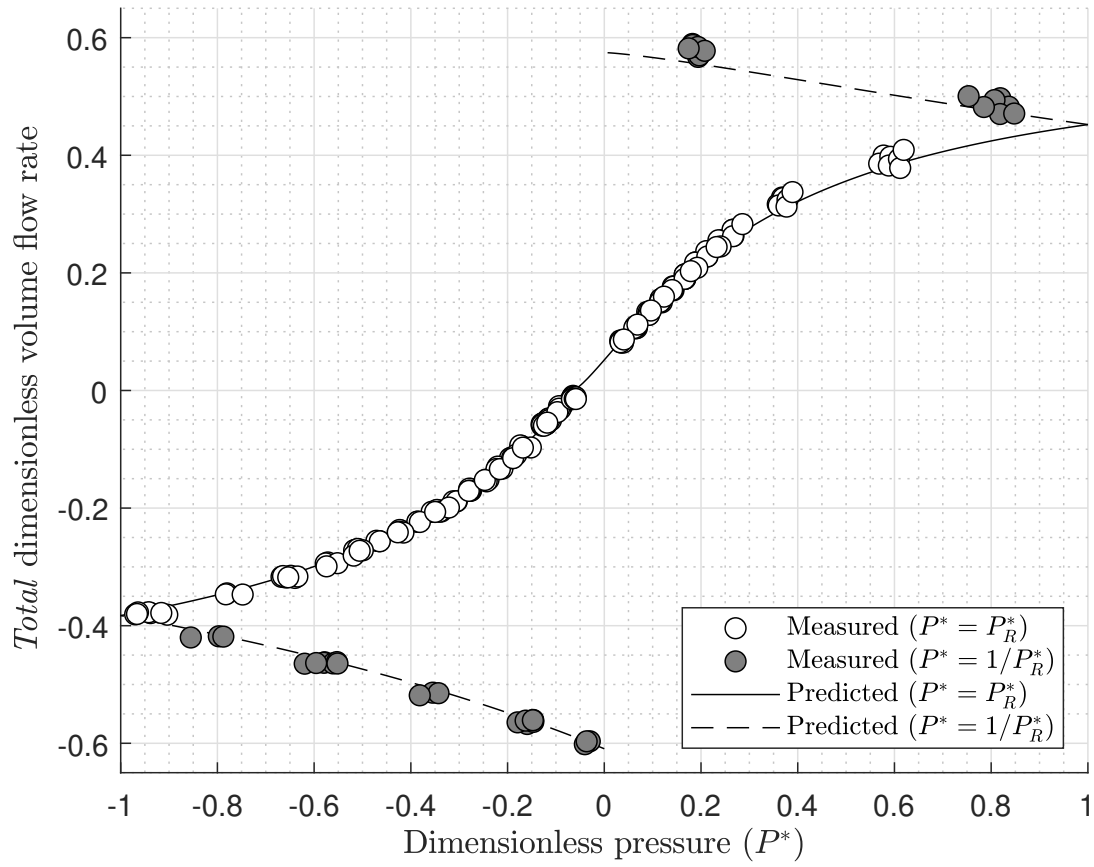
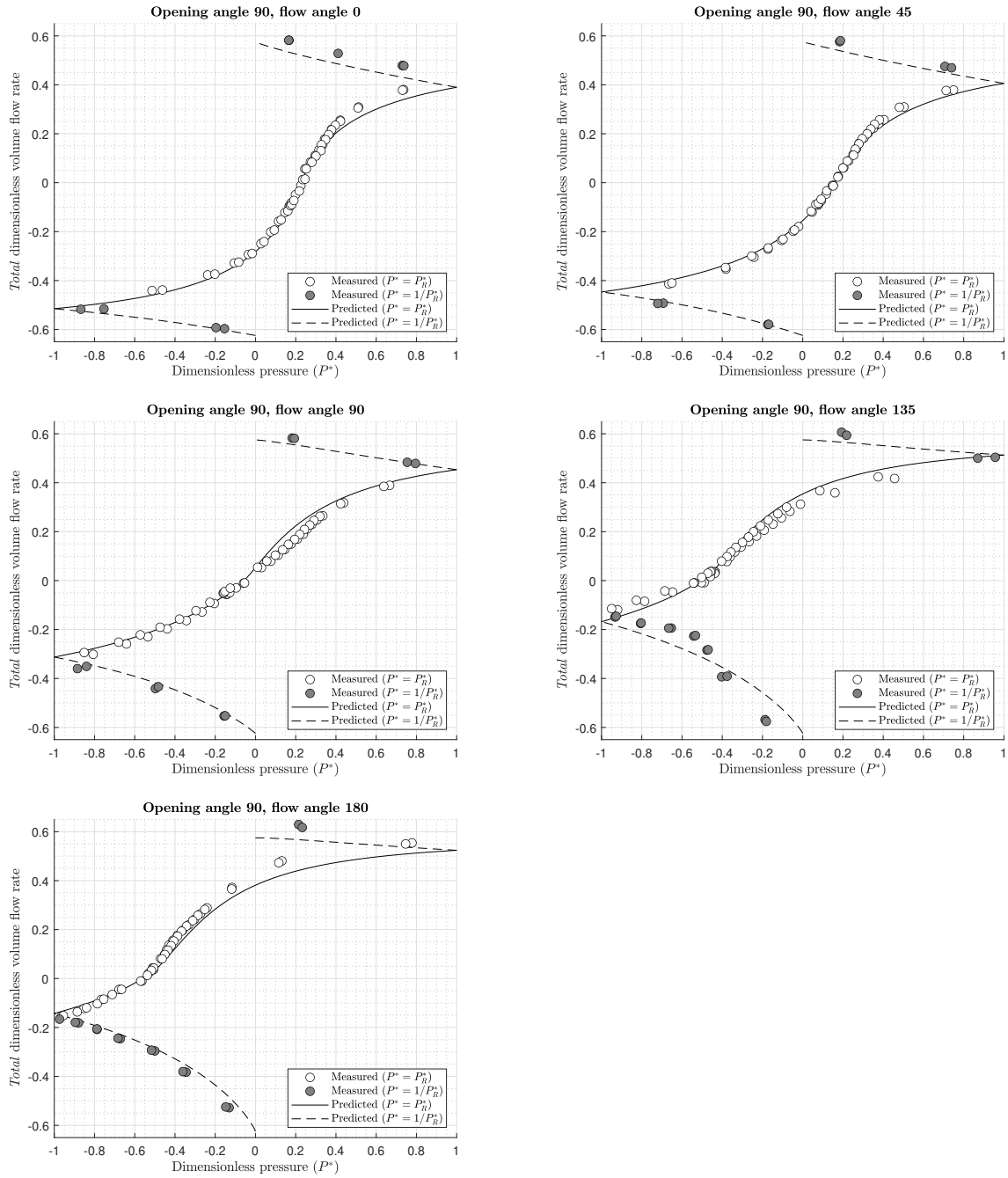
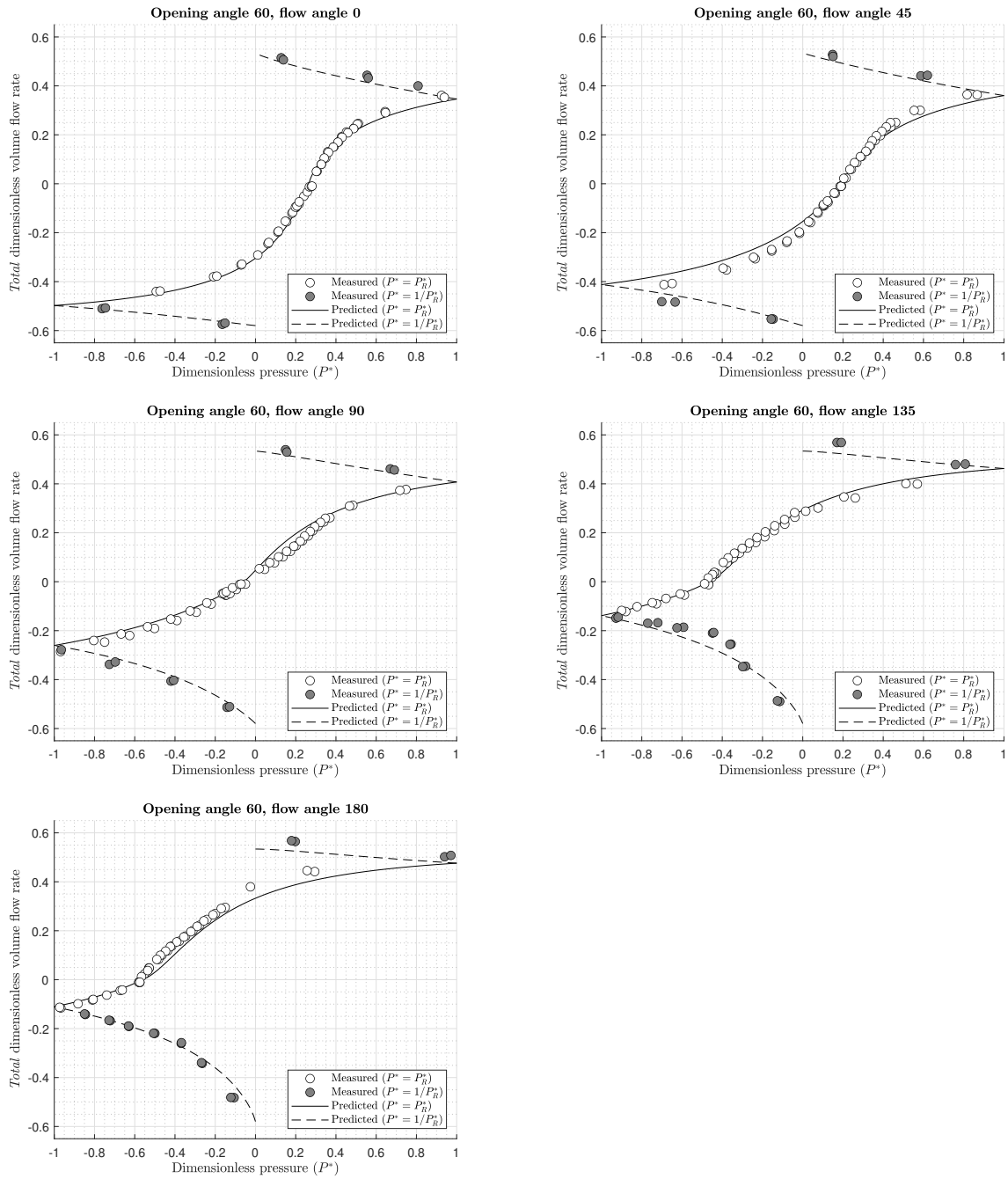


Figure F.1: Cross-flow characterisation curve for a square orifice

### F.3 Square, outward opening, hinged window



**Table F.1:** Cross-flow characterisation curves for a square, outward opening, hinged window at an opening angle of 90 degrees, for flow approach angles between 0 and 180 degrees.



**Table F.2:** Cross-flow characterisation curves for a square, outward opening, hinged window at an opening angle of 60 degrees, for flow approach angles between 0 and 180 degrees.

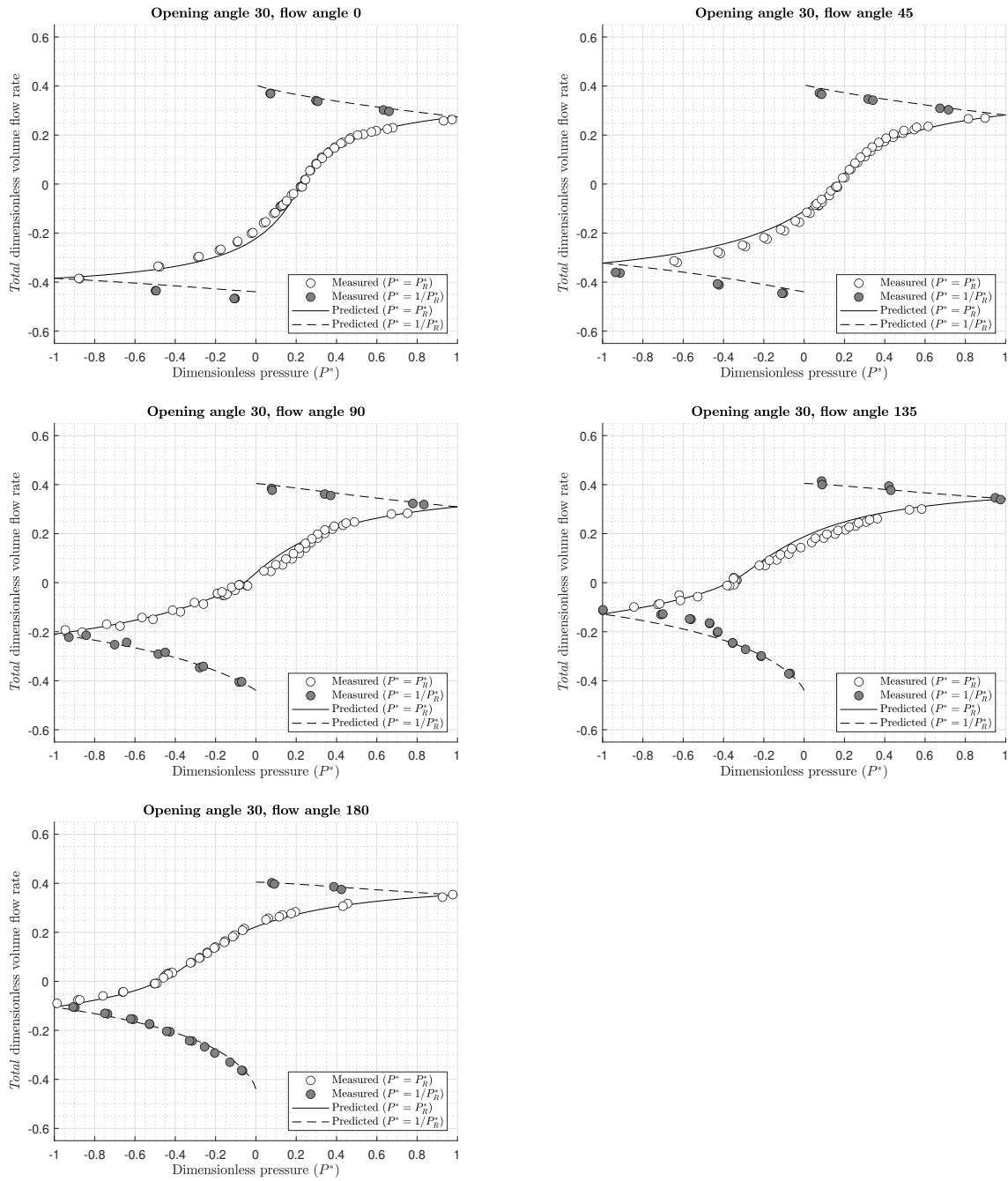


**Table F.3:** Cross-flow characterisation curves for a square, outward opening, hinged window at an opening angle of 30 degrees, for flow approach angles between 0 and 180 degrees.



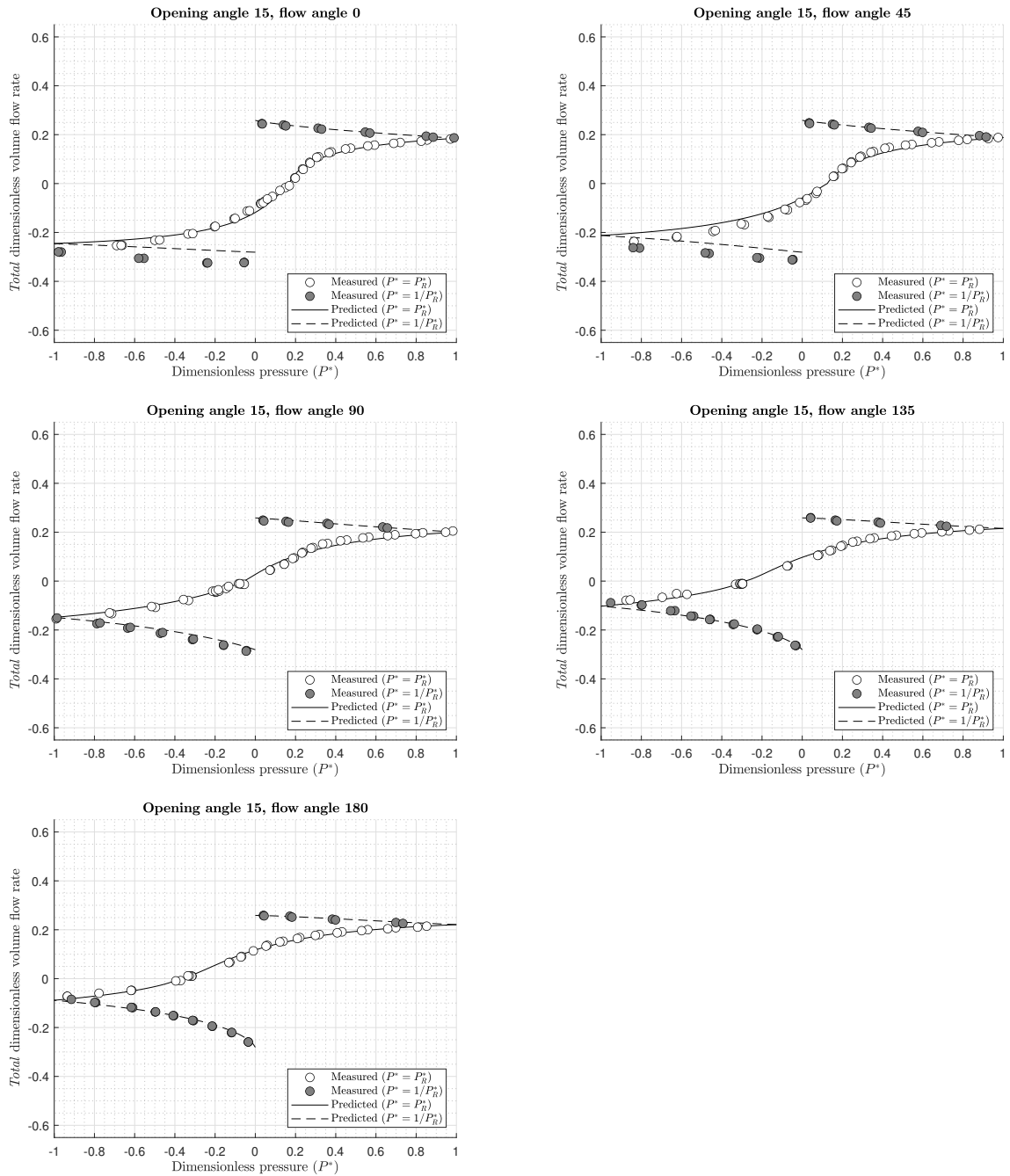


**Table F.4:** Cross-flow characterisation curves for a square, outward opening, hinged window at an opening angle of 15 degrees, for flow approach angles between 0 and 180 degrees.

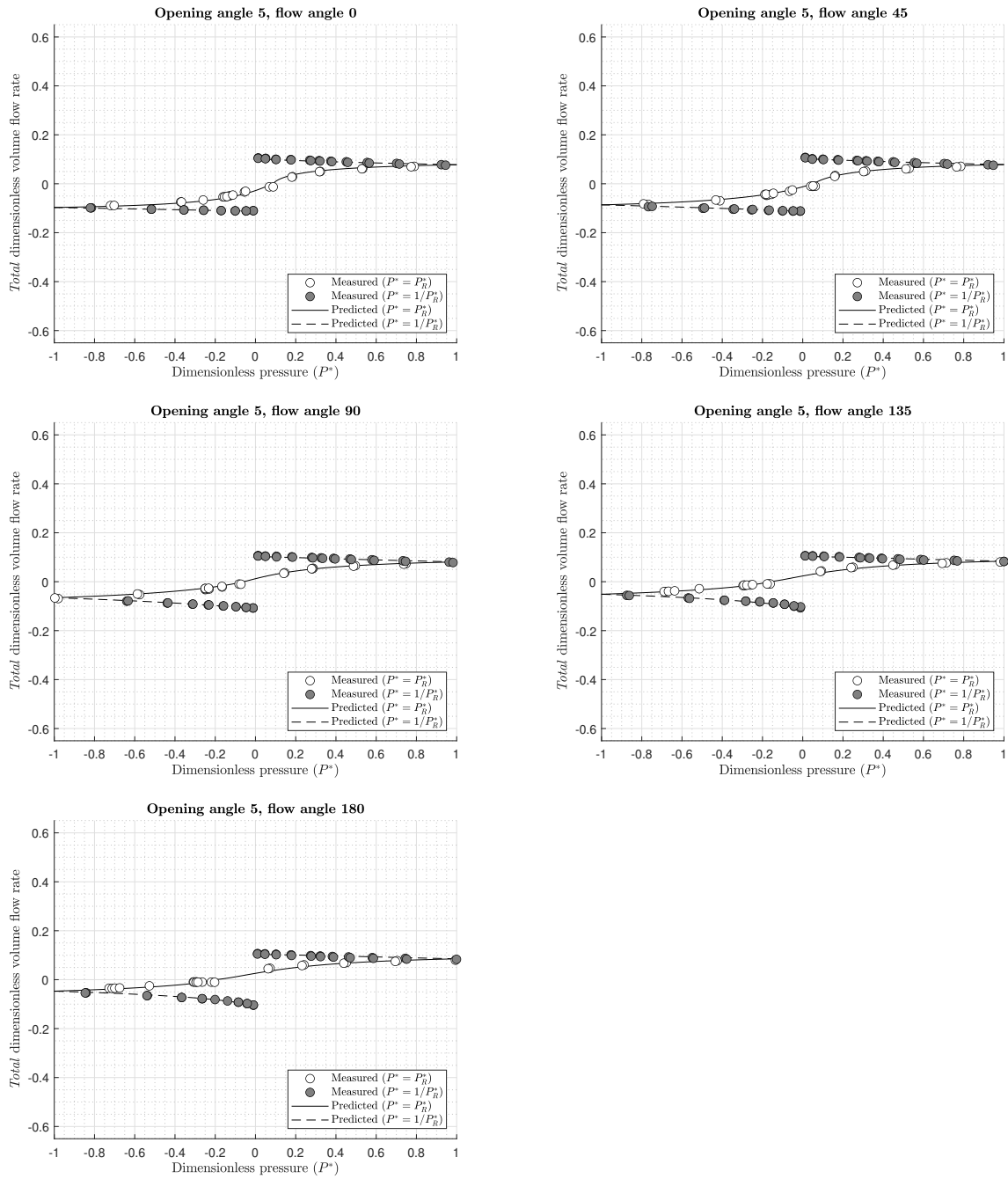


**Table F.5:** Cross-flow characterisation curves for a square, outward opening, hinged window at an opening angle of 5 degrees, for flow approach angles between 0 and 180 degrees.

## F.4 Square, inward opening, hinged window

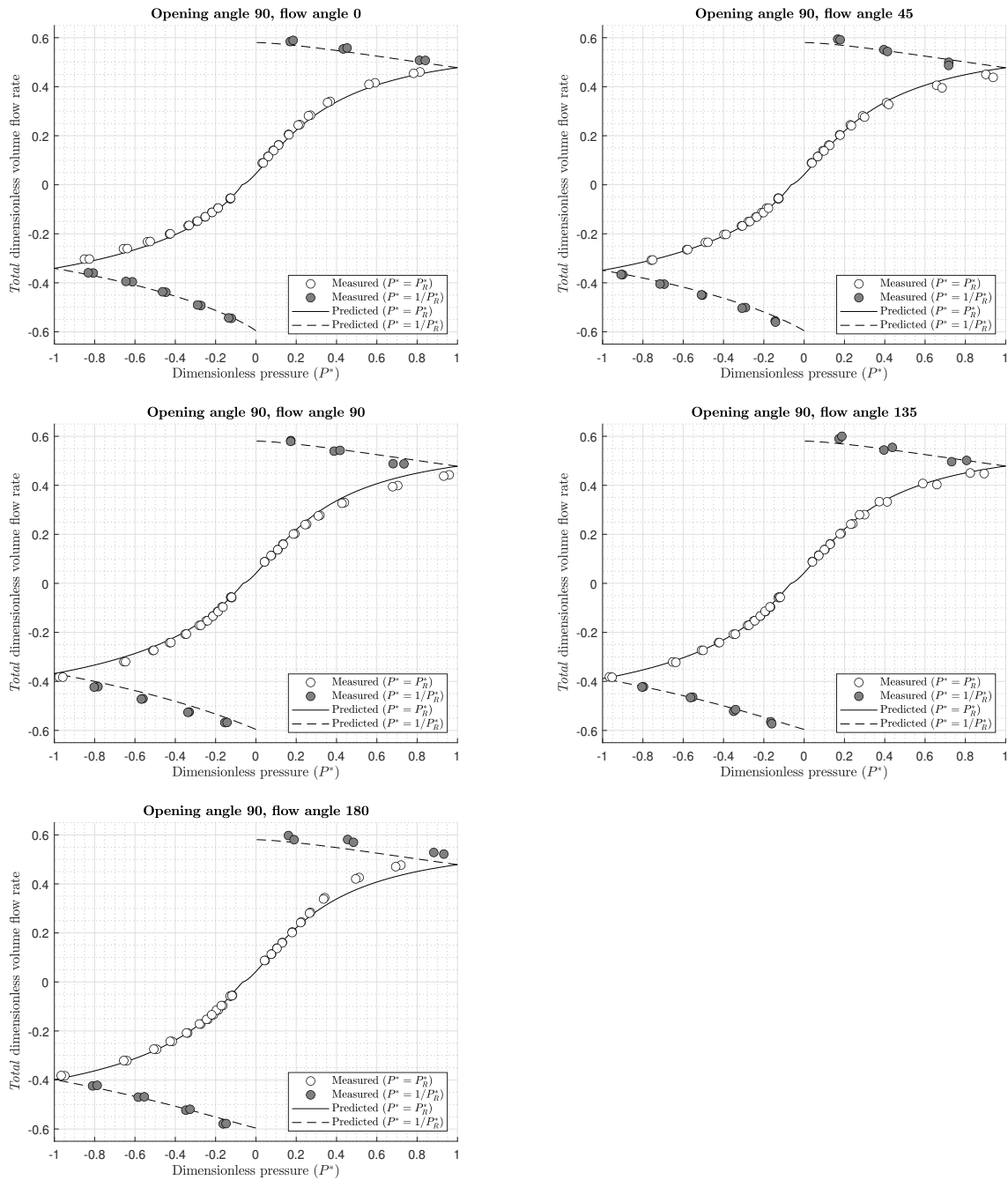


**Table F.6:** Cross-flow characterisation curves for a square, inward opening, hinged window at an opening angle of 90 degrees, for flow approach angles between 0 and 180 degrees.

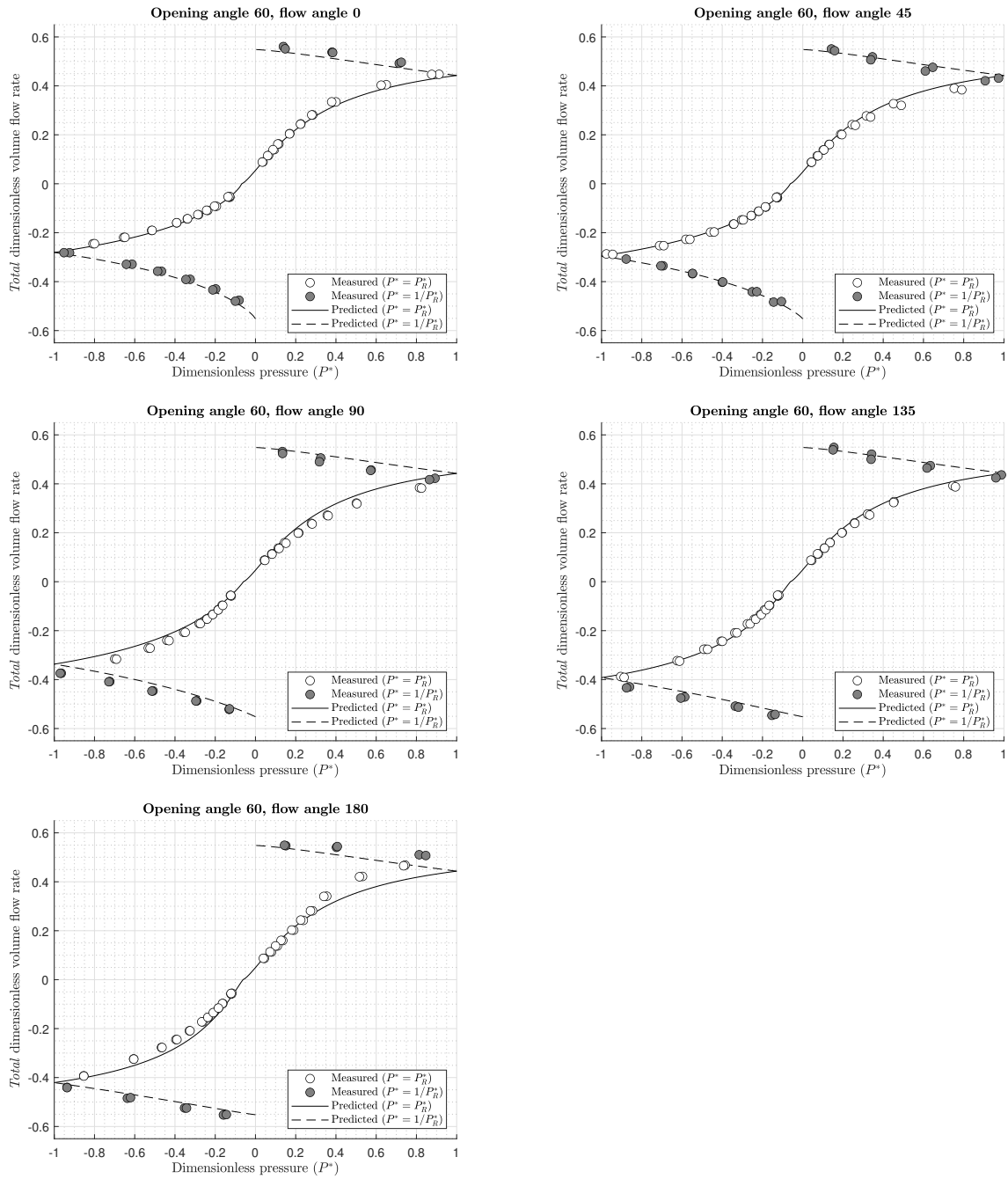


**Table F.7:** Cross-flow characterisation curves for a square, inward opening, hinged window at an opening angle of 60 degrees, for flow approach angles between 0 and 180 degrees.

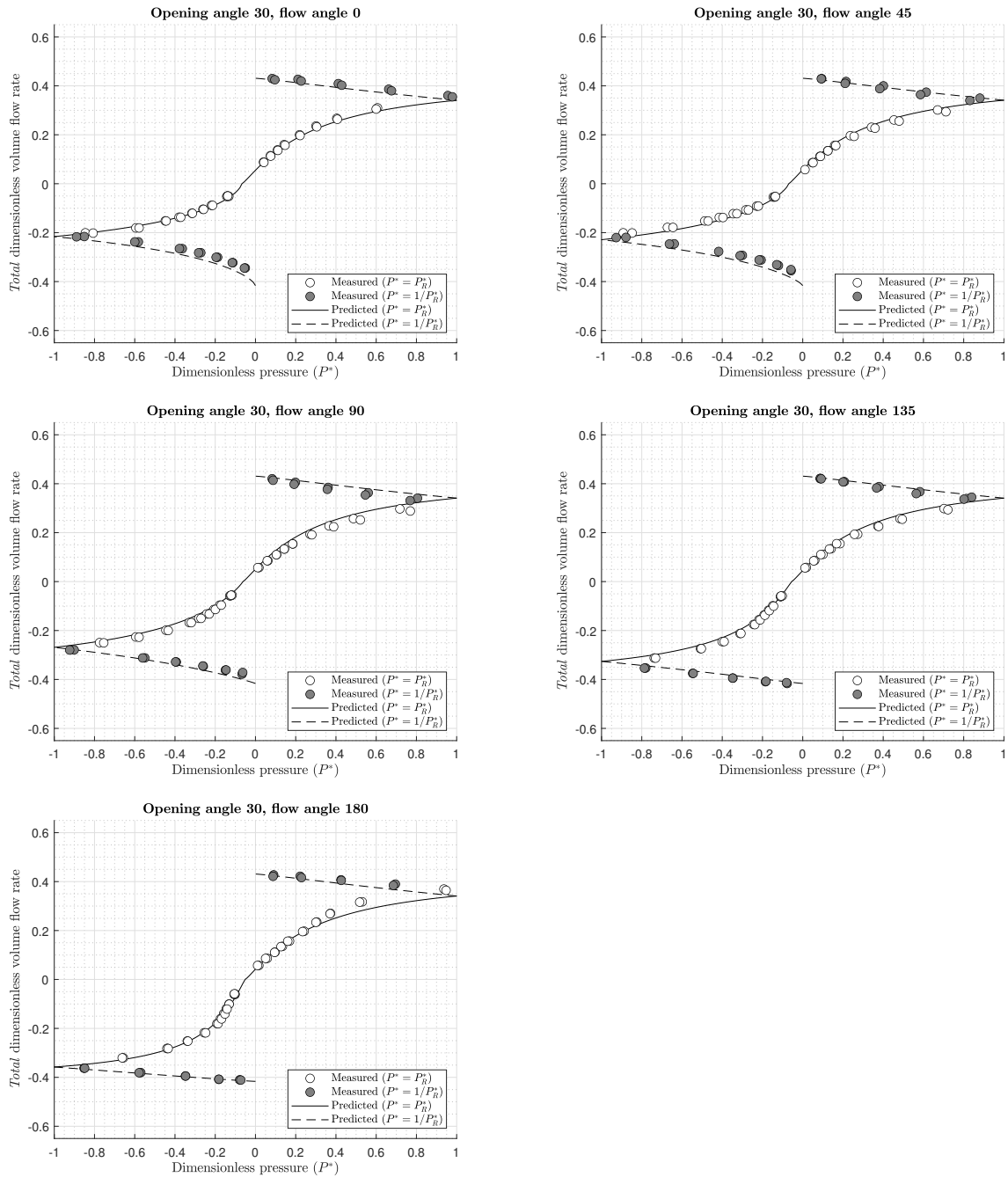


**Table F.8:** Cross-flow characterisation curves for a square, inward opening, hinged window at an opening angle of 30 degrees, for flow approach angles between 0 and 180 degrees.

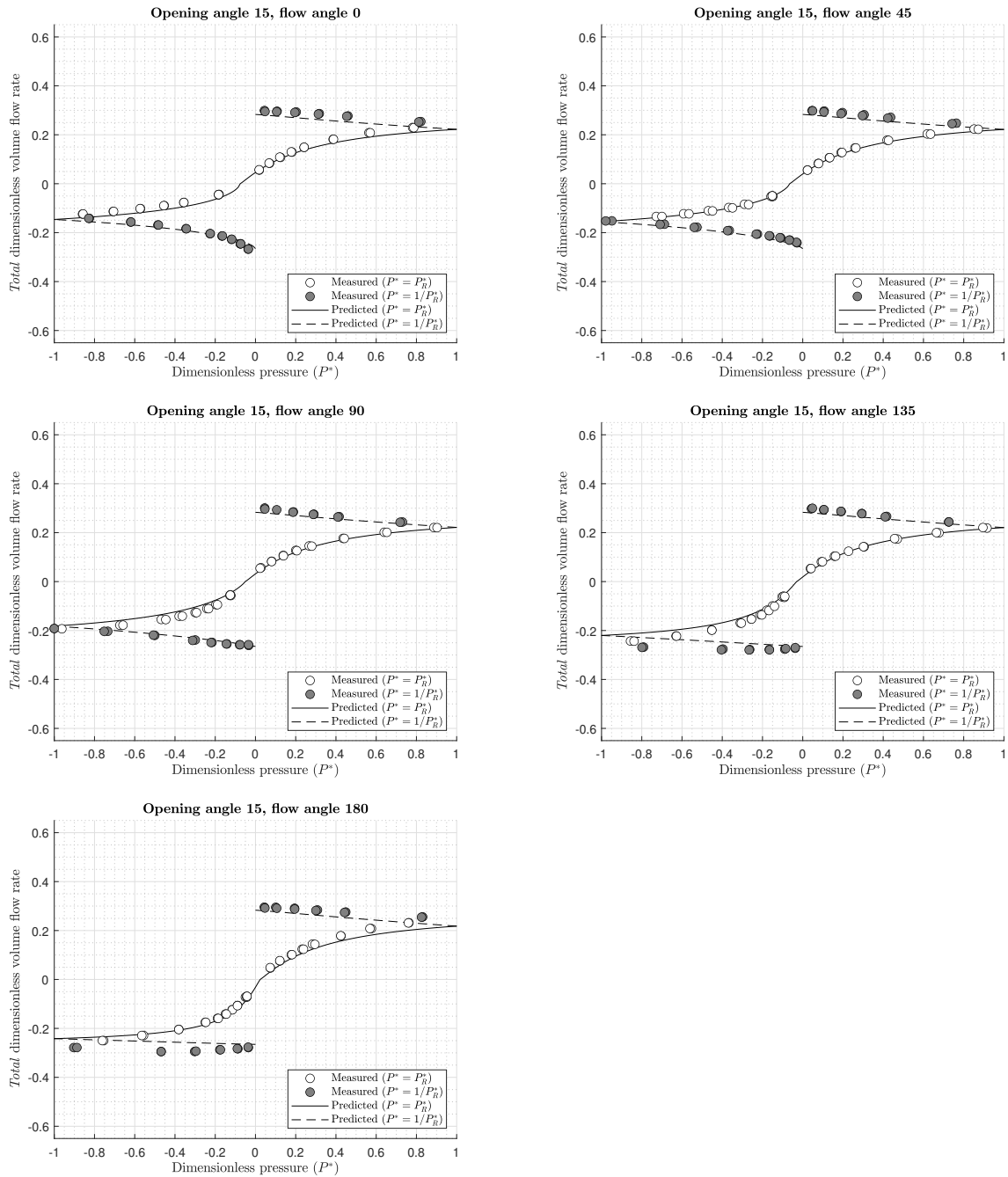


**Table F.9:** Cross-flow characterisation curves for a square, inward opening, hinged window at an opening angle of 15 degrees, for flow approach angles between 0 and 180 degrees.

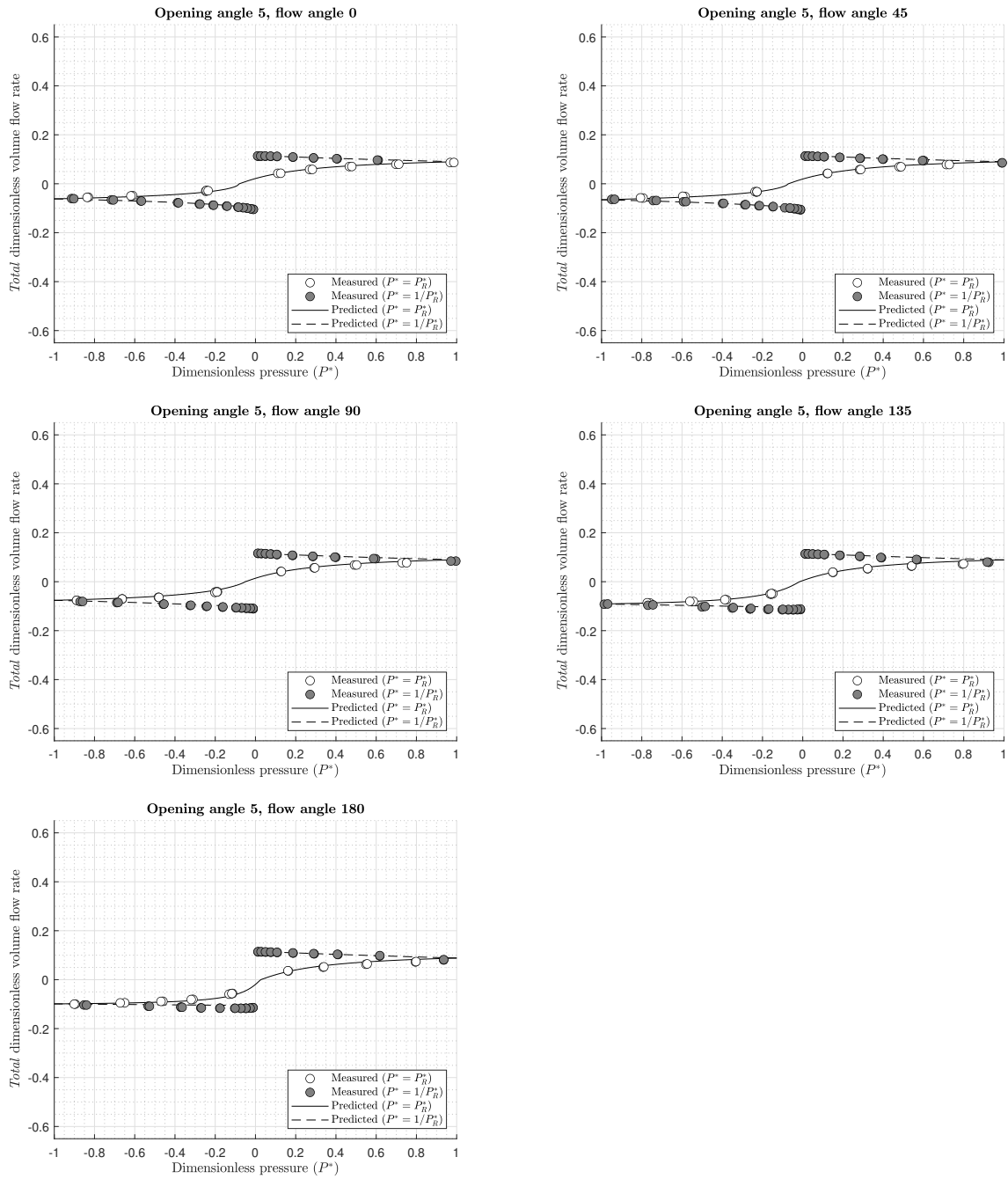


**Table F.10:** Cross-flow characterisation curves for a square, inward opening, hinged window at an opening angle of 5 degrees, for flow approach angles between 0 and 180 degrees.

## Appendix G

# Distributions of the cross-flow velocity coefficient and the direction of the cross-flow on a model building

### G.1 Introduction

The distributions of the cross-flow velocity coefficient and the *façade* cross-flow direction on the surface of a model building measured in Chapter 6 are presented here for a range of wind angles. Data for wind angles between 0 and 180 degrees are depicted. Data for wind angles between 180 and 360 degrees can be inferred by symmetry.



## G.2 Cross-flow velocity coefficient distributions

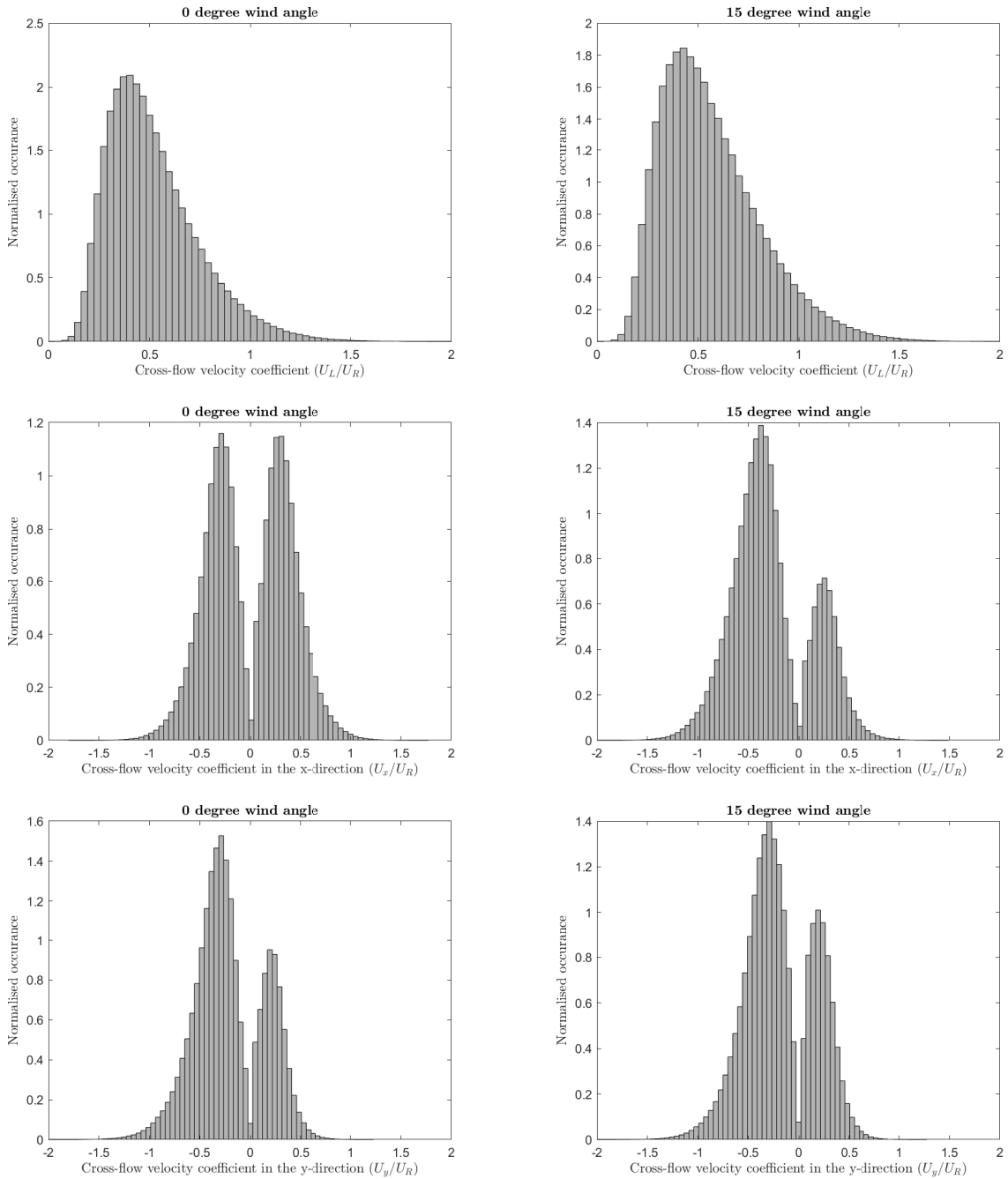


**Table G.1:** Cross-flow velocity coefficient distributions on the surface of a model cube at wind angles of 0 degrees (left) and 15 degrees (right). Distributions are presented for the cross-flow speed (top), the x-component of the cross-flow velocity (middle), and the y-component of the cross-flow velocity (bottom).

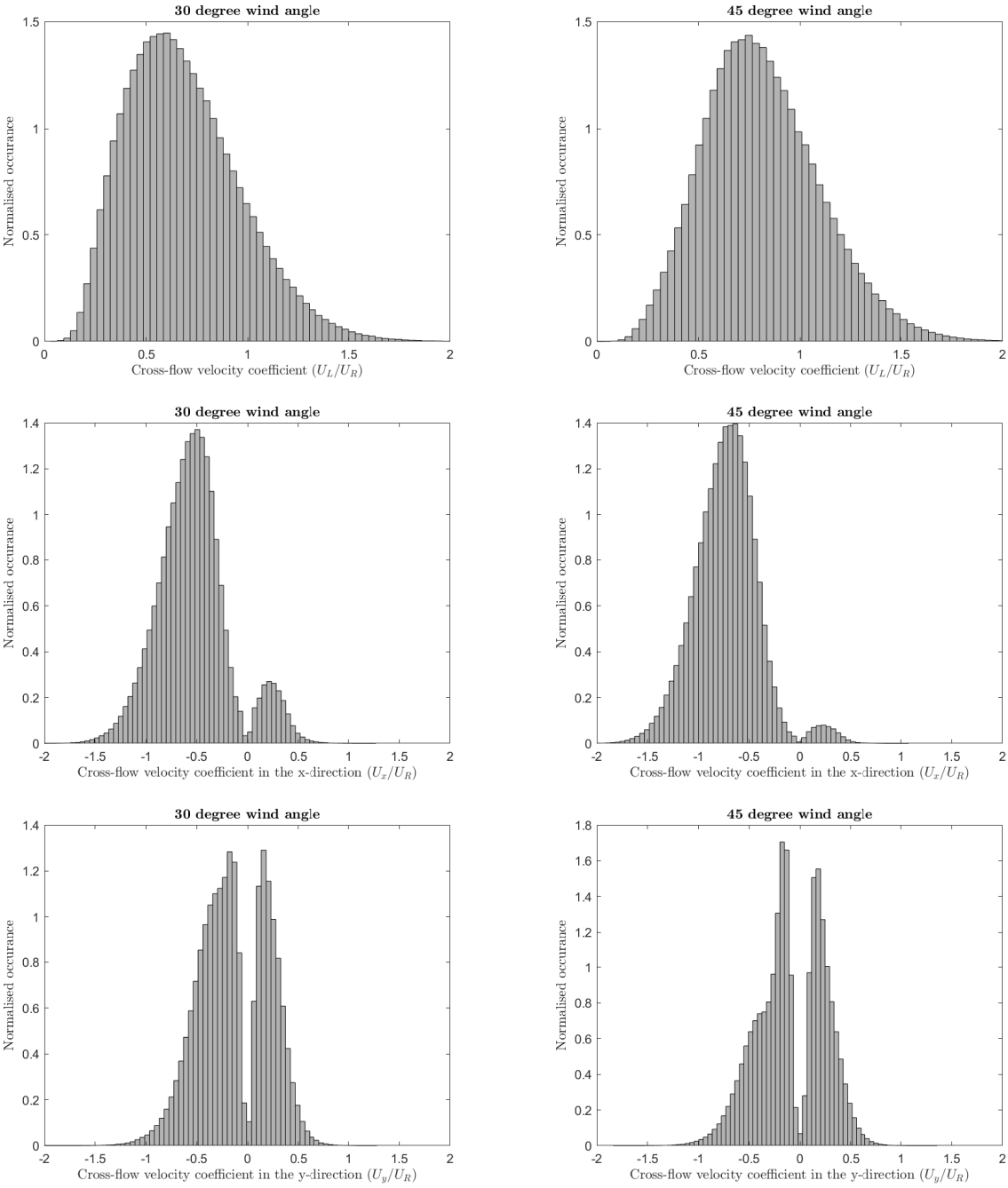


**Table G.2:** Cross-flow velocity coefficient distributions on the surface of a model cube at wind angles of 30 degrees (left) and 45 degrees (right). Distributions are presented for the cross-flow speed (top), the x-component of the cross-flow velocity (middle), and the y-component of the cross-flow velocity (bottom).

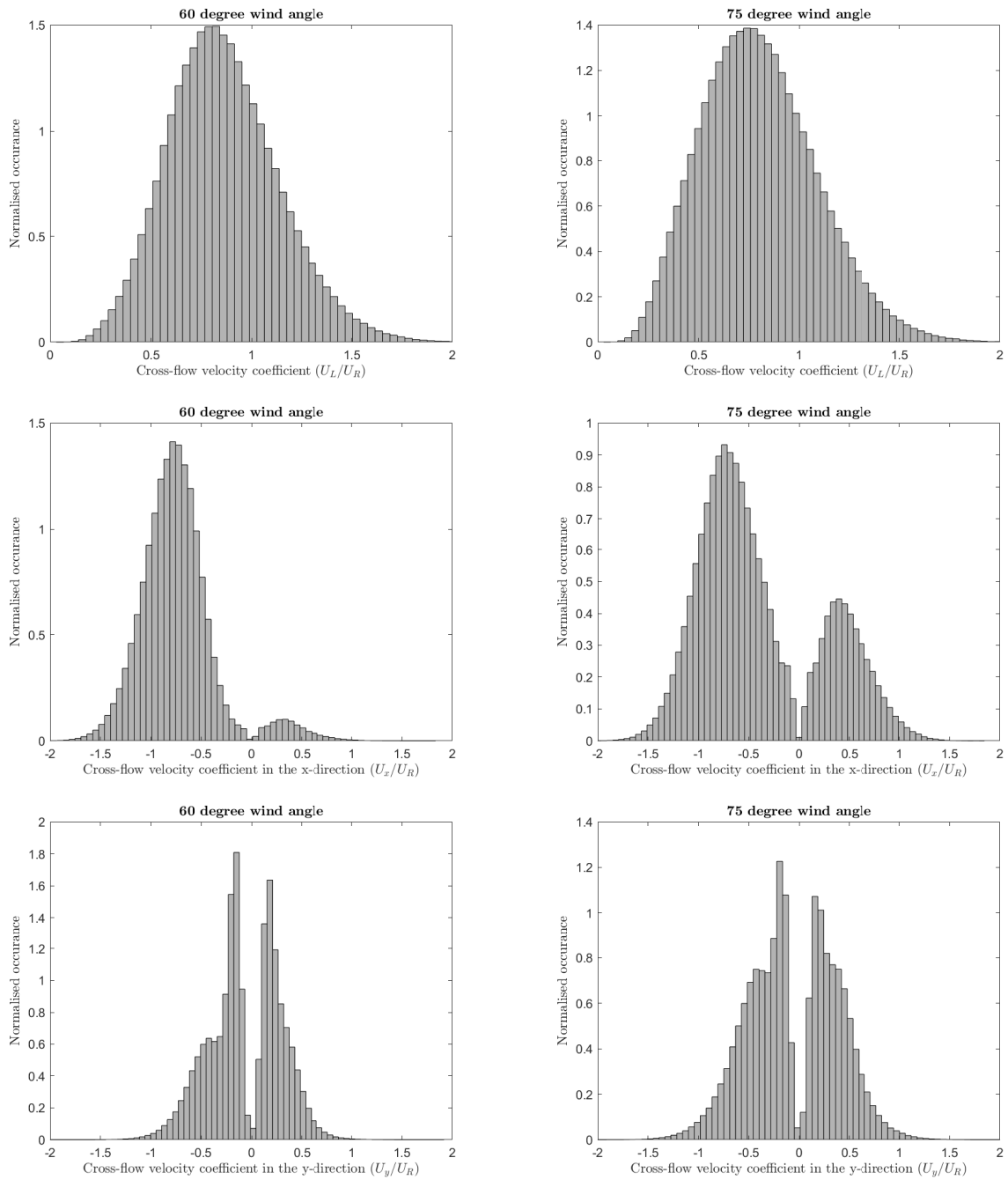


**Table G.3:** Cross-flow velocity coefficient distributions on the surface of a model cube at wind angles of 60 degrees (left) and 75 degrees (right). Distributions are presented for the cross-flow speed (top), the x-component of the cross-flow velocity (middle), and the y-component of the cross-flow velocity (bottom).

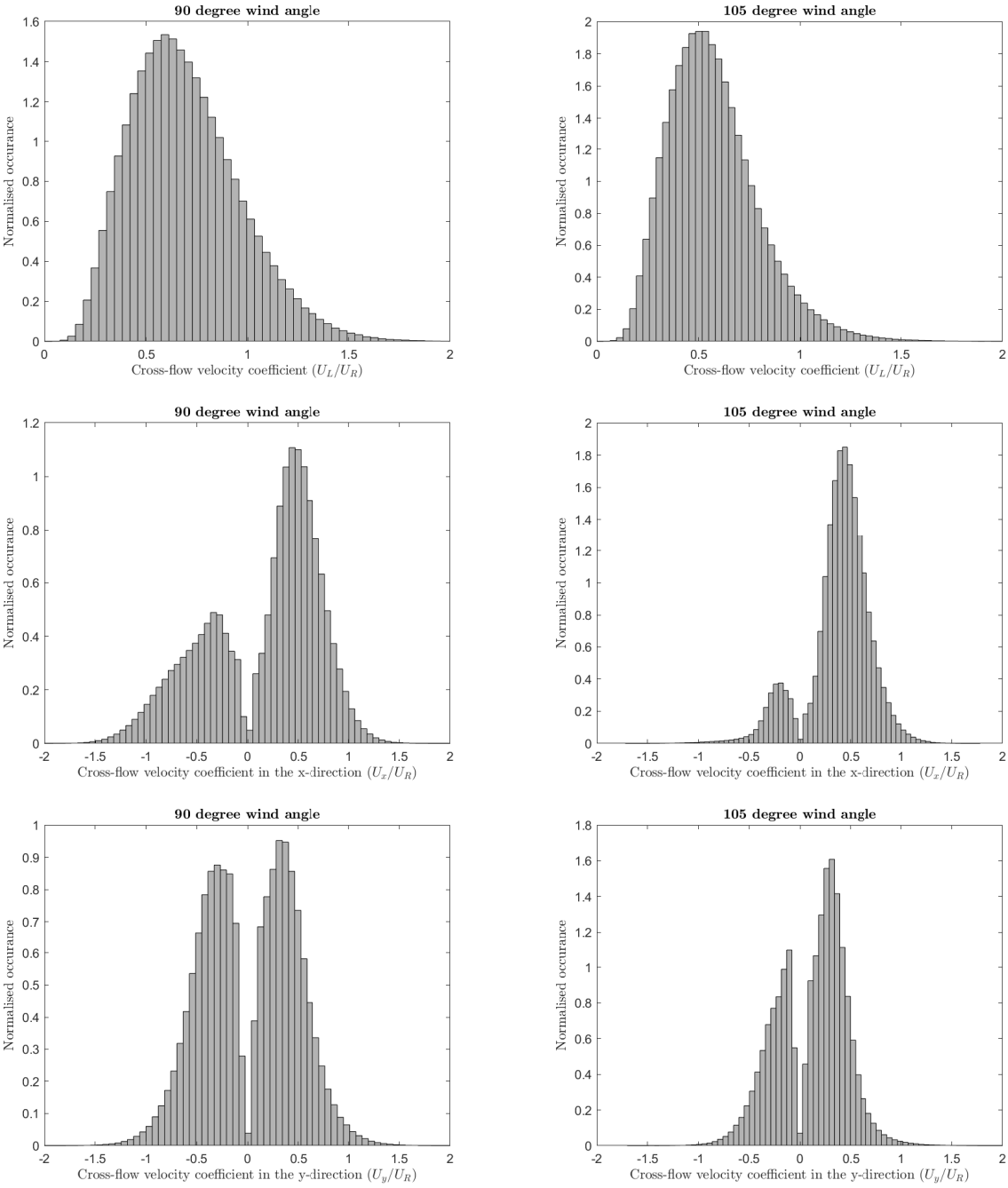


**Table G.4:** Cross-flow velocity coefficient distributions on the surface of a model cube at wind angles of 90 degrees (left) and 105 degrees (right). Distributions are presented for the cross-flow speed (top), the x-component of the cross-flow velocity (middle), and the y-component of the cross-flow velocity (bottom).

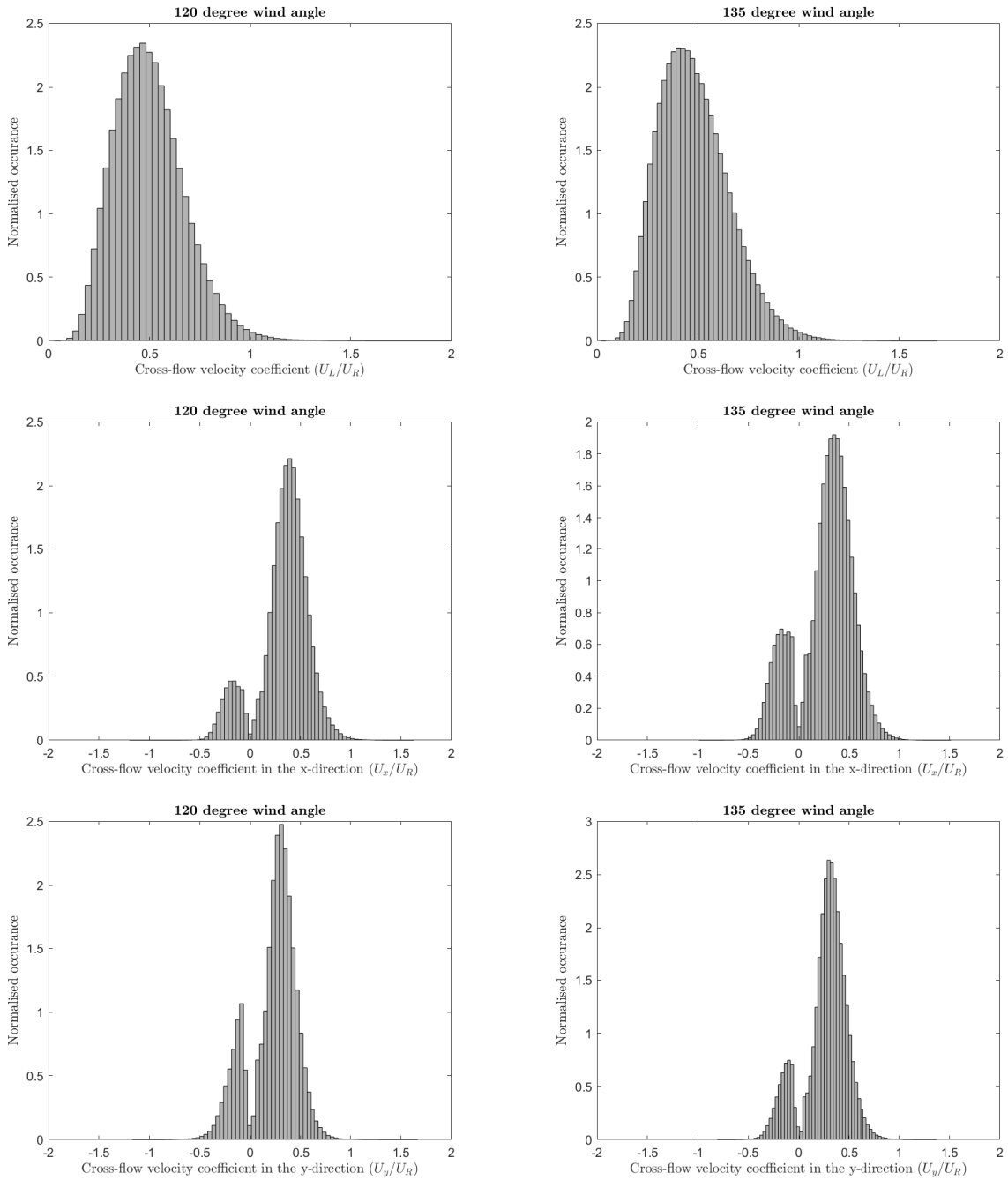


**Table G.5:** Cross-flow velocity coefficient distributions on the surface of a model cube at wind angles of 120 degrees (left) and 135 degrees (right). Distributions are presented for the cross-flow speed (top), the x-component of the cross-flow velocity (middle), and the y-component of the cross-flow velocity (bottom).

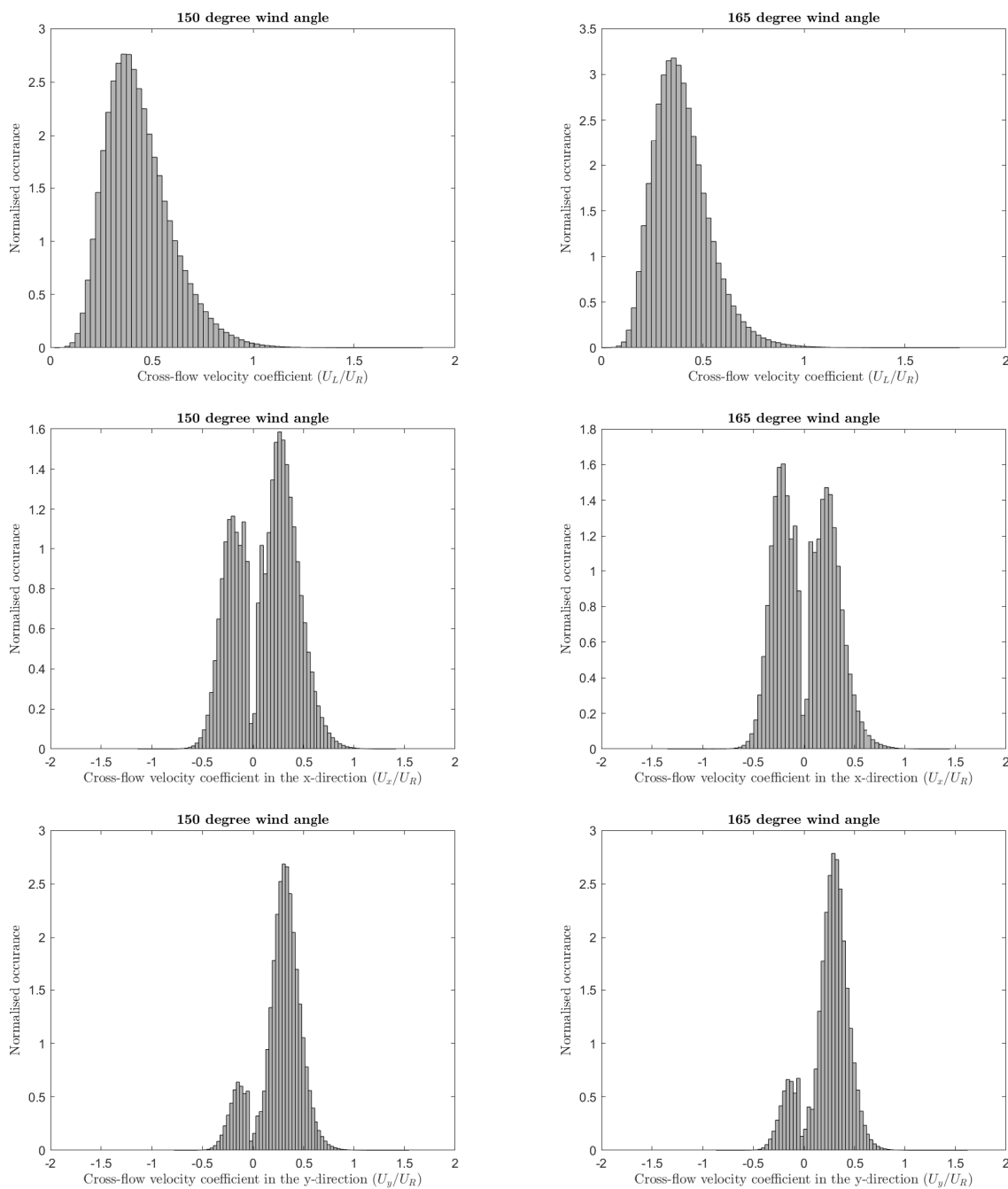


**Table G.6:** Cross-flow velocity coefficient distributions on the surface of a model cube at wind angles of 150 degrees (left) and 165 degrees (right). Distributions are presented for the cross-flow speed (top), the x-component of the cross-flow velocity (middle), and the y-component of the cross-flow velocity (bottom).

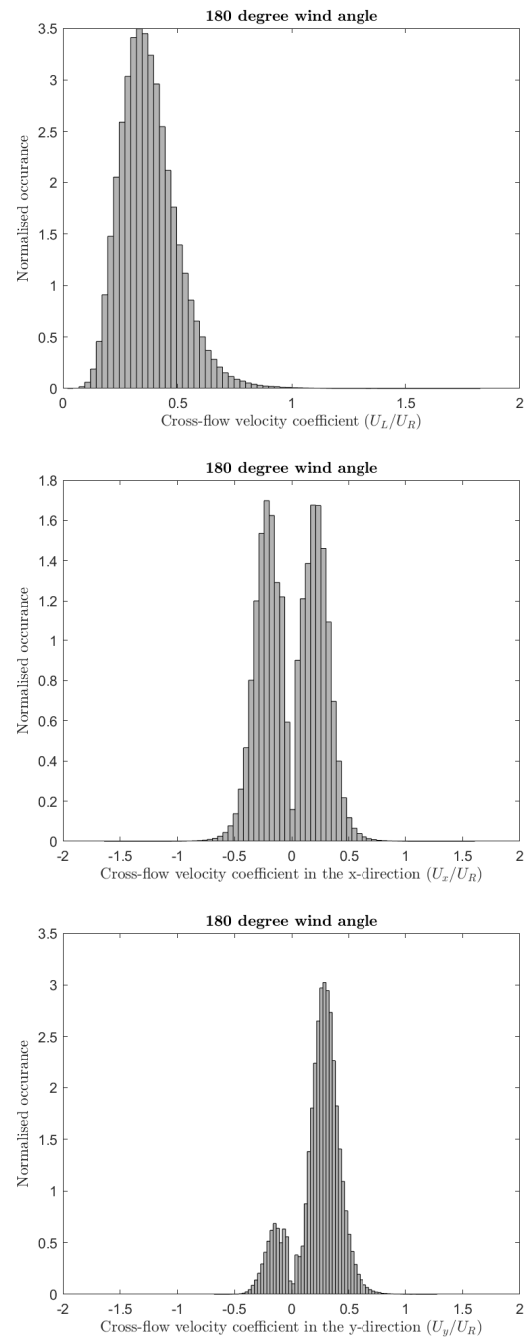


**Table G.7:** Cross-flow velocity coefficient distributions on the surface of a model cube at wind angles of 180 degrees. Distributions are presented for the cross-flow speed (top), the x-component of the cross-flow velocity (middle), and the y-component of the cross-flow velocity (bottom).

### G.3 Cross-flow direction

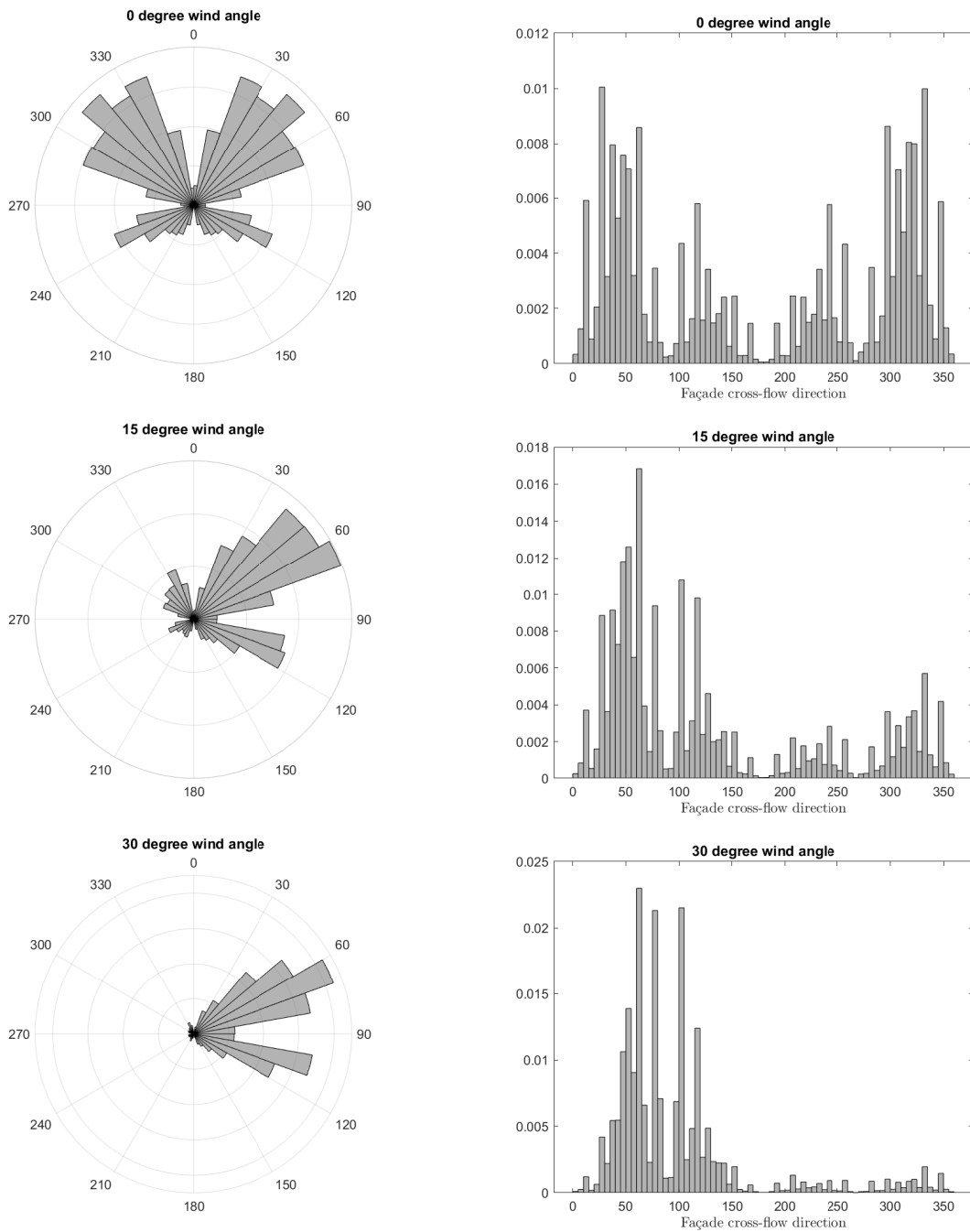


**Table G.8:** Normalised frequency distributions of *façade* cross-flow direction on the surface of a model cube at wind angles of 0 degrees (top), 15 degrees (middle), and 30 degrees (bottom).



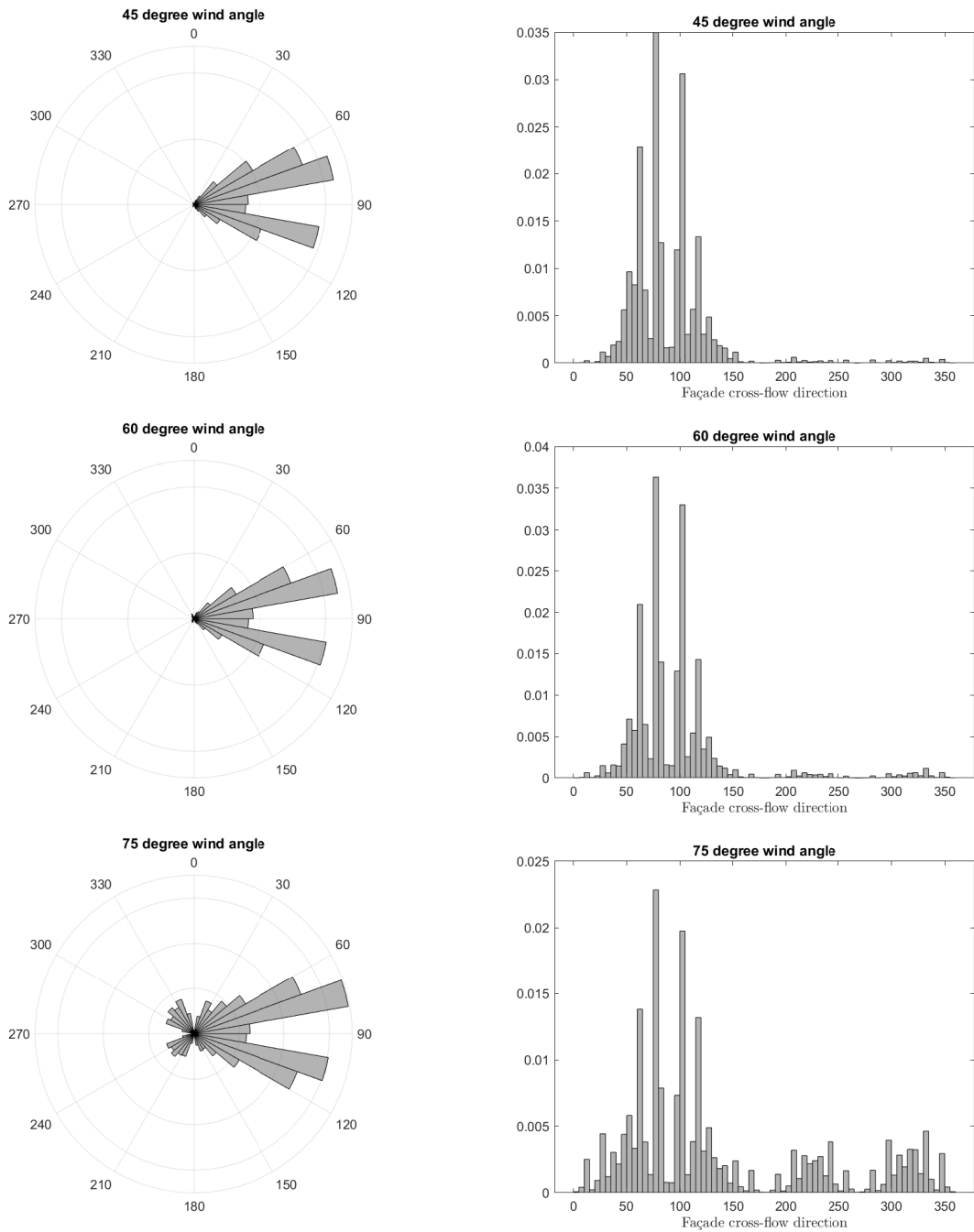


**Table G.9:** Normalised frequency distributions of *façade* cross-flow direction on the surface of a model cube at wind angles of 45 degrees (top), 60 degrees (middle), and 75 degrees (bottom).

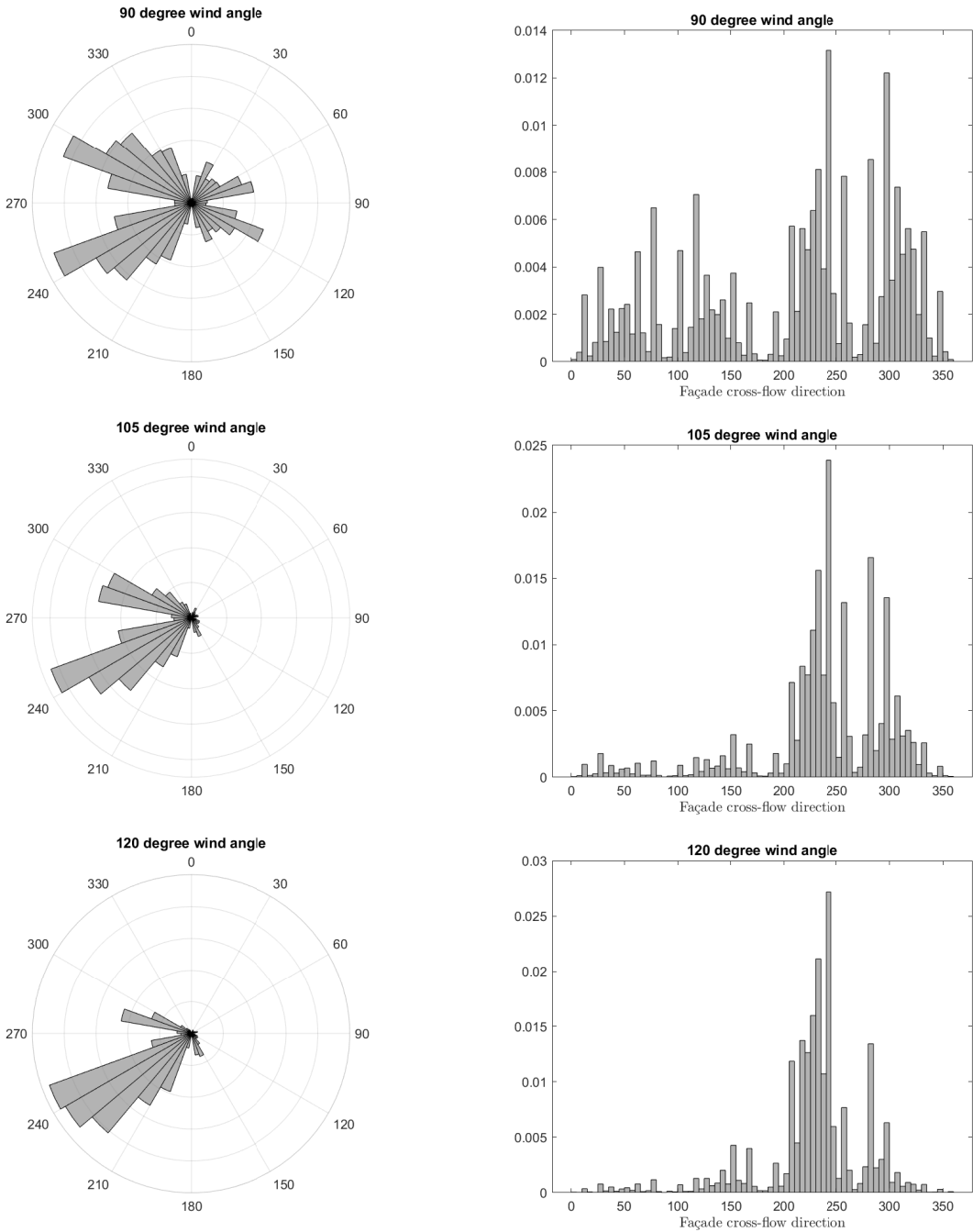
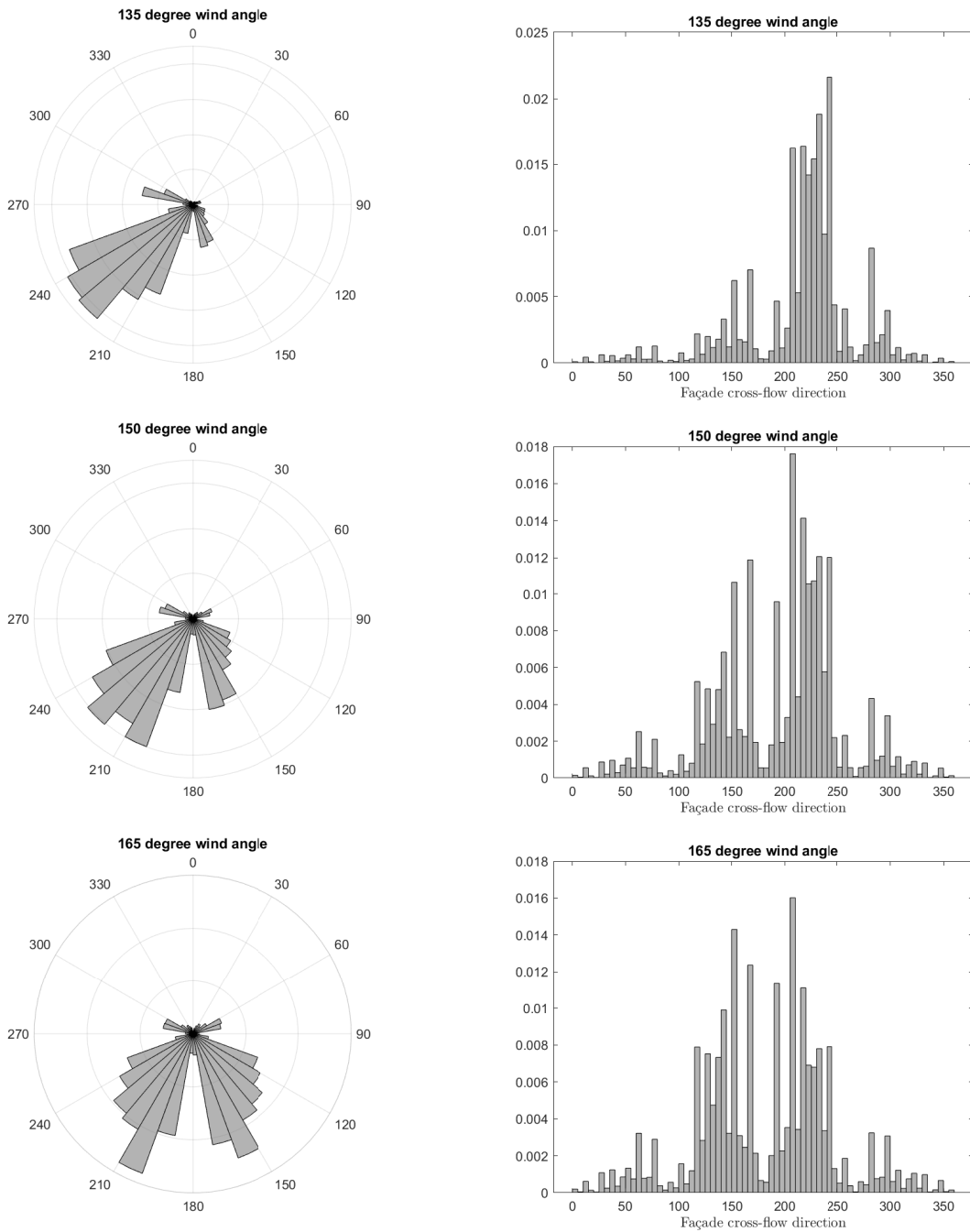


Table G.10: Normalised frequency distributions of *façade* cross-flow direction on the surface of a model cube at wind angles of 90 degrees (top), 105 degrees (middle), and 120 degrees (bottom).



**Table G.11:** Normalised frequency distributions of *façade* cross-flow direction on the surface of a model cube at wind angles of 135 degrees (top), 150 degrees (middle), and 165 degrees (bottom).

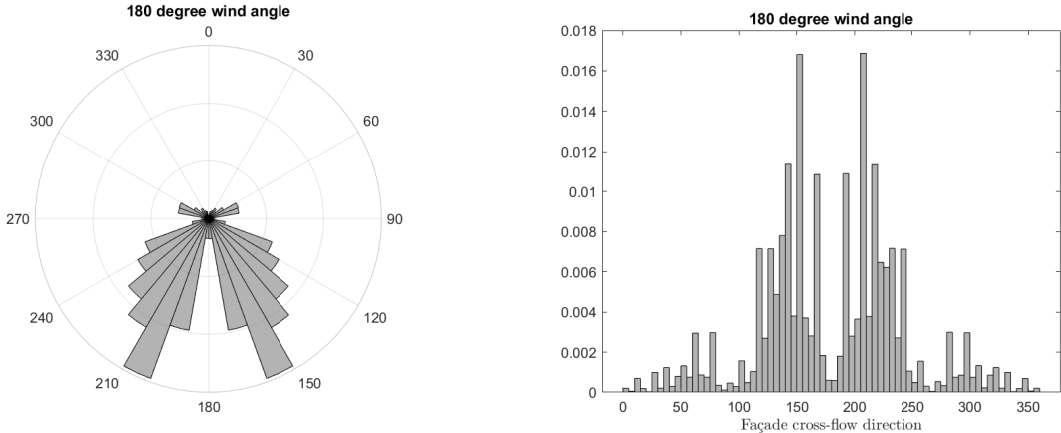


Table G.12: Normalised frequency distributions of *façade* cross-flow direction on the surface of a model cube at wind angles of 180 degrees.